The GEOTECHNICAL RESPONSE of RETAINING WALLS to SURFACE EXPLOSION

NAJLAA ABDUL-HUSSAIN

Thesis submitted to the University of Ottawa
in partial fulfillment of the requirements for the
Doctorate in Philosophy degree in Civil Engineering

Department of Civil Engineering
Faculty of Engineering
University of Ottawa

ABSTRACT

Retaining walls (RW) are among the most common geotechnical structures. They have been widely used in railways, bridges (e.g. bridges abutment), buildings, hydraulic and harbor engineering. Once built, the RW can be exposed to dynamic loads, such as those produced by earthquakes, machines, vehicles and explosions. They must remain operational in aftermath of the natural or human-induced dynamic events. Hence, the understanding of the geotechnical response of RW to these dynamic loads is critical for the safe design of several civil engineering structures such as railways, highways, bridges, and buildings. Although fairly reliable methods have been developed for assessing and predicting the response of RW to dynamic loads induced by earthquakes, there is very little information to guide engineers in the design of RW that are exposed to surface explosions (surface blast loadings). These methods for assessing RW response to earthquake loads cannot directly be applied to the design of RW subjected to surface blast loads. Indeed, blast loads are short duration dynamic loads and their durations are very much shorter than those of earthquakes. The predominant frequencies of a blast wave are usually 2-3 orders of magnitudes higher than those of earthquake wave, and the same can be said for blast wave acceleration as compared to the peak acceleration that results from an earthquake. Thus, RW response under blast loading could be significantly different from that under a loading with much longer duration such as an earthquake. There is a need to increase our understanding of the response of RW to surface explosion loadings since there is a significant increase of terrorist threat on important buildings and some lifeline infrastructures. Transportation structures (bridges, highway, and railway) are unquestionably being regarded as potential targets for terrorist attacks. The purpose of this PhD research is to investigate the geotechnical response of reinforced concrete retaining wall (RCRW) with sand as a backfill material to surface blast loads. The soil-RW model was subjected to a simulated blast load using a shock tube. The influence of the backfill relative density, backfill saturation, blast load intensity, and live load surcharge on the behaviour of RCRW with sand backfill was studied. The dimensions of the stem and heel of the retaining wall in this study were 650 mm (height) x 500 mm (width) x 60 mm (thickness) and 400 mm (width) x 500 mm (length) x 60 mm (thickness), respectively. Soil-RW model was placed inside a wooden box.

The overall height of the box was 1565 mm. The retained backfill extended behind the wall for 1300 mm.

Based on the results, it is found that the maximum dynamic earth pressures were recorded at a time greater than the positive phase duration regardless of the backfill condition. The total earth pressure distribution along the height of the wall showed that the magnitude of total earth pressure for loose and medium backfill at the mid-height of the wall slightly exceeded the dense backfill. In addition, the lateral earth pressures increased with the increase in the blast load intensities. On the other hand, under the same load conditions, an increase in the wall movement was noticed in loose backfill, and a translation response mode was evident in this condition. The mobilized passive resistance of the RW backfill induced by blast load was used to determine the force-displacement relationship. Finally, the susceptibility of the RW with saturated dense sand to liquefaction was examined, and it was ascertained that liquefaction was not triggered when the RW was subjected to a blast load of 50 kPa.

The results and findings of this PhD research will provide valuable information that can be used to evaluate the vulnerability of transportation structures to surface blast events as well as to develop guidance for their design.

To my parents

ACKNOWLEGMENTS

I would like to express my sincere gratitude to my supervisors, Dr. Mamadou Fall and Dr. Murat Saatcioglu for providing me with the opportunity to work on this research project as well as their continuous support. They instilled their trust in me and allowed me the freedom to work independently throughout my research.

I would like to show my appreciation to Dr. Gamal Elnabelsya and Dr. Muslim Majeed for their help throughout the experimental program. The experimental program could not have been completed without their assistance.

I would also like to thank my colleagues and friends who provided their support and assistance: Mr. Jean-Claude Célestin, Mr. Hyunchul Jung and Mr. Amirreza Saremi, Dr. Alameer Ali, Mr. Harshdeep Singh, Mrs. Ghada Ali, Dr. Imad Alainachi, Mr. Sada Haruna and Mrs. Zubaida Al-Moselly.

Finally, I would like to thank my husband Dr. Bessam Kadhom for his support throughout the project and in particular, his help in building the retaining walls and the box, and my children Reeham and Haider for their endless support and encouragement.

Table of Contents

List of Figures

List of Tables

LIST OF SYMBOLS AND ACRONYMS

RW	Retaining wall
RCRW	Reinforced concrete retaining wall
m	Mass
u	Displacement
ü	Acceleration
k	Spring constant (stiffness)
F(t)	External force
u(t)	Total displacement
$u_{\circ}$	Initial displacement
$v_{\circ}$	Initial velocity
ω	Angular frequency
t	Time
τ	Short duration of time known as the lag
dτ	Incremental time
F(τ)	Impulse of the force
t_d	Duration of the blast load of positive phase
T	Natural period of vibration of the structure
P_o	Ambient atmospheric pressure
P_{so}	Incident overpressure
W	Charge weight
R	Standoff distance
Z	Scaled distance
P_r	Reflected pressure
F_o	Peak force
I	Impulse
SDOF	Single degree of freedom
FEM	Finite element method
D_v	Maximum vertical displacement at the ground surface
ρ	Mass density
v_c	Seismic/longitudinal wave velocity in soil
h	Depth of soil layers
U	Wave velocity at any point of a pressure wave
C	Sound wave velocity
PV	Particle velocity
PPV	Peak particle velocity
v_s	Shear/torsional wave velocity
v_r	Rayleigh wave velocity
G	Shear modulus of the soil
K	Bulk modulus
v_p	Compression wave velocity
μ	Poisson’s ratio;
E	Modulus of elasticity of the soil
SHPB	Split Hopkinson Pressure Bar tests

MSE	Mechanically stabilized earth wall
P_{AE}	Maximum dynamic active force per unit width of the wall
K_{AE}	Total lateral earth pressure coefficient
γ	Unit weight of the soil
H	Height of the wall
φ	Angle of internal friction of the soil
δ	Angle of wall friction
i	Slope of ground surface behind the wall
β	Slope of the wall relative to the vertical
k_h	Horizontal wedge acceleration divided by g
k_v	Vertical wedge acceleration divided by g
g	Gravitational acceleration
P_A	Initial static earth pressure
ΔP_{AE}	Dynamic increment
K_A	Static lateral earth pressure coefficient
ΔK_{AE}	Dynamic increment coefficient
θ	Angle of the back of the wall with the vertical
W	Weight of the soil wedge
TNT	Trinitrotoluene
d_{perm}	Permanent wall displacement
d_w	Relative flexibility of the wall
d_θ	Relative flexibility of rotational base constraint
a_y	Yield acceleration
D_{50}	Mean grain size
D_{10}	Effective size
C_u	Uniformity coefficient
C_z	Coefficient of gradation
LC	Load cell
SG	Strain gauge
TSR	Total stress ratio
σ	Stress waves induced by blast loads
M_n	Nominal moment
A_s	Area of reinforcement on the tension face the section
f_y	Tensile strength of the reinforcement
d	Distance from the extreme fiber in compression to the centroid of the steel on the tension side of the member
f_c	Compressive strength of the concrete
b	Width of the compression face of the wall
DIF	Dynamic increase factor
r_u	Ultimate unit resistance of the section
L	Height of the stem
K_{LM}	Load-mass transformation factor
MDOF	Multiple degree of freedom
R_t	Resistance time history
$\dot{u}$	Velocity
$\ddot{u}$	Acceleration

c	Damping
I_e	Moment of inertia of cracked section
TRW	Top of retaining wall
SFL/SFLFP	Soil first layer
SSL/SSLFP	Soil second layer
STL/STLFP	Soil third layer
MIDRW	Mid height of retaining wall
SFRL/SFRLFP	Soil fourth layer
SFIL/SFILFP	Soil fifth layer
SSXL	Soil six layer
SFLSP	Soil first layer second panel
SFLTP	Soil first layer third panel
SSLSP	Soil second layer second panel
SSLTP	Soil second layer third panel
STLSP	Soil third layer second panel
STLTP	Soil third layer third panel
SFRLSP	Soil fourth layer second panel
MPr	Medium intensity reflected pressure
HPr	High intensity reflected pressure
TH	Theoretical
Exp	Experimental
PWP	Pore water pressure
Δu	Excess pore pressure
MPS	Water potential sensor
L	Loose backfill
M	Medium backfill
D	Dense backfill
Psat	Partially saturated backfill
Sat	Saturated backfill
Sur	Live load surcharge
r_u	Excess pore water pressure ratio
γ	Shear strain
Δ	Lateral deformation
τ_{max}	Shear stress

Chapter 1 Introduction

1.1 Problem Statement

Two pioneers that developed analytical solutions of the problem of lateral static earth pressures on retaining structures are Coulomb (1776) and Rankine (1857). Their work provides basis for static earth pressure analyses and design procedures. The prediction of actual forces and deformations on retaining walls under static condition is a complicated soil-structure interaction problem. The dynamic response of retaining walls is more complex as it depends on the mass and stiffness of the wall, the backfill and the underlying ground, the interaction among them and the nature of the input motions (Al Atik, 2008).

The damage mechanism of structures subjected to a blast wave will be different from structures subjected to a seismic motion (Hao and Wu, 2005; Lu and Fall, 2018a, b, c). Blast motions have higher amplitudes and frequency contents, but shorter duration than seismic motions.

The global terrorist attacks against structures have increased intensely in recent years. Many strategic buildings, commercial centers, industrial facilities, residential buildings and some lifeline infrastructures have been targeted in the last three decades. Transportation structures such as bridges, railways and highways are regarded as potential targets for terrorist attacks because of their importance as lifelines, and difficulties associated in protecting them. Different types of explosive devices are used for these attacks. The US Department of State reported more than 14,000 global terrorist attacks in 2007, killing more than 20,000 people (Buchan and Chen 2010). Few studies were conducted to evaluate underground structures (piles, tunnel, etc.) and embankment dams subjected to surface explosions as discussed later. However, there is no study available in the literature to address the vulnerability of retaining walls subjected to blast loading. There is a need to address this knowledge gap.

1.2 Objective

The objective of this research is to investigate the geotechnical response of retaining walls (RW) to surface blast loads by conducting experimental study (shock tube tests). The influence of the following factors on the response of RW to blast load is investigated:

- i- Influence of backfill relative density;
- ii- Influence of backfill saturation;
- iii- Blast load intensity;
- iv- Influence of live load surcharge.

1.3 Research Approach and Methods

The research approach and methods adopted in this study are schematically shown in Figure 1.1. To fulfill the objective of this research, an experimental technique (simulated blast testing) was conducted to assess the dynamic response of retaining walls subjected to blast loading. Simulated blast testing was conducted in a laboratory testing environment with a little potential of experimental hazards. The shock tube, which is available at the structures laboratory of the University of Ottawa, is used in this study.

The experimental program was divided into four test series. **Test Series # 1** was devoted to study the influence of various relative densities of backfill on the dynamic response of soil-RW model when subjected to blast loading. Three sand samples with various relative densities (loose, medium, and dense) were examined. **Test Series # 2** was dedicated to address the dynamic behaviour of soil-RW model along with the influence of different degrees of saturation. Three sand backfill samples with different saturation degrees (saturated, partially saturated, and dry) were tested. In **Test Series # 3**, the influence of blast load intensity on backfill retaining wall behaviour was investigated. In **Test Series # 4**, a live load surcharge was applied on the top of the backfill.

The influence of live load surcharge on behaviour of backfill retaining wall was addressed. For every test conducted in this study, the system (RW and soil) was subjected to a single blast shot.

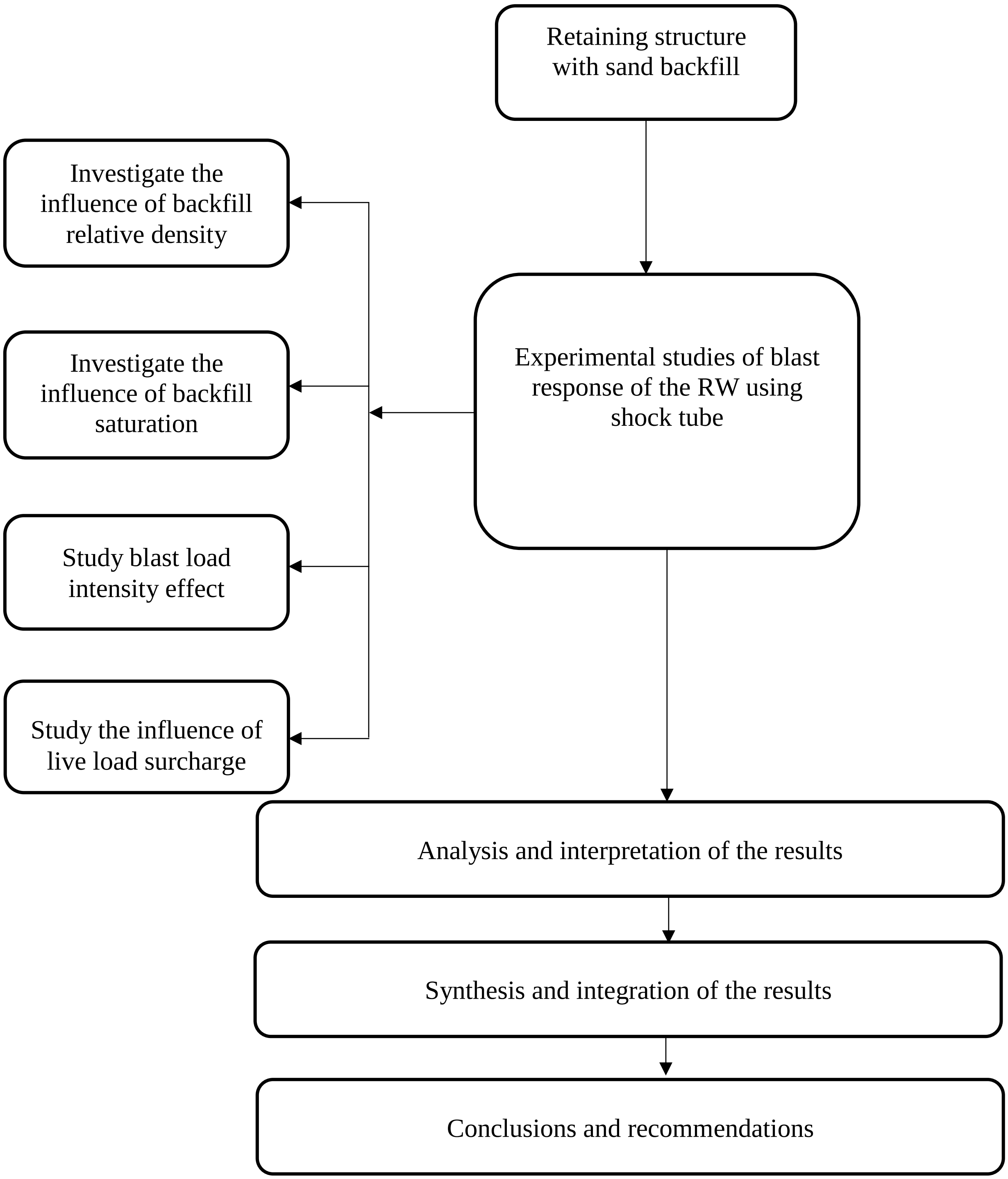

Figure 1.1: Research approach and methods

1.4 Tasks and Organization of the Thesis

This PhD manuscript is organized into seven chapters. **Chapter one** contains the introduction, which includes problem statement, objective and research approach and methods. **Chapter two** provides background and literature review. **Chapter three to five** are structured into a paper-based thesis format. It should be emphasized that because the main results of these chapters are presented as articles, some information is repeated in these chapters. The reason is that each article is independently written in accordance with the manuscript preparation instructions of the corresponding journal. The influence of various relative densities, degrees of saturation of backfill, blast load intensities, and live load surcharge on the dynamic response of soil-RW model was addressed in these chapters. **Chapter three** consists of technical paper I. The chapter addresses the effects blast shots on the lateral earth pressures of a sand backfill retaining wall. **Chapter four** includes technical paper II. This chapter deals with the influence of a single shot on the modes of wall movement of cantilever retaining walls. **Chapter five** contains technical paper III which describes the variations in the pore pressure due to blast loading. **Chapter six** provides a synthesis of the results as well as implications for geotechnical design of retaining structures while a summary of the major findings and conclusions are presented in **Chapter seven**.

Chapter 2 Theoretical and Technical Background

This chapter provides technical information and data that facilitate the understanding of the results presented in the thesis. This background information and data are discussed in five sections. The first section presents the fundamentals of air blast load effects, a general description of blast process, structural response to blast loading, material behaviour under high strain rates and blast wave-structure interaction. The second section is devoted to addressing the blast wave propagation in soil, general material stress-strain response, the dynamic deformation mechanism of soils under blast loading and cratering processes. The third section addresses the design of retaining walls. The fourth section provides a literature review on previous studies on the response of RW to dynamic loadings. Finally, the fifth section provides a detailed technical description of the shock tube and instruments used.

2.1 Fundamental of Air Blast Load Effects

2.1.1 Introduction

Air blasts generate dynamic impulsive loads. An impulsive load can be defined as a load (or pressure) applied on the target within a short period of time. Many analytical methods are available to calculate the dynamic response of a structure subjected to blast loading (Lu and Fall, 2018a,bc). The methods consist of simplified analysis using a single degree of freedom (SDOF) system and advanced methods like finite element method (FEM) ((Fujikura and Bruneau 2012). The equation of motion of undamped SDOF system is given by Equation 2.1 (Biggs, 1964).

$$m\ddot{u} + ku = F(t) \tag{2.1}$$

where,

m is mass;

u is displacement;

$\ddot{u}$ is acceleration of the mass;

k is spring constant (stiffness); and,

F(t) is external force.

The significance of damping in controlling the maximum response of a structure under impulsive loading is much less than the corresponding response of a structure subjected to periodic or harmonic loading. This is because the maximum response to an impulsive load is reached quickly, before the damping forces can absorb much energy from the structure (Lu et al. 2017). However, damping may be important during the free vibration phase of response, following the initial impulsive load.

The response of an undamped, linearly responding SDOF system subjected to general dynamic loading, including the effects of initial conditions, is given by Equation (2.2) (Mario Pas, 1991).

$$u(t) = u_\circ cos\omega t + \frac{v_\circ}{\omega} sin\omega t + \frac{1}{m\omega}\int_0^t F(\tau) sin\omega(t-\tau)d\tau \qquad (2.2)$$

where,

$u(t)$ is total displacement;

$u_\circ$ is initial displacement;

$v_\circ$ is initial velocity;

ω is angular frequency;

t is time

τ is short duration of time, known as the lag;

$d\tau$ is incremental time;

m is mass; and,

$F(\tau)$ is impulse of the force.

Based on the relationship between the duration of the blast load (t_d) and the natural period of vibration of the structure (T), the loading can be categorized into three design ranges; quasi-static (pressure loading), impulsive loading, and dynamic loading (Mays and Smith, 1995).

- Quasi-static (pressure loading)

When t_d is longer than T, the loading is referred to as quasi-static loading. In this case, the structure reaches its maximum displacement before the blast load undergoes any significant decay. The maximum displacement is a function of peak blast load and stiffness.

- Impulsive loading

Where t_d is shorter than T, the situation is described as impulsive loading. In this case, the blast load pulse decays before any significant displacement occurs. Since most deformation occurs at times greater than t_d, the displacement is a function of impulse, stiffness and mass.

- Dynamic loading

When t_d and T are close to each other, the assessment of the response is more complex. A complete solution of the equation of motion of the structure is required.

For designers, predicting the final state of the blast loaded structures is often the principal requirement rather than the detailed knowledge of the displacement-time history (Mays and Smith, 1995).

2.1.2 Explosion and Blast Process

Explosion can be defined as a rapid and sudden release of a large amount of energy to the atmosphere, forming a blast wave. Explosion can be classified as physical, nuclear, or chemical events (Ngo et al., 2007).

The detonation of a high explosive generates hot gases under pressure ranging between 100 and 300 kilobar (kb) associated with a temperature of about 3000 to 4000 °C (Ngo et al., 2007). When an explosion is initiated, a blast wave is formed and rapidly moved outward from the explosion center at very high speed in all directions. This leads to an increase in air pressure above the ambient atmospheric pressure (P_o). The rapid increase of pressure produced by the blast shock wave is called incident overpressure, or only overpressure (P_{so}) (Kadhom, 2015). When the shock front arrives at a given point, the overpressure at that point suddenly increases from zero to peak overpressure in less than a microsecond. The magnitude of the peak overpressure and the variation of the overpressure with time depends on the type and amount of explosive materials, the height of the explosion from the ground, and the distance from the explosion epicenter (Ngo et al., 2007; Lu and Fall 2017, 2015).

Typically, the blast pressure-time history profile consists of two phases, as shown in Figure 2.1. It can be seen that in the positive phase, the overpressure increases instantaneously from the ambient pressure to the peak pressure and then drops back to the ambient pressure over a period equal to t_d (positive phase duration). Conversely, in the negative phase, suction is produced, and as a result, the blast wind moves toward detonation centre rather than radiating away from it. The under-pressure at the negative phase is lower in magnitude and longer in duration than that of the positive phase (Draganic and Sigmund, 2012). Therefore, only the blast pressure profile's positive phase is considered in blast resistant design of structures (Biggs 1964).

The impulse of blast wave is defined as the area under the pressure-time curve. The positive phase impulse (I_o) can be found as follows (Clough and Penzien, 1975):

$$I_o=\int_0^{t_d} P(t)dt \qquad (2.3)$$

where,

P(t) is overpressure function with respect to time; and,

t_d is duration of positive phase.

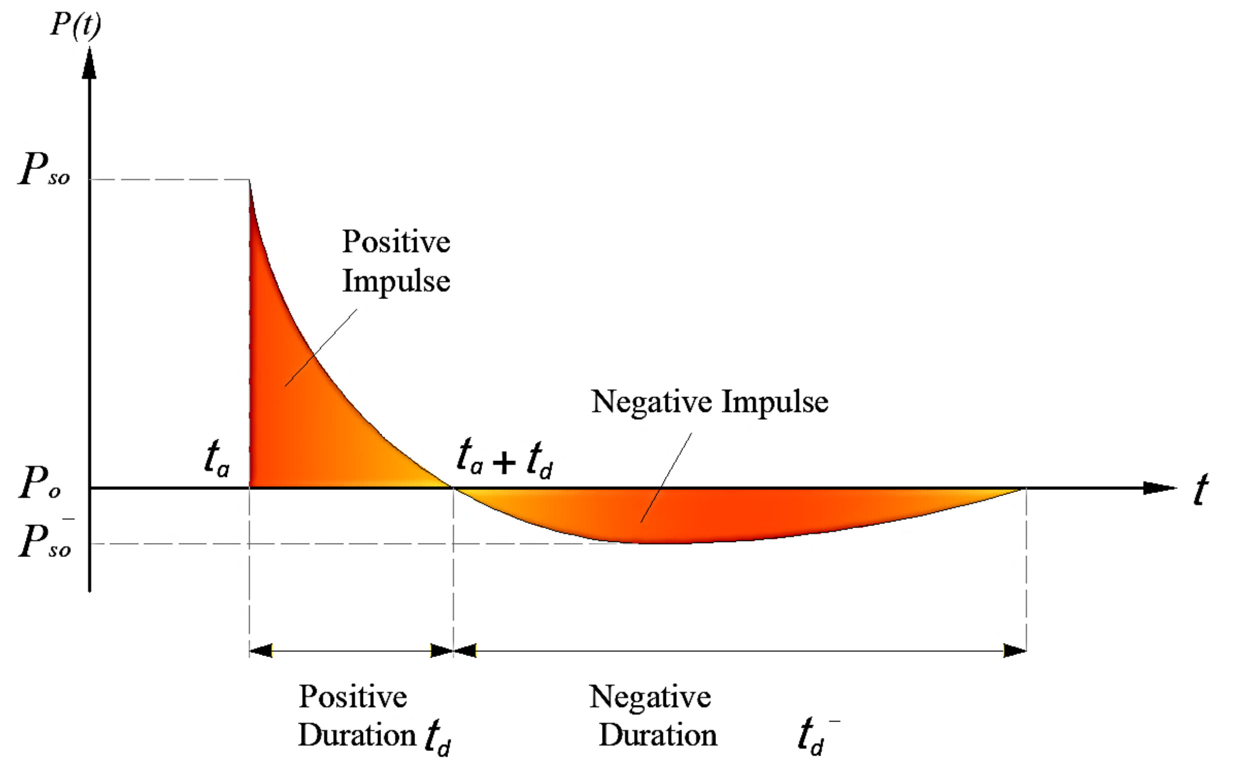

Figure 2.1: Blast wave pressure with time history (Kadhom, 2015)
P_o: Ambient atmospheric pressure; P_{so}: Peak overpressure

Charge weight (*W*) and standoff distance (*R*) between the blast center and the target are the two parameters that are used to determine the magnitude of a bomb threat. It is convenient to scale these blast parameters and express them as "scaled distance" (Z), where $Z = R/W^{1/3}$, also known as the Hopkinson-Cranz Scaling. This scaling law indicates that bombs with different change weights produce similar blast waves if their scaled distances are equal. Scale distance is frequently used in blast analyses and design (Kadhom, 2015, Jayasinghe, 2014 and Smith and Hetherington, 2011). The most common expressions that used in calculating the peak overpressure (P_{so}) as a function of scaled distance are shown in Table 2.1.

Table 2.1: Different expressions for predicting peak overpressure (Pso) (Ngo et al. 2007)

$P_{so} = \frac{6.7}{Z^3} + 1\ bar\ (P_{so} > 10\ bar)$ $P_{so} = \frac{0.975}{Z} + \frac{1.455}{Z^2} + \frac{5.85}{Z^3} - 0.019\ bar\ (0.1 < P_{so} < 10\ bar)$	Brode (1955)
$P_{so} = 6784\frac{W}{R^3} + 93\left(\frac{W}{R^3}\right)^{\frac{1}{2}}\ (bar)$	Newmark and Hansen (1961)
$P_{so} = \frac{1772}{Z^3} - \frac{114}{Z^2} + \frac{108}{Z}\ \ (kPa)$	Mills (1987)
where, P_{so} is the peak overpressure; W is the charge weight; R is the standoff distance between the blast center and the target; and, Z is the scaled distance	

Reflected pressure is generated as a result of blast wave reflection soon after the incident pressure interacts with a solid surface at an angle of incidence relative to the direction of wave (Figure 2.2). The reflected pressure (P_r) can be predicted using Equation 2.4 (Cormie et al. 2009).

$$\boldsymbol{P_r = 2P_{so}\left(\frac{7P_o + 4P_{so}}{7P_o + P_{so}}\right)} \tag{2.4}$$

where,

P_r is reflected pressure;

$\boldsymbol{P_o}$ is ambient atmospheric pressure; and,

$\boldsymbol{P_{so}}$ is peak overpressure.

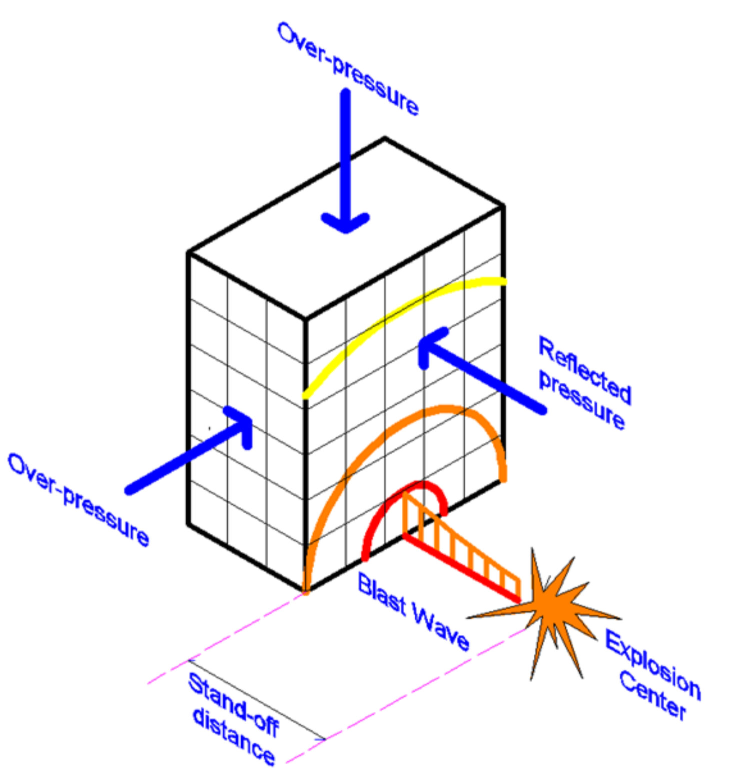

Figure 2.2: Blast loads on building (Kadhom, 2015)

2.1.3 Structural Response to Blast Loading

The analysis of dynamic response of a structure subjected to blast loading is a complex process since it involves the effects of high strain rates, non-linear behaviour of materials, and uncertainties in blast load characteristics (Ngo et al. 2007). To simplify the blast analysis, both the structure and loading can be idealized. The structure is idealized as a SDOF system, while the blast load is idealized as a triangular pulse having a peak force of F_o and positive phase duration t_d (Figure 2.3). The forcing function is determined as follows (Chopra, 2007):

$$F(t) = F_o(1 - \frac{t}{t_d}) \tag{2.5}$$

where,

F_o is peak force;

t_d is duration of positive phase; and,

t is time.

The area under the force-time curve is represented as blast impulse (I), and is given by:

$$I = \frac{1}{2} F_o t_d \tag{2.6}$$

Thus, the equation of motion for undamped SDOF system becomes (Biggs, 1964):

$$m\ddot{u} + ku = F_o(1 - \frac{t}{t_d}) \tag{2.7}$$

where,

m is mass of structure;

k is spring constant;

u is displacement of mass; and,

$\ddot{u}$ is acceleration of mass.

Large inelastic deformations are expected to occur in structural elements due to the effects of blast loads. Thus, it is necessary to determine the inelastic response. Dynamic inelastic response can be calculated using a step-by-step numerical solution to determine exact analysis results. However, a simplified method, called graphical solution, is often used in blast analysis and design of structural elements. This method involves the use of transformation factors to transform distributed mass and blast pressure to equivalent lumped mass and concentrated force, respectively. The resulting idealized mass-spring model is illustrated in Figure 2.3(a). Furthermore, elasto-plastic stiffness can be used to generate an equivalent idealized elasto-plastic SDOF model that represents the behavior of the element. Simple expressions and charts can then used to obtain the maximum dynamic response of the element for a corresponding resistance function and a given blast forcing function, as shown in Figure 2.4. Charts from TM 5-1300 (1990) are generally used to predict the maximum displacement of the element. This is illustrated in Figure 2.5.

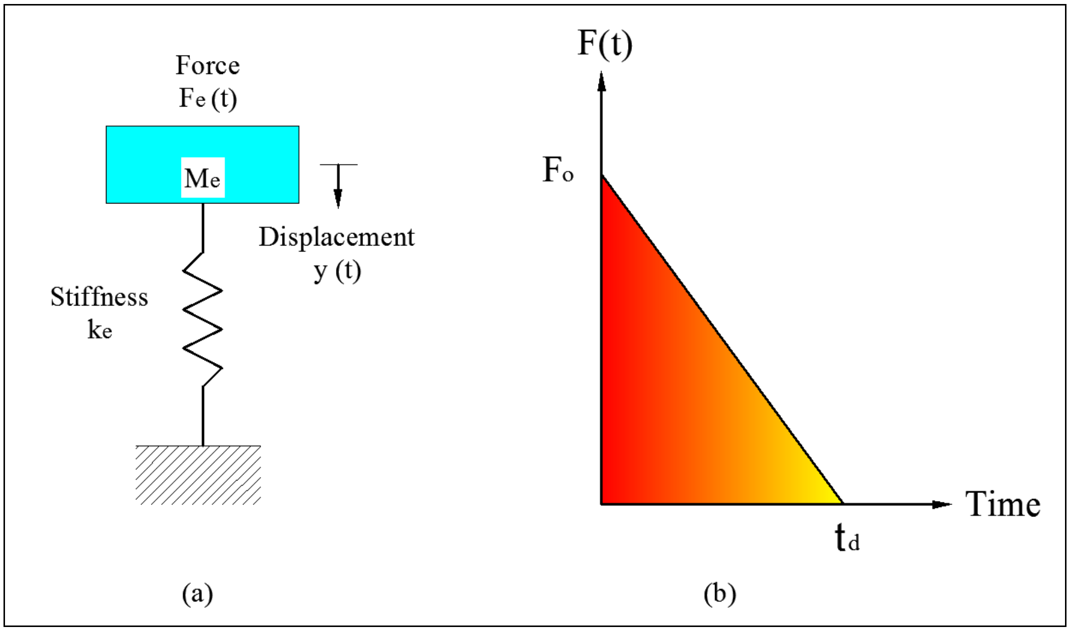

Figure 2.3: (a) Equivalent SDOF system and (b) Idealized blast loading (Kadhom, 2015)

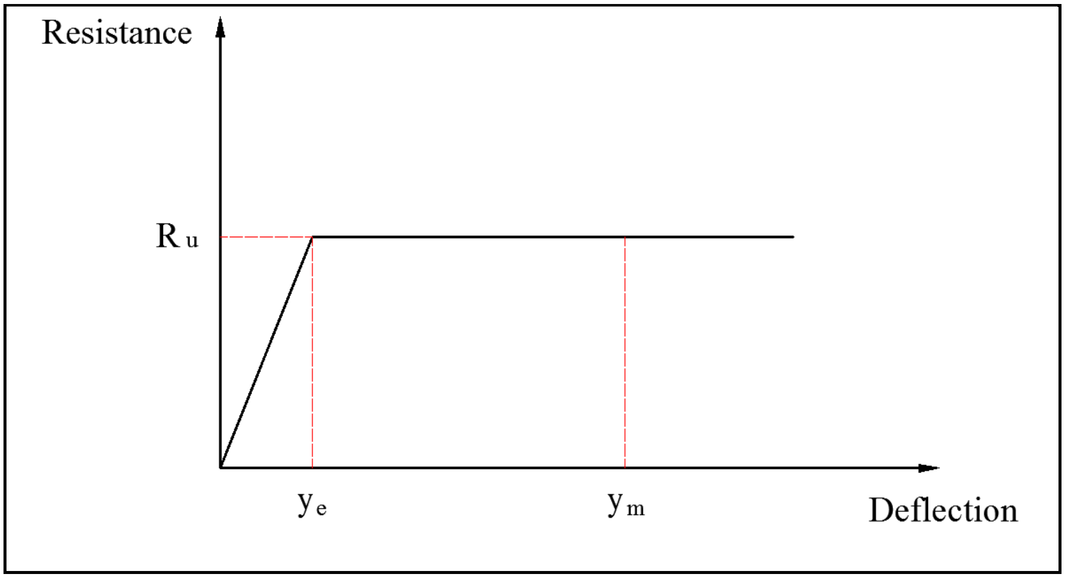

Figure 2.4: Simplified resistance function of an elasto-plastic SDOF system (Ngo et al. 2007 - reproduced by Kadhom, 2015)

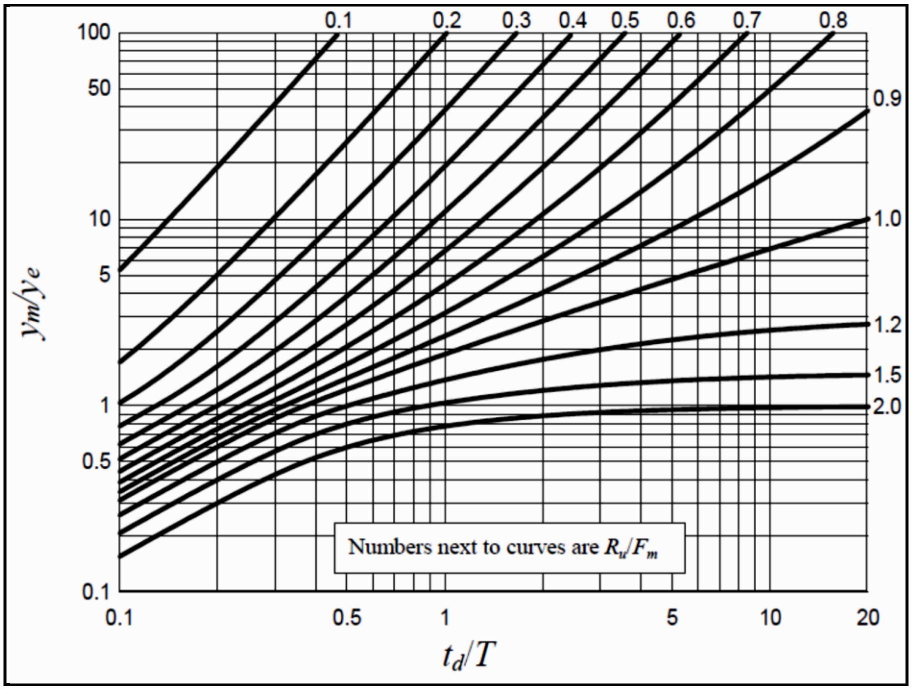

Figure 2.5: Maximum response of elasto-plastic SDF system to a triangular load (Ngo et al. 2007)

2.1.4 Material Behaviour under High Strain Rates

Very high strain rates result from blast loads. The high strain rates could alter the mechanical properties of materials, such as concrete and steel. Due to the strain rate effects, the steel reinforcement tensile strength and concrete compressive strength are significantly increased. Figure 2.6 shows the ranges of strain rates related to different types of loads.

Compressive stress-strain curves of plain concrete tested under different loading rates are illustrated in Figure 2.7. It can be seen that the compressive strength of concrete under dynamic loading is greater than concrete compressive strength under static load. In contrast, concrete stiffness is less sensitive under different loading conditions.

Compressive stress-strain curves of rocks (granite and marble) tested under different loading rates are also presented in Figures 2.8 and 2.9. It can be noted that the striking speed or loading rate has no effect on the stress-strain curves of granite before the first peak. However, after the utmost peaks, the stress-strain is related to the striking speed and broken state (Figure 2.8). At low striking speeds, and if the rock remains intact after being struck, the stress-strain curve after the utmost peak will rebound. When the striking speed is high, the strain increases continuously with stress, and the ability to withstand load decreases, even when the stress decreases to zero. The stress-strain curve of marble (Figure 2.9) is different from granite, as marble is softer than granite. The slope in the post-failure region (elastic modulus) is related to the striking speed or strain rate. Higher strain rate leads to larger elastic modulus (Shan et al., 2000).

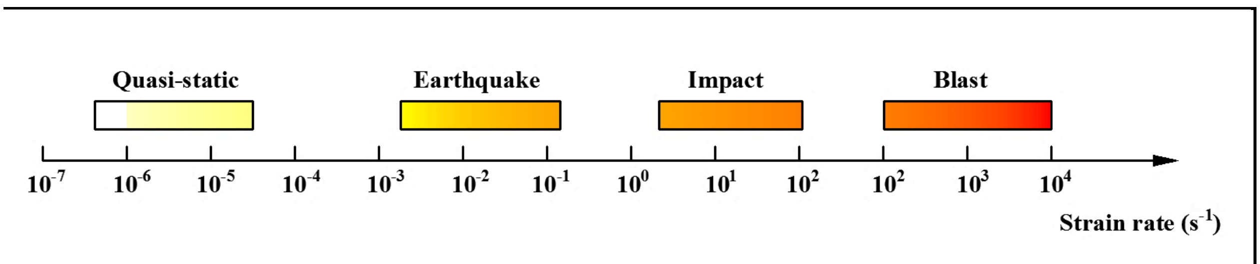

Figure 2.6: Strain rates associated with different type of loading (Ngo et al. 2007-reproduced by Kadhom, 2015)

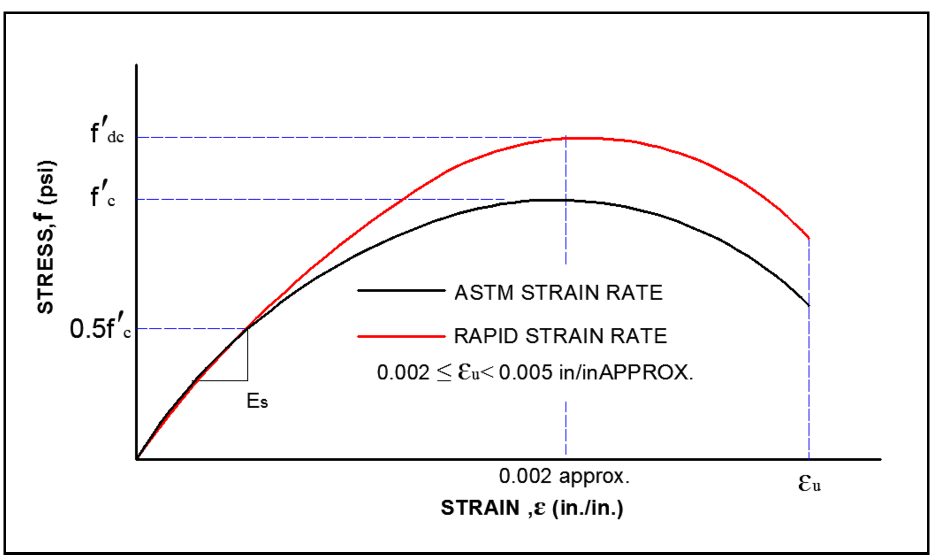

Figure 2.7: Typical stress-strain curve for concrete under slow and rapid loads (Kadhom, 2015)

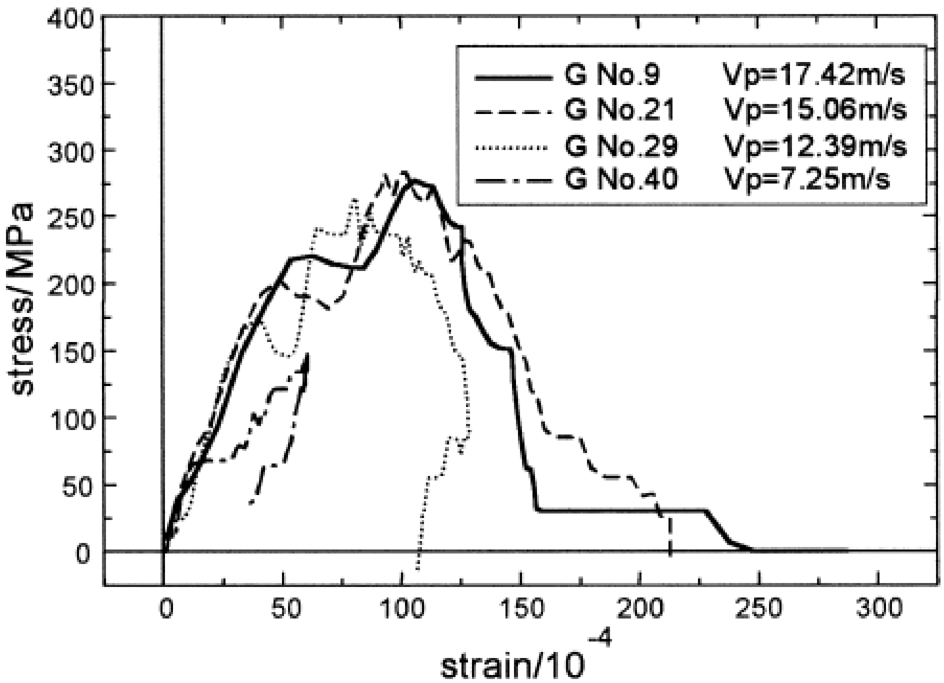

Figure 2.8: Complete dynamic stress-strain curves for granite (Shan et al., 2000)

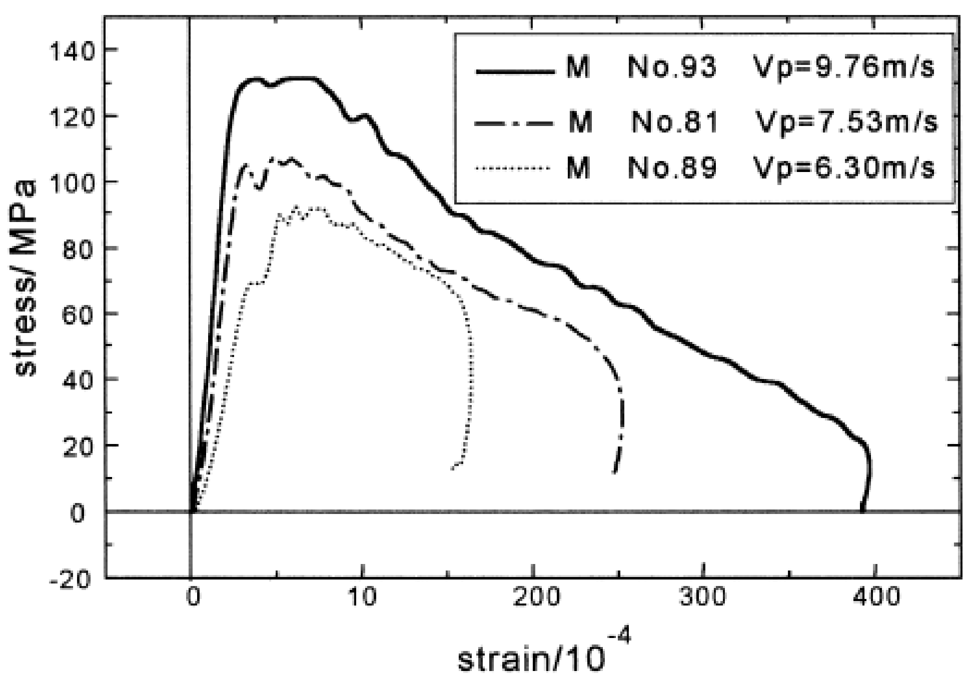

Figure 2.9: Complete dynamic stress-strain curves for marble (Shan et al., 2000)

2.1.6 Blast Wave-Ground Interaction

If the explosive materials are near or on the ground surface, the above-ground or shallow buried structures will be subjected to ground shock. The term “air induced ground shock” is used when the explosive energy is transmitted through the air. While direct transmission of energy through the ground is described as directly induced ground shock. The former results from the air blast wave compresses the ground surface and sends a stress pulse into the underground layers. The latter results when the explosive energy is directly transmitted through the ground.

The maximum vertical displacement at the ground surface (D_v) due to dynamic loads from air induced ground shock can be obtained as follows ((Ngo et al. 2007):

$$D_v = \frac{i_s}{1000\rho v_p} \tag{2.8}$$

where,

i_s is impulse;

ρ is mass density; and,

v_c is wave seismic velocity in soil.

An empirical formula is provided by TM 5-1300(1990) to estimate the vertical displacement in meter taking into account the depth of soil layers:

$$D_v = 0.09W^{\frac{1}{6}}(H/50)^{0.6}(P_{so})^{\frac{2}{3}} \tag{2.9}$$

where,

W is explosion yield in 10^9 kg;

H is depth of the soil layers; and,

P_{so} is peak incident overpressure.

The maximum vertical displacement at the ground surface (D_v) due to dynamic loads from direct ground shock can be predicted using the empirical equations derived by TM 5-1300(1990):

$$D_{v_{rock}} = \frac{0.25R^{\frac{1}{3}}W^{\frac{1}{3}}}{Z^{\frac{1}{3}}} \tag{2.10}$$

$$D_{v_{soil}} = \frac{0.17R^{\frac{1}{3}}W^{\frac{1}{3}}}{Z^{\frac{2}{3}}} \tag{2.11}$$

where,

$D_{v_{rock}}$ is maximum vertical displacement for rock;

$D_{v_{soil}}$ is maximum vertical displacement for dry soil;

R is actual effective distance from the explosion; and,

Z is scaled distance.

2.2 Blast Wave Propagation in Soil

2.2.1 Introduction

Numerous studies have been conducted in the field of soil mechanics since 1925. However, most of these studies were dedicated to the understanding of soil behaviour under static load conditions (Das, 1993). More attention has been paid to the effects of dynamic loads on soil behaviour and underground structures in the last 30 years.

Surface explosions result in high-stress dynamic loading that may induce ground surface deformation and result in structural failure. Underground or surface explosions lead to the crater, and a blast wave that propagates through the surrounding soil. High-intensity shock waves originate in the ground around nuclear or conventional explosions or near earthquake epicentres.

These shock waves decay into seismic P-waves or pressure waves as they propagate away from the source (Majtenyi and Foster, 1992).

2.2.2 Shock Wave Propagation

A number of effects such as shock waves, a fireball, and a high-velocity wind, which are generated by the detonation of high explosives in the air, may cause severe damages to a structure. A shock wave is formed when a pressure front (overpressure) moves at supersonic speeds and pushes on the surrounding medium. The particle velocity of this medium (air, water, soil) will increase too. As the blast wave travels outward from the explosion, another pressure (dynamic pressure) is produced from the air mass flow behind the shock wave. The dynamic pressure is a function of the density of the air behind the shock wave (Karlos and Solomos, 2013). The shock wave compresses the air, which leads to an increase in its density.

The shock wave velocity is a function of the peak overpressures, the ambient sound speed, and the ambient atmospheric pressure. The formation of pressure and shock waves over distance or time is shown in Figure 2.10 (Cooper, 1996). The pressure wave velocity at point C of the pressure wave profile (Figure 2.10 (a)) is higher than that at point A and B because the wave velocity increases with increasing of the pressure. Increasing the intensity of the pressure leads to a steeper wave profile, as shown in Figure 2.10 (b) and (c). When points C and B reach a vertical front aligned with point A, the wave profile becomes steeper, and the wave develops into a shock wave, as shown in Figure 2.10 (d).

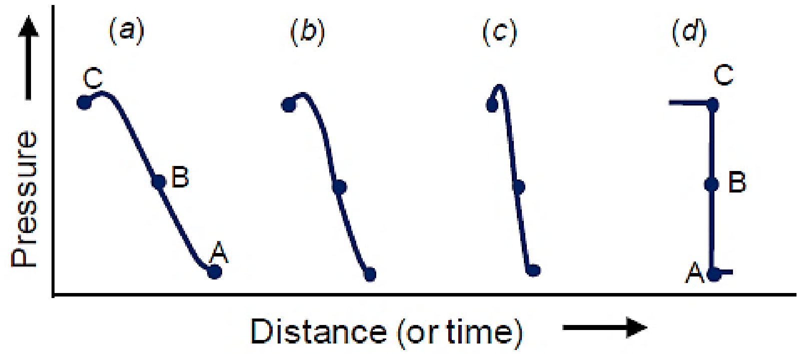

Figure 2.10: Pressure and shock wave profile vs. distance or time (Cooper 1996)

The shock wave velocity at any point along the wave can be calculated by adding the sound wave velocity and particle velocity as given in equation 2.12 (Busch, 2016).

$$U = C + PV \tag{2.12}$$

where,

U is wave velocity at any point of a pressure wave;

C is sound wave velocity; and,

PV is particle velocity.

Peak particle velocity (PPV) is used in practice to measure the damage in structures due to blast load, and it can be obtained as follows (R. Nateghi, 2012):

$$PPV = K\left(\frac{D}{Q^n}\right)^{-\beta} \qquad 2.13$$

where,

PPV is peak particle velocity;

K and β are factors that include effects of both relief during blasting and geology;

D is the distance from explosive source;

Q is the mass of the charge; and,

n is the square/cube root scaling.

The front of the wave is called the shock front, and it moves outward from the explosion center at a very high speed. The pressure of the air of the shock front is higher than the region behind it. The velocity and peak pressure of the shock front decrease as the shock front propagates outward from the explosion centre (Figure 2.11 (a to d)). The Attenuation in the amplitude of the pressure wave and the alteration of the wave shape are due to energy dissipation (damping). The pressure is then reduced to the region of elastic behaviour, and the square-pulse shock wave decays into a sound wave, as shown in Figure 2.11 (e).

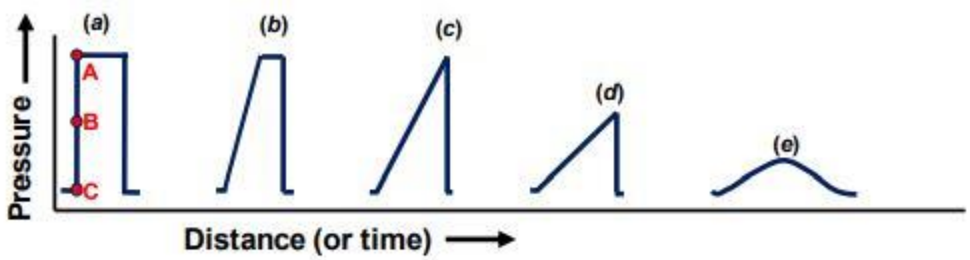

Figure 2.11: Attenuation of a square shock wave (Cooper 1996)

Explosion above or below the ground surface leads to the generation of body and surface waves. Body waves, which is consisted of compression (P), and shear (S) waves are dominant in buried explosions at a short-range while surface waves (Rayleigh or R waves) dominate surface explosions. As the R waves have a slower decay rate with distance, they dominate buried explosions at larger ranges. The propagation velocities of body and surface waves depend on the density and stiffness of the soil. Since S and R waves are associated with distortive movements in the soil, they travel at approximately the same speed (Smith and Hetherington, 2011).

$$v_r \approx v_s = \sqrt{\frac{G}{\rho}} \tag{2.14}$$

$$v_p = \sqrt{\frac{K}{\rho}} \tag{2.15}$$

$$K = \frac{2}{3} G \frac{(1+\mu)}{(1-2\mu)} \tag{2.16}$$

$$v_c = \sqrt{\frac{E}{\rho}} \tag{2.17}$$

where,

v_s is shear/torsional wave velocity in m/s^2;

v_r is Rayleigh wave velocity in m/s^2;

G is shear modulus of the soil in kPa;

ρ is density of the soil in kg/m^3;

K is bulk modulus in kPa;

v_p is compression wave velocity in m/s^2;

μ is Poisson's ratio;

v_c is seismic/longitudinal wave velocity in m/s^2; and,

E is modulus of elasticity of the soil in kPa.

2.2.3 General Material Stress-Strain Response

Most materials exhibit linear behaviour when low stress is applied. When the relationship between the strain produced in the material and the applied stress is proportional, the upper-bound limit is called elastic limit (Figure 2.12). As the stress increases beyond the elastic limit, the material exhibits plastic behaviour and behaves like a fluid. Thus, permanent deformation occurs, and the material does not return to its original shape after the stress is released. When the stress levels are between elastic and plastic limit, the material exhibits elastic-plastic behaviour. The stress levels of this region are around ten times the elastic limit (Busch, 2016). The plastic limit region is generally studied when dealing with blast waves.

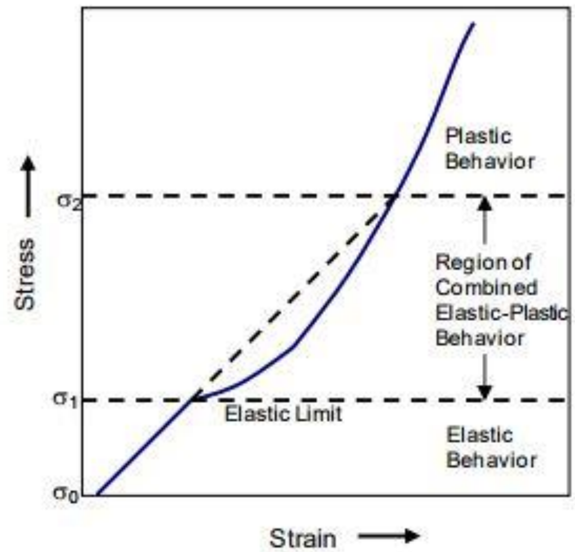

Figure 2.12: Compressive stress-strain curve for varying stress levels (Busch, 2016)

2.2.4 Dynamic Deformation Mechanism of Soils under Blast Loading

The soil consists of solid mineral particles (skeleton structure) and voids, which can be filled with water and/or air (Figure 2.13). These three components influence the response of the soil to blast loading. When surface explosion occurs, the soil remains in an undrained condition because of the rapid loading that prevents soil pore pressure from dissipating. During construction activities where loading occurs gradually, the soil response can be explained using conventional soil mechanics. However, conventional soil mechanics cannot be used to address the soil response under high-intensity pressure. The compressibility of the three phases must be taken into consideration when describing soil behaviour.

The deformation mechanisms of soil subjected to blast loading depends on the degree of saturation of the soil. When low pressure is applied to dry soil, the soil exhibits elastic deformation along the contact surfaces of the soil skeleton. However, as the pressure increases, the bonds between the soil particles are deformed, the skeleton is destroyed, and the soil is compacted. On the other hand, if saturated soil is subjected to a rapid dynamic loading, the deformation and the resistance of the soil would be determined by volumetric compression of the three phases, particularly of the mineral grains and water (Wang et al. 2004). Figure 2.14 depicts the typical compressibility response of a partially saturated soil (Busch, 2016).

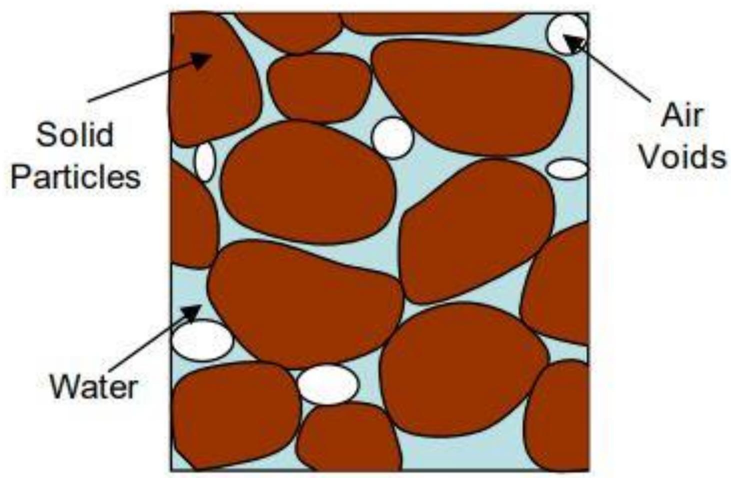

Figure 2.13: Phases of a soil (Busch, 2016)

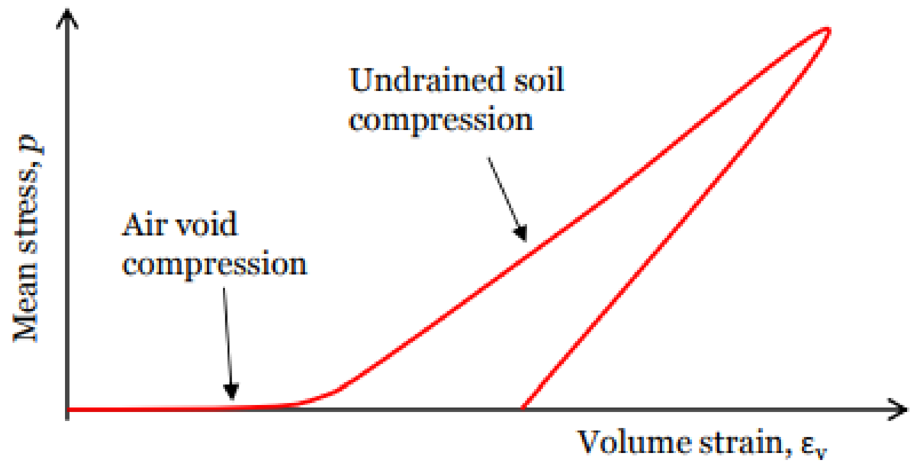

Figure 2.14: Typical compressibility response of a partially saturated soil (Busch, 2016)

2.2.5 Rate Dependency of Soil Behaviour

Soil behaviour is affected by the strain rate. The soil's strain rate can reach up to 10^3 % /s when the soil is subjected to blast loads (Xu, 2015). Different laboratory tests were conducted to determine special characteristics of soil behavior under such a high strain rate. Researchers used modified triaxial tests to investigate the soil behaviour under high strain-rate (Whitman 1970, Ehrgott and Sloan 1971, Carrol 1988, Abrantes and Yamamuro 2002, Huy et al. 2006, Yamamuro et al. 2011). Dry sand was often used as a test material because a high strain-rate prevents the water in the soil specimens from being drained. Figure 2.15 shows typical stress-strain curves and volumetric strain response curves of dry sand. It was noted that the soil might produce a higher peak shear strength and a higher tendency of dilation when loaded under a higher strain rate. Abrantes (2003) suggested that these behaviours are related to the particle rearrangement during the triaxial compression. When soil is sheared, soil particles tend to move and rotate against each other to accommodate the deformation (Xu, 2015). Under static loading, the particle rearrangement occurs along the easiest trajectory. However, increasing the strain rate changes the path of soil particles. As a result, more energy is consumed, leading to different behaviour than in the static cases. Furthermore, Karimpour and Lade (2010) mentioned that the crushing strength of soil particles is also dependent on the rate of loading. When soil is loaded at a high strain rate, there will not be enough time for the strain energy to accumulate. Less particle crushing happens, and therefore the soil specimens can generate a greater strength in macroscale (XU, 2015).

The compressibility of soil under high strain rates was also studied by conducting high strain rate triaxial tests, high strain rate uniaxial compression tests (Whitman 1970, Jackson et al. 1979, Farr 1990) and Split Hopkinson Pressure Bar (SHPB) tests (Charlie et al. 1990, Bragov et al. 2008, Martin et al. 2009, Huang et al. 2013). Based on the test results, it was noted that a larger modulus could be observed when the soil is loaded under a higher strain rate. A schematic diagram of soil's uniaxial compressive behavior is plotted according to the test results in Figure 2.16.

On the other hand, sand may exhibit other rate dependency patterns when subjected to low strain rates (Figures 2.17, 2.18). Different types of sand were tested in the laboratory to determine the patterns of rate-dependency. As shown in Figure 2.17, when the strain rate is increased stepwise, the stress-strain curve temporarily jumps to a higher location and then gradually rejoins the original curve (Matsushita et al. 1999; Tatsuoka et al. 2002; Kiyota and Tatsuoka 2006; Di Benedetto 2007). A unique stress-strain curve was obtained due to monotonic loading tests with different constant strain rates **(**Xu, 2015). Figure 2.18 showed the rate-dependency of Albany Sand, Hime gravel, Monterey sand (Enomoto et al. 2007a, b, Tatsuoka et al. 2008). When the strain rate is increased stepwise, the stress-strain curves first overshoot and then join a curve lower than the one for the initial strain rate. On the other hand, sand strength decreases with the increase of strain rate in monotonic loading tests **(**Xu, 2015).

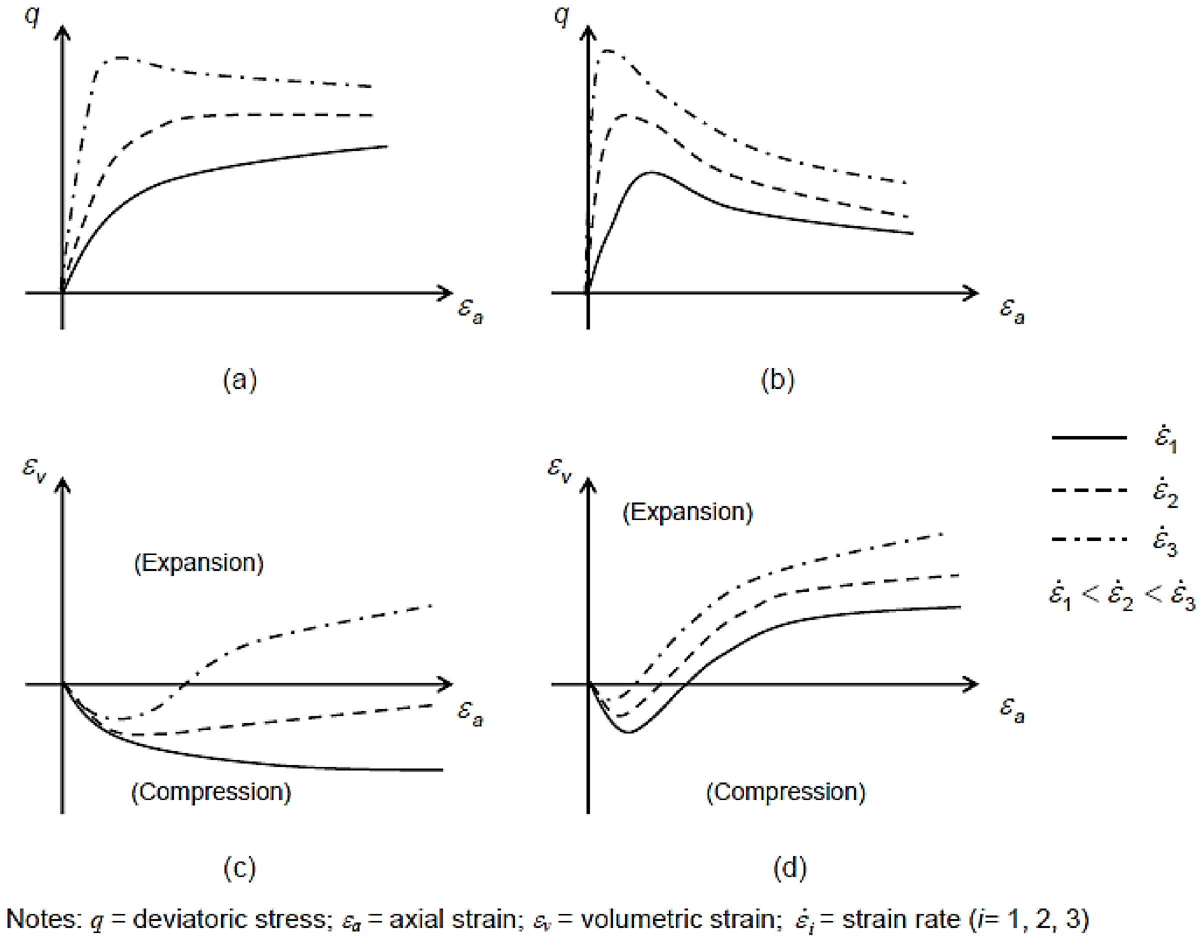

Figure 2.15: Schematic diagram of sand behavior observed in high strain-rate triaxial tests: (a) stress-strain curves for loose sand; (b) stress-strain curves for dense sand; (c) volumetric strain response curves for loose sand; and (d) volumetric strain response curves for dense sand **(**Xu, 2015)

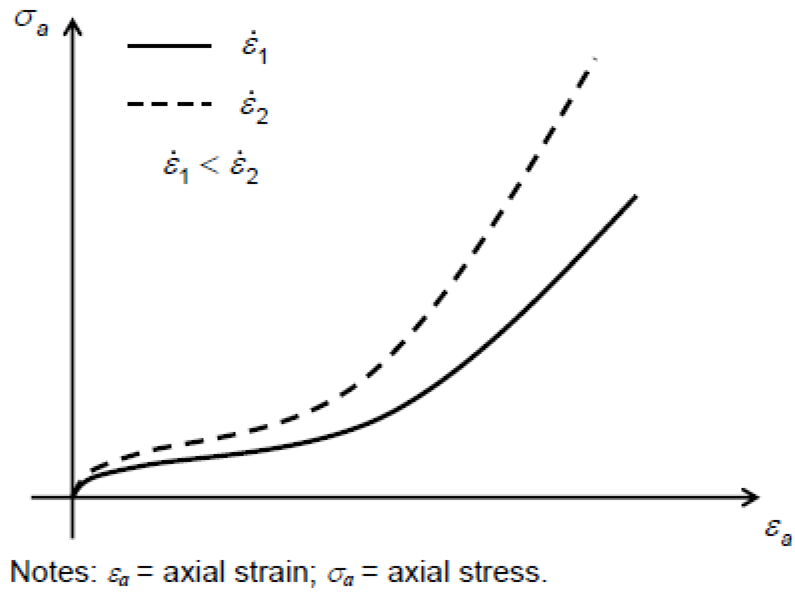

Figure 2.16: Schematic diagram of compression behavior of sand under high strain rate (Xu, 2015)

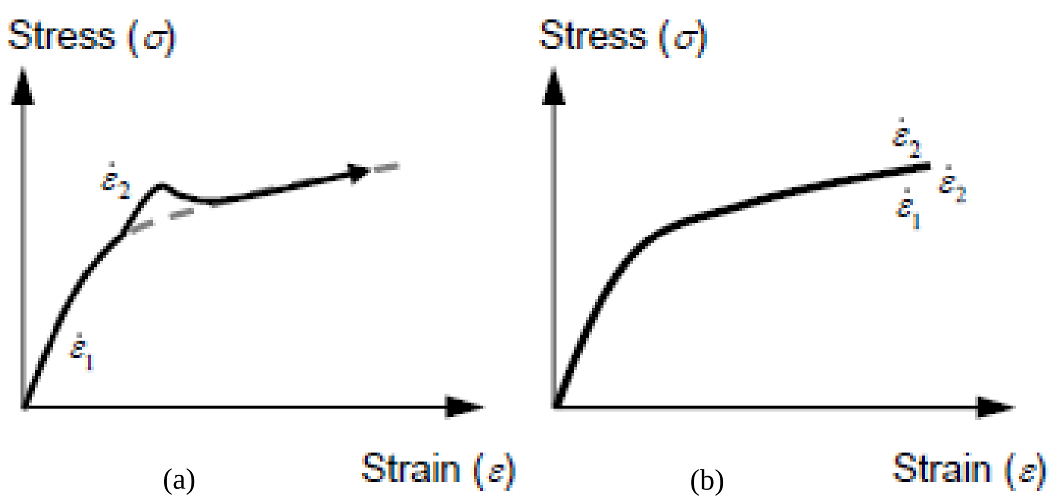

Figure 2.17: Stress strain curves due to changes in strain rate in sand in plain strain tests: (a); tests with stepwise changed strain rate, (b); monotonic loading tests with different constant strain rates (Xu, 2015)

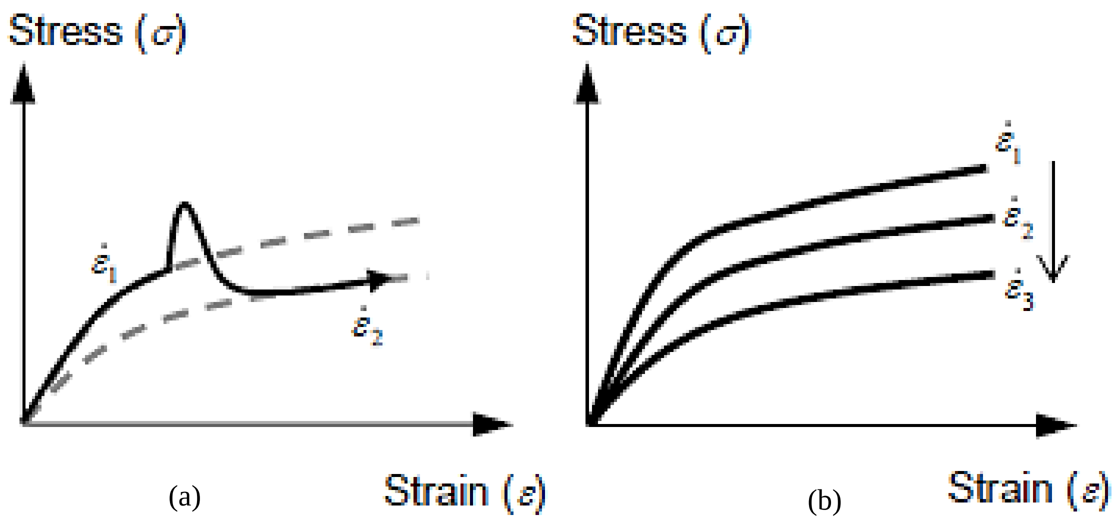

Figure 2.18: Stress strain curves due to changes in strain rate in triaxial tests on Albany Sand, Hime gravel, Monterey sand: (a); tests with stepwise changed strain rate, (b); monotonic loading tests with different constant strain rates (Xu, 2015)

$$\dot{\varepsilon}_1 < \dot{\varepsilon}_2 < \dot{\varepsilon}_3$$

2.2.6 Cratering Processes

Soils exposed to the surface explosion are subjected to air-induced ground shock that compresses the ground surface and sends a stress pulse into the underground layers, which results in the formation of a crater. Figure 2.19 represents a schematic of the crater geometry from an explosive event. As mentioned previously, shock waves and generation of gaseous products are produced by detonation of explosives in a very short period. The explosion first generates an initial shock that scours and compacts the soil, resulting in plastic flow and the formation of an initial “true” crater (Zimmie et al. 2010). Detonation gases are infused into the ground and eject soil (termed “ejecta”) into the air as they expand. As a rarefaction wave travels into the compressed soil, the direction of the soil particle velocity reverses and forms more ejecta (Cooper 1996). Some of the ejecta are deposited back into the true crater as a fallback, and the resulting crater geometry after this event is termed the “apparent” crater (Zimmie et al. 2010).

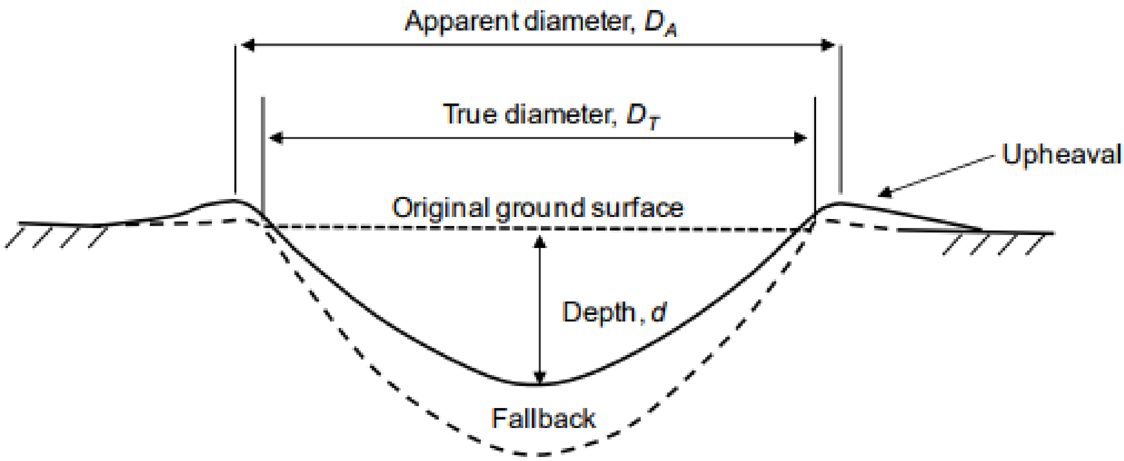

Figure 2.19: Crater geometry from an explosive event (Zimmie et al. 2010)

Moisture content, shear strength, porosity and compressibility are the properties that influence cratering behavior. Soil water content has a significant impact on crater size. Increasing moisture content leads to a reduction of the soil's shear strength, which causes the formation of large craters. Saturated soils subjected to blast loading result in the largest craters. Porosity and compressibility of soil affect the amount of energy that is transferred into the soil. Soils with low relative density (loose soils) permit more energy to be transmitted into the soil and form larger craters (Zimmie et al. 2010).

2.2.7 Blast Induced Increase in Pore Water Pressure

Liquefaction may occur in saturated soil subjected to blast loads due to blast-induced cyclic shearing (Xu, 2015; Lu and Fall, 2016). Field blasting tests were conducted by researchers to evaluate the potential of liquefaction by measuring the excess pore water pressures induced by blasting. Gohl et al. (2001) performed 16 borehole blast tests in a silty sand layer with charge weights of 2 – 6 kg and borehole depths of 8 – 12 m. It was noted that peaks water pressure occurred when the blast pulses reached the transducer. After the tests, the pore water pressure ratio was measured, and it was 62.5%. This ratio indicates that complete liquefaction did not happen. Ashford et al. (2004) carried out a blast-induced liquefaction test in the hydraulic fill and sand layers in San Francisco. Two sets of blast tests were conducted. In each set, 16 charges (each charge is equivalent to 0.5 kg TNT) were detonated in the boreholes at a depth of 3.6 m below the ground surface. Peak pore water pressure ratios of 90 – 100% were measured by the transducers located within a distance of 5.5 m to the center of the charge ring. In this experiment, liquefaction happened, and sand boils were observed 3 – 5 min after the detonation. Al-Qasimi et al. (2005) carried out single and multiple detonation tests in a level deposit of loose, saturated, sand-size mine tailings. It was noted that the threshold peak particle velocity for liquefaction in multiple detonation tests was smaller than that in single detonation tests. It is also found that the peak pore pressure ratio induced by the blast was proportional to the square root of the peak particle velocity, the inverse of the cube root of the initial effective vertical stress and the inverse of the fifth root of the relative density. Charlie et al. (2013) conducted field tests on saturated sands of different relative densities. Liquefaction was observed at locations with a cubic-root scaled distance smaller than 10. The study found that the threshold values of peak radial particle velocity and peak strain for inducing soil liquefaction increases as the relative density and confining pressure increase.

2.3 Retaining Walls

2.3.1 Introduction

Retaining walls (RW) are structures designed and constructed to provide lateral support to the soil. They have been widely used in railways, bridges, building, hydraulic and harbour engineering. There are two types of retaining walls; conventional retaining walls (Figure 2.20) and mechanically stabilized earth (MSE) walls (Figure 2.21). Conventional retaining walls consist of gravity retaining walls, semi-gravity retaining walls, cantilever retaining walls, and counterfort retaining walls. Gravity retaining walls, which are also called rigid retaining walls, are thick and stiff and depend on the self-weight to resist external pressures. While cantilever retaining walls are less thick and more flexible than gravity retaining walls (Das, 2016).

Mechanically stabilized earth walls (MSE) are gravity type retaining walls in which the soil is reinforced by thin reinforcing elements (steel, fabric, fiber, etc.). MSE walls are flexible, and their main components are backfill (granular soil), reinforcing strips (thin and wide strips placed at regular intervals), and a cover on the front face (skin) (Das, 2016).

Conventional retaining wall fails in the following types: sliding, overturning, global failure, and bearing capacity failure (Figure 2.22). Retaining wall fails in sliding when the lateral earth pressures exceed the horizontal resisting forces at the base of the wall. Overturning happens when the overturning moments exceed the stabilizing moments of the wall. Gross instability of the soils behind and beneath the retaining wall leads to stability failure of a slope including the retaining wall. This failure refers to as a global failure. Bearing capacity failure occurs when the foundation soil fails to support the weight of the retaining wall. Cantilever retaining wall may fail by the flexural failure of the wall in addition to the failure mentioned above mechanisms. If the applied bending moment exceeds the wall's flexural strength, flexural failure will occur (Jung, 2009).

The terms yielding and non-yielding retaining walls are used in the analysis of RW. When retaining walls can move sufficiently to develop active earth pressures or passive earth pressures, the walls are called yielding retaining walls. However, some retaining structures do not satisfy this movement condition, such as basement walls. These walls are referred to as non-yielding retaining walls (Mikola, 2012).

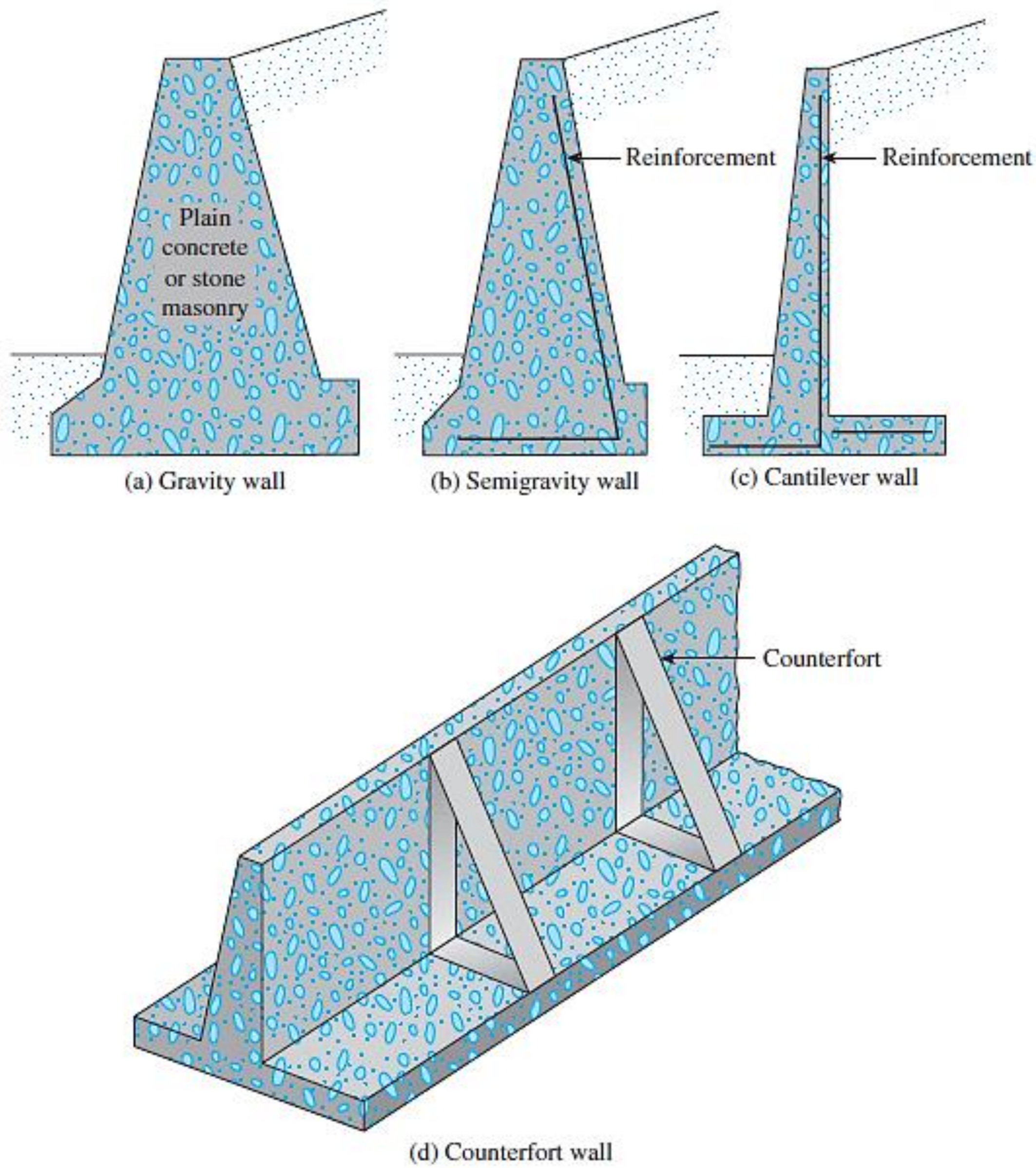

Figure 2.20: Types of conventional retaining walls (Das, 2016)

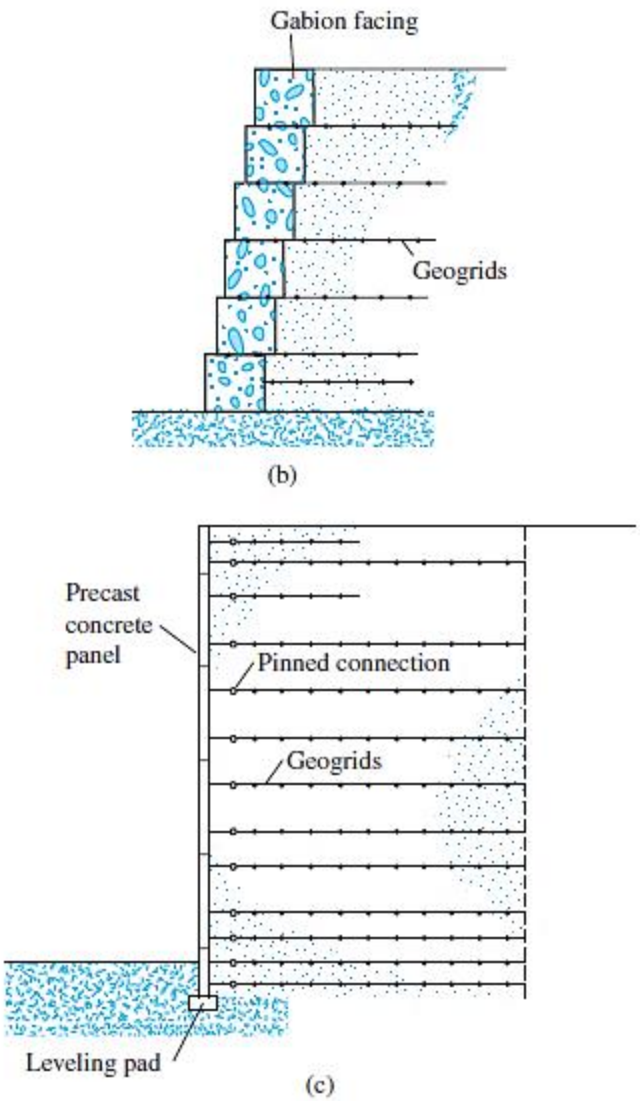

Figure 2.21: Mechanically stabilized earth walls with geogrid reinforcement: (b) wall with gabion facing; (c) concrete panel-faced wall (Based on Berg et al., 1986) (Das, 2016)

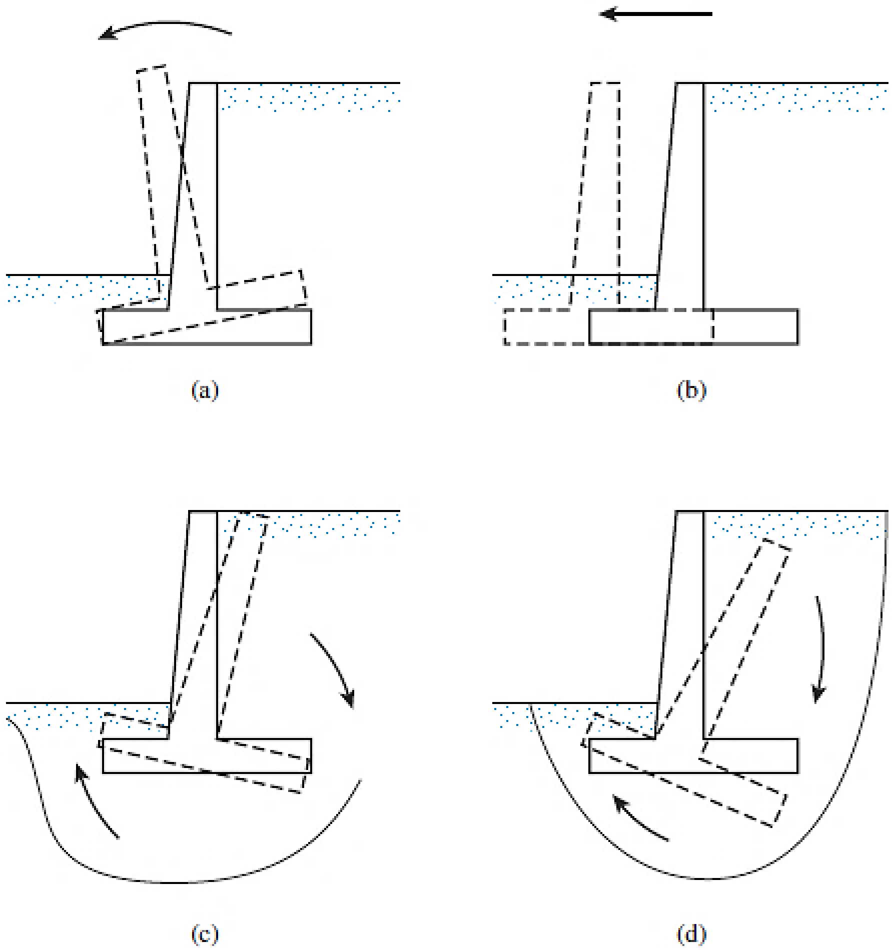

Figure 2.22: Failure of retaining wall: (a) by overturning; (b) by sliding; (c) by bearing capacity failure; (d) by deep-seated shear failure (Das, 2016)

2.3.2 Background on Design of Retaining Walls

The analysis and design of earth retaining structures are one of the oldest and most fundamental studies in the geotechnical engineering field. Coulomb and Rankine provided the first scientific applications to design RW by defining the solution of the lateral static earth pressure problem. Their earth pressure theories are developed based on limit state analyses (Mikola, 2012 and Al Atik, 2008).

Following the Great Kwanto Earthquake in 1923, many researchers focused their studies on the problem of seismically induced lateral earth pressures on retaining structures and basement walls. Permanent deformations of retaining structures were noticed in many historical earthquakes. Below is a brief explanation of the theories and methods that have been developed to predict the dynamic response of retaining walls when subjected to seismic forces.

2.3.2.1 Pseudo-static equilibrium methods:

The Mononobe-Okabe method (1929) and the Seed-Whitman method (1970) are used to predict seismic earth force acting on a retaining wall. These methods are representative of Pseudo-static equilibrium methods, which are also called rigid plastic methods with force-based approaches. Modifications of the Mononobe-Okabe and the Seed-Whitman methods were provided by Koseki (1998) and Zhang (1998).

a) Mononobe-Okabe method (1929)

Mononobe and Matsuo (1929) and Okabe (1926) provided the earliest method to predict retaining walls' dynamic behaviour during earthquakes. Mononobe-Okabe method (M-O method) is an extension of Coulomb’s static earth pressure theory. The inertial forces due to the horizontal and vertical backfill accelerations are included in Coulomb’s theory. The M-O forces diagram is shown in Figure 2.23.

The main assumptions of the methods are as follows (Seed and Whitman, 1970): (1) the retained backfill is a dry granular soil; (2) sufficient movement in the wall to produce minimum active earth pressure in the backfill that leads to mobilize the maximum shear strength of the backfill along the sliding failure surface; (3) the failure surface in the backfill passes through the toe of the wall and is a plane with an inclination angle measured from the horizontal plane; (4) constant vertical and horizontal accelerations of the backfill throughout the soil wedge are used; (5) the resultant force of the lateral earth pressure acts at a third of the wall height (H), above the wall base; and (6) inertial effects of the wall itself are neglected.

Based on the M-O method, static equilibrium of the soil wedge is utilized to determine the active lateral pressure as presented in Figure 2.23. The maximum dynamic active thrust per unit width of the wall, P_{AE}, is given by (Al-Atik, 2008):

$$P_{AE} = \frac{1}{2}\gamma H^2(1 - k_v)K_{AE} \qquad 2.18$$

$$K_{AE} = \frac{cos^2(\varphi - \theta - \beta)}{cos\theta . cos^2\beta . \cos(\delta + \beta + \theta)\left[1 + \sqrt{\frac{\sin(\varphi + \delta)\sin(\varphi - \theta - i)}{\cos(\delta + \beta + \theta)\cos(i - \beta)}}\right]^2} \qquad 2.19$$

where,

P_{AE} is maximum dynamic active force per unit width of the wall;

K_{AE} is total lateral earth pressure coefficient;

γ is unit weight of the soil;

H is height of the wall;

φ is angle of internal friction of the soil;

δ is angle of wall friction;

i is slope of ground surface behind the wall;

β is slope of the wall relative to the vertical;

$\theta = tan^{-1}(\frac{k_h}{1-k_v})$;

k_h is horizontal wedge acceleration divided by g;

k_v is vertical wedge acceleration divided by g; and,

g is gravitational acceleration.

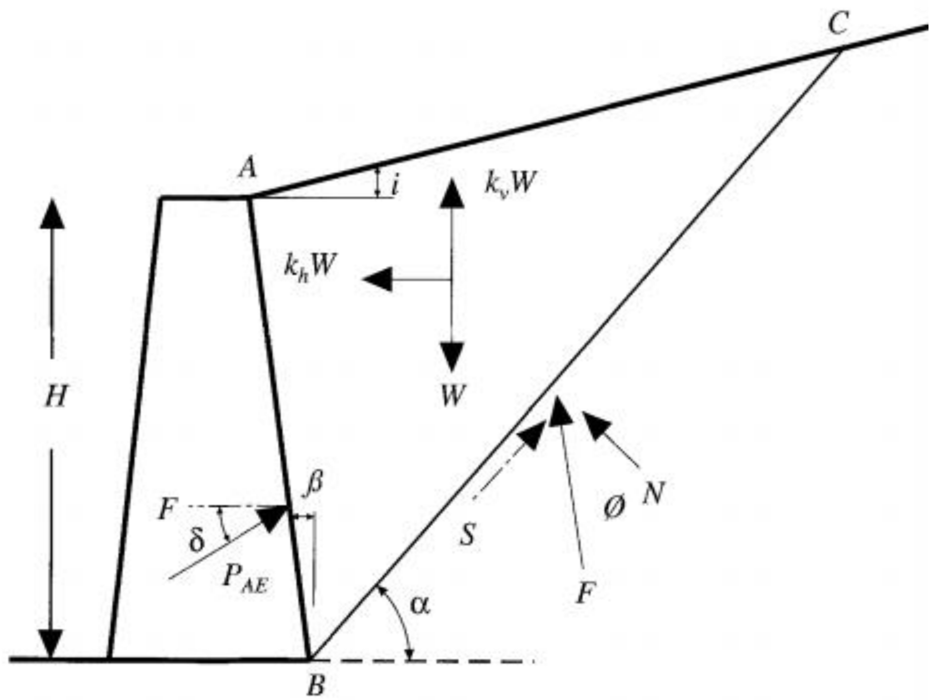

Figure 2.23: Equilibrium of forces in Mononobe-Okabe analysis (Wood 1973)

b) Seed-Whitman method (1970)

Seed and Whitman (1970) performed a parametric study to estimate the influences of angle of wall friction, the friction angle of the soil, the backfill slope, and the vertical and horizontal acceleration on dynamic earth pressures. The results of their study showed that peak total earth pressure acting on a RW can be divided into the initial static pressure and the dynamic increment due to the base motion. The following equation gives the relationship between the static, dynamic increment, and total lateral earth pressure:

$$P_{AE} = P_A + \Delta P_{AE} \qquad 2.20$$

$$K_{AE} = K_A + \Delta K_{AE} \qquad 2.21$$

where,

P_{AE} is total lateral earth pressure;

P_A is initial static earth pressure;

ΔP_{AE} is dynamic increment;

K_{AE} is total lateral earth pressure coefficient;

K_A is static lateral earth pressure coefficient; and,

ΔK_{AE} is dynamic increment coefficient.

Seed and Whitman (1970) further proposed the following expression for the case of backfill soil with friction angle of 35°, a vertical wall, and horizontal backfill slope:

$$K_{AE} = (\tfrac{3}{4})k_h \quad 2.22$$

$$\Delta P_{AE} = (\tfrac{3}{8})k_h \gamma H^2 \quad 2.23$$

Based on the review of laboratory test results by Mononobe and Matsuo (1929), Jacobsen (1939), and Ishii et al. (1960), Seed and Whitman (1970) concluded that the dynamic lateral resultant force, ΔP_{AE}, acted at a height from 0.5H to 0.67H above the wall base (Figure 2.24). The authors also noticed that peak ground acceleration happens only one instant of time and has no sufficient duration to significantly move the wall. Therefore, it is recommended to reduce the ground acceleration of about 85% of the peak value in retaining walls' seismic design. Lastly, Seed and Whitman (1970) stated that "many walls adequately designed for static earth pressures will automatically have the capacity to withstand earthquake ground motions of substantial magnitudes and in many cases, special seismic earth pressure provisions may not be needed."

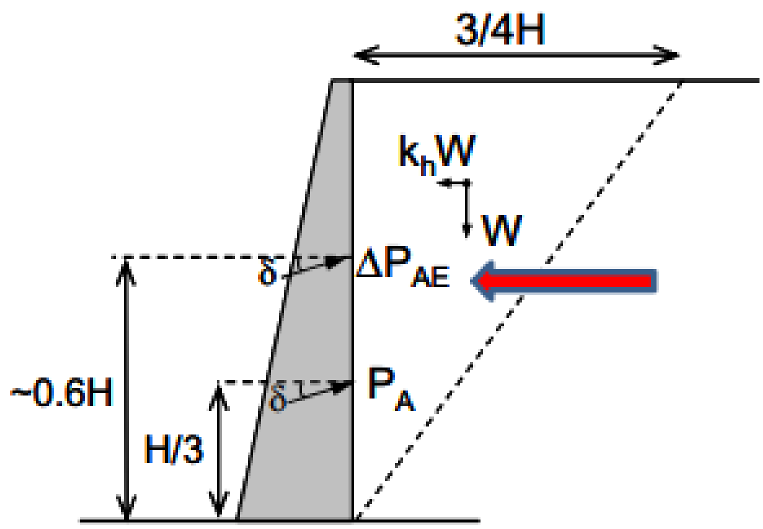

Figure 2.24: Forces considered in Seed-Whitman analysis (Mikola, 2012)

c) <u>Koseki's method (1998)</u>

Koseki (1998) proposed a method to resolve the problem of unrealistically high active seismic earth thrust provided by M-O method at high seismic load when the maximum acceleration is larger than 0.5 g. In M-O method, a flatter failure plane is formed in the backfill with increasing horizontal acceleration.

In Koseki's method, the initial active failure occurs at $k_h = 0$, and the failure plane is calculated based on the peak frictional resistance angle of the backfill. Along the initial failure plane, the shear resistance angle of the backfill soil decreases to the residual resistance angle, with a slight movement of the wall. The secondary active failure occurs when the mobilized frictional angle along the potential failure plane reaches the peak frictional resistance angle. The secondary failure plane is flatter than the initial one (Jung, 2009).

d) Zhang's method (1998)

Zhang et al. (1998) proposed a method to predict the distribution of the seismic earth pressures on a wall and the resultant force of the pressure. Most limit equilibrium methods are built on the assumption that a sufficient movement in retaining wall leads to induce active earth pressures or passive earth pressures. Zhang's method introduced the concept “intermediate soil wedge” associated with mobilized frictional resistance. In the “intermediate soil wedge,” a critical surface plane is assumed in the backfill soil such that no adequate displacement in the wall to mobilize the shear strength of the soil.

2.3.2.2 Methods based on displacements of retaining walls

Neither the permanent displacement of a retaining wall due to seismic loading nor the effects of movements of the wall on the seismic earth pressure behind the wall are addressed in the pseudo-static equilibrium methods. To address the abovementioned issue, Richards-Elms (1979), Whitman-Liao (1985), and Steedmann and Zeng (1996) proposed wall displacement-based methods for seismic design of retaining structures.

a) Richards-Elms method (1979)

Richards and Elms (1979) proposed a method based on allowable permanent wall displacement for the seismic design of gravity walls. The Newmark sliding block theory (1965), which was originally developed to evaluate seismic slope stability, is used to estimate the permanent wall displacements. Per the Newmark sliding block theory, lateral displacement of the block occurs when the ground acceleration exceeded the critical or yield acceleration of the soil mass. The yield acceleration is defined as the minimum acceleration which causes the wall to move permanently along the wall's base. The yielding acceleration is a function of frictional angle of the backfill, frictional angle between the wall and the soil, and angle of the back of the wall with the vertical.

$$a_y = \left[tan\varphi_b - \frac{P_{AE}\cos(\delta+\theta) - P_{AE}\sin(\delta+\theta)}{W}\right]g \qquad 2.24$$

where,

a_y is yield acceleration;

P_{AE} is resultant force of earth pressures against the wall;

φ_b is frictional angle of the backfill;

δ is frictional angle between the wall and the soil;

θ is angle of the back of the wall with the vertical;

W is weight of the soil wedge; and,

g is gravitational acceleration.

To solve equation 2.20, Richards and Elms recommended that the resultant force (P_{AE}) is to be calculated using the Mononobe-Okabe method. Since P_{AE} is a function of a_y in the M-O equation, the above equation should be solved iteratively with the M-O equation.

Richards-Elms also proposed an approximate equation to determine the permanent wall displacement (d_{perm}), which is based on Franklin and Chang (1977) work.

$$d_{perm} = 0.087\frac{v_{max}^2 a_{max}^3}{a_y^4} \qquad 2.25$$

where,

d_{perm} is permanent wall displacement in (inch);

v_{max} is peak ground velocity in (in/sec);

a_{max} is peak ground acceleration in (ft/sec^2); and,

a_y is threshold yielding acceleration in (ft/sec^2).

b) Whitman-Liao method (1985)

Whitman and Liao (1985) proposed a probabilistic method to predict permanent wall displacements for seismic design of retaining structures. The method considers the effects of modelling error, uncertainty due to statistical variability of ground motions, and uncertainty of soil properties on permanent displacement. Therefore, Whitman and Liao stated that the permanent displacement is not a certain value but a range of values with a probabilistic distribution.

c) Steedmann and Zeng method (1996)

Steedmann and Zeng (1996) used the Newmark's sliding block theory to predict a gravity wall's permanent rotational movement with a rigid foundation when subjected to seismic loading.

A rocking model rotating about the wall base is used by Steedmann and Zeng (1996) to predict the movement. Rocking is defined as a permanent rotational movement of the wall.

The rocking displacement is calculated by integration of the rotational velocity of the wall over time. The model was validated by laboratory centrifuge tests (Chul Min Jung, 2009).

2.3.2.3 Methods based on elasticity

Elastic methods are mostly used in the design of gravity retaining walls built on a rock foundation and basement walls that consider as rigid walls and yield very small displacement. The first publications of the elastic analytical solutions for seismic response of a rigid wall were by Scott (1973), and Wood (1973). Veletsos and Younan (1997), and Psarropoulos et al. (2005) extended the analytical solutions for flexible retaining walls with a rigid body motion.

a) Scott's solutions (1973)

An analytical, linear elastic model called the "continuous shear beam" model, to calculate the dynamic earth pressure acting on a rigid retaining wall fixed at its base is developed by Scott (1973). Based on the results of the analyses, Scott concluded that when the backfill soil is assumed to have constant elastic material properties with depth, the lateral earth pressure distribution forms a cosine shape along the depth, with the maximum magnitude of the earth pressure at the top of the wall, and zero at the bottom of the wall. The resultant force is acting at a distance of 0.64H above the wall base. However, suppose the backfill soil is assumed to have elastic properties increasing with depth. In that case, the lateral earth pressure distribution forms a triangular shape along the depth, with the maximum magnitude of the earth pressure at the top of the wall and zero at the bottom of the wall. The point of application of the resultant active pressure is about 0.67H above the wall base.

b) Wood's solutions (1973)

Wood (1973) also provided analytical solutions using a linear elastic model to calculate the seismic earth pressure acting on a rigid retaining wall fixed at its base. Modal superposition dynamic analysis for an elastic structural beam that is excited at its base is used to obtain the solutions. The analytical solutions were compared with numerical solutions. Based on both solutions' results, Wood concluded that for a rigid wall, the analysis should be based on elastic theory. However, when a large displacement is created due to seismic loading, the wall-soil system's analysis should be based on a plastic theory. Therefore, the M-O method can be used to provide an approximate solution. Wood also noted that using the elastic theory to calculate the seismic earth pressure for a rigid wall was twice as large as the pressure determined by M-O method. Wood recommended using a nonlinear model for the backfill soil to avoid the discrepancy in the elastic theory results and the plastic limit state.

c) Veletsos and Younan (1994 and 1997)

Based on Wood's study, Veletsos and Younan (1994) provided analytical solutions for the seismic response of a rigid retaining wall with an elastic backfill. The backfill was assumed as a semi-infinite layer of linear elastic material that was bonded to a rigid base. Constant damping ratio was introduced to the backfill. The study addresses the effects of the frequency of an input motion on the response of the wall system.

Veletsos and Younan (1997) developed an analytical solution for a flexible retaining wall that can rotate at its base. Failure mechanism in flexible retaining wall during seismic excitation is due to flexural bending and rotation at the base. In this model, the flexible retaining wall is fixed at its base to prevent rotational and horizontal movement. Veletsos and Younan observed that forces acting on flexible walls are less than those acting on rigid walls. Veletsos and Younan introduced two non-dimensional parameters to investigate the dynamic behavior of the soil-wall retaining system due to the influences of the retaining wall flexibility and the rotational movement of the wall. The first parameter is the relative flexibility of the wall with respect to the retained medium, d_w, and the following expression gives it:

$$d_w = \frac{12(1 - v_w^2)G_s H^3}{E_w t_w^3} \qquad 2.26$$

The second parameter is the relative flexibility of the rotational constraint at the base of the wall with respect to the retained medium, d_θ, and defined as follows:

$$d_\theta = \frac{G_s H^2}{R_\theta} \qquad 2.27$$

where,

v_w is the Poisson's ratio of the wall;

G_s is the shear modulus of the soil;

H is the height of the wall;

E_w is the Young's modulus of the wall;

t_w is the thickness of the wall; and,

R_Θ is a linear elastic rotational spring with elastic constant.

d) Psarropoulos et al. (2005)

The analytical solution developed by Veletsos and Younan (1997) was numerically verified by Psarropoulos et al. (2005) using a finite-element method (FEM). The method investigated parametrically in detail the effects of flexural bending of the wall and rotation at the base. The results showed that the dynamic earth pressure on a retaining wall determined from the numerical model is in good agreement with Veletsos and Younan's analytical solution. Furthermore, a non-uniform soil layer with stiffness increasing linearly with depth induces a smaller seismic earth thrust on the wall than a uniform soil layer. Lastly, it is inaccurate to assume that complete bonding between the soil and the flexible retaining wall as tensile stresses may develop at the interface.

2.3.2.4 Field investigation

Field investigation following an earthquake can give a good indication of the seismic behaviour of retaining walls. The information available on the field performance of retaining walls in the recent major earthquake is limited due to the lack of well documented retaining structures failures in non-liquefiable backfills (Al-Atik, 2008). The seismic response of retaining walls during an earthquake depends on the presence of liquefaction-prone loose cohesionless backfills (Gazetas et al. (2004). Case histories from recent major earthquakes (such as San Fernando (1971), Loma Prieta (1989), Northridge (1994), Kobe (1995), Chi-Chi (1999), Kocaeli (1999), and Athens (1999)) show that retaining structures with saturated loose backfill are vulnerable to strong seismic loading. On the other hand, flexible retaining walls with dry sands or saturated clayey soils have exhibited better performance during earthquake events (Al-Atik, 2008).

2.4 Review of Previous Studies on the Response of RWs to Dynamic Loadings and Blast Effects on Geotechnical Structures

2.4.1 Review of Previous Studies on the Response of RWs to Dynamic Loadings

Significant dynamic lateral earth pressure behind a soil retaining wall can result from an intensive ground motion. This pressure can create excessive lateral displacement behind abutments/retaining walls and can cause damage bridge superstructures (Al Homoud and Whitman, 1999; Bakeer and Ishibashi, 1990).

Many experimental studies have been conducted to understand the mechanism of load transfer from the backfill to the wall when subjected to seismic loading, for examples:

<u>Sherif et al. (1982)</u>

Shaking table tests were performed by Sherif et al. (1982) on a rigid retaining wall to calculate the dynamic, active earth pressure and to determine the point of application of the resultant active pressure. It was observed that the active state initiated in the backfill soil when the horizontal displacement of the wall reaches about 1/6000 of the wall height (H). This value is less than the one generally used to define the active state, 1/1000 H. It was also noticed that the static and dynamic earth pressure on the wall in the tests were approximately 30% higher than the values estimated by the Coulomb's equation and M-O method, respectively. Based on the test result, the authors concluded that the angle of the friction mobilized behind the wall should be used to define the active state in the backfill soil. Furthermore, Wood's solution (1973) overestimates the magnitude of seismic earth pressure on a rigid retaining wall fixed to the base.

Ishibashi and Fang (1987)

Ishibashi and Fang (1987) conducted experimental works to investigate the dynamic earth pressure acting on the rigid retaining wall based on different failure mechanisms. The authors studied various movement types: rotation about the base of the wall, rotation about the top, translation, and combination of rotation and translation about the base. Based on the results, it was noticed that the total dynamic earth pressure for rotation about the base and rotation about the top was about 30% and 10%, respectively, higher than the values determined by M-O method. In addition, the point of application of the resultant force is influenced by each type of wall movement.

Koseki et al. (1998) and Watanabe et al. (2003)

Different models of retaining walls, including gravity retaining walls, cantilever retaining walls, and MSE walls, were tested by Koseki et al. (1998) and Watanabe et al. (2003) using a shaking table. It was observed that the major failure type in the retaining wall models was overturning with tilting of the wall. The results showed that the resultant forces on walls obtained from the shaking table tests were smaller than the values calculated from the M-O method. It was also observed that the M-O method might overestimate the seismic earth pressure on a wall at high seismic loads. The M-O method can be used to estimate the resultant earth pressure on a wall subjected to a seismic excitation of less than a_{max} = 0.3g. Lastly, the MSE walls are more ductile than gravity or cantilever walls, and their seismic performance is more effective than conventional walls.

Tiznado and Rodriguez-Roa (2011)

Tiznado and Rodriguez-Roa (2011) investigated the seismic behavior of gravity retaining walls on normally consolidated granular soils using a series of 2D finite-element analyses. Chilean seismic waves were applied at the bedrock level. Backfill and foundation soil behaviour were represented by an advanced non-linear constitutive model. It was found that seismic amplification effects in both soil foundation and backfill have a strong influence on the permanent displacements of the wall. The authors stated that the accelerations generated on soil behind the wall is different from the accelerations applied at the bedrock level. In this study, design charts were derived using numerical analyses to predict lateral displacements at the base and top of gravity retaining walls located at sites with similar seismic characteristics to the Chilean subduction zone. Using the design charts, seismic wall rotation can be estimated too.

Akhlaghi et al. (2013)

Akhlaghi et al. (2013) investigated the effects of mechanical properties of the soil and the wall on the dynamic response of a cantilever retaining wall using finite element analysis. The paper also addressed the effects of amplitude and frequency of the harmonic motion on the response of the wall. The results showed that the dynamic response of the RW increases as the soil density and amplitude of harmonic load increase. On the other hand, an increase in the values of friction angle, cohesion, elasticity, damping of the soil and the wall's stiffness lead to decrease the dynamic response. Furthermore, the study showed that permanent displacement produces when the input motions coincide with the natural period of the backfill.

Ertugrul and Trandafir (2014)

Ertugrul and Trandafir, 2014 presented their study on flexible cantilever retaining walls with deformable inclusions under the effect of seismic earth pressures. In this study, 1-g shaking table tests were performed on small-scale, flexible cantilever wall models with deformable inclusions and without geofoam inclusions. Granular cohesionless material and composite backfill were used in this experiment. The composite backfill consists of a deformable geofoam inclusion and granular cohesionless material. Two different polystyrene materials were utilized as deformable inclusions. The results obtained from the retaining walls with deformable inclusions were compared with those of the models without geofoam inclusions. Reduction (up to 50%) in dynamic earth pressures was observed in the retaining walls with deformable inclusions. The percentage of reduction was dependable on the inclusion characteristics and the wall flexibility. The authors stated that the efficiency of load and displacement reduction decreased as the wall model's flexibility ratio increased. While the dynamic load reduction efficiency of the deformable inclusion increased as the amplitude and frequency ratio of the seismic excitation increased.

Kloukinas et al. (2015)

Kloukinas et al. (2015) studied the earthquake response of cantilever retaining walls through theoretical analyses and shaking table testing. Limit analysis and wave propagation methods were used in the theoretical investigations. The experimental program included different combinations of retaining wall geometries, soil configurations and input ground motions. Three types of instruments, uniaxial accelerometers, linear variable differential transducer (LVDT), and strain gauges, were used for the measurement of accelerations, displacements and strains, respectively. The retaining wall model was made of aluminum alloy 5083 plates. Dry, yellow Leighton Buzzard silica sand, at different compaction levels, was used for both the backfill and the foundation soil layer. The study provided a calculation of the dynamic earth pressure and its point of application. Modes of wall movement such as sliding versus rocking of the wall base and the corresponding failure mechanisms were addressed as well. It was concluded that the seismic Rankine analysis proposed in this study offers an exact solution for the pseudo-static seismic earth pressure acting on the vertical virtual back of the retaining wall. The authors stated that the experimental results confirmed the prediction of the theoretical stress limit analysis. When the retaining wall was subjected to seismic loads, it was shown that the soil thrust maximized the bending moment on the wall stem as the wall was moving toward the backfill (passive state).

Wang et al. (2015)

The seismic response of geogrid reinforced rigid retaining walls with saturated backfill sand using large-scale shaking table test models were investigated by Wang et al., 2015. Geogrid reinforced rigid retaining structures and unreinforced soil retaining structures were used in this experimental study. The backfill soil behind the walls was fine sand. A cohesive soil was used below the foundation of the walls. Low strength, plastic geogrid was selected for this study. Various instruments were used to measure accelerations, displacements, and pore water pressures. Three seismic waves were applied in the tests. They were near-field seismic waves in Shifang (SF wave), far-field seismic waves in Songpan (SP wave) during the Wenchuan earthquake in China in 2008, and middle-far-field seismic waves in Taft (TA wave) in the United States. The results showed that the seismic lateral deformation modes of the walls were inclining outwards, and in some situations, they were protruding swelling. The lateral displacements of the reinforced wall model were less than the ones of the unreinforced wall model. The geogrid reduced the seismic settlement at the surface of the backfill. It was also noticed that the geogrid layers could effectively decrease the development of excess pore pressures and dissipate excess pore water pressures at a quicker rate. The authors concluded that geogrids for the reinforced soil rigid retaining wall have a good seismic resistance ability.

Deyanova et al. (2016)

The results of a parametric study to evaluate the dynamic response of earth-retaining gravity walls were presented by Deyanova et al., 2016. Advanced numerical modelling (FLAC 7.0) was used in the analyses. Seventeen sets of ten fully non-linear time-history analyses were performed using different wall dimensions, ten compatible spectrum records, two types of backfill (loose sand and dense sand), and one soil type foundation (dense sand). The results were compared with the European Committee for Standardization (EN 1997-1 and EN 1998-5) and Newmark's sliding block procedures. The study concluded that the residual horizontal displacements from a set of 10 spectrum-compatible records vary significantly (from 5 cm to 55 cm). It was also noted that the ground settlement behind the wall is not proportional to the amount of horizontal displacement or tilting, and the disturbed portion of the backfill behind the wall extended to a distance larger than the height of the wall. The authors stated that the EN 1998-5 procedure tends to underestimate the residual displacements. The authors also stated that some well-known Newmark's block-on-plane methods tend to underestimate the wall's permanent horizontal displacement when the yielding accelerations are obtained from static equilibrium using the M–O soil wedge. The study recommended that “if the wall with backfill of dense sand is designed for static loads with an over-design factor ($ODF_{sliding}$) for sliding greater than 1.3 or the wall with backfill of loose sand is designed with an $ODF_{sliding}$ greater than 1.2 (according to [EN 1997-1]), the wall is unlikely to fail in regions of medium-high seismicity with PGA ranging from 0.2 g to 0.35 g”.

Wagner and Sitar (2016)

Wagner and Sitar, 2016 presented experimental and analytical studies of the seismic response of stiff and flexible retaining structures. A series of geotechnical centrifuge model tests were conducted on different types of structures with cohesionless and cohesive backfill. The stiff retaining wall was represented by a U-shaped channel that can deflect but cannot translate or rotate about its base. At the same time, the flexible retaining wall was represented by a free-standing cantilever wall that can translate and rotate. A numerical simulation of the centrifuge experiments was developed in FLAC 2-D. The findings of this study were compared with the Mononobe-Okabe (M-O) method. In general, the results showed that the M-O method of analysis provides a reasonable upper bound for the response of stiff retaining structures. In contrast, the M-O method tends to overestimate the loads for flexible retaining structures. It was also noted that the dynamic forces for deeply embedded structures did not increase with depth and gradually became a small fraction of the overall load on the walls.

Candia et al. (2016)

Seismic response of retaining walls with cohesive backfill, using a series of centrifuge tests, was studied by Candia et al., 2016. An embedded basement wall (6 m in height) and a cantilever wall (6 m in height) were modeled in the centrifuge with a scaling length factor of 1/36 and tested at 36-g of centrifuge acceleration. The soil used in the experiment was lean clay. The results showed that the initial contact stresses between the wall and soil were reduced due to the natural soil cohesion and compaction. On the other hand, the dynamic loads were not influenced by cohesion or compaction. It was also noticed that the dynamic earth pressures increase approximately linearly with depth for both walls and the resultant applied at 0.33 H (H is the height of the wall).

Konai et al. (2017)

Konai et al., 2017 investigated the effect of excavation depth on the ground surface settlement for embedded cantilever retaining wall using finite difference program FLAC-2D. The model consisted of a two-dimensional (plane strain) finite-difference analysis of small excavation. Two cantilever retaining walls, which are 200 mm in height and 2.4 mm in thickness, made of Plexiglass, are embedded in dry sand. A hysteretic model was used to model the soil under seismic conditions. The numerical model results were validated by comparing them with the laboratory shake table test results. Same as the numerical model, small-scale laboratory shake table tests of embedded cantilever walls were conducted on dry sand. The study concluded that the maximum lateral displacement of the wall occurred near the ground surface and the maximum bending moment occurred below the excavation level. It is also noted that the maximum ground surface settlement occurred near the wall. The maximum distance behind the wall that can be affected by surface settlement due to seismic events is approximately 0.8 times the wall's total depth.

Jo et al. (2017)

Jo et al., 2017 conducted a study to evaluate the seismic earth pressure for inverted T-shape stiff retaining wall in cohesionless soils when dynamic centrifuge was implemented. Two dynamic centrifuge tests were conducted to assess the magnitude and distribution of the dynamic earth pressure and the inertial forces effect of the inverted T-shape cantilever retaining wall. Two different stem heights were selected, 5.4 m and 10.8 m, at the prototype scale to address the effect of the wall height during seismic events. The natural periods of the walls were estimated based on the assumption that the RW was a fixed SDOF with distributed mass and elasticity. Dry medium silica sand was used in this experiment. Real earthquake and sine wave motions (Ofunato, Hachinohe and sine wave) were used in the study. The results found in this experimental study were compared with the results calculated by the M-O and the Seed and Whitman (S-W) methods. Based on the results, it was concluded that the dynamic earth pressure changed with time, and the lateral earth pressure was not static during an earthquake. The dynamic earth pressure distribution is close to a triangular shape, and the point of dynamic thrust is located at 0.33 H above the wall base, which is not what was proposed by Seed and Whitman (1970). The M-O and S-W methods overestimated the coefficient of dynamic earth pressure for the model with a height of 10.8 m. In this study, the wall's inertial moment contributed to the total dynamic moment by approximately 50–60%.

Yazdandoust, Majid (2017)

Yazdandoust, 2017 investigated the behavior and performance of steel-strip reinforced-soil retaining walls during seismic loading. The experimental program consisted of a series of 1-g shaking table tests on 0.9 m high reinforced-soil wall models using different strip lengths. Variable amplitude harmonic excitation at different peak accelerations and durations were applied to the models. A wet mixture of sand and silt with different relative densities was used for the backfill, reinforced zone and foundation. The results showed that the deformation mode of walls depends on the length of strips. It was noted that the main mode of deformation was a bulge of the facing and rotation about the wall base. The author found that the threshold acceleration corresponding to the onset of plastic displacements was equal to 0.5 g for all models, despite the steel strip's lengths. On the other hand, threshold acceleration corresponding to the initiation of active wedge failure was dependent on strip length.

Pain et al. (2017)

Pain et al., 2017 studied the seismic rotational stability of gravity retaining walls by modified pseudo-dynamic method. Rotational stability analysis of gravity retaining wall on rigid foundation was addressed using limit equilibrium method. The soil behind the wall was dry cohesionless backfill. The authors concluded that the solution satisfied the zero-stress boundary condition at the free ground surface. It was noted that acceleration amplified towards the ground surface and it is time-dependent and non-linear. The authors stated that amplification of accelerations towards the ground surface depends on the height of the wall, shear wave velocity of backfill soil, a damping ratio of backfill soil and frequency content of input excitation. Stability factor (F_W) is proposed in this study to determine the safe weight of the retaining wall against rotational failure.

Lin et al. (2018)

The seismic response of a combined retaining structure was addressed by Lin et al. (2018) using a shaking table test and numerical simulation. The combined retaining structure is used to support a steep slope. It consisted of a rigid structure, such as a gravity wall, to be used as a lower structure and a flexible structure, such as an anchoring frame beam, to be used as an upper structure. Wenchuan, Da-Rui and Kobe ground motions with different amplitudes were applied in both horizontal and vertical directions. The experimental results were compared with the results obtained from the numerical simulation. The results showed that the soil's horizontal acceleration response below the frame beam was more intensive than the horizontal acceleration response of the soil behind the gravity wall. The horizontal acceleration near the bottom of the frame beam was significantly amplified. An increase in the axial stress of anchors was noticed due to seismic excitation. The upper structure experienced shear and tension failures. Based on the results, the authors recommended that an enhancement in seismic design was required for the upper structure of the combined retaining structure, especially at the bottom portion. An anchor with a high tensile strength should be used in the design of such a structure.

Jadhav and Prashant (2020)

Jadhav and Prashant (2020) proposed a displacement-based design methodology for cantilever retaining walls with shear key to improve the retaining structure performance when subjected to seismic loading. A two-dimensional plane strain finite element model of a cantilever retaining wall was developed. The model consists of a cantilever retaining wall with a shear key at the base and dry loose sand as backfill. Different sizes and locations for the shear key were implemented in this study. The model was subjected to four input ground motions (0.12 g, 0.24 g, 0.36 g, and 0.6 g). The numerical model was validated using case studies. The results showed that when the shear key was placed at the heel of the cantilever retaining wall, the translation movement was restricted by about 40 %. Design factors were proposed to estimate peak rotational displacements, residual rotational displacements and peak sliding displacements by comparing the results from the finite element model analysis with the double wedge model.

2.4.2 Review of Previous Studies on Blast Effects on Geotechnical Structures and Soils

There is a demand in recent years to understand the dynamic behaviour of above ground and underground structures subjected to air blast. Previous studies addressed the dynamic response of various structural members under air blast load effects using different load application techniques. These techniques include: i) field blast test (involving the detonation of explosives), ii) quasi-static tests simulating blast pressure, and iii) shock wave generated by a shock tube.

Researchers also investigated cases where the height of detonation of the bomb is close to the ground surface. In this case, an explosion on or near the ground surface can generate both air-blast pressure and ground shock on structures that are close to the detonation point. Since the wave propagation velocities are different for soils and air, the ground shock exciting the structure foundation could occur before the arrival of air blast pressure to the structure.

Shim (1996)

Shim (1996) conducted centrifuge tests at 440 g-ton to investigate piles' response in saturated soil under buried blast loading. The objectives of the study were to understand the propagation of ground shock from the source of detonation, crater formation, the buildup of pore water pressure that may lead to liquefaction, and the response of piles. The author used a commercially available detonator equivalent to the selected conventional weapon to simulate the blast loading. Aluminum tube model piles were used in this experiment and placed in a container filled with saturated soil. Nine models were tested, consisting of five free-field tests and four model pile tests in the same soil environment. Based on the test results, empirical relations for the free-field motion were developed for practical uses. Blast-induced liquefaction was noted in the range of 1 to 2 radii of the crater. Due to liquefaction, large plastic deformations occurred in the piles that led to severe damage of the pile. The author stated that centrifuge modelling was shown to be a powerful tool for the study of buried structures subjected to an explosion.

Ashford et al. (2004)

Ashford et al. (2004) presented a study on blast-induced liquefaction for full-scale foundation testing. In this paper, a pilot test program was conducted to find the suitable charge weight, delay, and pattern that can be used to trigger liquefaction for full-scale testing of deep foundations. The authors selected the Treasure Island site, a National Geotechnical Experimentation Site in the USA, as a test location because of the loose nature of the hydraulic fill combined with a high groundwater table. In this study, two sets of blasts were carried out. For each blast, a total of sixteen 0.5 kg TNT-equivalent charges were detonated. In both cases, charges were detonated two at a time with a 250-ms delay between explosions. After a few seconds of the detonation, the pore water transducers indicated the occurrence of liquefaction. Sand boils began to form at several transducer boreholes as well as at some blast hole locations after 3-5 minutes. The excess pore pressure ratio was determined as a function of scaled distance from the blast point. The authors found that peak particle velocity attenuated rapidly and was generally below the upper-bound limit based on Narin van Court and Mitchell (1995) data. It was noted that settlement was around 2.5% of the liquefied soil layer, and about 85% of the settlement transpired 30 minutes after the blast event. The results showed that reduction in soil strength occurred after blasting; however, the strength had substantially increased after several weeks.

Fujikura et al. (2008)

Fujikura et al., 2008 addressed the development and experimental validation of a multi-hazard bridge pier-bent concept. It is a bridge pier system that can provide an acceptable level of protection against collapse under seismic and blast loading. The experimental program consisted of a multicolumn pier-bent with concrete-filled steel tube (CFST) columns. The CFST system was subjected to blast loading. A satisfactory ductile behavior was noted from CFST columns of bridge pier specimens when subjected to blast loads. The results from the experiments were compared with the obtained results from the simplified method of analysis assuming an equivalent single degree of freedom system. The comparison of the results showed that the blast effective pressures acting on a circular column are equal to 0.45 to that of the blast pressures applied on a flat surface.

Luccioni et al. (2009)

Luccioni et al., 2009 presented a study on the generation of craters due to underground explosions. This study aimed to prove the accuracy of numerical simulation of craters produced by underground explosions. The authors used several numerical approaches with different model and processors for the soil. The numerical approach was validated by comparing its results with the experimental results. A good agreement was found between the crater diameter determined by an Euler processor for the soil and that determined by a Lagrange processor. The crater obtained by the latter model was deeper than the former model. It was also noted that the depth of crater obtained from both model was higher than the one observed in the experimental results. The final shape of the crater determined by Euler processor was a better representative of the actual crater shape. The authors concluded that the crater diameter was not influenced by the shape of the explosive load and the type of soil.

Yang et al. (2010)

Yang et al. (2010) discussed blast-resistant analysis for Shanghai metro tunnel in the soft soil using dynamic nonlinear finite element software LS-DYNA. The safety of the tunnel lining based on the failure criterion was evaluated in this analysis. It was assumed that the explosion would occur above the metro tunnel at the air-soil interface. Based on the tunnel structure's symmetries and the blast load, a 1/4 symmetrical geometrical model with a size of 25 m × 25 m × 30 m was used. The study considered three cases of TNT charge; 300, 500 and 1000 kg, and two depths were used for the tunnel, 7 m and 14 m. Furthermore, two research paths were selected to analyze the dynamic responses of the tunnel lining. The first path was along the transverse direction, 5 typical points were selected around the cross-section. The second path was along the longitudinal direction. The model was analyzed for horizontal distance ranging between 0 and 20 m from the explosion center.

The numerical results showed that the vulnerable areas of the tunnel were the upper portion of the tunnel lining cross-section in the directions of 0° to 22.5° and horizontal distances of 0 to 7 m from the centre of the explosion.

Kumar et al. (2010)

Kumar et al. (2010) studied the response of a semi-buried structure subjected to noncontact blast loading. Finite element analysis was carried out using ABAQUS. Mild steel panels of thickness 30 mm were used to build the structure model. Buried depth of the structure was varied. The structure was supported by a hard surface made of lean concrete. The roof was made of corrugated steel. The structure was modelled using shell elements. The effect of soil-structure interaction was addressed by using Wolf's spring-dashpot-mass elements. Blast loading was modelled using linearly decaying pressure-time history based on equivalent Trinitrotoluene (TNT) and standoff distance. In this study, the effect of scaled distance, type of soil and buried depth were presented. The results showed that the soil-structure interaction and the type of soil play an important role in the structure's dynamic behaviour. It was also noted that increasing the buried depth led to a reduction of the displacement and von Mises stress in the structure.

Charlie et al. (2013)

Charlie et al. (2013) presented results from experimental field program using spherical stress waves to induce residual excess pore pressure and liquefaction in large saturated sand specimens. Twenty-two single spherically-shaped explosive charges ranging from 0.00045 to 7.02 kg were suspended and detonated in water located over saturated sand. A specimen container, with a diameter of 4.27 m and a height of 1.83, was placed at the bottom of a test pit that was excavated to a depth of 5.5 m below the ground surface. The open top of the container was placed at the same level of the site ground water table. The open bottom was sealed with an impermeable pond liner. In this study, loose, dense and very dense saturated sand was used. The authors concluded that sand relative densities influence attenuation laws for PPV, peak pressure, peak pore water pressure and residual pore pressure. The study also found that as the relative density and effective stress of soil increase, peak radial particle velocity and peak strain for inducing liquefaction in soil increase.

Xia et al. (2013)

Xia et al. (2013) presented a case study to address the effects of tunnel blast excavation on the surrounding rock mass and adjacent existing tunnels' lining systems. Field tests and numerical simulation are carried out to analyze the damage of the surrounding rock and the lining system under different blast loads. The case study was based on the Damaoshan highway tunnel project in China, which comprises a new tunnel located between two existing tunnels. The rock around the tunnels was consisted of clayey soil and weathered granite. Blast vibration monitoring and sound wave tests were conducted to study the characteristics of blast vibrations in the existing tunnels subjected to blasting in the adjacent new tunnel. It was noticed that, for a given blast load, the peak particle velocity (PPV) and the rock damage extent decrease with the excavation progress. A relationship was established between the rock damage extent around the tunnels and the PPV on the existing tunnel wall. A PPV of 0.22 m/s in the existing adjacent tunnel was proposed for the Damaoshan tunnel project to limit the damage extends to approximately 1.6 m at the exit and entrance portion. The authors stated that when the PPV was less than 0.3 m/s, no failure occurred in the linings or at the rock–lining interfaces of the existing tunnels.

Dogan et al. (2013)

Dogan et al. (2013) evaluated the effects of blast-induced ground vibration on a new residential zone. Field experimental study was conducted to measure ground vibrations induced by surface and underground TNT blast operations. The soil consisted of alternating layers of gravelly, sandy and clayey units. The values of PPV and horizontal acceleration were recorded in two directions at three stations. The authors concluded that the PPV values for underground blasts are smaller than those measured for surface blasts for the same scaled distance. It was also found that the frequency resulted from underground blasts ranges between 10 and 15 Hz, with all values smaller than 40 Hz. For surface explosions, the frequency distribution was clustered in the ranges of 20–30 Hz and 55–70 Hz.

Jayasinghe (2014)

Jayasinghe (2014) studied the response and the damage of reinforced concrete pile foundations embedded in a homogeneous single soil profile subjected to surface explosions and underground explosions. A comprehensive finite element modelling technique was used to evaluate the response. The model of the pile foundation system was developed using the finite element software LS-DYNA. In this research, the influence of soil type, the pile reinforcement and the spacing between piles in a pile group was studied. The results from the experimental program conducted by Shim (1996) and Woodson and Baylot (1999) were used to validate the modelling technique, and the concrete material model. The results showed that longitudinal reinforcement in a pile significantly affected the pile's blast response. Reduction in the pile deformations was noticed with the increase in the longitudinal reinforcement.

Furthermore, the blast response of the pile foundation was influenced by explosive charge weight and shape. The author stated that the blast pressures generated by a cylindrical charge were significantly greater than those generated by a spherical or a cubic charge. The effects of buried explosions were more significant on the blast response and damage of the pile than surface explosions under the same conditions. The study showed that soil properties had a strong impact on the blast response of pile foundations. Piles in saturated soil and loose dry soil were more vulnerable to blast loads than piles embedded in partially saturated soil, subjected to the same buried explosion.

<u>Mobaraki and Vaghefi (2015)</u>

Mobaraki and Vaghefi, 2015 presented numerical study of the depth and cross-sectional shape of a tunnel under surface explosion. The dynamic responses of a buried tunnel in depths of 3.5 m, 7 m, 10.5 m, and 14 m under surface explosion was evaluated in this paper. Surface detonation of 1000 kg TNT charge and sandy soil were used. The cross-sectional shape of the tunnel was modeled as the Kobe box shape, semi ellipse, circular and horseshoe shape tunnel. The finite element software LS-DYNA was used to model and analyze the impact of the surface explosion on the buried tunnel. The results showed that the box shape tunnel demonstrated higher resistance to surface explosion than the circular and horseshoe tunnels but lower resistance than the semi ellipse tunnel. The maximum residual deformation of the Kobe tunnel occurred at the center of the wall. It was also noticed that the blast load impact on the tunnel decreased with the increase of distance from the blast center.

<u>Gao et al. (2016)</u>

An exact solution for three-dimensional (3D) dynamic response of a cylindrical lined tunnel in saturated soil to an internal blast load was presented by Geo et al., 2016. The solutions were derived by using Fourier transform, and Laplace transform. The surrounding soil was modeled as a saturated medium based on Biot's theory, and the lining structure modeled as an elastic medium. The numerical solutions for the lining and surrounding soil's dynamic response were determined using a numerical method of inverse Laplace transform, and Fourier transform. It was found that the dynamic responses, such as radial displacement, radial stress, pore water pressure, decreased sharply in an oscillating manner as the time elapsed. On the other hand, the dynamic responses attenuated exponentially with increasing distance away from the explosion source center in the tunnel's radial and axial direction. The authors stated that the proposed solutions could be used to evaluate the damage caused by the explosion to surround areas of the tunnel at any given elapsed time apart from the section at the source of the explosion.

Han et al. (2016)

The interaction between subway tunnels and soils subjected to medium internal blast loading was studied by Han et al. (2016). A series of numerical simulations were carried out to analyze this study using the software LSDYNA. Dense saturated soil was used. The authors observed that tunnel lining exhibited different failure modes due to different amounts of explosives. When a relatively large amount of explosive was used, severe rupture first appeared in the explosive vicinity and then propagated along the tunnel due to lining vibration. However, reducing the intensity of the blast loads led to less damage and fractures. The phase lag of vibration caused these fractures. Results showed that soil liquefied with blast loading from 50-200 kg TNT equivalents. Soil failed progressively due to vibration of the tunnel and blast loading. During extensive lining failure, the risk of liquefaction was reduced as only a small portion of blast energy propagated into the soil. However, when the lining failure was less severe, soil liquefaction occurred. Strong vibration in the lining causes more energy to propagate to the surrounding soil.

Karinski et al. (2016)

Karinski et al. (2016) addressed the Mach stem phenomenon for shaped obstacles buried in soil. In this paper, the explosion characteristics of a buried explosive charge in proximity to a rigid cylindrical obstacle was investigated. The model was designed as a line-charge explosion close to a circular cross section rigid obstacle buried in a homogeneous isotropic irreversibly compressible soil medium. The study investigated the pressure distribution along an obstacle. It was found that for a short standoff distance and high-intensity pressure, the pressure distributions' envelope showed three maximum values that were located at distance away from the axis of symmetry. The pressure distribution analysis showed that the second (absolute-primary) and third (secondary) peaks are caused by the Mach stem effect appearing in a soil medium with full locking.

Jiang et al. (2020)

Jiang et al. (2020) presented a study that assessed the safety of buried pressurized gas pipelines subjected to blasting vibration. Blasting is a common technique that is used in the excavation of urban metro foundation pits in China. The second stage of Wuhan Metro line 8 was chosen as a case study in this paper to address the effects of the blasting excavation of the foundation pits on the adjacent gas pipelines. Using the data obtained from the field, a mathematical model was proposed to describe the attenuation of peak particle velocity (PPV) of ground surface soils. The authors also established a 3D numerical calculation model to analyze a buried gas pipeline's blasting vibration response, with a 0.4 MPa internal operating pressure. Based on the numerical simulation analysis of the buried gas pipeline, it was noticed that the highest values of PPV and peak von-Mises stress occurred on the pipeline side facing the explosion. The authors recommended that the pipeline should be suspended or operating at low pressure during blasting events to avoid dangers.

2.4.3 Conclusions

From the review of the available literature, it was noticed that the pseudo-static approach was implemented for evaluating seismic stability of retaining walls. In this approach, the M-O equation was used to estimate the lateral earth pressures. The M-O method was derived by modifying Coulomb's static earth pressure theory to account for inertial forces. However, one of the limitations is that the method was derived for a dry granular backfill. Therefore, for saturated backfill, it has become a common practice to assume that pore water moves with the soil grains (Lai, 1998). On the other hand, movements of the RW due to seismic loading was not addressed in the pseudo-static equilibrium method. Thus, many studies addressed this issue by proposing a wall displacement-based approach (such as, Richards-Elms, 1979; Whitman-Liao, 1985; and Steedmann and Zeng, 1996).

Since the introduction of the M-O method, many experimental and analytical studies have been conducted to understand the mechanism of load transfer from the backfill to the wall when subjected to seismic loading. These studies investigated the dynamic lateral earth pressure and modes of wall movement on rigid and flexible retaining walls due to seismic motions (section 2.4.1).

Furthermore, there is a demand in recent years to understand the dynamic behaviour of above ground and underground structures subjected to air blasts. Various studies addressed the dynamic response of various structural members under air blast load effects. Other studies investigated the effect of blast loads on underground structures such as tunnels and piles (section 2.4.2).

It can be concluded from the review of the available literature that past research did not address the dynamic response of soil retaining walls due to blast loading. Therefore, the geotechnical response of retaining walls when subjected to blast load was examined in this study.

2.5 Shock Tube

Dynamic behaviours of different engineering components subjected to blast loads can be investigated using either actual explosives or blast simulators (Dusenberry 2010). Shock tubes are the most common blast simulators employed by different research organizations (Lloyd, 2015 and Burrell, 2012). Like those produced by actual explosions, shock waves are generated when the driver pressure forces air into the specimen at high velocities. Conducting blast tests by shock tube testing is cost and time effective. Moreover, these tests can be run within an environment subjected to far less restrictions than those in which real blast tests are performed (Dusenberry 2010).

Shock tube testing facility located at the Blast Research Laboratory of the University of Ottawa (Figures 2.25 and 2.26) has been used by several researchers (e.g., Kadhom, 2015 and Lloyd, 2010) to simulate the blast loading on different structural components since 2009. The shock tube consists of four main sections. The driver and the spool are the first and second sections, respectively. These are the sections in which the shock energy is built-up in the form of compressed air and the firing action takes place based on the diaphragm's targeted pressure capacity (Kadhom, 2015). The driver section's inside diameter pipe is 597 mm, and the wall thickness of 19 mm. The length of the driver section ranged between 305 mm and 5185 mm in 305 mm increments. The driver section length can be modified to produce a wide range of pressure-impulse combinations. The spool section is a 90 mm long FIKE Combination Disk Holder (Fike 2005). The spool section's flanges are designed to connect with the flanges on the driver and the flange located between the spool and the beginning of the expansion section. The flanges have 30° inlets that mate with protrusions on the coupling flanges of the driver and expansion section (Figure 2.27). When held together with 20 Grade 8 high-strength threaded rods 31.75 mm in diameter, the driver-spool-expansion section flanges clamp the diaphragms in place (Lloyd, 2010). Two diaphragms are used in the shock tube's operation, one on each end of the spool section. The diaphragm consists of three square sheets of 813 mm grade 1100 aluminum foil with different thicknesses. Twenty holes 38 mm in diameter are placed on the foils in a circular pattern on a radius of 374.65 mm and with an inclination angle of 18° between holes. The holes are provided to hold the driver and spool to the expansion section through twenty threaded rods.

The blast wave formed in the driver section propagates and expands through the expansion section, which starts from 597 mm in diameter and ends with a square test area of 2033 mm by 2033 mm. The test specimen is attached to the square steel frame located at the front of the shock tube. The length of the expansion section is 7 m.

When the test specimen is a column or a beam, the pressure formed by the shock wave is collected by a steel load transfer system that covers the entire end of the shock tube, referred to as the “steel curtain.” This steel curtain's function is to transfer the blast pressure formed by the shock tube to the test specimen as a uniformly distributed load. However, the steel curtain is not needed if the test specimen is large enough (e.g., slabs or wall) to cover the entire mouth of the shock tube. In this case, the blast pressure is transferred directly to the specimen.

Lloyd (2010) performed test shots with the shock tube to address the effect of driver length and driver pressure on reflected pressure reflected impulse and positive phase duration. The results showed that longer driver lengths provided shock waves with longer positive phase durations, and increasing driver pressures led the shock waves to have higher reflected pressures. The maximum reflected pressure that can be produced using the shock tube is about 100 kPa. Pressure gauges located at the front of the shock tube are used to measure the reflected pressure.

The shock tube is operated manually by incrementally increasing the driver pressure and the spool pressure to the anticipated level and then trigger firing by draining pressure from the spool section to cause aluminum foil diaphragms rupture. Two static pressure gauges are used to monitor the pressures on the driver and spool sections. As the firing of the shock tube initiated, the spool section is brought to atmospheric pressure, which leads to high-pressure differential between the spool section and the driver section. Due to the formation of this high pressure, the first diaphragm is ruptured. When this diaphragm ruptures, the compressed air from the driver section expands into the spool section and hits the second diaphragm. As a result, the second diaphragm is ruptured, and the shock wave is allowed to move through the expansion section.

Figure 2.25: Shock tube (Kadhom, 2015)

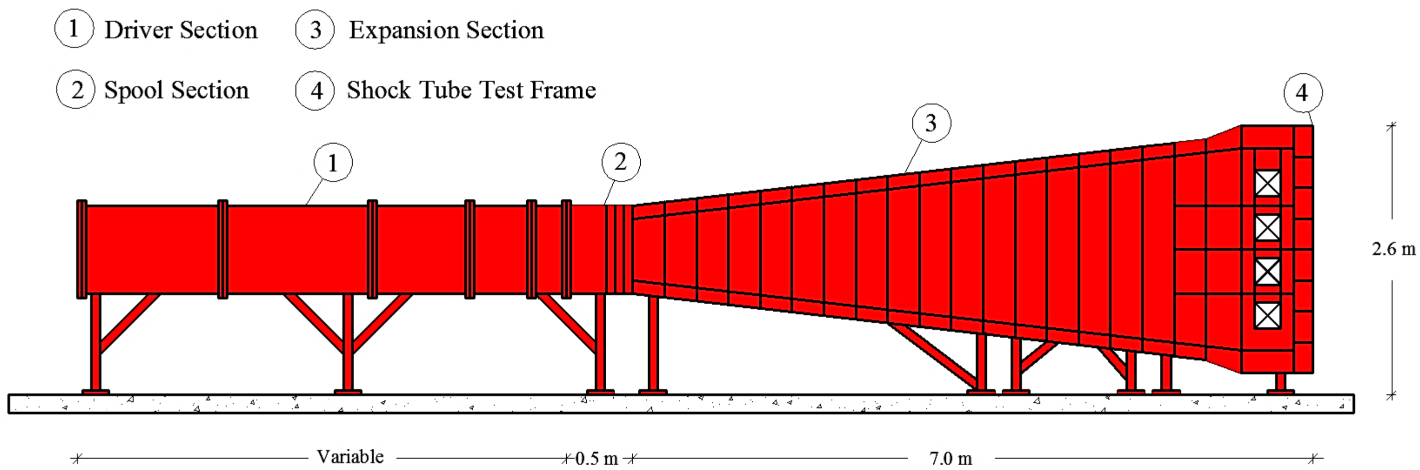

Figure 2.26: Shock-tube sections (schematic) (Kadhom, 2015)

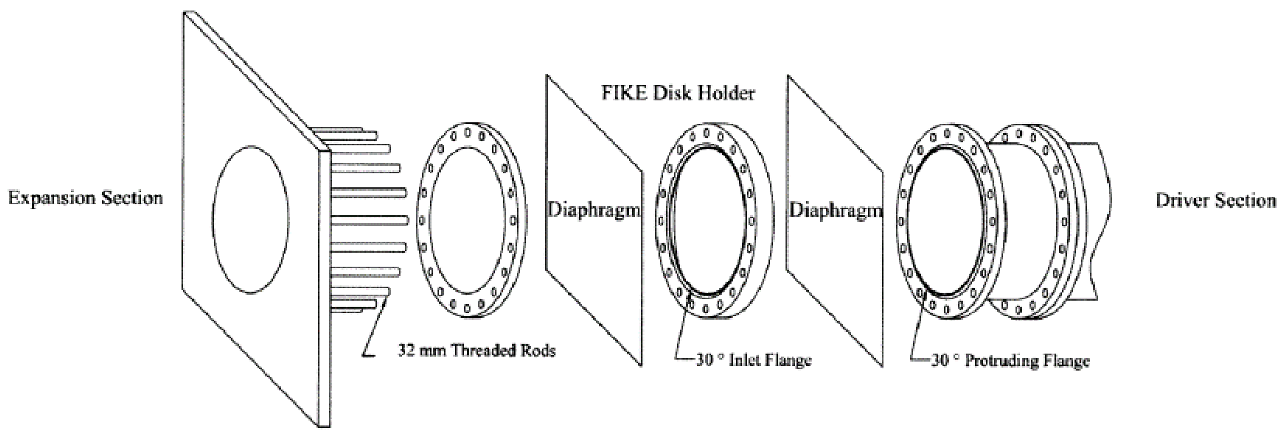

Figure 2.27: Detailing of disk holder (spool section) and diaphragm sections of shock tube (Lloyd, 2010)

2.6 Monitoring Soil Parameters

A number of instruments were used in the soil-RW model to capture the dynamic response of the model during the blast event.

Soil pressure gauge

The KDE-PA and KDF-PA are soil pressure gauges that have an outside diameter of 50 mm. As they are small in size and have a dual-diaphragm structure, they are commonly used to conduct model experiments. The difference between the two models is how the cable is attached to the gauge body (Figure 2.28). The soil pressure gauges can be used to measure dynamic earth pressure. Their maximum capacities range between 200 kPa and 2MPa (manufacturing sheet; Tokyo Measuring Instruments Laboratory).

Three KDE-PA and one KDF-PA soil pressure gauges were used in this study. The KDF-PA model was used to measure the dynamic earth pressure below the foundation, and the rest were placed in the backfill.

Pressure transducer

The PX309 pressure gauge model was used to measure the pore pressure in the backfill and the foundation layers. The pressure transducer can measure pressures up to 100 kPa and its response time is less than one millisecond. It has high stability and low drift. Figure 2.29 displays the dimensions of the pressure sensor.

Dielectric water potential sensor

The MPS sensor measures the water potential and temperature of the soil and other porous materials. The sensor reading ranges between -9 kPa and -100,000 kPa. The MPS measures the water content of porous ceramic discs and converts the measured water content into water potential using the ceramic's moisture characteristic curve. The air entry potential of the largest pores in the ceramic is about -9 kPa (Operator's Manual). Figure 2.30 shows the MPS sensor.

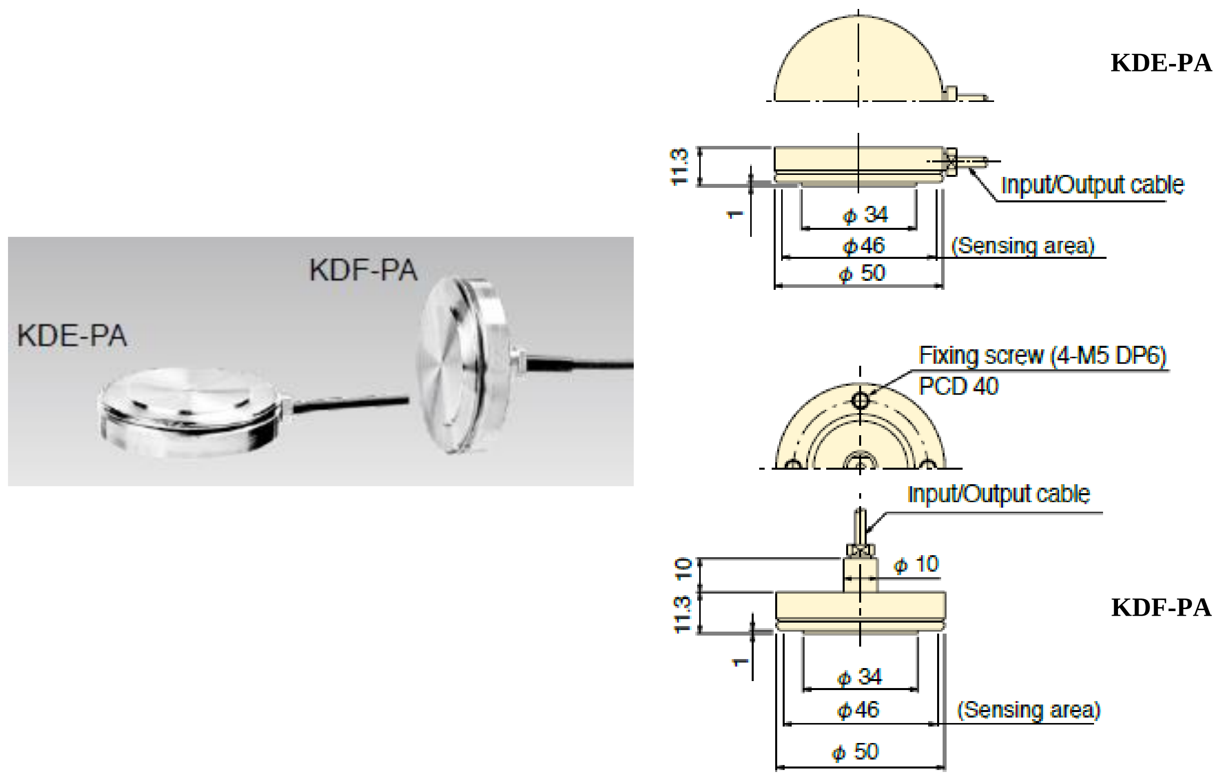

Figure 2.28: Soil pressure gauges (manufacturing sheet; Tokyo Measuring Instruments Laboratory)

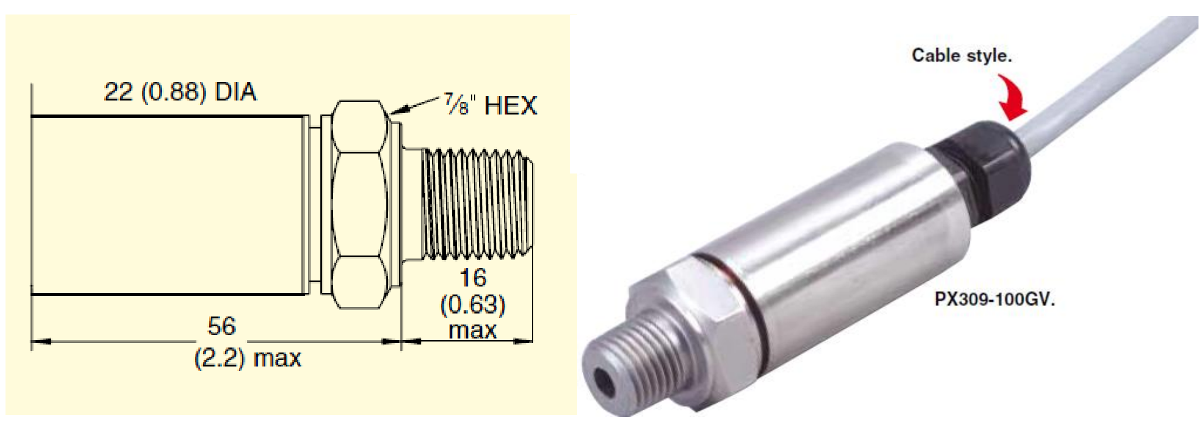

Figure 2.29: Pressure transducer; dimensions in mm (inch) (manufacturing sheet Omega)

Figure 2.30: Dielectric water potential sensors (Operator's Manual; Decagon Devices, Inc.)

2.7 Phantom Camera

Phantom camera is a digital high speed imaging system capable of recording thousands of high resolution frames per second (User Manual Revision 3.1, 2018). The Phantom imager with advanced CMOS (Complementary Metal Oxide Semiconductor) technology, and the Phantom Camera Control software are the main components of the system. These components form a system that provides high speed and resolution images. The most common method to control the camera systems is using a computer.

2.8 ProAnalyst Software

ProAnalyst is a video analysis software that is capable of automatically tracking objects in one or two dimensions. The tracked and analyzed data can be graphed, filtered, and exported in various formats from or within the ProAnalyst software (ProAnalyst Guide). The software can be used to measure and track velocity, position, size, acceleration, and other characteristics. ProAnalyst works with many videos (from AVI to MJPEG). In this study, the software was used to track and measure the displacement, velocity, and acceleration of the wall and the soil particles.

2.9 Summary and Conclusion

Explosion can be defined as a rapid and sudden release of a large amount of energy to the atmosphere forming a blast wave. The rapid increase of pressure produced by the blast wave is called the overpressure. The charge weight (W) and standoff distance (R) between the blast center and the target are the two elements that are used to identify the magnitude of a bomb threat. The term scaled distance ($Z = R/W^{1/3}$) is adopted in most blast analyses and design parameters. The analysis of dynamic response of a structure subjected to blast loading is a complex process since it involves the effect of high strain rates, non-linear behaviour of materials, and uncertainties in blast load characteristics (Ngo et al. 2007). To simplify the blast analysis, the structure is idealized as a SDOF system, while the blast load is idealized as a triangular pulse.

Underground or surface explosions lead to the formation of a crater, and a blast wave that propagates through the surrounding soil. The shock wave velocity is a function of the peak overpressures, the ambient sound speed, and the ambient atmospheric pressure. Body and surface waves are generated when the ground surface is subjected to explosion. The propagation velocities of body and surface waves depend on the density and stiffness of the soil. The deformation mechanisms of soil subjected to blast loading depends on the degree of saturation of the soil. When blast load is applied to dry soil, the bonds between the soil particles are deformed, the skeleton is destroyed, and the soil is compacted. However, if saturated soil is subjected to rapid dynamic loading, the deformation and the resistance of the soil would be determined by volumetric compression of the three phases, particularly of the mineral grains and water.

The analysis and design of earth retaining structures are one of the oldest and most fundamental studies in the geotechnical engineering field. Coulomb and Rankine provided the first scientific applications to design RW by defining the solution of the lateral static earth pressure problem. Their earth pressure theories are developed based on limit state analyses. Following the Great Kwanto Earthquake in 1923, many researchers focused their studies on the dynamic response of retaining structures and basement walls due to seismic loading. However, it can be observed from the review of the available literature that past research did not address the dynamic response of soil retaining walls due to blast loading. Therefore, it is essential to understand the geotechnical response of retaining walls when subjected to a blast load in order to fill the gap in previous studies.

2.10 References

Abrantes, A. E. (2003). Three-Dimensional Stress-strain Behavior of Cohesionless Material Subjected to High Strain Rate, PhD thesis, Clarkson University, Potsdam, New York, U.S.

Abrantes, A. E., and Yamamuro, J. A. (2002). Experimental and Data Analysis Techniques Used for High Strain Rate Tests on Cohesionless Soil. Geotechnical Testing Journal, 25(2), 128-141.

Akhlaghi, T., Hamidi, P., Nikkar, A. (2013). Investigation of Dynamic Response of Cantilever Retaining Walls Using FEM. International Journal of Basic Sciences & Applied Research, 2 (6), 657-663.

Al Atik, L. F. (2008). Experimental and Analytical Evaluation of Seismic Earth Pressures on Cantilever Retaining Structures. Doctoral thesis, University of California, Berkeley.

Al-Homoud AS., Whitman RV. (1999). Seismic analysis and design of rigid bridge abutments considering rotation and sliding incorporating non-linear soil behavior. Soil Dynamics and Earthquake Engineering, 18, 247–77.

Al-Qasimi, E. M., Charlie, W. A., and Woeller, D. J. (2005). Canadian Liquefaction Experiment (CANLEX): Blast-induced ground motion and pore pressure experiments. Geotechnical Testing Journal, 28(1), 9-21.

American Concrete Institute (ACI) 1998.

American Society of Civil Engineers (ASCE) 1997.

An, J., Tuan, C. Y. Cheeseman, B. A. Gazonas, G. A. (2011). Simulation of Soil Behavior under Blast Loading. International Journal of Geomechanics, ASCE, 11(4), 323-334.

Ashford, S. A., Rollins, K. M., and Lane, J. D. (2004). Blast-induced liquefaction for full scale foundation testing. Journal of Geotechnical and Geoenvironmental Engineering, 130(8), 798-806.

Bakeer RM, Bhatia SK, Ishibashi I. (1999). Dynamic earth pressure with various gravity wall movements. Proceedings of ASCE Specialty Conference on Design and Performance of Earth-Retaining Structures, Ithaca, NY, 88–99.

Bakir, P. G. (2013). Vibration of single degree of freedom systems. Lecture notes.

Bathurst RJ, Hatami K. (1998). Influence of reinforcement properties on seismic response and design of reinforced-soil retaining walls. Proceedings of the 51st Canadian Geotechnical Conference, Edmonton, Alberta, 2, 79–86.

Bathurst RJ, Hatami K. (1998). Seismic response analysis of a geo-synthetic reinforced soil retaining wall. Geosynthetics International, 5(1- 2):127–166.

Biggs, J. M. (1964). Introduction to Structural Dynamic, McGraw-Hill, Inc. U.S.

Bouamoul, A., Fillion-Gourdeau, F., Toussaint, G., Durocher, R. (2014). An empirical model for mine-blast loading. Defence Research and Development Canada.

Bragov, A. M., Lomunov, A. K., Sergeichev, I. V., Tsembelis, K., and Proud, W. G. (2008). Determination of physicomechanical properties of soft soils from medium to high strain rates. International Journal of Impact Engineering, 35(9), 967-976.

Bragov, A.M., Lomunov, A.K., Sergeichev, I.V., Proud, W., Tsembelis, K. and Church, P. (2005). A Method for Determining the Main Mechanics Properties of Soft Soils at High Strain Rates and Load Amplitudes up to Several Gigapascals, Tech. Phys. Lett., 31(6), 530-531.

Burrell, R. (2012). Performance of Steel Fiber Reinforced Concrete Columns under Shock Tube Induced Shock Wave Loading. MS Thesis, Department of Civil Engineering, University of Ottawa, Ontario, Canada.

Busch, C. L. (2016). Understanding the behavior of embankment dams under blast loading, The University of New Mexico, Albuquerque, New Mexico, U.S.

Canadian Standard Association (CSA) 1994.

Candia, G., Mikola, R. G., Sitar, N. (2016). Seismic response of retaining walls with cohesive backfill: Centrifuge model studies. Soil Dynamics and Earthquake Engineering 90, 411–419.

Carrier, M., Heffernan, P.J., Wight, R.G., Braimah, A. (2009). Behaviour of Steel Reinforced (SRP) Strengthening RC members under Blast Load. Canadian Journal of Civil Engineering, 36.

Carrol, W. F. (1988). A fast triaxial shear device. Geotechnical Testing Journal, 11(4), 276-280.

Cavallaro, A., Maugeri, M., Mazzarella, R. (2001). Static and Dynamic Properties of Leighton Buzzard Sand from Laboratory Tests. International Conferences on Recent Advances in Geotechnical Earthquake Engineering and Soil Dynamics.

Charlie, W. A. (2000). Discussion of War Damages and Reconstruction of Peruca Dam by Ervin Nonveiller, Josip Rupcic, and Zvonimir Sever. Journal of Geotechnical and Geoenvironmental Engineering, 126(9), 854-855.

Charlie, W. A., Bretz, T. E., Schure, L. A., and Doehring, D. O. (2013). Blast-induced pore pressure and liquefaction of saturated sand. Journal of Geotechnical and Geoenvironmental Engineering, 139(8), 1308-1319.

Charlie, W. A., Ross, C. A., and Piece, S. J. (1990). Split-Hopkinson pressure bar testing of unsaturated sand. Geotechnical Testing Journal, 13(4), 291-300.

Cooper, P. W. (1996). Explosives engineering, Wiley-VCH Publications, New York, NY.

Crawford, J. E., Malvar, L. J., Morrill, K. B., and Ferritto, J. M. (2001). Composite Retrofits to Increase the Blast Resistance of Reinforced Concrete Buildings TR-P-01-13, 10th International Symposium on Interaction of the Effects of Munitions with Structures, San Diego, CA.

Das, B. M. (2016). Principles of Foundation Engineering, Eighth Edition, Boston, MA, U.S.

Das, B. M. (1999). Principles of Foundation Engineering, Fourth Edition, Pacific Grove, CA, U.S.

Das, B. M. (1993). Principles of Soil Dynamics, Second Edition, Stamford, CT, U.S.

Deyanova, M., Lai, C. G., Martinelli, M. (2016). Displacement–based parametric study on the seismic response of gravity earth-retaining walls. Soil Dynamics and Earthquake Engineering, 80, 210–224.

Di Benedetto, H. (2007). Small strain behaviour and viscous effects on sands and sand-clay mixtures. In Soil Stress-Strain Behavior: Measurement, Modeling and Analysis, Springer, Dordrecht, Netherlands, 159-190.

Dobry, R. (2014). Simplified methods in soil dynamics. Soil Dynamics and Earthquake Engineering, 61-62, 246–268.

Dogan, O., Anil, Ö., Akbas, S. O., Kantar, E., and Tuğrul Erdem, R. (2013). Evaluation of blast-induced ground vibration effects in a new residential zone. Soil Dynamics and Earthquake Engineering, 50, 168-181.

Draganic, H., Sigmund, V. (2012). Blast loading on structures. Tehnicki vjesnik 19 (3), 643-652.

Dusenberry, D. O. (2010). Hand Book for Blast Resistant Design of Buildings, John Wiley&Sons, Inc, USA.

Ehrgott, J. Q., and Sloan, R. C. (1971). Development of a Dynamic High-pressure Triaxial Test Device, U.S. Army Engineering Waterways Experiment Station, Vicksburg. Mississippi. U.S.

Enomoto, T., Kawabe, S., and Tatsuoka, F. (2007a). Viscosity of round granular materials in drained triaxial compression. In Proceedings of 13th Asian Regional Conference on Geotechnical Engineering and Soil Mechanics, Kolkata, India, 19-22.

Enomoto, T., Tatsuoka, F., Shishime, M., Kawabe, S., and Di Benedetto, H. (2007b). Viscous property of granular material in drained triaxial compression. In Soil Stress-Strain Behavior: Measurement, Modeling and Analysis, Springer, Dordrecht, Netherlands, 383-397.

Ertugrul, Ozgur L., Trandafir, Aurelian C. (2014). Seismic earth pressures on flexible cantilever retaining walls with deformable inclusions. Journal of Rock Mechanics and Geotechnical Engineering 6, 417-427.

European Committee for Standardization. (2004). Geotechnical design. Part 1: general rules. Brussels: CEN.

European Committee for Standardization. (2004). Design of structures for earthquake resistance. Part 5: foundations, retaining structures and geotechnical aspects. Brussels: CEN.

Farr, J. V. (1990). One-dimensional loading-rate effects. Journal of Geotechnical Engineering, 116(1), 119-135.

Fujikura, S., Bruneau, M., Lopez-Garcia, D. (2008). Experimental Investigation of Multihazard Resistant Bridge Piers Having Concrete-Filled Steel Tube under Blast Loading. Journal of Bridge Engineering, ASCE, 13 (6), 586-594.

Gao, M., Zhang, J.Y., Shen, Q.S., Gao, G.Y., Yang, J., Li, D.Y. (2016). An exact solution for three-dimensional (3D) dynamic response of a cylindrical lined tunnel in saturated soil to an internal blast load. Soil Dynamics and Earthquake Engineering 90, 32–37.

Gohl, W. B., Howie, J. A., and Rea, C. E. (2001). Use of controlled detonation of explosives for liquefaction testing. In Proceedings of 4th International Conference on Recent Advances in Geotechnical Earthquake Engineering and Soil Dynamic and Symposium in Honor of Professor W.D. Liam Finn, San Diego, California, U.S.

Han, Y., Zhang, L., Yang, X. (2016). Soil-Tunnel Interaction under Medium Internal Blast Loading. Advances in Transportation Geotechnics. The 3rd International Conference on Transportation Geotechnics. Procedia Engineering, 143, 403–410.

Hao, H., Wu, C. (2005). Numerical study of characteristic of underground blast induced surface ground motion and their effect on above-ground structures part II. Effects on structural responses. Soil Dynamics and Earthquake Engineering 25, 39-53.

Hatami, K., Bathurst, R.J. (2000). Effect of structural design on fundamental frequency of reinforced-soil retaining walls. Soil Dynamics and Earthquake Engineering 19, 137-157.

Henrych J. (1979). The dynamics of explosion and its use. Chapter 5, Elsevier; New York.

Huang, J., Xu, S., and Hu, S. (2013). Effects of grain size and gradation on the dynamic responses of quartz sands. International Journal of Impact Engineering, 59, 1-10.

Hudaverdi, T. (2012). Application of multivariate analysis for prediction of blast-induced ground vibrations. Soil Dynamics and Earthquake Engineering 43, 300-308.

Huy, N. Q., Van Tol, A. F., and Holscher, P. (2006). Laboratory Investigation of the Loading Rate Effects in Sand. Technical report, Delft University of Technology, Delft, The Netherlands.

Jackson, J. G., Ehogott, J. Q., and Rohani, B. (1979). Loading Rate Effects on Compressibility of Sand. Miscellaneous Paper SL-79-24, Structure laboratory, U.S. Army Engineering Waterways Experiment Station, Vicksburg, Mississippi, U.S.

Jadhav, P. R. and Prashant, A. (2020). Computation of seismic translational and rotational displacements of cantilever retaining wall with shear key. Soil Dynamics and Earthquake Engineering 130, 59-66.

Jayasinghe, L.B. (2014). Blast response and Vulnerability assessment of piled foundations. Queensland University of Technology, Brisbane, Australia.

Jayasinghe, L.B. D.P. Thambiratnam, N. Perera, J.H.A.R. Jayasooriya. (2014). Blast response of reinforced concrete pile using fully coupled computer simulation techniques. Computer and Structures 135, 40-49.

Jayasinghe, L.B. D.P. Thambiratnam, N. Perera, J.H.A.R. Jayasooriya. (2013). Computer simulation of underground blast response of pile in saturated soil. Computer and Structures 120, 86-95.

Jiang, N., Zhu, B., He, X., Zhou, C., Luo, X., Wu, T. (2020). Safety assessment of buried pressurized gas pipelines subject to blasting vibrations induced by metro foundation pit excavation. Tunnelling and Underground Space Technology 102, 103448.

Jichong, A. (2010). Soil Behavior under Blast Loading. University of Nebraska–Lincoln.

Jo, S-B, Ha, J-G, Lee, J-S, Kim, D-S. (2017). Evaluation of the Seismic Earth Pressure for Inverted T-Shape Stiff Retaining Wall in Cohesionless Soils via Dynamic Centrifuge. Soil Dynamics and Earthquake Engineering 92, 345–357.

Jung, C.M. (2009). Seismic loading on earth retaining structures. Purdue University, West Lafayette, Indiana.

Kadhom, B. (2015). Blast Performance of Reinforced Concrete Columns Protected by FRP Laminates. Doctoral thesis, University of Ottawa, Ontario, Canada.

Karimpour, H., and Lade, P. V. (2010). Time effects relate to crushing in sand. Journal of Geotechnical and Geoenvironmental Engineering, 136(9), 1209-1219.

Karinski, Y.S., Feldgun, V.R., Racah, E., Yankelevsky, D.Z. (2016). The Mach stem phenomenon for shaped obstacles buried in soil. Advances in Engineering Software 101, 98–105.

Karlos, V., Solomos, G. (2013). Calculation of blast loads for application to structural components. European Laboratory for Structural Assessment.

Kinney, G. F., Graham, K. J. (1985). Explosive Shocks in Air.

Kiyota, T., and Tatsuoka, F. (2006). Viscous property of loose sand in triaxial compression, extension and cyclic loading. Soils and Foundations, 46(5), 665-684.

Kloukinas, P., Scotto di S., Anna, P., Augusto, D., Matthew, E., Aldo, L. Simonelli, A., Taylor, C., Mylonakis, G. (2015). Investigation of Seismic Response of Cantilever Retaining Walls: Limit Analysis vs Shaking Table Testing. Soil Dynamics and Earthquake Engineering, 77, 432–445.

Konai, S., Sengupta, A., Deb, K. (2017). Effect of excavation depths on ground surface settlement for embedded cantilever retaining structure due to seismic loading. Procedia Engineering, 199, 2342–2347.

Kumar, M., Matsagar, V.A. and Rao, K.S. (2010). Blast Loading on Semi-Buried Structures with Soil-Structure Interaction, Proceeding of the IMPLAST Conference, Rhode Island, USA.

Lai, Susumu. (1998). Rigid and Flexible Retaining walls during Kobe Earthquake. Fourth International Conference on Case Histories in Geotechnical Engineering, St. Louis, Missouri, 108-127.

Lee, W.Y. (2006). Numerical modeling of blast induced liquefaction, DAI, 67, no. 06B, 3305.

Lewis, B.A. (2004). Manual for LS-DYNA soil material model 147, Federal Highway Administration, FHWA-HRT-04-095, McLean, VA.

Lin, Y-L, Cheng, X-M, and Yang, G-L. (2018). Shaking table test and numerical simulation on a combined retaining. Soil Dynamics and Earthquake Engineering, 108, 29–45.

Liu, H. (2009). Dynamic Analysis of Subway Structures under Blast Loading. Department of Civil Engineering, the City College of New York.

Lloyd, A. (2015). Blast Retrofit of Reinforced Concrete Columns. Doctoral thesis, University of Ottawa, Ontario, Canada.

Lloyd, A. (2010). Performance of Reinforced Concrete Columns under Shock Tube Induced Shock Wave Loading. Master thesis, University of Ottawa, Ontario, Canada.

Lu, G., Fall, M. (2018a). State-of-Art modeling of soil behaviour under blast loadings. Geotechnical and Geological Engineering, 36: 3331–3355.

Lu, G., Fall, M., (2018b). Simulation of blast induced liquefaction susceptibility of subsurface fill mass. Geotechnical and Geological Engineering: An International 36(3), 1683-1706.

Lu, G., Fall, M., (2018c). Modeling post-blasting stress and pore pressure distribution in hydrating fill mass at early age. ASCE International Journal of Geomechanics, 18(8), 04018090.

Lu, G., Fall, M., Cui, L (2017). A multiphysics-viscoplastic cap model for simulating the blast response of cemented tailings backfill. Journal of Rock Mechanics and Geotechnical Engineering, 9(3), 551-564.

Lu, G., Fall, M. (2017). Modelling blast wave propagation in a subsurface geotechnical structure made of an evolutive porous material. Mechanics of Materials, 108, 21-39.

Lu G., Fall M, (2016). Modeling blast-induced liquefaction of tailings backfill at early ages. GeoVancouver 2015 – the 69th Canadian Geotechnical Conference (CGC), Oct. 1-4 2016, Vancouver, Canada CD rom.

Lu, G., Fall, M. (2015). A coupled chemo-viscoplastic model for cemented tailings backfill under blast loading. International Journal of Numerical and Analytical Methods in Geomechanics, 40,1123-1149.

Lu, Y., Wang, Z., Chong, K. (2005). A comparative study of buried structure in soil subjected to blast load using 2D and 3 D numerical simulations. Soil Dynamics and Earthquake Engineering, 25, 275-288.

Luccioni, B., Ambrosini, D., Nurick, G., Snyman, I. (2009). Craters produced by underground explosions. Computers and Structures, 87, 1366–1373.

Malvar, L.J., Crawford, J.E., Wesevich, J.W., and Simons, D.A. (1997). A plasticity concrete material model for DYNA3D, International journal of impact engineering, 19 (9-10), 847-873.

Manolis, G. D., Dineva, P. S. (2015). Elastic waves in continuous and discontinuous geological media by boundary integral equation methods: A review. Soil Dynamics and Earthquake Engineering, 70, 11-29.

Martin, B. E., Chen, W., Song, B., and Akers, S. A. (2009). Moisture effects on the high strain rate behavior of sand. Mechanics of Materials, 41(6), 786-798.

Matsushita, M., Tatsuoka, F., Koseki, J., Cazacliu, B., Di Benedetto, H., and Yasin, S. J. M. (1999). Time effects on the prepeak deformation properties of sands. In Proceedisn of 2nd International Conference on PreFailure Deformation Characteristics of Geomaterials, Torino, Italy, 681-689.

Mays, G C and Smith, P D. (1995). Blast Effects on Buildings.

Mikola, R. G. (2012). Seismic Earth Pressures on Retaining Structures and Basement Walls in Cohesionless Soils. Thesis, University of California, Berkeley.

Mobaraki, B., Vaghefi, M. (2015). Numerical study of the depth and cross-sectional shape of tunnel under surface explosion. Tunnelling and Underground Space Technology, 47, 114–122.

Nagy, N.M., Eltehawy, E.A., Elhanafy, H.M., and Eldesouky, A. (2009). Numerical modelling of geometrical analysis for underground structures, 13th international conference on Aerospace science & aviation technology, Egypt.

Narin van Court, W. A., and Mitchell, J. K. (1995). New insights into explosive compaction of loose, saturated, cohesionless soils. Soil Improvement for Earthquake Hazard Mitigation, ASCE Geotech. Spec. Pub. 49, ASCE, 51–65.

Nateghi, R. (2012). Evaluation of blast induced ground vibration for minimizing negative effects on surrounding structures. Soil Dynamics and Earthquake Engineering 43, 133-138.

National Building Code Canada (NBCC) 2010.

Ngo, T., Mendis, P., Gupta, A. & Ramsay, J. (2007). Blast Loading and Blast Effects on Structures – An Overview. EJSE Special Issue: Loading on Structures.

Pain, A., Choudhury, D., Bhattacharyya, S K. (2017). Seismic rotational stability of gravity retaining walls by modified pseudo-dynamic method. Soil Dynamics and Earthquake Engineering 94, 244–253.

Prevost, J. H., Scanlan, R. H. (1983). Dynamic soil-structure interaction: Centrifugal modeling. Soil Dynamics and Earthquake Engineering 2, 212-221.

Richardson GN, Lee KL. (1975). Seismic design of reinforced earth walls. Journal of the Geotechnical Engineering Division, 101(GT2), 167–88.

Rix, V. and Valdes, J.R. (2013). Vibratory Motion and Single Degree of Freedom Systems. San Diego State University.

Rose, T.A., Smith, P.D., Mays, G.C. (1995). The effectiveness of walls designed for the protection of structures against airblast from high explosives. Institution of Civil Engineers-Structures and Buildings 110-1, 78-85.

Semblat, J., Luong, M., and Gary, G. (1999).3D-Hopkinson Bar: new experiments for dynamic testing on soils. Soils and Foundations, 39(1), 1-10.

Shim, H-S., (1996). Response of piles in saturated soil under blast loading, Doctoral thesis, University of Colorado, Boulder, US.

Song, B., Chen, W., and Luk, V. (2009). Impact compressive response of dry sand. Mechanics of Materials, 41(6), 777-785.

Talhi, K., Bensaker, B. (2003). Design of a model blasting system to measure peak p-wave stress. Soil Dynamics and Earthquake Engineering 23, 513–519.

Tatsuoka, F., Di Benedetto, H., Enomoto, T., Kawabe, S., and Kongkitkul, W. (2008). Various viscosity types of geomaterials in shear and their mathematical expression. Soils and Foundations, 48(1), 41-60.

Tatsuoka, F., Ishihara, M., Di Benedetto, H., and Kuwano, R. (2002). Time-dependent shear deformation characteristics of geomaterials and their simulation. Soils and Foundations, 42(2), 103-129.

Tiznado, J.C., Rodrı´guez-Roa, F. (2011). Seismic lateral movement prediction for gravity retaining walls on granular soils. Soil Dynamics and Earthquake Engineering 31, 391–400.

Verruijt, A. (2010). Theory and Applications of Transport in Porous Media. Delft University of Technology, Delft, Netherlands.

Wagner, N., Sitar, N. (2016). On seismic response of stiff and flexible retaining structures. Soil Dynamics and Earthquake Engineering 91, 284–293.

Wang, L., Chen, G., Chen, S. (2015). Experimental study on seismic response of geogrid reinforced rigid retaining walls with saturated backfill sand. Geotextiles and Geomembranes 43, 35-45

Wang, Z., Lu, Y. (2003). Numerical analysis on dynamic deformation mechanism of soils under blast loading. Soil Dynamics and Earthquake Engineering 23, 705–714.

Whitman, R. V. (1970). The Response of Soils to Dynamic Loading. Report No. 26, Final Report, U.S. Army Engineer Waterways Experiment Station, Vicksburg, Mississippi, U.S.

Williamson, E. B., Bayrak, O., Marchand, K. A., Davis, C., Williams G., Holland, C. (2011) Performance of Bridge Columns Subjected to Blast Loads I, Journal of Bridge Engineering, ASCE.

Wood, JH. (1973). Earthquake induced soil pressures on structures. PhD Thesis, California Institute of Technology, Pasadena, CA.

Wu, C., Lu, Y. and Hao, H. (2004). Numerical prediction of blast-induced stress wave from large-scale underground explosion. International Journal for Numerical and Analytical Methods in Geome. chanics, 28:93–109.

Xia, X., Li, H.B., Li, J.C., Liu, B., Yu, C. (2013). A case study on rock damage prediction and control method for underground tunnels subjected to adjacent excavation blasting. Tunnelling and Underground Space Technology, 35, 1–7.

Xu, T. (2015). Numerical simulation of embankment dams subjected to blast loadings, PhD Thesis. The Hong Kong University of Science and Technology, Hong Kong.

Yamamuro, J. A., Abrantes, A. E., and Lade, P. V. (2011). Effect of strain rate on the stress-train behavior of sand. Journal of Geotechnical and Geoenvironmental Engineering, 137(12), 1169-1178.

Yang, Y., Xie, X., and Wang, R. (2010). Numerical simulation of dynamic response of operating metro tunnel induced by ground explosion, Journal of rock mechanics and geotechnical engineering, 2 (4), 373-384.

Yazdandoust, M. (2017). Investigation on the seismic performance of steel-strip reinforced-soil retaining walls using shaking table test. Soil Dynamics and Earthquake Engineering 97, 216–232

Zimmie, T. F., Abdoun, T., Tessari, A. (2010). Physical modeling of explosive effects on tunnels. Fourth International Symposium on Tunnel Safety and Security, Frankfurt, Germany, 159–168.

Chapter 3 Technical Paper I: Blast Induced Lateral Earth Pressures on Retaining Structures with Sand Backfill

Najlaa Abdul-Hussain, Mamadou Fall, Murat Saatcioglu

3.1 Abstract

Over the past two decades, civilian infrastructures have become a target for terrorist attacks. These attacks often appear in the form of bomb blasts. Understanding the behaviour of bridge abutments/retaining walls under blast loads is crucial in preventing progressive collapse of the entire structure and saving lives. Earth retaining structures provide vertical support to the bridge superstructures at the ends of bridges. Many studies have addressed the blast load effects on bridge decks and piers. However, there have not been any studies investigating the response of retaining walls due to blast loading. An experimental study was conducted to investigate the effects of blast loads on the behaviour of reinforced concrete retaining wall (RCRW) with sand as a backfill material. The soil-RW model was subjected to a simulated blast load using a shock tube. The influence of the backfill relative density, backfill saturation, blast load intensity, and live load surcharge on the behaviour of RCRW with sand backfill was studied. The dimensions of the stem and heel of the retaining wall in this study were 650 mm (height) x 500 mm (width) x 60 mm (thickness) and 400 mm (width) x 500 mm (length) x 60 mm (thickness), respectively. Soil-RW model was placed inside a wooden box. The overall height of the box was 1565 mm. The retained backfill extended behind the wall for 1300 mm. Based on the results, it was noted that the maximum dynamic earth pressures were recorded at a time greater than the positive phase duration regardless of the backfill condition. The total earth pressure distribution along the height of the wall showed that the magnitude of total earth pressure for loose and medium backfill at the mid-height of the wall slightly exceeded the dense backfill. In addition, the lateral earth pressures increased with the increase of the blast load intensities. The dynamic earth pressure coefficient (ΔK_{bd}) was back-calculated using the dynamic thrust. Relationships between ΔK_{bd} and accelerations of the wall and the backfill were determined. The maximum dynamic resistance function was reached when high-intensity pressure is applied. Yield was not reached, and intensities of the shots were below the design capacity of the section. The findings of this research will provide valuable information that can be used to evaluate the vulnerability of transportation structures (e.g., bridges) to surface blast events and the development of guidelines for their design.

Keywords: Blast load, Retaining wall, Lateral earth pressure, Dynamic resistance function

3.2 Introduction

Recent terrorist attacks have shown that there is an increase of terrorist threats on important buildings and some lifeline infrastructures. Transportation structures such as bridges are being regarded as potential targets for terrorist attacks because these structures are very accessible and difficult to protect. Another source of blast threats on transportation structures is accidental explosions that often occur due to vehicular collisions. Access control measures such as locating critical buildings at "standoff" distance away from the public access streets or by installing barriers to stop car bombs from driving too close to the structures are some of the major protection measures against car bomb attacks. These are effective measures for buildings since they prevent vehicles from being close to structures. However, these measures are not applicable for transportation structures due to the nature of these structures. As a result, engineers and researchers realized the importance of studying the blast load effects on bridges. Researchers investigated cases where the detonation of the bomb was on the deck of the bridge or close to the piers supporting the bridge superstructure (Andreou et al., 2016, Deng and Jin, 2009, and Agrawal and Yi, 2008**)**. For many bridge types, explosions under the span are of high concern as the blast waves strike all bridge elements. The abutment is one of these elements, being a portion of a bridge that provides the vertical support to the bridge superstructure and resists lateral soil pressures (Chen and Duan, 2014). Therefore, it is crucial to study the dynamic effects on abutments and the geotechnical response of the backfill material due to blast loading. Research that addresses the response of retaining walls (RWs) to blast loading is currently lacking in the literature.

Earth retaining structures are one of the earliest and most common geotechnical structures, designed to support vertical or near vertical slopes of soil. The soil behind the retaining walls exerts active or passive lateral earth pressure on them. The increase of lateral pressure can lead to sliding and/or tilting of retaining structures. The solution to the lateral static earth pressure problem was first developed by Coulomb and Rankine (Mikola, 2012 and Al Atik, 2008). Their earth pressure theories were based on the limit-state analyses that used a pseudo-static analysis and considered the soil to be perfectly plastic. On the other hand, Mononobe and Matsuo (1929), and Okabe (1926) provided the earliest method to predict the dynamic behaviour of retaining walls during earthquakes. The method is representative of the pseudo-static equilibrium method, which also called the rigid plastic method with force-based approaches. The dynamic behaviour of the retaining structures is a complex soil structure interaction problem that can be influenced by the response of backfill, inertial force of the soil, flexural responses of the wall and the type of dynamic loads (Jo et al., 2017).

Excessive dynamic lateral earth pressure on retaining structures can cause severe damages. The increase of lateral earth pressure during earthquakes induces sliding/tilting of the RW. The majority of failure cases due to seismically induced lateral earth pressure implicated waterfront structures such as quay walls and bridge abutments (Das, 2011). Seed and Whitman (1970) stated that one of the reasons for some of the RW failures is the increase in the lateral earth pressure behind the wall. Al Atik, (2008) found that the maximum dynamic earth pressure occurs when the inertial force acts in the passive direction.

The dynamic behaviour of structures subjected to blast loads is different than structures subjected to a seismic motion (Hao and Wu, 2005). Blast motions have higher amplitudes and frequency contents, but shorter duration than seismic motions. An impulsive loading is defined as a load that is applied during a short period. Various analytical techniques are used to determine the dynamic response of a structure subjected to blast loading. These methods range from simplified analysis using a single degree of freedom (SDOF) system to more sophisticated methods like the finite element method (FEM) (Fujikura and Bruneau 2012). The maximum response to an impulsive load is reached in a very short time, before the damping forces can absorb considerable energy from the structure and therefore, the damping force was assumed to be zero. The Equation of Motion of the undamped SDOF system is given below (Biggs, 1964).

$$m\ddot{u} + ku = F(t) \tag{3.1}$$

where,

m is mass;

u is displacement;

$\ddot{u}$ is acceleration of the mass;

k is spring constant (stiffness); and,

F(t) is external force.

The analysis of the dynamic response of a structure subjected to blast loading is a complex process since it involves the effect of high strain rates, non-linear behaviour of materials, and uncertainties in blast load characteristics (Ngo et al. 2007). Soil behaviour is dependent on the strain rate. The strain rate can reach up to 10^3 %/s when soil is subjected to blast loading (XU, 2015). Yet, no studies on the effect of blast loads on retaining structures have been performed. There is a need to address this knowledge gap for the reasons discussed above.

In this paper, backfills with various relative densities and degrees of saturation were subjected to different blast shot intensities to evaluate the dynamic lateral earth pressure behind the RW. Moreover, the actual blast resistance function of the reinforced concrete retaining wall (RCRW) investigated was obtained experimentally during this study.

3.3 Experimental Program

3.3.1 Description of Test Specimens and Material Properties

3.3.1.1 Backfill soil

Sand is commonly used as a backfill material for retaining wall systems. The high permeability of sand helps in releasing the hydrostatic pressure behind the wall stem. Sand has been used extensively in experimental research (e.g. Jo et al., 2017, Kloukinas et al., 2015, and Mikola and Sitar, 2013) to address the dynamic response of soil retaining walls due to seismic loads.

In this research, both the backfill and foundation soil layers consisted of sand. The grain size distribution and sand properties were determined, according to the ASTM (American Society for Testing and Materials) C136/C136M−14 Standard for Sieve Analysis of Fine and Coarse Aggregates, at the Geotechnical Laboratory of the University of Ottawa. The sand had a mean grain size (D_{50}) of 0.54 mm, an effective size (D_{10}) of 0.21 mm, a uniformity coefficient (C_u) of 3.05 and a coefficient of gradation (C_z) of 0.9. Based on Unified Soil Classification, the sand was classified as poorly graded sand ($Cu < 6$ and/or $1 > Cc > 3$) (Das, 2014). Figure 3.1 depicts the grain size distribution of the sand.

The specific gravity of the sand was 2.64, and it was determined according to the ASTM D854-14 Standard for Specific Gravity of Soil Solids by Water Pycnometer. Minimum and maximum dry densities of 13.0 kN/m^3 and 18.8 kN/m^3, respectively, were found following the procedure prescribed by the ASTM D4254-16 Standard for Minimum Index Density and Unit Weight of Soils and Calculation of Relative Density, and D4253-16 Standard for Maximum Index Density and Unit Weight of Soils Using a Vibratory Table, respectively. The friction angle of the sand was 34° and it was determined using the direct shear test described in the ASTM, D3080-11 Standard for Direct Shear Test of Soils under Consolidated Drained Conditions. Table 3.1 summarizes the key geotechnical properties of the sand.

3.3.1.2 Wall

The L shape reinforced concrete retaining wall model, depicted in Figure 3.2, was used in this study. The RW was designed using the Rankine earth pressure theory for stability. The RW was checked for overturning, sliding along the base and bearing capacity failure. The RW was modelled at the 1/10th scale. The dimensions of the stem and the heel of the retaining wall in this study were 650 mm (height) x 500 mm (width) x 60 mm (thickness) and 400 mm (width) x 500 mm (length) x 60 mm (thickness), respectively, as shown in Figures 3.2 and 3.3.

Two RWs were constructed at the Structural Laboratory of the University of Ottawa. The second wall was built as a replacement in case of failure of the first wall. Both concrete RWs were reinforced longitudinally and laterally with 6.3 mm rebars spaced at 50 mm c/c. The details of retaining wall reinforcement are presented in Figure 3.3. A concrete mixer and an electric concrete vibrator were used for mixing and consolidating the fresh concrete, respectively. The heel of the retaining wall was first cast, and 14 days later the stem was cast (Figure 3.2). The specimens were covered with two layers of wet burlap and plastic sheet for 30 days of curing at the end of each casting process. Seven concrete cylinders (100 mm diameter x 200 mm height) were prepared for standard cylinder tests. The cylinders were prepared and cured according to the ASTM C31/C31M-19 Standard for Making and Curing Concrete Test Specimens in the field. The cylinders were also cured for 30 days following the same curing conditions as for the RC wall. The compressive strength of the concrete was 38 MPa at the age of 120 days. Concrete cylinders were tested according to the ASTM C39/C39M-18 Standard for Compressive Strength of Cylindrical Concrete Specimens.

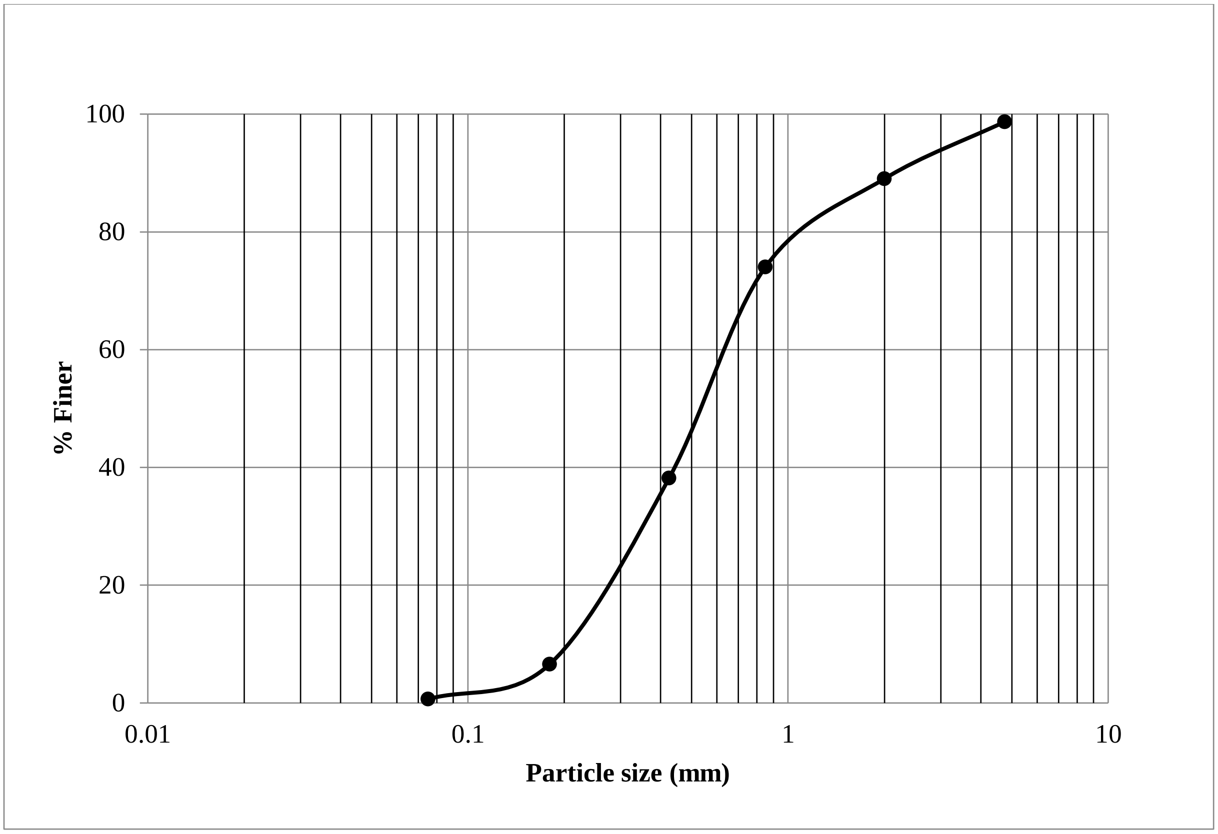

Figure 3.1: Grain size distribution of the sand

Table 3.1: Geotechnical properties of the sand

Descriptions	**Values**
Grain size distribution effective size (D_{10})	0.67 mm
Uniformity coefficient (C_u)	3.05
Coefficient of gradation (C_z)	0.9
Specific gravity (Gs)	2.64
Maximum unit weight	18.8 kN/m^3
Minimum void ratio	0.38
Minimum unit weight	13.0 kN/m^3
Maximum void ratio	0.99
Friction angle	34°

3.3.1.3 Model geometry and instrumentation

As mentioned earlier, sand was used in the current study as the: (1) backfill material behind the retaining wall, and (2) foundation soil under the heel of the retaining wall (Figures 3.4 and 3.6). The sand was placed in a box (1300 mm in length, 500 mm in width, and 1565 mm in height) that was made of wood. The soil below the foundation/heel was a dense layer with a relative density of 80 %. The height of the foundation layer was 915 mm while the height of the backfill behind the stem was 650 mm for an overall height of 1565 mm. The retained backfill extended behind the wall for 1300 mm, which was two times the RW height. The backside of the box was made of a flexible material (reinforced rubber sheet) in order to prevent soil confinement. One side of the box's wall was made of plexiglass in order to capture the movement of the soil-RW model by a high-definition camera during testing. Furthermore, the sand in the box was surrounded by an impermeable membrane to avoid water leakage. The restricted testing area was considered during the selection of the model geometry.

Various instruments were placed in the soil-RW model to capture the dynamic response of the model during the blast event. Four soil pressure gauges were used to measure pressure in the soil (Figure 3.4). Four strain gauges were attached to the rebars of the stem to monitor the strains in the wall. Two strain gauges were placed at 30 mm from the base of the wall, and the other two were located at 250 mm from the base (Figure 3.5). The sensors were connected to a high-speed data acquisition system that was employed for the collection of test data. The ProAnalyst software (software guide) was used to capture the soil particles' movement and to track the transient and permanent displacements of the wall. Two high-definition cameras were used in this experimental program. These cameras with their digital high-speed imaging system, were capable of recording thousands of high-resolution frames per second. Yellow beads were added to the sand particles facing the plexiglass side to track the movement of these particles during the test. Soil model preparation was conducted at the Blast Research Laboratory of the University of Ottawa.

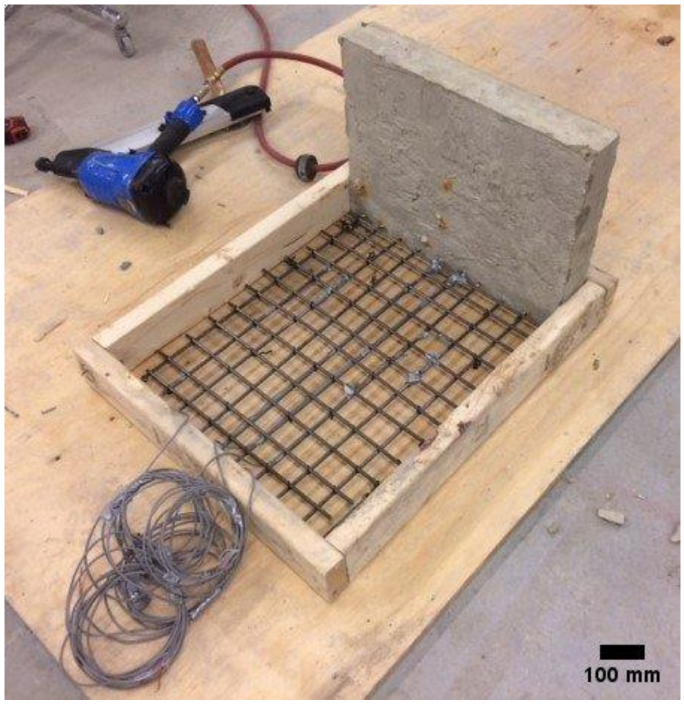

Figure 3.2: Reinforced concrete retaining wall

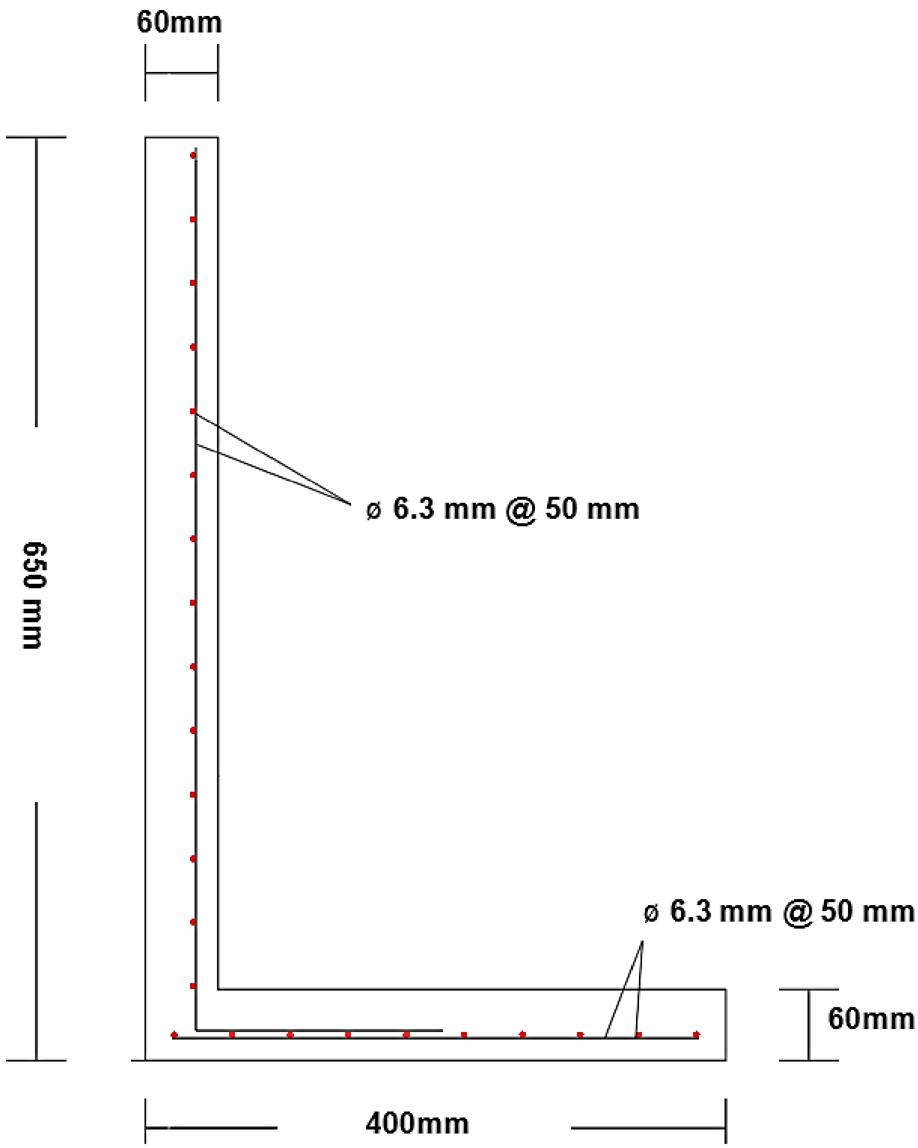

Figure 3.3: Details of retaining wall reinforcement

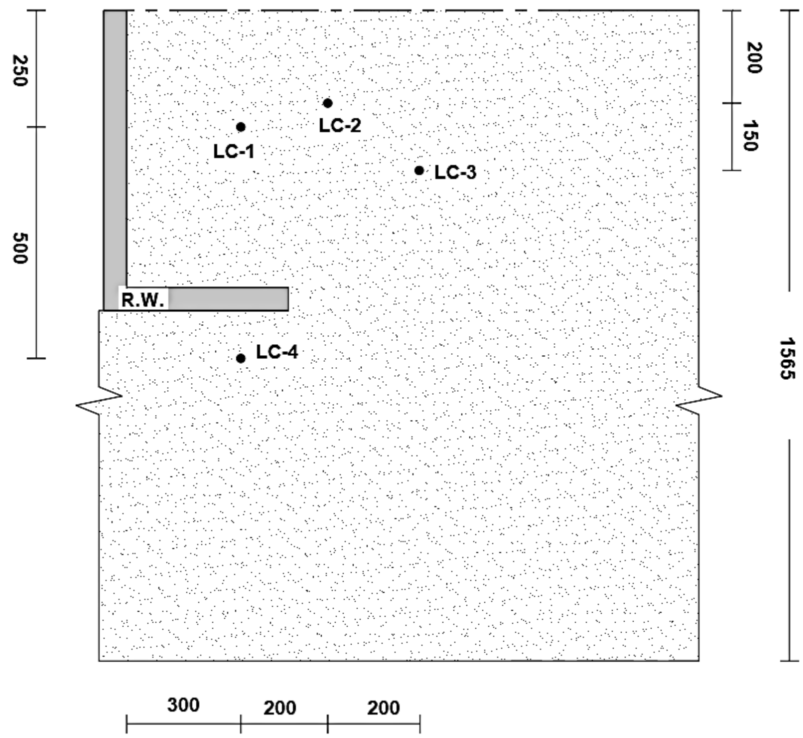

Figure 3.4: Locations of soil pressure gauges (dimensions in mm)
LC: Load cell, which represents soil pressure gauge; R.W: Retaining wall

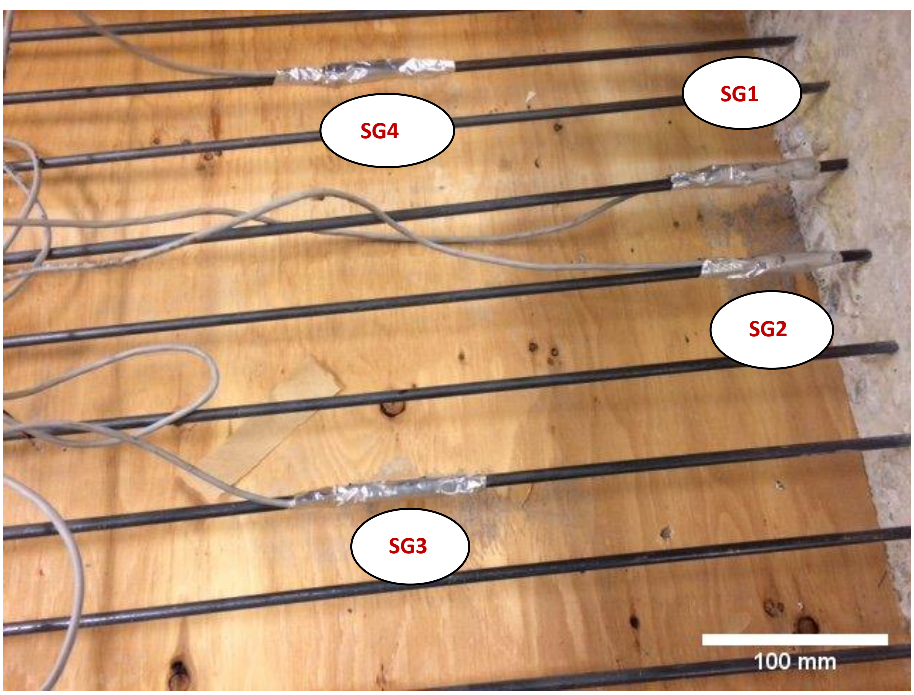

Figure 3.5: Positions of strain gauges on rebars
SG: Strain gauge

3.3.2 Test Procedure

The test was devoted to studying the influence of various relative densities, degrees of saturation of the backfill and live load surcharge on the dynamic response of soil-RW model when subjected to different blast load intensities. For every test conducted in this study, the system (RW and soil) was subjected to a single blast shot.

3.3.2.1 Relative density of the sand backfill and foundation

Three sand samples with various relative densities (loose, medium, and dense) were prepared and then subjected to a pressure simulating a blast-induced shock wave. Relative density of 30 %, 45 %, and 65 % were used for loose soil, medium soil, and dense soil, respectively (Das, 2016). Table 3.2 shows the state of granular soils at different ranges of relative density.

The space between the bottom of the wooden box and the bottom of the RW footing was filled with 200 mm thick successive layers of sand. Each sand layer was densified using a mechanical vibration technique to reach a relative density of 80 %. The backfill was also formed by pouring sand in equal successive layers of 200 mm thick. Each sand layer was manually compacted to the desired relative density. Figure 3.6 shows the steps for the box preparation and soil compaction.

Once compaction of a layer was completed, three samples were taken and tested to confirm that the required relative density was obtained. This process was repeated for each layer. A vibrating table compaction test was conducted to determine the optimum moisture content and maximum dry density. The test was run in accordance with the ASTM D4253-16 Standard for Maximum Index Density and Unit Weight of Soils Using a Vibratory Table. Water content of 2 – 3 % was chosen to reach the required relative densities in the foundation and the backfills (loose, medium, and dense).

Table 3.2: General correlation between relative density and denseness of a cohesionless soil (Das, 2016)

Relative density, Dr (%)	Description
0-15	Very loose
15-35	Loose
35-65	Medium
65-85	Dense
85-100	Very dense

3.3.2.2 Degree of saturation of the sand backfill and foundation

Three sand backfill samples with different saturation degrees (100 %, 85 %, and 13 %) were tested. To achieve the fully saturated condition, the ground water table was maintained at the surface level. The soil is considered partially saturated when the degree of saturation is around 85 %. To satisfy this condition, the ground water table was kept at 250 mm below the top surface of the backfill. This means, the layer below the water table was saturated and the layer above the water table was partially saturated. When the degree of saturation is 0 %, the soil reaches dry condition. However, dry backfill is not applicable in the field. Therefore, in this study, moist backfill with a degree of saturation of 13 % was used instead of the dry condition. The degree of saturation of moist soil was calculated by dividing the volume of water by the volume of void in the soil. The volume of void can be determined by knowing the moist and dry densities of the sand while the volume of water can be calculated from the water content and specific gravity of the sand (Das, 2016 and Craig, 2004). The backfill was compacted to meet in-situ dry density (Federal Highway administration (FHWA) specifications, 2008 and Morris and Delphia, 1999). The dry density of the backfill was 16 kN/m^3 which was within the acceptable range recommended by the above mentioned specifications. The degree of saturation of the foundation was 100 % when the degree of saturation of the backfill was 100 % and 85 %. On the other hand, the degree of saturation of the foundation was 13 % when the degree of saturation of the backfill was 13 %.

3.3.2.3 Blast loads intensity

Three driver pressures were adopted in this study. A driver pressure of 137 kPa resulted in a maximum reflected pressure (P_r) of 26 kPa. The second driver pressure was equal to 241 kPa, which resulted in a maximum P_r of 47 kPa. Lastly, a driver pressure of 379 kPa was used to generate a maximum P_r of 71 kPa. The reflected pressures were selected to cause a different level of damage on the RW-soil system, ranging from elastic to full plastic failure. However, full plastic failure was not reached in this experiment (more details in section 3.4.5). Furthermore, a scaling chart (Cormie, Mays, and Smith, 1995) was used to match the reflected pressures from this paper to a specific explosive. For example, detonation of a 227 kg TNT hemispherical charge at a distance of 36 m produced a reflected pressure of 71 kPa.

3.3.2.4 Live load surcharge

Lateral earth pressure, lateral hydrostatic pressure, and vertical traffic loads that generate extra lateral load on the RW are the three major loads acting on a RW. Highway traffic load equivalent surcharge can be neglected if the traffic load location is far enough from the wall (Chen and Duan, 2014). As per AASHTO design codes (AASHTO 2002, 2012), live load surcharge can be equivalent to a soil height of 600 mm placed on the top level of the wall.

To address the influence of live load surcharge on the behaviour of RW backfill in this study, 60 mm (wall is modeled at the 1/10th scale) of soil was added to the top level of the backfill. This added layer was compacted to achieve the in-situ required density.

Figure 3.6: Steps of box preparation and soil compaction

The box was built in stages. **Step 1** represents the first stage of the box. The height of this portion of the box was 400 mm. The sand for the foundation layer had been compacted using a mechanical vibration technique (modified electrical drill). **Step 2** shows the second stage of the box; the height of the box reached 800 mm. **Step 3** presents the front view of the specimen showing location of the wall. In this step the compaction of the foundation was completed and the wall was placed in the box. **Step 4** shows the side view of the box where the plexiglas is located. The box was moved in front of the shock tube and was ready to be filled with the backfill layers.

3.3.3 Test Setup

3.3.3.1 Soil-retaining wall model

All tests in this study were conducted using the shock tube at the Blast Research Laboratory of the University of Ottawa. The test specimen (soil-RW model) was placed at the centre of the shock tube's mouth. The rest of the shock tube mouth was covered with a very stiff steel plate. The test specimen consisted of a reinforced concrete retaining wall and a box filled with sand. The top of the box was left open to allow soil filling and compaction. The RCRW was placed on the side of the box that faced the shock tube, as shown in Figure 3.6. The test specimen was attached to the shock tube by straps to prevent the specimen from moving away from the shock tube during the blast test. The blast pressure formed by the shock tube was transferred directly to the test specimen, and it was uniformly distributed over the area of the RCRW. The shock tube was controlled by a firing system to start the test. Figure 3.7 shows the test setup adopted in this study.

In-situ, soils usually experience a stress history that can change the soil structure. Many factors, such as climatic environment changes or made-man construction, can lead to a changing stress state or stress history in soils. A total stress ratio (TSR) is used as a measure of the stress history of compacted soil (Nishimura et al., 1999). TSR is the ratio of the compaction pressure to the current confining pressure.

In order to limit the effect of stress history, backfill material was removed from the box after each test. Then the sand was mixed and reused to refill the box. The backfill material was compacted to meet the required compaction level for each test.

Soil under the wall's footing level (heel) was not disturbed by the blast shocks applied; thus, except for the loose backfill condition test, this soil was not compacted after each test. Once the loose backfill condition test was carried out, the RC wall was removed, and portions of the box were disassembled. The soil below the heel was dug out, mixed on a tarp, then put back and compacted again to reach the required relative density. Prior to excavation of the foundation layers, the sand was tested to determine if there was any change in the soil's relative density below the RW. The results showed that the TSR was 1.02, which was within the acceptable range, and the changes were insignificant. Figure 3.8 shows the wall removal and box disassembly.

3.3.3.2 Blast loading protocol

Prior to testing, the specimen was attached firmly to the shock tube, using three straps (Figure 3.9). Strain gauges and pressure sensors were connected to the data acquisition system. The two high-speed video cameras were set up and connected to the data acquisition and laptop used for video monitoring. Trigger signal was induced to confirm that the data acquisition and the cameras were recording at the same time. Then, the driver and spool sections of the shock tube were filled up to the required level of pressurized air. The test started by draining pressure from the spool section, which led to an imbalance in pressures on both sides of the aluminum diaphragm. As a result, the aluminum diaphragm was ruptured, and the pressurized air was passed at very high speed towards the expansion shock tube nozzle.

3.3.3.3 Data acquisition

The data acquisition used in this research was two digital oscilloscopes readings at 100,000 Hz (samples per second). Four channels recorded strain readings, four channels recorded pressure readings, and two channels were used to record reflected pressure. The sensors were responsible for measuring the reflected pressure located at the side and bottom of the shock tube's mouth.

Figure 3.7-1: Test setup (a) covering the shock tube's mouth with a stiff plate; (b) placing the test specimen at the centre of the shock tube; (c) fastening the test specimen to the shock tube using straps

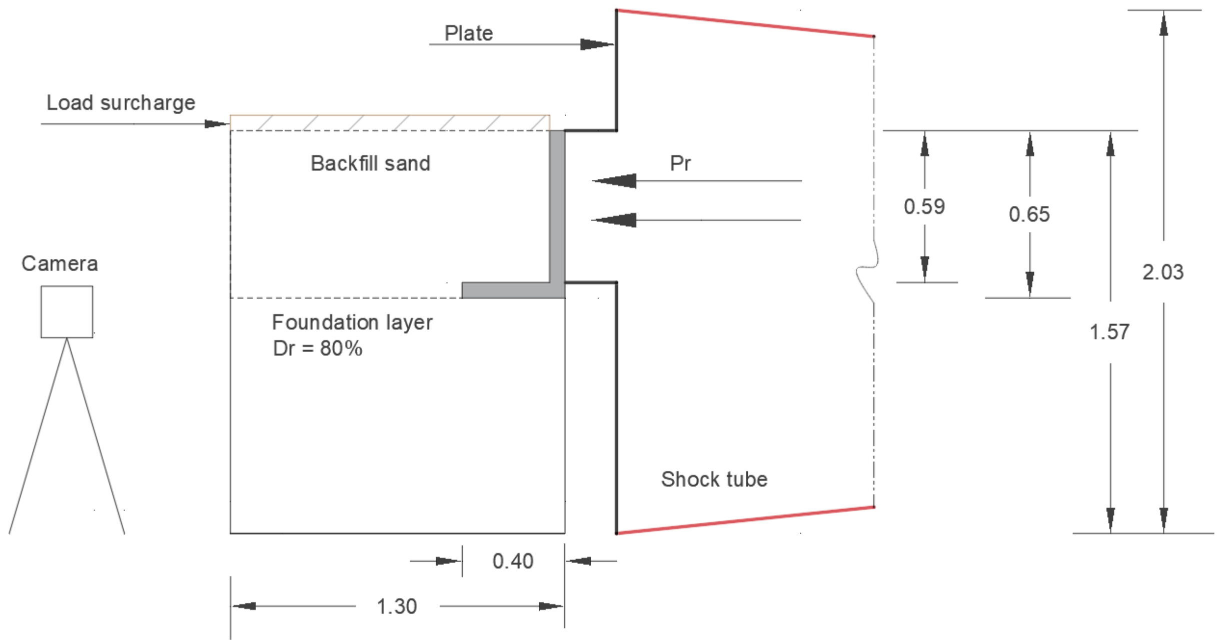

Figure 3.7-2: Test setup and preparation; dimensions in m (schematic)
Figure 3.7: Test setup

Figure 3.8: Wall removal and box disassembly after the test with loose backfill condition
(a): front view of the test specimen after the removal of the RW and a portion of the box. (b): The RW was left aside until the box and the foundation layer were fixed

Figure 3.9: Test preparation at the Blast Research Laboratory of the University of Ottawa
The test specimen was placed in front of the shock tube mouth, fastened with straps to prevent any movement during the blast test. The camera was facing the side view of the box, where the plexiglass was located, to capture sand particles movement.

3.3.3.4 Shock tube

The shock tube consists of four main sections (Figure 3.10). The driver and the spool are the first and second sections, respectively. These are the sections in which the shock energy is built-up, and the firing action happens. The length of the driver section ranges between 305 mm and 5185 mm in 305 mm increments. Based on the required peak reflected pressure and total impulse, a driver length is selected. The driver length has a minor influence on the reflected pressure but has an effect on the impulse (Lloyd, 2010). Since the impulse should be given equal consideration as the reflected pressure (Mays and Smith, 1995), in this experiment, the length of the driver section was kept at 2743 mm. The blast wave formed in the driver section propagates and expands through the expansion section, which starts from 597 mm in diameter and ends with a square test area of 2033 mm by 2033 mm. The test specimen was attached to the opening of the steel plate located at the front of the shock tube. The length of the expansion section is 7 m. The shock tube is operated manually by incrementally increasing the driver pressure and the spool pressure to the anticipated level and then trigger firing by draining pressure from the spool section to cause the aluminum foil diaphragms to rupture.

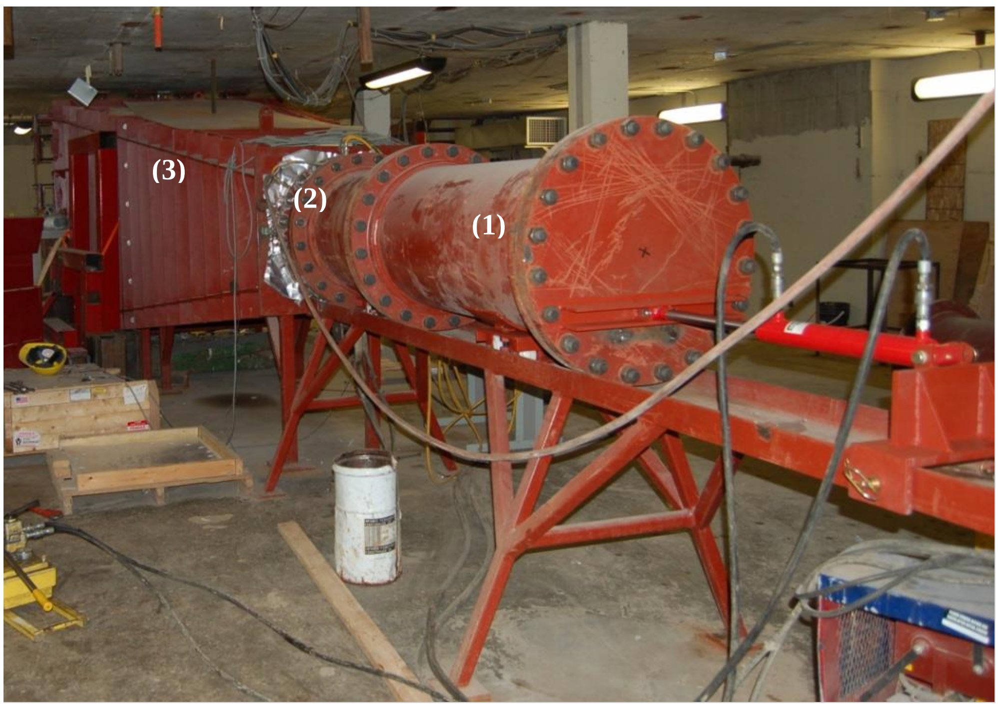

Figure 3.10: Shock tube (1) driver section; (2) diaphragm**s**; (3) expansion section (Kadhom, 2015)

3.4 Results and Discussion

3.4.1 Blast Load Intensity

As mentioned above, three driver pressures were adopted in this study. A driver pressure of 137 kPa resulted in a maximum reflected pressure (P_r) of 26 kPa and a reflected impulse over the positive phase of 324 kPa.ms. The duration of the positive phase was 24.8 millisecond (ms) (Figure 3.11a). A second driver pressure of 241 kPa, resulted in a maximum reflected pressure of 47 kPa and a reflected impulse over the positive phase of 509 kPa.ms. The duration of the positive phase was 24.8 ms (Figure 3.11b). Lastly, a driver pressure of 379 was used to generate a maximum reflected pressure of 71 kPa and a reflected impulse over the positive phase of 721 kPa.ms. The duration of the positive phase was 23 ms (Figure 3.11c).

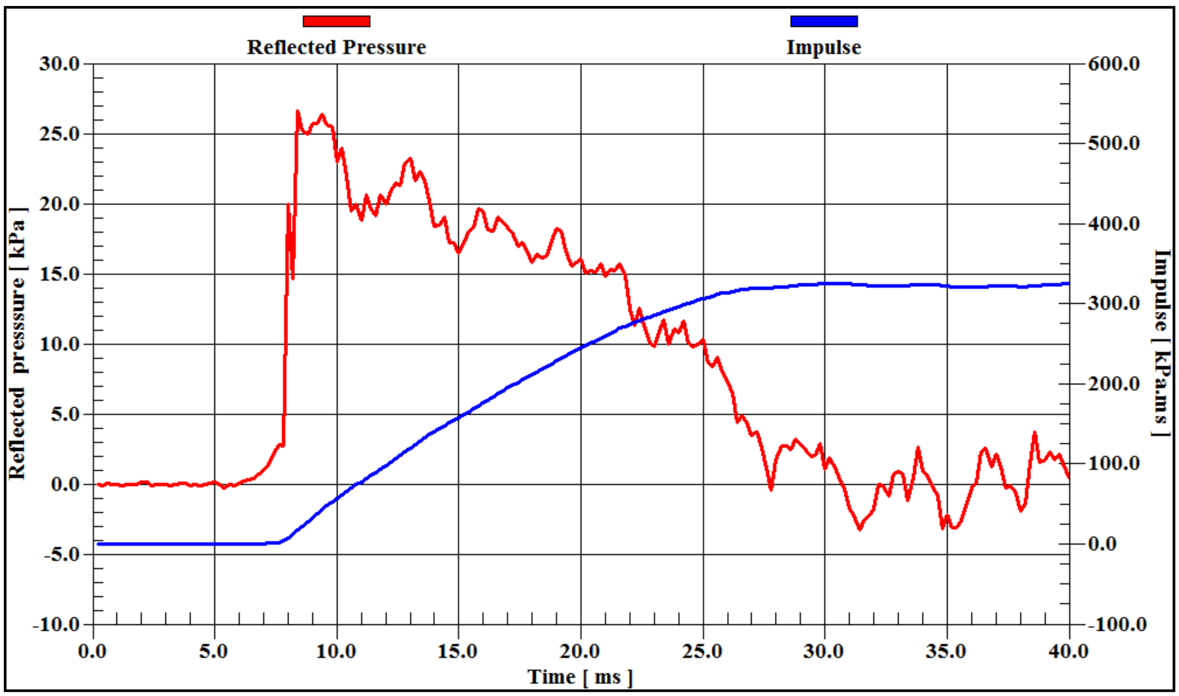

(a)

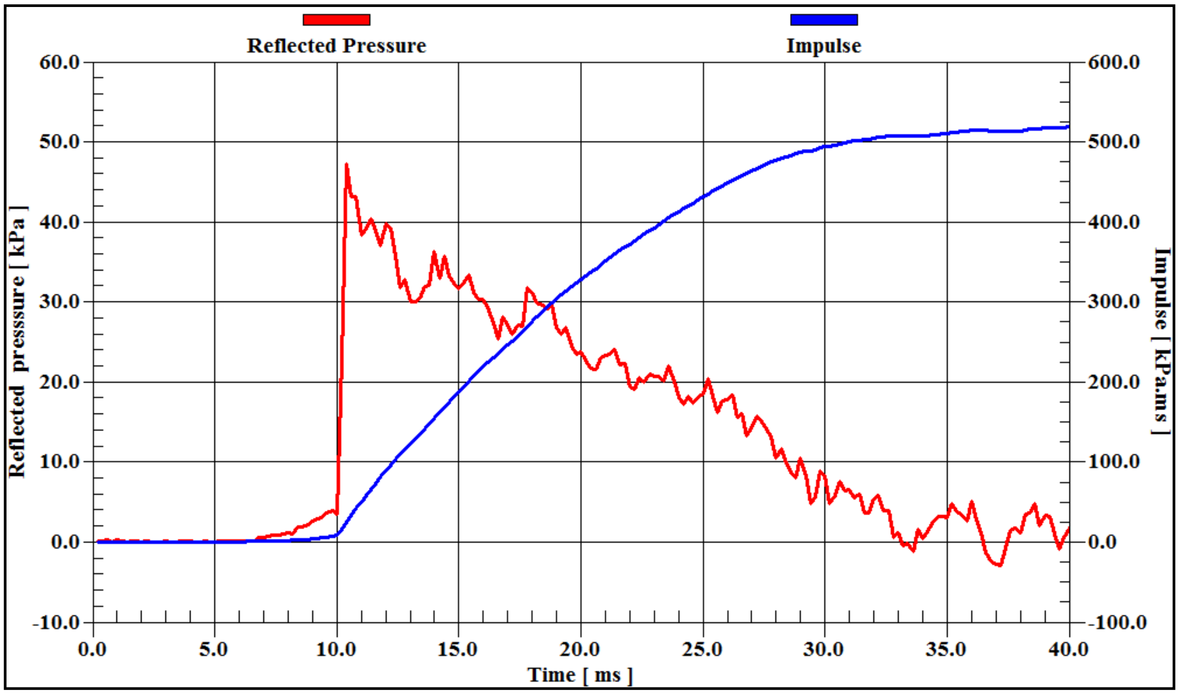

(b)

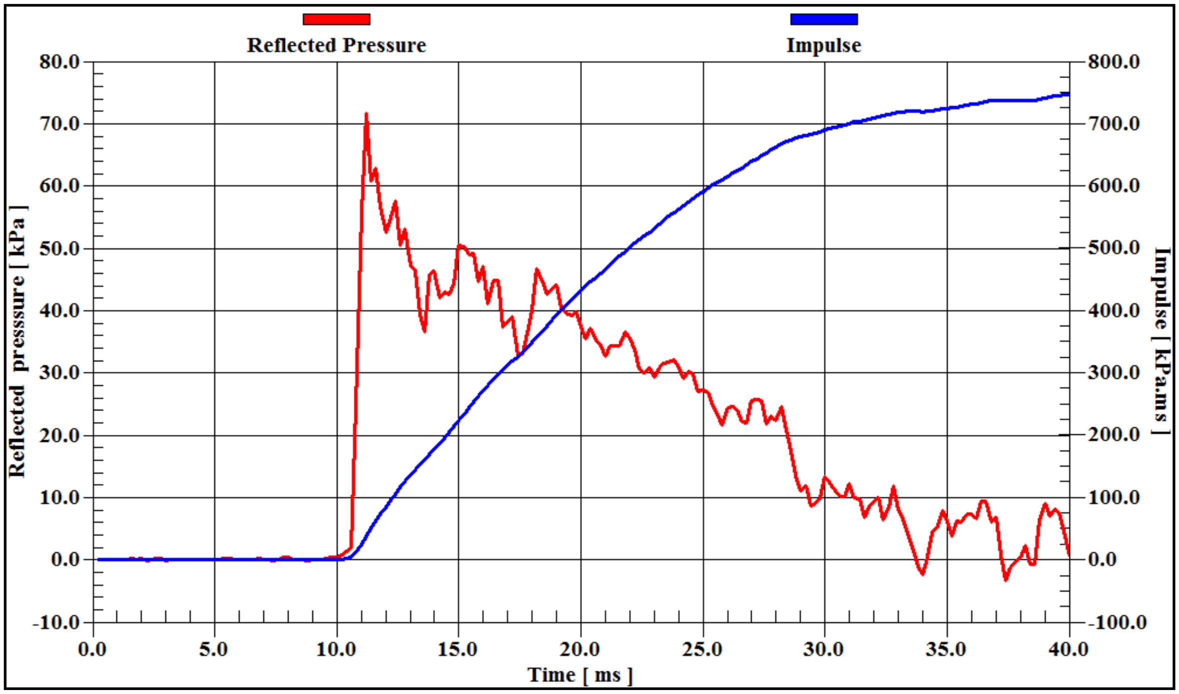

(c)

Figure 3.11: Time history of reflected pressures

3.4.2 Dynamic Earth Pressure

Table 3.3 gives the locations of the four soil pressure gauges used to measure the dynamic earth pressures. The readings from these gauges represent the total lateral earth pressure (static and dynamic) induced by blast loading. Total lateral earth pressure time-history profiles were plotted for all conditions, except for the partially saturated soil as no readings were recorded (Figure 3.12). It can be seen that the maximum dynamic earth pressures were obtained at a time greater than the positive phase duration regardless of the backfill condition. The maximum response occurred when the blast load decayed, which is the case with impulsive loading. In the impulsive loading, the positive phase duration is shorter than the natural period and thus, the load decayed before the backfill sand had time to respond (Mays and Smith, 1995). Furthermore, it was noted that minimum values of total earth pressures were recorded directly after the peak reflected pressures, and then the pressures increased to reach the maximum at the end of the positive phase duration. This trend was more obvious in two sets of the experiment: loose backfill condition and highest reflected pressure. The application of blast loads on the stem led to the activation of the passive lateral earth pressure behind the wall. Since the active earth pressure was exerted on the wall prior to the application of blast load, it was assumed that the difference between the active and passive lateral earth pressures gave the minimum values mentioned above. In addition, it can be observed from Figure 3.12 that the maximum lateral earth pressures were recorded at LC-4. The relationship between the effective stress and the lateral earth pressure is proportional. Therefore, an increase in the effective stress with depth leads to an increase in the lateral earth pressure. As a result, the maximum lateral pressure values were found below the foundation, which was the deepest point measured in this test (LC-4). However, the lateral earth pressure at LC-3 showed higher pressure (32.0 kPa) than at LC-4 (26.9 kPa) in the loose backfill condition test (Figure 3.12-a). Since loose backfill provided less support to the RW during the blast event, the reflected pressure created high inertial forces for the wall and backfill (section 3.4.3 for more details). This led to a change in the stress state and structures of the backfill and thus induced higher lateral pressure behind the RW in comparison to the pressure below the heel.

Table 3.3: Locations of soil pressure gauges

Soil pressure gauges	Depth from the top of the wall	Horizontal distance behind the wall
LC-1	250 mm	300 mm
LC-2	200 mm	500 mm
LC-3	350 mm	700 mm
LC-4	750 mm	300 mm

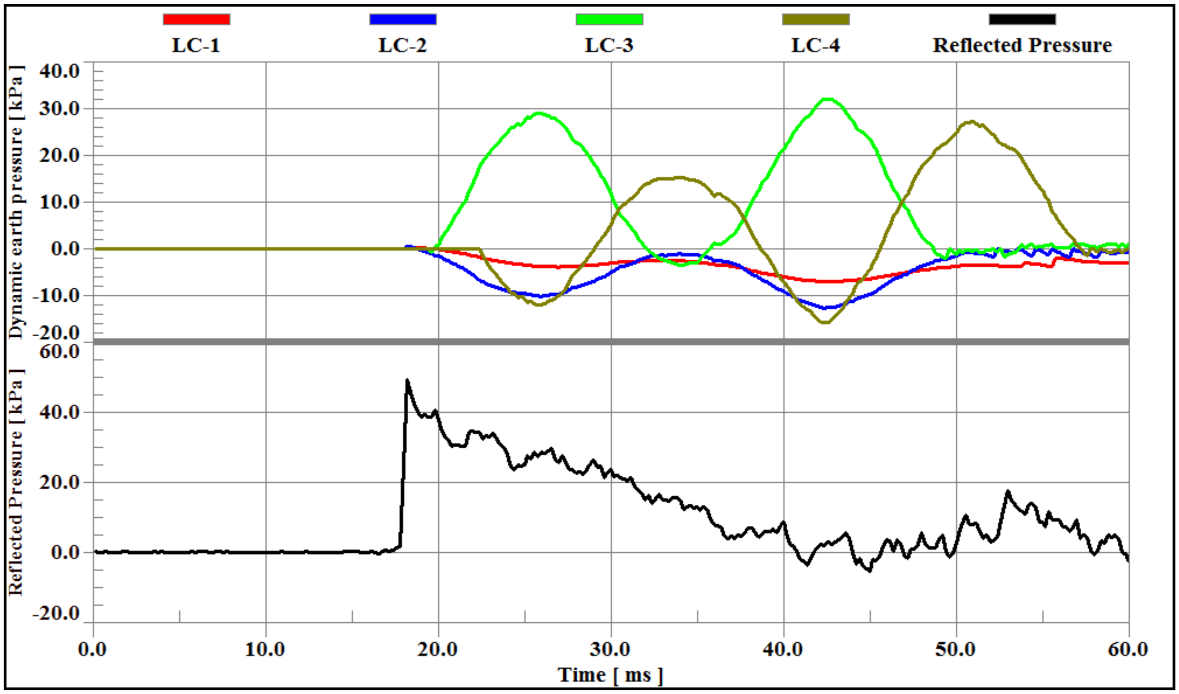

(a)

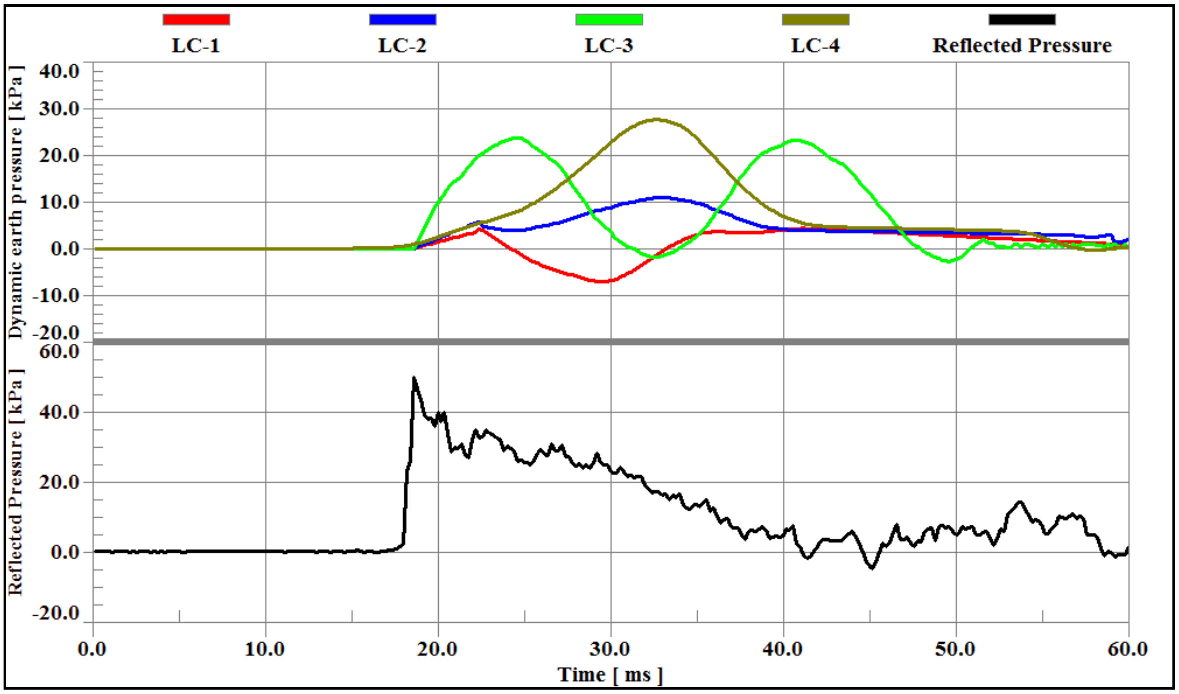
LC-1
LC-2
LC-3
LC-4
Reflected Pressure
Dynamic earth pressure [kPa]
Reflected Pressure [kPa]
Time [ms]

(b)

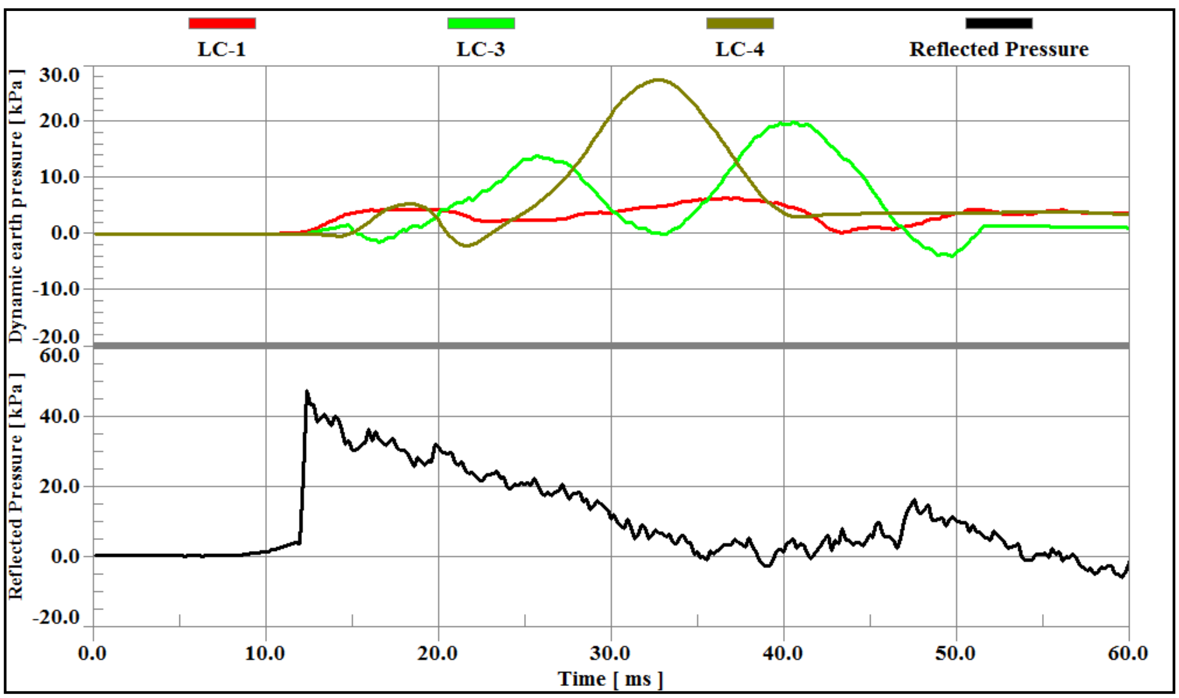
LC-1
LC-3
LC-4
Reflected Pressure
Dynamic earth pressure [kPa]
Reflected Pressure [kPa]
Time [ms]

(c)

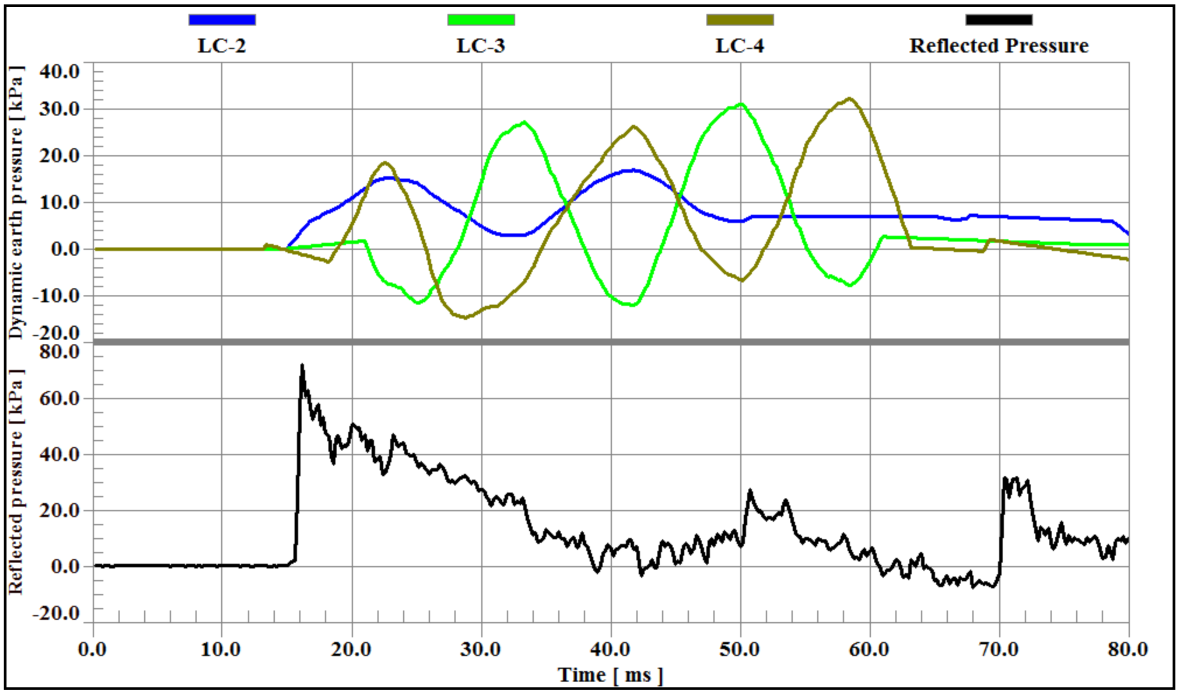

LC-2
LC-3
LC-4
Reflected Pressure
Dynamic earth pressure [kPa]
40.0
30.0
20.0
10.0
0.0
-10.0
-20.0
Reflected pressure [kPa]
80.0
60.0
40.0
20.0
0.0
-20.0
0.0
10.0
20.0
30.0
40.0
50.0
60.0
70.0
80.0
Time [ms]

(d)

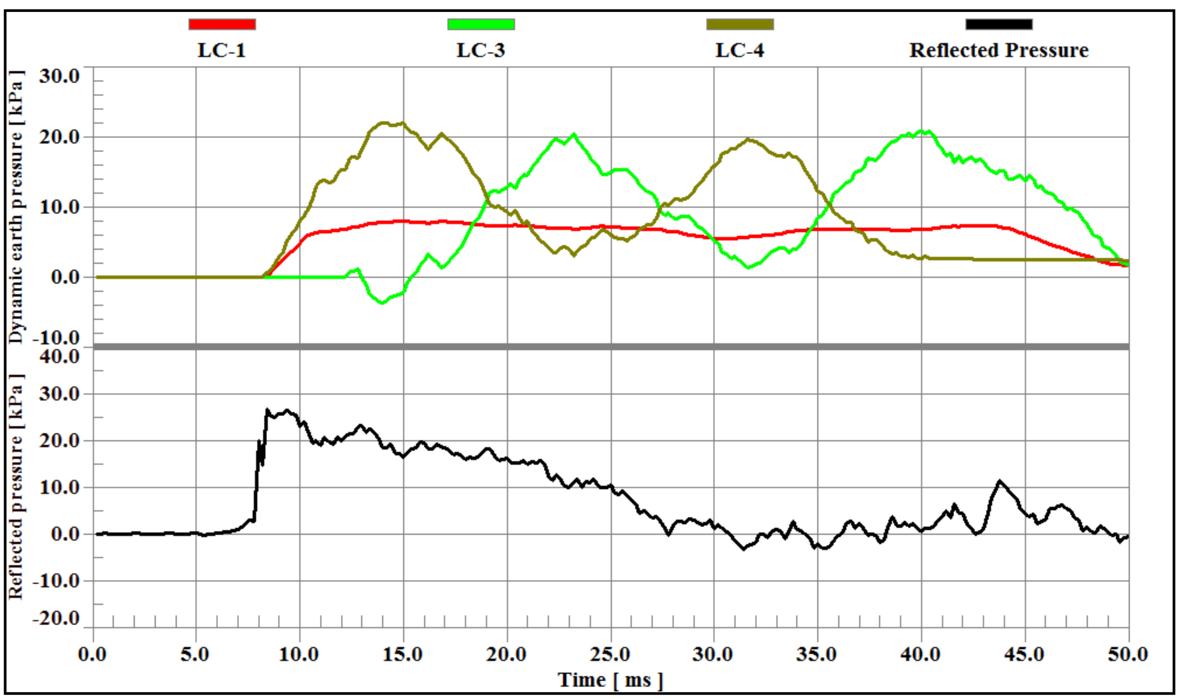

LC-1
LC-3
LC-4
Reflected Pressure
Dynamic earth pressure [kPa]
30.0
20.0
10.0
0.0
-10.0
Reflected pressure [kPa]
40.0
30.0
20.0
10.0
0.0
-10.0
-20.0
0.0
5.0
10.0
15.0
20.0
25.0
30.0
35.0
40.0
45.0
50.0
Time [ms]

(e)

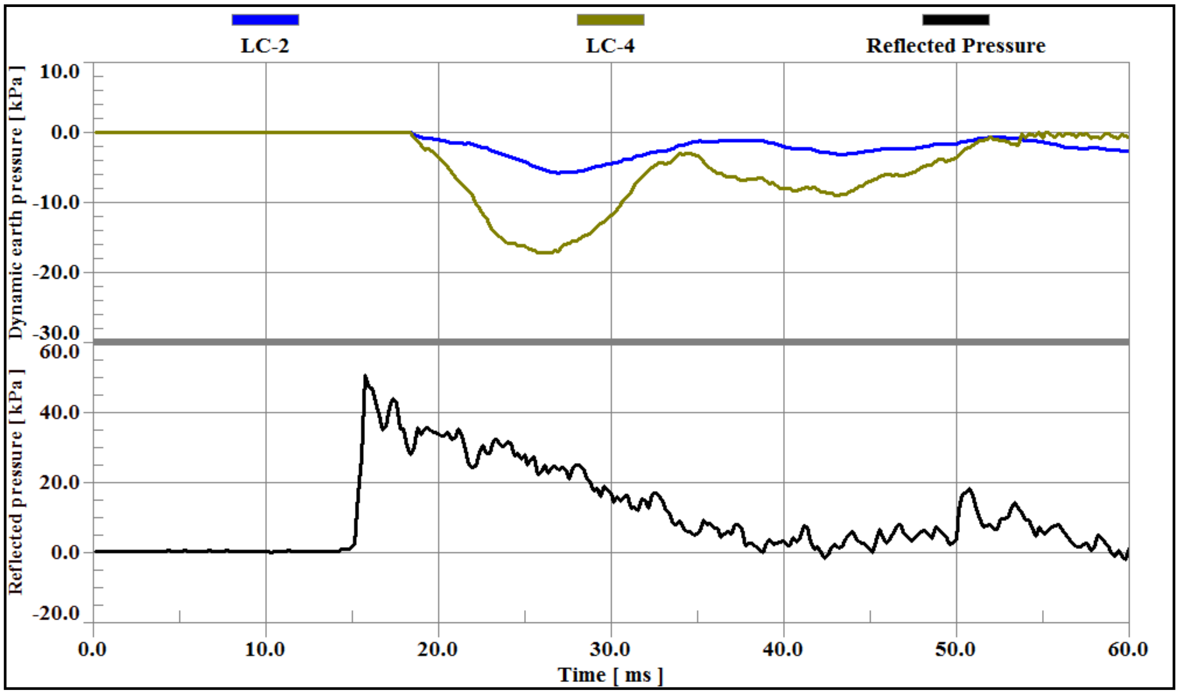

(f)

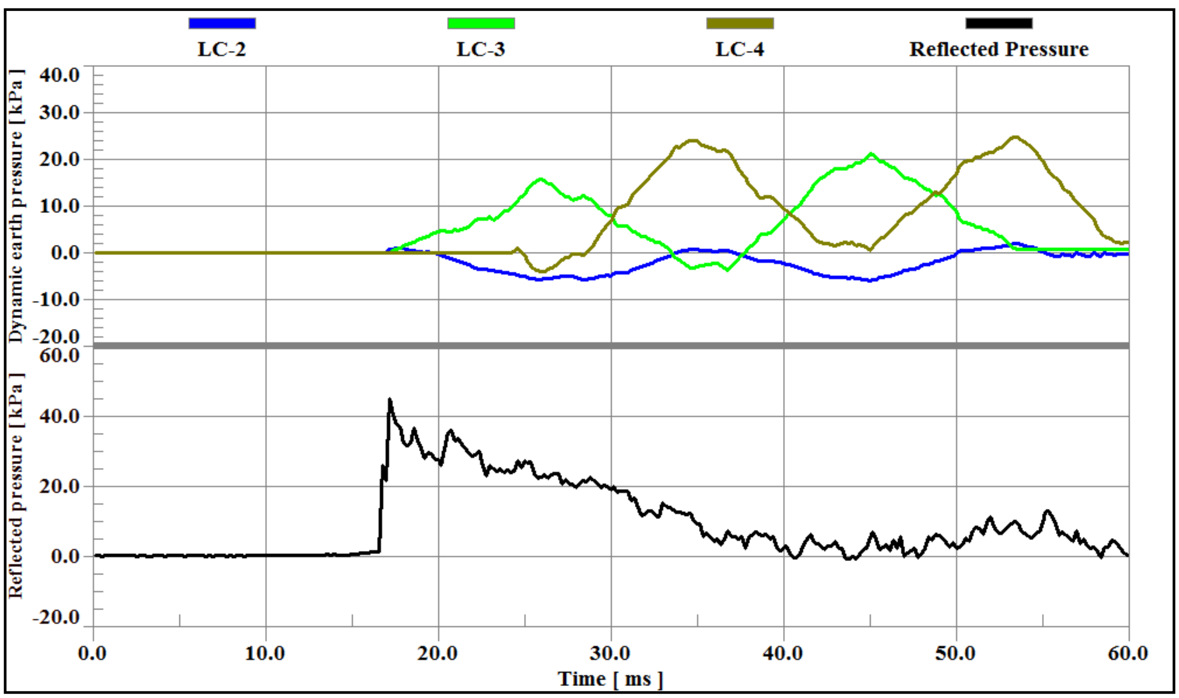

(g)

Figure 3.12: Total lateral earth pressure time history profiles (a) loose backfill; (b) medium backfill; (c) dense backfill; (d) dense backfill, Pr =71kPa; (e) dense backfill, Pr =26 kPa; (f) fully saturated backfill; (g) live load surcharge

Figure 3.13 depicts the maximum total earth pressure distribution along the height of the wall for backfill with different relative densities, blast load intensities, saturated backfill and backfill under the live load surcharge effect (pressure values for this figure were taken from LC-1 and LC-4). It was noticed that the magnitude of total earth pressure for loose and medium backfill at the mid-height of the wall slightly exceeded the dense backfill. Furthermore, the lateral earth pressures increased with the increase of blast load intensities. In this study, the highest lateral earth pressure was reported at a reflected pressure of 71 kPa, which was the highest applied pressure. As a blast pressure wave propagated through the sand, an immediate movement of sand particles occurred. The particles moved with a velocity called peak particle velocity, which was proportional to the pressure at the same point. The relationship between the stress waves and the peak particle velocity depends on the density of the soil and the compressive wave velocity, which is called acoustic impedance (Shim, 1995; Smith and Hetherington, 1994) as shown in Equation 3.2. Therefore, increasing the blast load intensity generated higher compressive wave velocity and thus higher stress in the sand. On the other hand, under the same load condition, increasing the density of the sand led to a reduction in the compressive wave velocity, and consequently lowered lateral earth pressure in the backfill.

$$\sigma = \rho v_p PPV \tag{3.2}$$

σ is the stress waves induced by blast loads.

ρ is the density of the soil.

v_p is the compressive wave velocity.

PPV is the peak particle velocity.

On the other hand, when saturated backfill was used, a reduction in the total earth pressure was noticed and lower values were obtained in comparison with the other reported conditions.

However, results obtained from previous studies on saturated soil subjected to blast loads, Jayasinghe (2014) and An (2010), showed that saturated soil had the highest peak pressures. Furthermore, the density of the soil and the shock velocity increased with the rise in water content. These results are in conflict with the results obtained in this paper. The reason for this discrepancy might be due to the fact that saturated backfill exerted static active earth pressure on the RW prior to the application of the blast load. When the RW was subjected to blast loading, the dynamic pressure propagated through the saturated backfill in the opposite direction to the static active earth pressure. The resultant pressure was the difference between these two pressures which represented the total lateral pressure in the saturated backfill. The theoretical static active earth pressures were also determined and plotted in Figure 3.13. It can be seen that the static active earth pressure for saturated backfill applied the highest pressures on the wall due to the effect of pore water pressure. In general, the maximum total earth pressures increased with the depth of the backfill for all tests. It is worth mentioning that the chosen values of maximum lateral earth pressures were time independent. Tests showed that the maximum values of the dynamic earth pressures did not happen at the same time and their distribution altered with time (Figure 3.12).

Similar trends were noticed when the dynamic earth pressure distributions of this study were compared with the results obtained by seismically induced lateral earth pressure on RW (Jo et al., 2017, Mikola, 212 and Al Atik, 2008).

The dynamic thrust (P_d) can be calculated by linearly fitting the area of the dynamic earth pressure (Figure 3.13). While the dynamic moment can be determined by multiplying the dynamic thrust by its arm, which is 0.33 H. The value for the moment arm was chosen based on the shape of the dynamic earth pressure distribution (Figure 3.13) and as suggested by M-O method, Jo et al.

(2017), Mikola, (2012) and Al Atik, (2008). The dynamic earth pressure coefficient (ΔK_{bd}) was back-calculated using the dynamic thrust as follows:

$$\Delta K_{bd} = 2P_{ad}/\gamma H^2 \quad (3.3)$$

Figure 3.14a represents the dynamic earth pressure coefficient as a function of the top of the wall's acceleration. The data from this figure was taken from loose, medium, and dense backfill conditions that were subjected to a blast load of 47 kPa and dense backfill condition subjected to a blast load of 71 kPa. Data from saturated and partially saturated backfill was not considered in this figure because of the different moisture content. Moreover, the live load surcharge condition was also not considered due to a difference in the load condition.

It can be seen from Figure 3.14a that for the same load condition, the ΔK_{bd} and the acceleration for the RW with loose backfill had higher values than with medium and dense backfill. The ΔK_{bd} was determined from the dynamic thrust and the density of the soil (Equation 3.3). The values for the dynamic thrust for loose, medium, and dense backfill were close (Figure 3.13). Therefore the controlling factor was the density of the soil. Since the relationship between the ΔK_{bd} and the density is inversely proportional, an increase in the density led to a decrease in the ΔK_{bd}. Regarding the acceleration, the support provided by the loose backfill to the RW was lower in comparison to the medium and dense backfill conditions which caused the RW to be subjected to a higher acceleration and impact.

When the RW was subjected to a blast pressure of 71 kPa, the value for ΔK_{bd} was the highest. Increasing the blast pressure led to an elevation in the blast thrust and as a result raised the value for ΔK_{bd} since the relationship between them is proportional (Equation 3.3). The best-fit equation for the data from Figure 3.14a was shown below:

$$\Delta K_{bd} = 0.0215a_t + 1.5936 \quad (3.4)$$

Figure 3.14b shows the same values of ΔK_{bd} as a function of the backfill's acceleration

$$\Delta K_{bd} = 0.0201a_t + 1.8467 \tag{3.5}$$

It was noticed from Figures 3.14a and 3.14b that the dynamic earth pressure coefficient increased with amplification of the acceleration. As mentioned above, when the blast pressure was raised, the dynamic thrust was intensified which led to an increase in ΔK_{bd}.

It is well-known that RWs are designed to support the pressures exerted by soil and traffic loads. Therefore, it is important to estimate the lateral earth pressure in order to effectively design RWs. The dynamic lateral earth pressure can be predicted if the dynamic earth pressure coefficient and the effective stress are known. The effective stress can be determined by multiplying the density of soil by the height of soil. The dynamic earth pressure coefficient can be obtained from equation 3.3 or 3.4 determined in this study. In other words, if the soil's acceleration induced by blast loads is identified, the dynamic earth pressure can be calculated and thus the effect of blast loads can be included in the analysis and design of RWs.

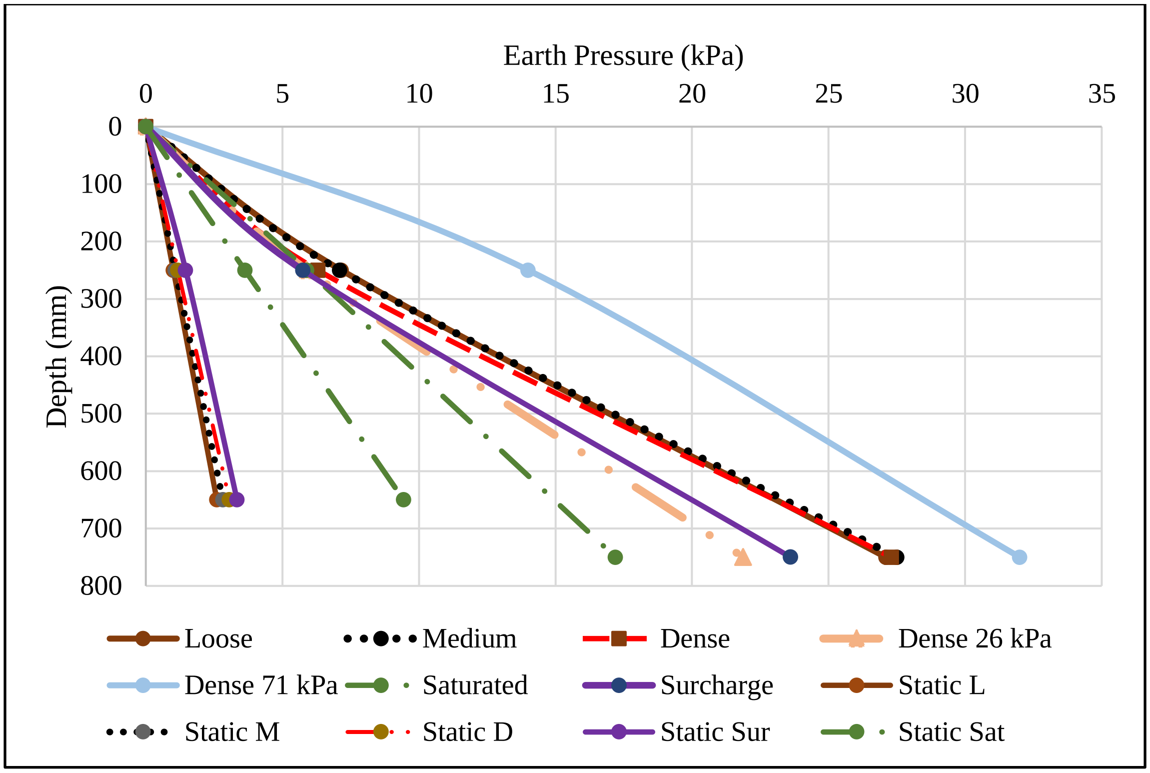

Figure 3.13: Total and static earth pressure distribution along the height of the wall for backfill with different relative densities, blast load intensities, saturated backfill and backfill under live load surcharge

The figure shows the total and static earth pressures for the backfill in loose and medium conditions when subjected to a reflected pressure (Pr) of 47 kPa. Meanwhile reflected pressures of 26 kPa, 47 kPa and 71kPa were used for dense backfill with a degree of saturation of 13 % for all conditions except saturated backfill. **Static L** stands for static lateral earth pressure for loose sand; **Static M** stands for static lateral earth pressure for medium sand; **Static D** stands for static lateral earth pressure for dense sand; **Static Sur** stands for static lateral earth pressure under live load surcharge effect; **Static Sat** stands for static lateral earth pressure for saturated dense sand.

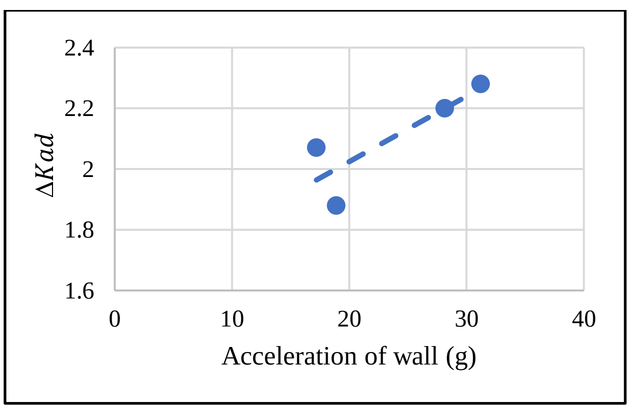

(a)

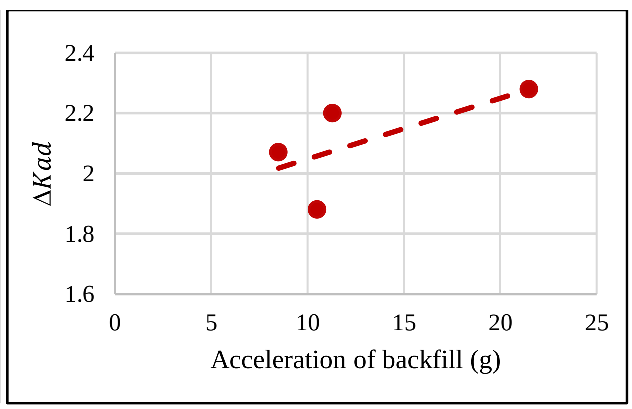

(b)

Figure 3.14: Dynamic earth pressure coefficient as a function of: (a) wall's acceleration; (b) backfill's acceleration

3.4.3 Inertial Forces

Wall and backfill inertial forces were evaluated using the acceleration data (Figure 3.15). It can be seen that the inertial forces of the backfill had a higher amplitude than the inertial forces of the wall for all conditions. The reason for that is the mass of the backfill was larger than the mass of the RW and as the inertial forces resulted from multiplication of the mass and the acceleration, larger mass led to higher amplitude. The dense backfill condition subjected to a reflected pressure of 71 kPa exhibited the highest inertial forces in the wall and backfill. Appling higher blast pressure led to higher acceleration than other conditions and thus higher inertial forces. Furthermore, loose backfill resulted in higher inertial forces in the wall compared to medium and dense backfill conditions when subjected to a reflected pressure of 47 kPa. A noticeable lag was observed between the response of wall and backfill inertial forces in loose condition. This can be explained by the fact that loose backfill conditions provided less support to the RW. Therefore, the pressure from the blast produced higher acceleration on the wall with loose backfill when compared with other conditions. Besides, densification might have occurred when the reflected pressure passed through the loose backfill. As a result, time-lag was generated between the responses of the wall and the backfill.

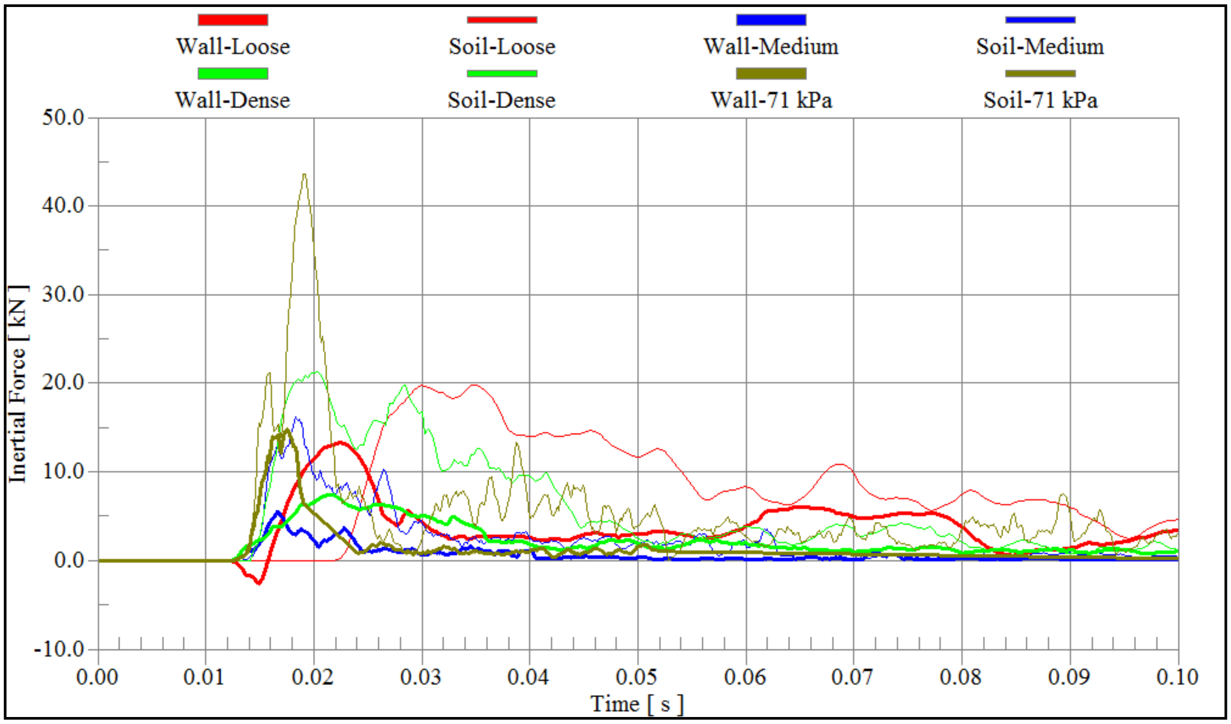

Figure 3.15: Wall and backfill inertial forces time history

Wall-Loose, Wall Medium, and Wall-Dense: Wall inertial forces for loose, medium and dense backfill conditions, respectively, with 13% degree of saturation under reflected pressure of 47 kPa; Wall-71 kPa: Wall inertial force for dense backfill, with 13% degree of saturation under reflected pressure of 71 kPa; Soil-Loose, Soil-Medium, and Soil-Dense: backfill inertial forces for loose, medium and dense conditions, respectively, with 13% degree of saturation under reflected pressure of 47 kPa; Soil-71 kPa: backfill inertial force for dense sand condition, with 13% degree of saturation under reflected pressure of 71 kPa.

3.4.4 Moment Capacity of the Retaining Wall

The development of force-deflection relationships for the overall structure or each member is crucial to determine the dynamic response of the structure or member. The force-deflection relationships are called resistance functions, and they are usually nonlinear (Ngo et al., 2007).

In order to calculate a resistance function, the inelastic section capacities should be determined first. The compressive and tensile stresses of the section were computed to determine the nominal moment capacity of the wall. The wall was made of concrete with a compressive strength of 38 MPa and had ten rebars with a diameter of 6.3 mm and a yield strength of 521 MPa (the yield strength of reinforcement was tested by Hasak, (2015), Kadhom, (2015), and Burrell, (2012). A dynamic increase factor (DIF) was applied to static strength values to incorporate the effect of material strength increase when subjected to rapid loading effects like a blast. The DIF is defined as the ratio of dynamic material strength to static material strength, and it is a function of material type and strain rate. The DIFs for reinforcing bars and concrete are 1.17 and 1.19, respectively (Jacques, 2016 and ASCE, 2010). The moment was calculated using equation 3.6 (MacGregor and Wight, 2006, Ferguson and Cowan, 1981), as follows:

$$M_n = A_s f_y (DIF_s)\left(d - \frac{a}{2}\right) \tag{3.6}$$

$$a = \frac{A_s f_y (DIF_s)}{0.85 f_c b (DIF_c)} \tag{3.7}$$

where,

M_n is nominal moment, MN.m.

A_s is area of reinforcement on the tension face the section, mm^2.

f_y is tensile strength of the reinforcement, MPa.

d is distance from the extreme fiber in compression to the centroid of the steel on the tension side of the member, mm.

f_c is compressive strength of the concrete, MPa.

b is width of the compression face of the wall, mm.

DIFs; DFIc is dynamic increase factor for reinforcing bars and concrete, respectively.

The ultimate resistance (Ru) was then calculated using Equation 3.8 (UFC, 2008) and it was 20 kN.

$$r_u = \frac{2M_n}{L^2} \tag{3.8}$$

where,

r_u is ultimate unit resistance of the section, kN/m.

L is height of the stem, m.

3.4.5 Blast Resistance of Reinforced Concrete Retaining Wall

The development of internal resistance for structural elements to resist blast loads is based on material stress and section properties. It is crucial to determine the relationship between resistance and deflection in order to design or analyze the response of an element. In blast analyses, resistance is represented as a nonlinear function to demonstrate elastic and inelastic behaviour (ASCE, 2010).

The blast resistance of RCRW under different conditions was investigated by using experimentally obtained force-deformation relationships in the form of resistance functions. These functions were determined from the measured acceleration and applied force-time histories for each test. Wall accelerations were measured using a high-definition camera. The acceleration time-histories of the wall were obtained using ProAnalyst software. The dynamic resistance-time histories (R_t) were computed from the equation of motion (Equation 3.9). The applied blast force was determined by multiplying the peak reflected pressure by the area of the stem facing the shock tube. This area was obtained by multiplying 0.5 m by 0.59 m. The peak reflected pressure was calculated by dividing the maximum value of the calculated positive impulse by 0.5 t_d. This is based on the assumption that the reflected pressure decayed linearly from its peak value to zero within a time equal to t_d. The inertia force function was determined by multiplying the equivalent mass by the acceleration time history (a_t). The equivalent mass (consisted of the mass of the stem plus the mass of the backfill resulted from the static active earth pressure) was multiplied by the load-mass transformation factor (K_{LM}). The K_{LM} for cantilever varied between 0.78 for elastic range and 0.66 for plastic range (UFC, 2008).

$$F_t = K_{LM} M a_t + R_t \tag{3.9}$$

where,

F_t is blast force time history, kN.

K_{LM} is load-mass transformation factor.

M is mass, kg.

a_t is acceleration time history, m/s^2.

R_t is resistance time history, kN.

Figure 3.16 represents the resistance time history function obtained from subjecting the RW to different blast load intensities with backfill of various relative densities. Figure 3.16a-d shows graphically the application of the equation of motion. In this figure, the resistance time history function was the result of subtracting the inertial force time history from the applied force time history. It can be seen that the maximum dynamic resistance function was reached when high intensity pressure was applied (71 kPa). This is attributed to the fact that the opposing internal forces generated by the wall should be equal to the applied force (Equation 3.9). Therefore, an increase in blast load intensity forced the wall to reach higher response ranges (ASCE, 2010 and Smith and Hetherington, 1994). It is important to mention that the maximum resistance of the section was still below the ultimate resistance of the wall, which was calculated in section 3.4.4 of this paper. Nevertheless, hairline cracks were noted on the stem facing the shock tube (Figure 3.17). The presence of cracks might be evidence of the development of a post-cracking response on a portion of the stem facing the blast load. Internal resistance continued to increase while the stress in different parts of the member escalated in response to the applied force. As a result, part of the member might develop a post-cracking response while the other portions of the section were still in the elastic region (Biggs, 1964).

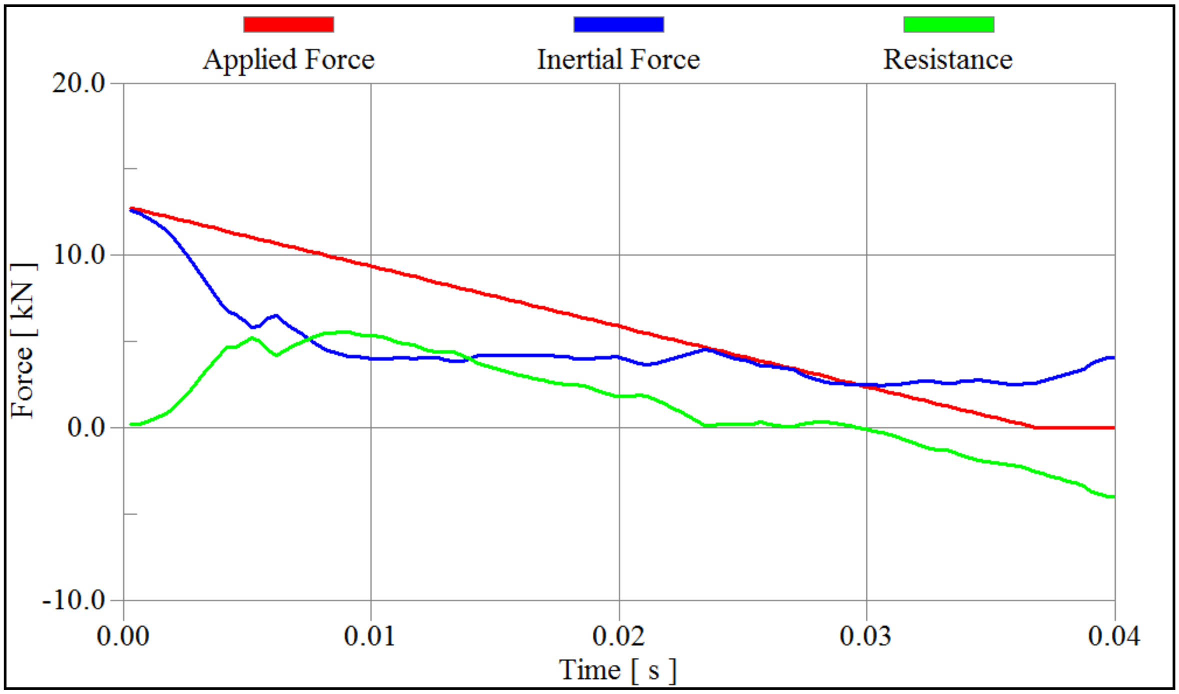
Applied Force
Inertial Force
Resistance
20.0
10.0
0.0
-10.0
Force [kN]
0.00
0.01
0.02
0.03
0.04
Time [s]

(a)

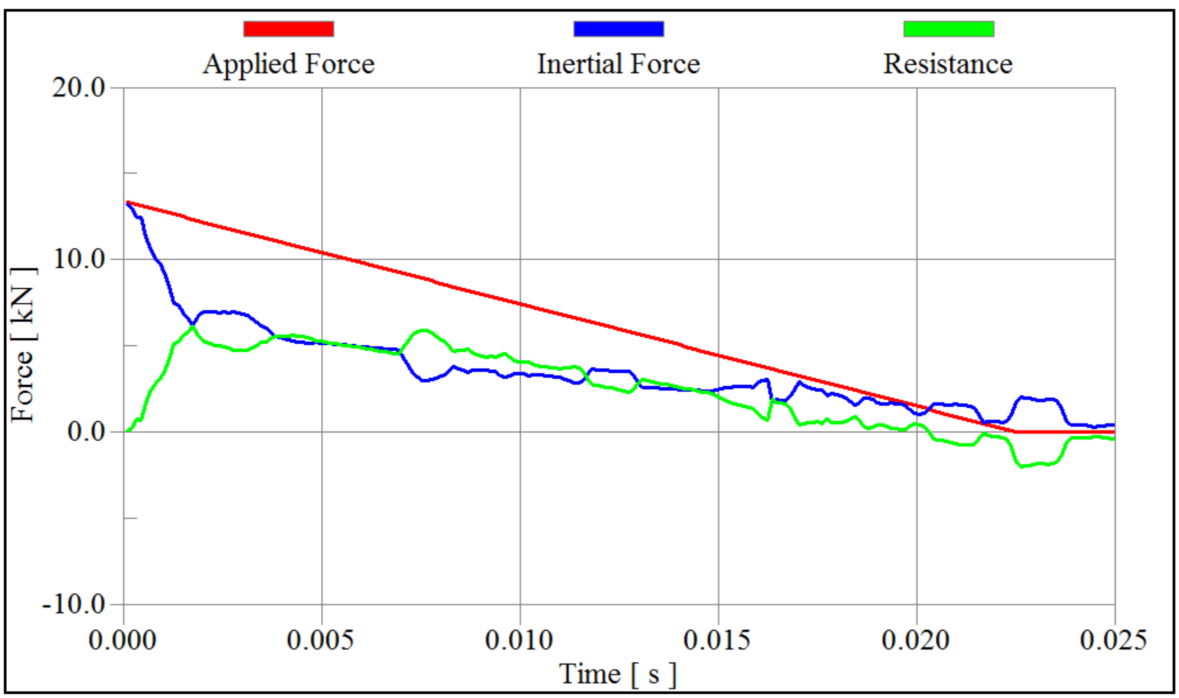
Applied Force
Inertial Force
Resistance
20.0
10.0
0.0
-10.0
Force [kN]
0.000
0.005
0.010
0.015
0.020
0.025
Time [s]

(b)

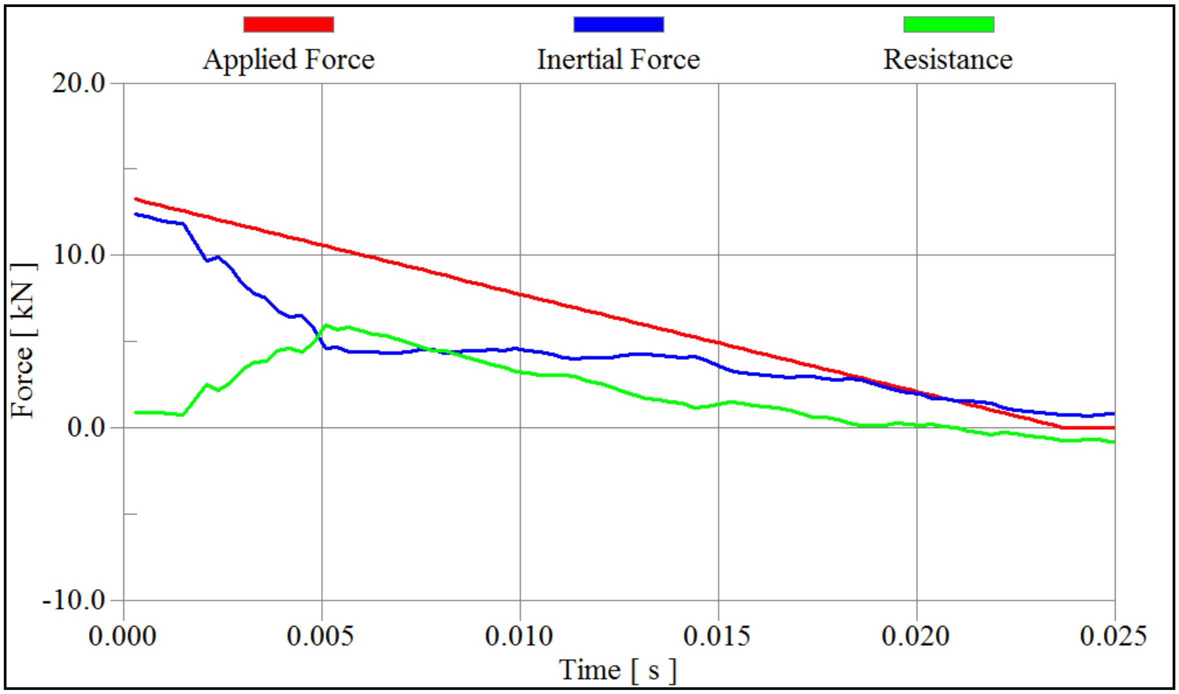

(c)

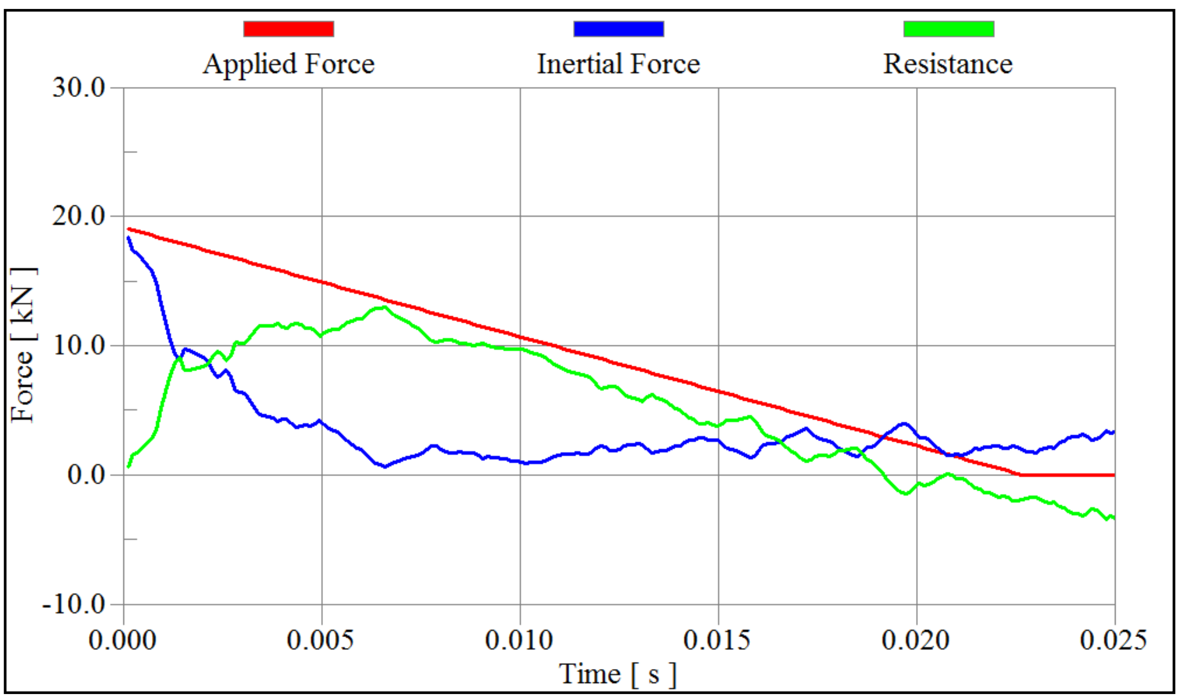

(d)

Figure 3.16: Resistance time history of RW with (a) loose backfill, blast force of 13.75 kN; (b) medium backfill, blast force of 13.75 kN; (c) dense backfill, blast force of 13.75 kN; (d) dense backfill, blast force of 19.2 kN

Figure 3.17: Hairline cracks on the stem facing the shock tube

Figure 3.18 illustrates the dynamic resistance displacement relationships of the RW with sand backfill. Three curves that represent RW with loose, medium, and dense backfill were subjected to a blast force of 13.75 kN, and one curve representing RW with dense backfill was subjected to a blast force of 19.2 kN. All curves show the same pattern. Often, the resistance displacement relationship proportioned linearly up to the elastic limit. As the passive state was reached in the RW backfill, the resistance remained approximately constant while the displacement continued increasing until it reached the maximum. Though, before approaching the maximum displacement limit, the resistance rebounded with a slope approximately parallel to the elastic portion of the resistance curve. This confirms the post-cracking response of the RW when tested under the shown blast intensities.

On the other hand, the relative density of the backfill had no distinctive impact on the maximum resistance of the wall. However, it affected the shape of the resistance-deflection curve. Note that the area under the curve represents the total strain energy available to resist the blast load.

It can be seen from Figure 3.18 that for the same load condition, the RW with medium and loose backfills exhibited larger deformations than the RW with dense backfill. This is because loose and medium backfills provided less support to the RW and thus more deflections took place.

The elastic stiffness of the wall is clearly shown by the slope of the dynamic resistance function in the elastic region (Figure 3.19).

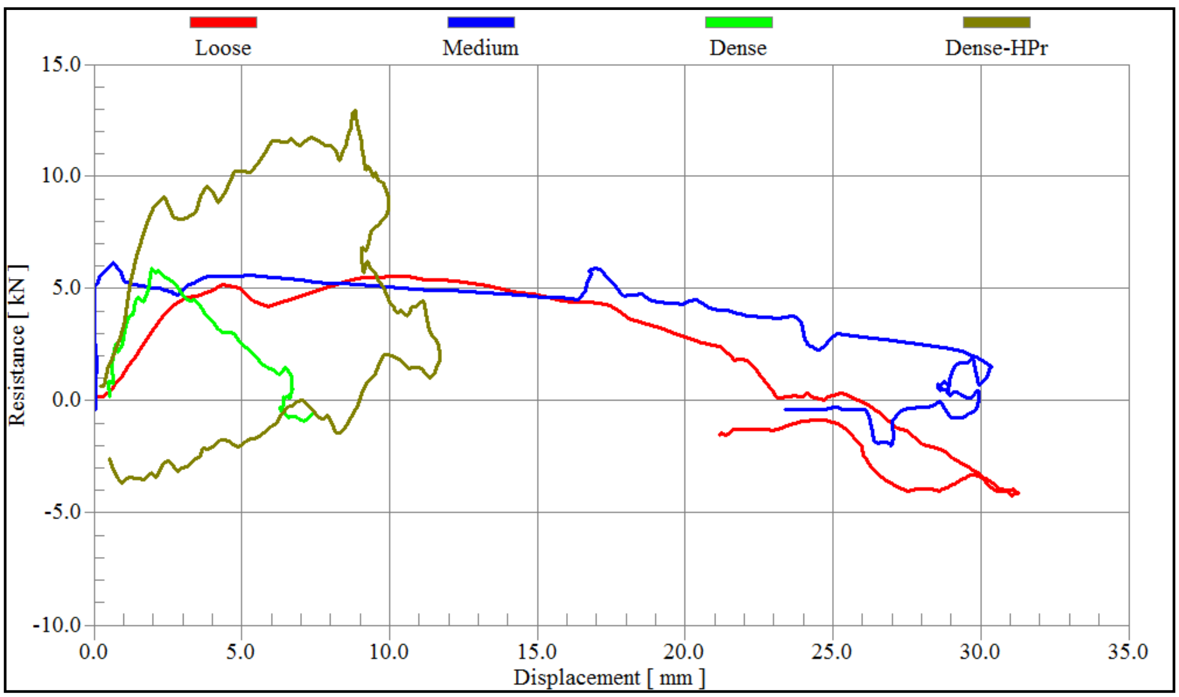

Figure 3.18: Resistance displacement function of RW with sand backfill

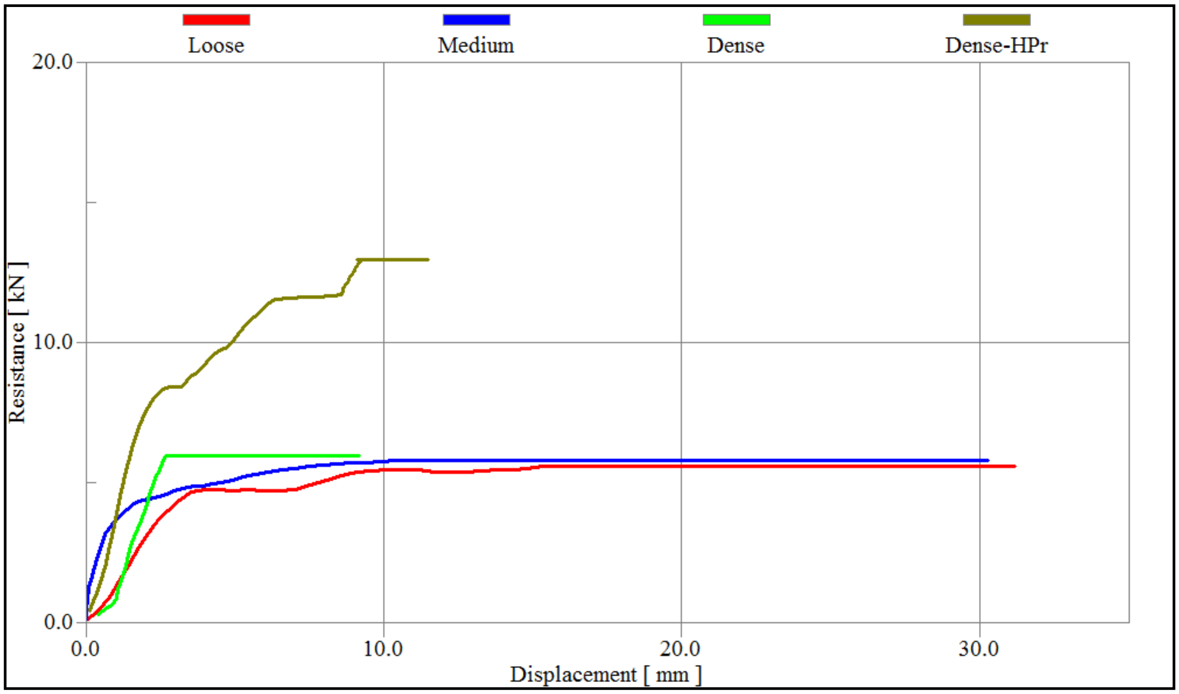

Figure 3.19: Dynamic resistance function of RW with sand backfill in the elastic region

Four strain gauges were attached to the tension steel of the stem. Two strain gauges (SG-1 and SG-2) were placed 30 mm from the base of the wall, and SG-3 and SG-4 were located at 250 mm from the base (Figure 3.5). It was noticed during the tests that SG-4 was defective; therefore, no results were obtained from this strain gauge. The readings from SG-2 and SG-3 were minimal and were not considered here, because they might be malfunctioned. Readings of SG-1 are displayed in Figure 3.20. In this figure, the strain time history of the RW with different relative densities backfill, load intensities and degree of saturation are shown. It can be observed that the wall with loose backfill subjected to blast pressure of 47 kPa had a peak tensile strain around 0.0025, while the wall with the highest pressure and dense backfill had a peak strain of about 0.0016. The readings of the strain gauge comply with the results of the lateral earth pressure and inertial forces mentioned in sections 3.4.2 and 3.4.3 respectively. The highest responses were for the RW with loose backfill and the RW with the highest blast pressure (71 kPa). The results from the strain gauge showed that yield was not reached, and the intensities of the shots were below the design capacity of the section.

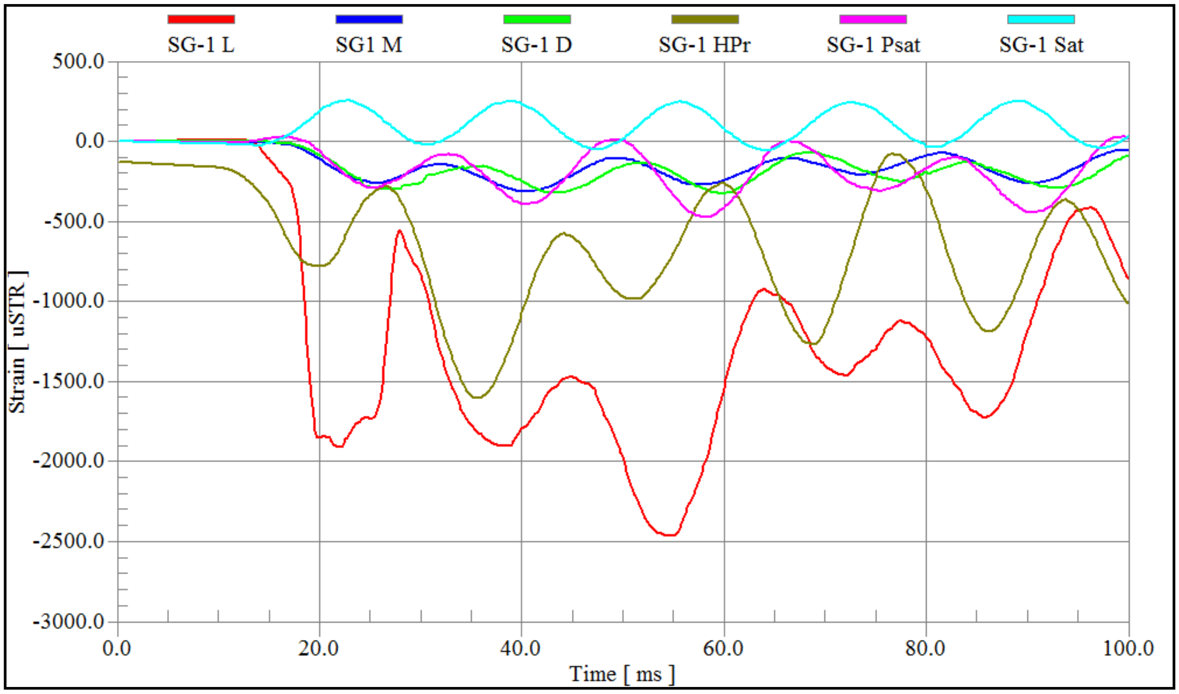

Figure 3.20: Strain time history of the RCRW
SG-1 L: strain gauge in loose backfill; SG1 M: strain gauge in medium backfill; SG-1 D: strain gauge in dense backfill; SG-1 HPr: strain gauge in dense backfill subjected to a reflected pressure of 71 kPa; SG-1 Psat: strain gauge in partially saturated backfill; SG-1 Sat: strain gauge in saturated backfill

3.5 Summary and Conclusion

In this paper, an L shape reinforced concrete retaining wall with sand as a backfill material was subjected to simulated blast load. The blast load was generated by the shock tube at the Blast Research Laboratory of the University of Ottawa. Various instruments were placed in the soil-RW model to evaluate the dynamic response of the model during the blast event. An image analysis technique was used to capture the soil particles' movement and to track the transient and permanent displacements of the wall.

Sand backfills with various relative densities and degrees of saturation were subjected to different blast shot intensities (26 kPa, 47 kPa, and 71 kPa) to evaluate the dynamic lateral earth pressure behind the RW. Furthermore, the blast resistance of the RCRW was investigated by using experimentally obtained force-deformation relationships in the form of resistance functions.

The dynamic earth pressures were measured along the height of the wall using soil pressure gauges. It was noticed that the maximum dynamic earth pressures were recorded at a time greater than the positive phase duration regardless of the backfill condition. The maximum total earth pressure distribution along the height of the wall was determined. It was seen that the magnitude of total earth pressure for loose and medium backfill at the mid-height of the wall slightly exceeded the dense backfill. Moreover, it was observed that there was a lateral earth pressure increase with an increase in blast load intensities. The dynamic earth pressure coefficient was back calculated using the dynamic thrust. Relationships between ΔK_{bd} and accelerations of the wall and backfill were obtained.

Moment capacity of the retaining wall and the ultimate resistance were theoretically calculated. The maximum experimentally obtained blast resistance of reinforced concrete retaining wall was reached when a high-intensity pressure was applied. Results from strain gauges confirmed that yield was not reached, and intensities of the shots were below the design capacity of the section.

The results from this study can be used to assess the vulnerability of transportation structures (e.g., highways) to blast loading and to develop guidelines for their design.

3.6 References

Al Atik, L. F. (2008). Experimental and Analytical Evaluation of Seismic Earth Pressures on Cantilever Retaining Structures. Doctoral thesis, University of California, Berkeley.

American Society of Civil Engineers (ASCE). (2010). Design of Blast-Resistant Buildings in Petrochemical Facilities, Second Edition.

Bakr, J. A. (2018). Displacement-Based Approach for Seismic Stability of Retaining Structures. Doctoral thesis, School of Mechanical, Aerospace and Civil Engineering. University of Manchester.

Biggs, J. M. (1964). Introduction to Structural Dynamic, McGraw-Hill, Inc. U.S.

Burrell, R. (2012). Performance of Steel Fiber Reinforced Concrete Columns under Shock Tube Induced Shock Wave Loading, MS Thesis, Department of Civil Engineering, University of Ottawa, Ontario, Canada.

Chen, W-F, Duan, L. (2014). Substructure Design. Bridge Engineering Handbook, Second Edition.

Das, B. M. (2016). Principles of Foundation Engineering, Eighth Edition, Boston, MA, U.S.

Das, B. M. (1999). Principles of Foundation Engineering, Fourth Edition, Pacific Grove, CA, U.S.

Das, B. M. (1993). Principles of Soil Dynamics, Second Edition, Stamford, CT, U.S.

Federal Highway Administration, United States Department of Transportation. (2008). Standard Specifications for Construction of Roads and Bridges on Federal Highway Projects FP-14.

Ferguson, P. M. and Cowan, H. J. (1981). Reinforced concrete Fundamentals, Fourth Edition.

Fujikura, S., Bruneau, M., Lopez-Garcia, D. (2008). Experimental Investigation of Multihazard Resistant Bridge Piers Having Concrete-Filled Steel Tube under Blast Loading. Journal of Bridge Engineering, ASCE, 13 (6), 586-594.

Geotechnical Design Procedure (GDP-9). (2015). Liquefaction Potential of Cohesionless Soils. State of New York Department of Transportation, Geotechnical Engineering Bureau.

Hao, H., Wu, C. (2005). Numerical Study of Characteristic of Underground Blast Induced Surface Ground Motion and Their Effect on Above-Ground Structures Part II. Effects on Structural Responses. Soil Dynamics and Earthquake Engineering, 25, 39-53.

Hasak, A. (2015). Performance of FRP Strengthened concrete Columns under Simulated blast loading. Master thesis, Department of Civil Engineering, University of Ottawa, Ontario, Canada.

Jacques, E. (2016). Characteristics of Reinforced Concrete Bond at High Strain Rates. Doctoral thesis, University of Ottawa, Ontario, Canada.

Jo, S-B, Ha, J-G, Lee, J-S, Kim, D-S. (2017). Evaluation of the Seismic Earth Pressure for Inverted T-Shape Stiff Retaining Wall in Cohesionless Soils via Dynamic Centrifuge. Soil Dynamics and Earthquake Engineering 92, 345–357.

Kadhom, B. (2015). Blast Performance of Reinforced Concrete Columns Protected by FRP Laminates. Doctoral thesis, University of Ottawa, Ontario, Canada.

Kloukinas, P., Scotto di S., Anna, P., Augusto, D., Matthew, E., Aldo, L. Simonelli, A., Taylor, C., Mylonakis, G. (2015). Investigation of Seismic Response of Cantilever Retaining Walls: Limit Analysis vs Shaking Table Testing. Soil Dynamics and Earthquake Engineering, 77, 432–445.

Lloyd, A. (2015). Blast Retrofit of Reinforced Concrete Columns. Doctoral thesis, University of Ottawa, Ontario, Canada.

Lloyd, A. (2010). Performance of Reinforced Concrete Columns under Shock Tube Induced Shock Wave Loading. Master thesis, University of Ottawa, Ontario, Canada.

MacGregor, J. G. and Wight, J. K. (2006). Reinforced Concrete Mechanics and Design, Fourth Edition.

Mays, G.C. and Smith, P.D. (1995). Blast Effects on Buildings. First edition.

Mikola, R. G. (2012). Seismic Earth Pressures on Retaining Structures and Basement Walls in Cohesionless Soils. Thesis, University of California, Berkeley.

Mikola, R. G. and Sitar, N. (2013). Seismic Earth Pressures on Retaining Structures in Cohesionless Soils. Department of Civil and Environmental Engineering University of California, Berkeley.

Mittal, R. K., Gupta, M.K. and Singh, S. (2004). Liquefaction Behaviour of Sand during Vibrations. 13th World Conference on Earthquake Engineering, Vancouver, B.C., Canada, 1-6.

Morris, D. V., and Delphia, J. G. (1999). Specifications for Backfill of Reinforced-Earth Retaining Walls. Texas Department of Transportation in Cooperation with the U.S. Department of Transportation Federal Highway Administration.

MULTIQUIP INC. (2011). Soil Compaction Handbook.

National Research Council. (1985). Liquefaction of Soils during Earthquakes, Washington DC.

Nishimura, T., Hirabayashi, Y., Fredlund, D. G., and Gan, J. K.-M. (1999). Influence of Stress History on the Strength Parameters of an Unsaturated Statically Compacted Soil. Canadian Geotechnical Journal, 36, 251–261.

Ngo, T., Mendis, P., Gupta, A. & Ramsay, J. (2007). Blast Loading and Blast Effects on Structures-an Overview. EJSE Special Issue: Loading on Structures.

Sladen, J. A., D'Hollande, R. D., AND Krahn, J. (1985). The Liquefaction of Sands, a Collapse Surface Approach. Canadian Geotechnical Journal, 22.

Smith, P. D. and Hetherington, J. G. (2011). Blast and ballistic loading of structures.

TM 5-1300. (1990). Structures to Resist the Effects of Accidental Explosions. Departments of the Army, the Navy, and the Air Force.

Tsuchida, H. (1970). Prediction and Countermeasure against the Liquefaction in Sand Deposits, 3.1-3.33 in Abstract of the Seminar in the Port and Harbor Research Institute in Japanese.

Unified Facilities Criteria (UFC). (2008). Structures to Resist the Effects of Accidental Explosions. Departments of the Defense.

Xu, T. (2015). Numerical simulation of embankment dams subjected to blast loadings, PhD Thesis. The Hong Kong University of Science and Technology, Hong Kong.

Chapter 4 Technical Paper II: Blast Response of Cantilever Retaining Wall: Modes of Wall Movement

Najlaa Abdul-Hussain, Mamadou Fall, Murat Saatcioglu

4.1 Abstract

Excessive displacements behind retaining walls (RWs) in the form of translation or rotation failure induced by intentional or unintentional blast loads can cause severe damage to retaining structures. For the past few decades, there has been an increase in awareness regarding the safety of highway bridges from blast loads. Since abutments/RWs are portions of bridges, investigating their behaviour under blast loads is important. As there have not been any studies investigating the dynamic response of retaining walls due to blast loading, an experimental study was conducted to examine the influence of blast loads on the dynamic behaviour of reinforced concrete retaining wall (RCRW) with sand as a backfill material. A shock tube was used to generate blast loads on the soil-RW model. The influence of the relative density, backfill saturation, blast load intensity, and live load surcharge on the blast behaviour of RCRW with sand backfill was studied. The results showed that the modes of wall movement were affected by the backfill relative density, blast load intensities, and degree of saturation. Under the same load conditions, an increase in the wall movement was noticed in loose backfill, and a translation response mode was evident in this condition. A relationship between wall relative movements and mobilized earth pressure coefficients was determined. The mobilized passive resistance of the RW backfill induced by blast load was used to determine the force-displacement relationship. Acceleration time histories for RW/backfill were found for all conditions. The findings of this research will help to properly evaluate and design bridges' abutment and to develop resilient infrastructure systems.

Keywords: Blast load, Retaining wall, Relative movements, Passive resistance.

4.2 Introduction

The sustainability of retaining walls (RWs) is crucial because they are one of the most important engineering infrastructures and are widely used for highways, bridges, tunnels, mines, and military defences. Geotechnical engineers design RWs to resist lateral earth pressure force. The static earth pressure theories were first presented in 1776 and 1857 by Coulomb and Rankine, respectively. The effect of the wall displacement on the development of static earth pressure was not taken into consideration in these theories because they were based on force-based methods. The Mononobe-Okabe method (M-O method) was proposed by Okabe (1926) and Mononobe and Matsuo (1929) to predict the seismic earth pressure. The M-O method was also a force-based method as it was developed based on Coulomb's earth pressure theory. Since then, substantial research has been accomplished to further develop the M-O method and to propose new analytical, numerical and experimental approaches and solutions in order to understand the influence of seismic earth pressure on RWs. Researchers also addressed the permanent displacement of a retaining wall due to seismic loading and the effects of wall movements on the seismic earth pressure behind the wall (Steedman and Zeng, 1991, Whitman-Liao, 1985, and Richards-Elms, 1979). The relationship between earth pressure and wall displacement was also investigated. Studies showed that a large displacement was required to reach the passive state; however, a small displacement was sufficient to develop the active state (Table 4.1). The modes of wall movement had a considerable impact on the magnitude and distribution of earth pressure (Bakr, 2018). Researchers proposed analytical and numerical methods to predict the lateral earth pressures based on the mode of RW movement (e.g., Liu, 2013, Peng et al., 2012, Wilson and Elgamal, 2010, Potts and Fourie, 1986 and Bang, 1985). A formulation of passive force-displacement capacity for the design of an abutment-backfill system was presented by Shamsabadi et al. (2005).

Permanent deformations may occur if retaining structures are exposed to excessive dynamic loads. In many historical earthquakes, these deformations caused major damages to retaining structures (Bakr 2018). Cases of bridge failures were reported due to excessive abutment displacement induced by seismic forces (Psarropoulos et al., 2009). However, in some cases, the deformations were negligibly small (Al-Atik, 2008).

The use of explosive devices has been relevant for hundreds of years; however, the interest in the design of blast resistant structures (specifically, military structures) first appeared during and after World War II. An unclassified document on weapons and penetration capabilities was published following the war by the Office of Scientific Research and Development in 1946 (Agrawal and Yi, 2009). During the past half-century, manuals on protective structures were developed to address the threats of nuclear and conventional weapons (ASCE, 1985, Crawford et al., 1974, and Newmark and Haltiwanger, 1962). The effect of accidental explosions on the resistance of structures was addressed as well (USDOA, 1990).

Due to the increase of terrorist activities in the last few decades, many design guidelines for building structures were published (ASCE, 1999, and 2005; DOD, 2003; GSA, 2003; ISC, 2001). In 2006, draft manuals were published by the National Institute of Standards and Technology that put the efforts from previous researchers into practice (Agrawal and Yi, 2009). These manuals provided a range of structural data and design procedures that can help engineers to design blast-resistant structures, which can be used to address the issue of blast load effects on highway bridges. However, it was noticed that none of the available literature addresses the dynamic response of RWs due to blast loading.

Therefore, in the present study, backfill materials with various relative densities and degrees of saturation were subjected to different blast shot intensities to evaluate the modes of RW movement. Furthermore, the mobilized passive resistance of the RW backfill due to blast loading was used to determine the force-displacement relationship.

Table 4.1: Relative movements required to reach active and passive earth pressures (Clough and Duncan, 1991)

Type of Backfill	∆/H (active)	∆/H(passive)
Dense sand	0.001	0.01
Medium dense sand	0.002	0.02
Loose sand	0.004	0.04
Compacted silt	0.002	0.02
Compacted lean clay	0.010	0.05

Note: ∆: movement of top of wall; H: height of wall

4.3 Experimental Program

4.3.1 Description of Test Specimens and Material Properties

4.3.1.1 Backfill Soil

Sand is commonly used as a backfill material for retaining wall systems. The high permeability of sand helps in releasing the hydrostatic pressure behind the wall stem. Sand has been used extensively in experimental research (e.g. Jo et al., 2017, Kloukinas et al., 2015, and Mikola and Sitar, 2013) to address the dynamic response of soil retaining walls to seismic loads. In this study, both the backfill and foundation soil layers consisted of sand. The grain size distribution and sand properties were determined, according to the ASTM (American Society for Testing and Materials) C136/C136M−14, at the Geotechnical Laboratory of the University of Ottawa. The sand had a mean grain size (D_{50}) of 0.54 mm, an effective size (D_{10}) of 0.21 mm, a uniformity coefficient (C_u) of 3.05 and a coefficient of gradation (C_z) of 0.9. Figure 4.1 depicts the grain size distribution of the sand.

The specific gravity of the sand was 2.64, and it was determined according to the ASTM D854-14. Minimum and maximum dry densities of 13.0 kN/m^3 and 18.8 kN/m^3 were found following the procedure prescribed by the ASTM D4254-16 and D4253-16, respectively. The friction angle of the sand was 34° and it was determined using the direct shear test described in the ASTM, D3080-11. Table 4.2 summarizes the soil properties of this research.

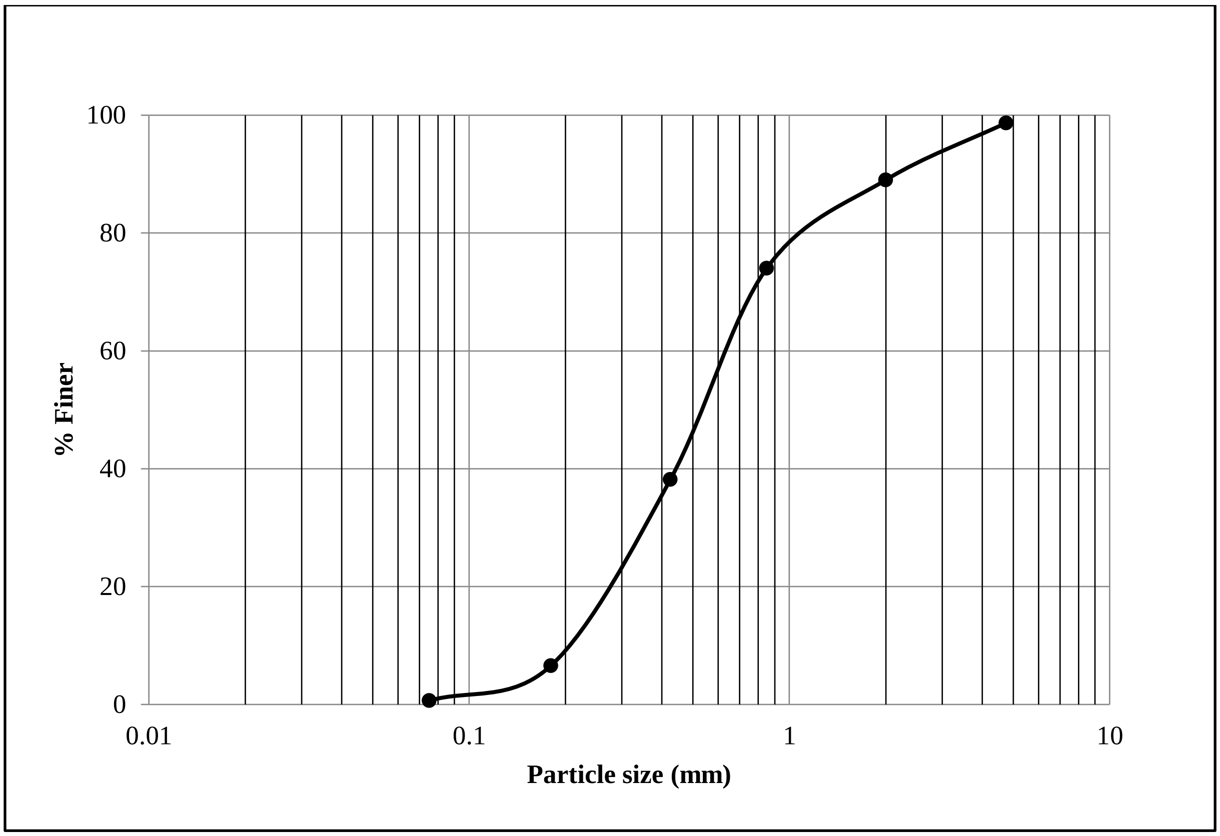

Figure 4.1: Grain size distribution of silica sand

Table 4.2: Soil properties

Descriptions	Values
Effective diameter (D_{10})	0.67 mm
Uniformity coefficient (C_u)	3.05
Coefficient of gradation (C_z)	0.9
Specific gravity (G_s)	2.64
Maximum unit weight	18.8 kN/m^3
Minimum void ratio	0.38
Minimum unit weight	13.0 kN/m^3
Maximum void ratio	0.99
Friction angle	34°

4.3.1.2 Wall

The reinforced concrete retaining wall model, depicted in Figure 4.2, had an L shape. The RW was designed using the Rankine earth pressure theory for stability. The RW was checked for overturning, sliding along the base and bearing capacity failure. The RW investigated was modelled at the 1/10th scale. As shown in Figures 4.2 and 4.3, the dimensions of the stem and the heel of the retaining wall in this study were 650 mm (height) x 500 mm (width) x 60 mm (thickness) and 400 mm (width) x 500 mm (length) x 60 mm (thickness), respectively.

Two RWs were constructed at the Structural Laboratory of the University of Ottawa. The second wall was built as a replacement in case of failure of the first wall. Both concrete RWs were reinforced longitudinally and laterally with 6.3 mm rebars spaced at 50 mm c/c. The details of retaining wall reinforcement are presented in Figure 4.3. A concrete mixer and an electric concrete vibrator were used to mix and consolidate the fresh concrete, respectively. The heel of the retaining wall was first cast, and 14 days later, the stem was cast (Figure 4.2). At the end of each casting process, the specimens were covered with two layers of wet burlap and a plastic sheet in order to allow for curing for 30 days. Seven concrete cylinders (100 mm diameter x 200 mm height) were prepared for standard cylinder tests. The cylinders were prepared and cured according to the ASTM C31/C31M-19. The cylinders were also cured for 30 days following the same curing approach adopted for the RC wall. The compressive strength of the concrete was 38 MPa after 120 days. Concrete cylinders were tested according to the ASTM C39/C39M-18.

4.3.1.3 Model geometry and instrumentation

As mentioned earlier, sand was used as the: (1) backfill material behind the retaining wall, and (2) foundation soil under the heel of the retaining wall (Figures 4.4 and 4.5). The sand was placed in a box (1300 mm in length, 500 mm in width, and 1565 mm in height) that was made of wood. The soil below the foundation was a dense layer with a relative density of 80 %. The height of the foundation layer was 915 mm while the height of the backfill behind the stem was 650 mm for an overall height of 1565 mm. The retained backfill extended behind the wall for 1300 mm, which was two times the RW height. The backside of the box was made of a flexible material (reinforced rubber sheet) in order to prevent soil confinement. One side of the box's wall was made of plexiglass in order to capture the movement of the soil-RW model using a high definition camera during the testing event.

Furthermore, the soil in the box was surrounded by an impermeable membrane to avoid water leakage. The restricted testing area was considered during the selection of the model geometry.

The ProAnalyst software (software guide) was used to capture the soil particles' movement and track the transient and permanent displacements of the wall. Two high definition cameras were used in this experimental program. These cameras, equipped with a digital high-speed imaging system, were capable of recording thousands of high-resolution frames per second. Yellow beads were added to the sand particles facing the plexiglass to track the movement of these particles during the test. Soil model preparation was conducted at the Blast Research Laboratory of the University of Ottawa.

Figure 4.2: Reinforced concrete retaining wall
Shown in the image is the process of casting for the stem. The heel of the retaining wall had already been cast.

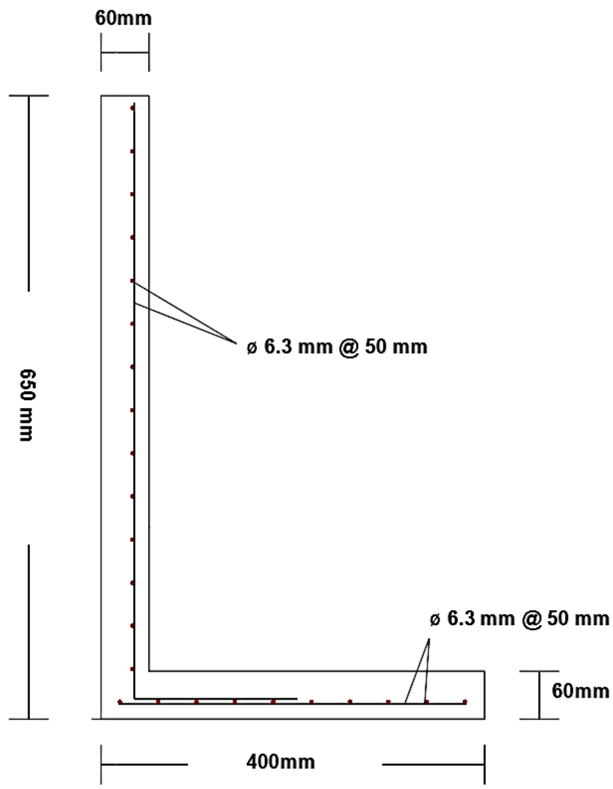

Figure 4.3: Details of retaining wall reinforcement

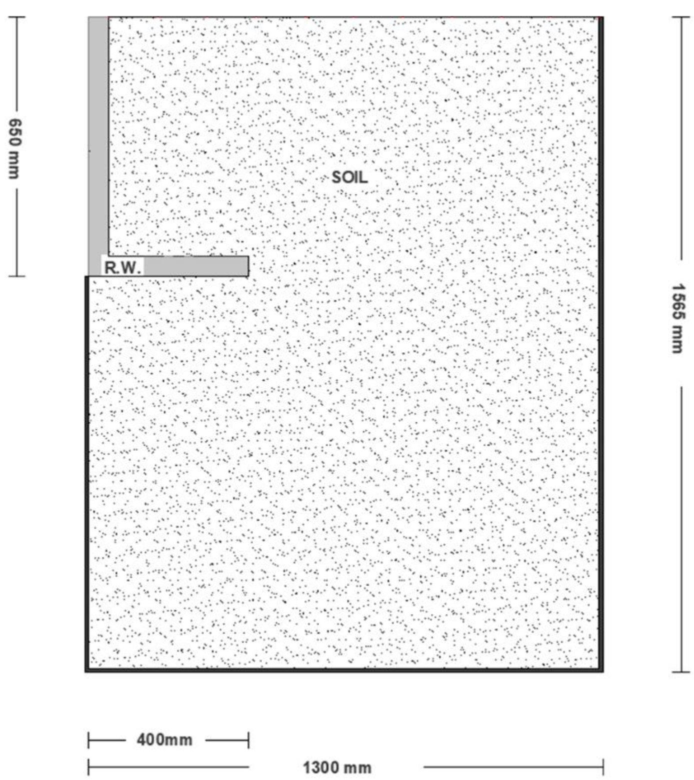

Figure 4.4: Soil-Retaining Wall model (schematic)

4.3.2 Test Procedure

The test was devoted to studying the influence of various relative densities, degrees of saturation of backfill and live load surcharge on the dynamic response of soil-RW model when subjected to different blast load intensities. For every test conducted in this study, the system (RW and soil) was subjected to a single blast shot.

4.3.2.1 Relative density

Three sand samples with various relative densities (loose, medium, and dense) were subjected to pressure simulating a blast-induced shock wave. Relative densities of 30 %, 45 %, and 65 % were used for loose soil, medium soil, and dense soil, respectively. Table 4.3 shows the state of granular soils at different ranges of relative density.

The space between the bottom of the wooden box and the bottom of the RW footing was filled with 200 mm thick successive layers of sand. Each sand layer was densified using a mechanical vibration technique (modified electrical drill) to reach a relative density of 80%. The backfill was also formed by pouring sand in equal successive layers of 200 mm thick. Each sand layer was manually compacted to the desired relative density. Figure 4.5 shows the steps for the box preparation and soil compaction.

Once compaction was completed, three samples from each layer were taken and tested to confirm that the required relative density was obtained. This process was repeated for each layer. A vibrating table compaction test was conducted to determine the optimum moisture content and maximum dry density. The test was run in accordance with the ASTM D4253-16. A water content of 2 – 3 % was chosen to reach the required relative density in the foundation and the backfills (loose, medium, and dense).

Table 4.3: General correlation between relative density and denseness of a cohesionless soil (Das, 2016)

Relative density, Dr (%)	**Description**
0-15	Very loose
15-35	Loose
35-65	Medium
65-85	Dense
85-100	Very dense

4.3.2.2 Degree of saturation

Three sand backfill samples with different saturation degrees (100 %, 85 %, and 13 %) were tested. To achieve the fully saturated condition, the ground water table was maintained at the surface level. The soil is considered partially saturated when the degree of saturation is around 85 %. To satisfy this condition, the ground water table was kept at 250 mm below the top surface of the backfill. This means, the layer below the water table was saturated and the layer above the water table was partially saturated. When the degree of saturation is 0%, the soil reaches the dry condition. However, dry backfill is not applicable or common in the field. Therefore, in this study, moist backfill with a water content of 2% (corresponding to a degree of saturation of 13 %) was used instead of the dry condition. The degree of saturation of moist soil was calculated by dividing the volume of water by the volume of void in the soil. The volume of void can be determined by knowing the moist and dry densities of the sand while the volume of water can be calculated from the water content and specific gravity of the sand (Das, 2016 and Craig, 2004). The backfill was compacted to meet in-situ dry density (Federal Highway Administration, FHWA, specifications, 2008 and Morris and Delphia, 1999). The dry density of the backfill was 16 kN/m^3, which was within the acceptable range recommended by the above-mentioned specifications. The degree of saturation of the foundation was 100 % when the degree of saturation of the backfill was 100 %

and 85 %. On the other hand, the degree of saturation of the foundation was 13 % when the degree of saturation of the backfill was 13 %.

4.3.2.3 Blast loads intensity

The influence of blast load intensity on the behaviour of the retaining wall backfill was investigated. Three driver pressures were adopted in this study. A driver pressure of 137 kPa resulted in a maximum reflected pressure (Pr) of 26 kPa. The second driver pressure was equal to 241 kPa, which resulted in a maximum Pr of 47 kPa. Lastly, a driver pressure of 379 kPa was used to generate a maximum Pr of 71 kPa. The reflected pressures were selected to cause a different level of damage on the RW-soil system, ranging from elastic to full plastic failure. However, full plastic failure was not reached in this experiment (more details in the results section). Furthermore, a scaling chart (Cormie, Mays, and Smith, 1995) was utilized to match the reflected pressures used in this paper to a specific field blast parameter. For example, detonation of a 227 kg TNT hemispherical charge at a distance of 36 m produced a reflected pressure of 71 kPa.

4.3.2.4 Live load surcharge

Lateral earth pressure, lateral hydrostatic pressure, and vertical traffic loads that generate supplemental lateral load on the RW are the three major loads acting on a RW. Highway traffic load equivalent surcharge can be neglected if the traffic load location is far enough from the wall (Chen and Duan, 2014). As per AASHTO design codes (AASHTO 2002, 2012), live load surcharge can be equivalent to a soil height of 600 mm placed on the top level of the wall.

To address the influence of the live load surcharge on the behaviour of RW backfill in this study, 60 mm (wall is modeled at the 1/10th scale) of soil was added to the top level of the backfill. This added layer was compacted to achieve the in-situ required density.

Figure 4.5: Steps of box preparation and soil compaction

The box was built in stages. **Step 1** shows the top view of the box, representing the first stage of the box. The height of this portion of the box was 400 mm. The sand for the foundation layer had been compacted using a mechanical vibration technique (modified electrical drill). **Step 2** displays the completion of the side of the box where the plexiglass is located. **Step 3** presents the back view of the specimen. The box was moved in front of the shock tube and was ready to be filled with the backfill layers.

4.3.3 Test Setup

4.3.3.1 Soil-retaining wall model

All tests in this study were conducted using the shock tube at the Blast Research Laboratory of the University of Ottawa. The test specimen (soil-RW model) was placed at the centre of the shock tube's mouth. The rest of the shock tube mouth was covered with a very stiff steel plate. The test specimen consisted of a reinforced concrete retaining wall and a box filled with sand. In order to prevent confinement, the backside of the box was made of a flexible membrane (reinforced rubber sheet). The top of the box was left open to allow soil filling and compaction. The RCRW was placed on the side of the box that faced the shock tube, as shown in Figure 4.5. The test specimen was attached to the shock tube by straps to prevent the specimen from moving away from the shock tube during the blast test. The blast pressure formed by the shock tube was transferred directly to the test specimen, and it was uniformly distributed over the area of the RCRW. The shock tube was controlled by a firing system to start the test. Figure 4.6 shows the test setup adopted in this study.

In-situ, soils usually experience a stress history that can change the soil structure. Many factors, such as climatic environment changes or man-made construction, can lead to a changing stress state or stress history in soils. A total stress ratio (TSR) is used as a measure of the stress history of compacted soil (Nishimura et al., 1999). TSR is the ratio of the compaction pressure to the current confining pressure.

In order to limit the effect of stress history, backfill material was removed from the box after each test. The sand was then mixed and reused to refill the box. The backfill material was compacted to meet the required compaction level for each test.

The soil under the wall's footing level (heel) was not disturbed by the blast shocks applied; thus, with the exception of the loose backfill condition test, the soil was not compacted after each test. Once the loose backfill condition test was carried out, the RC wall was removed, and portions of the box were disassembled. The soil below the heel was dug out, mixed on a tarp, then put back and compacted again to reach the required relative density. Prior to the excavation of the foundation layers, the sand was tested to determine if there was any change in the soil's relative density below the RW. The results showed that the TSR was 1.02, which was within the acceptable range, indicating that the changes were insignificant.

4.3.3.2 Blast loading protocol

Prior to testing, the specimen was attached firmly to the shock tube, using three straps (Figure 4.7). The two high-speed video cameras were set up and connected to the data acquisition device and a laptop was used for video monitoring. A trigger signal was induced to confirm that the data acquisition device and cameras were recording at the same time. The driver and spool sections of the shock tube were then filled up to the required level of pressurized air. The test started by draining pressure from the spool section, which led to an imbalance in pressures on both sides of the aluminum diaphragm. As a result, the aluminum diaphragm was ruptured, and the pressurized air was passed at a very high speed towards the expansion shock tube nozzle.

4.3.3.3 Data acquisition

The data acquisition device used in this research was two digital oscilloscopes readings at 100,000 Hz (samples per second). Two channels were used to record reflected pressure. The sensors were responsible for measuring the reflected pressure located at the side and bottom of the shock tube's mouth.

Figure 4.6-1: Test setup (a) covering the shock tube's mouth with a stiff plate; (b) placing the test specimen at the centre of the shock tube; (c) fastening the test specimen to the shock tube using straps

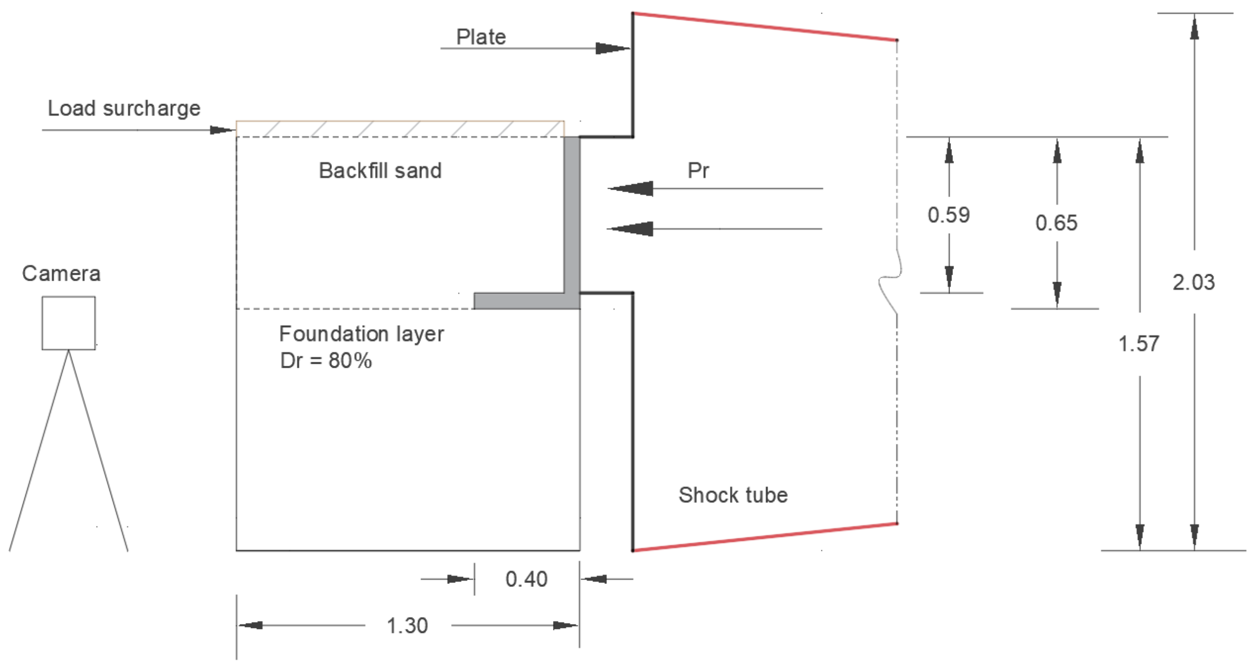

Figure 4.6-2: Test setup and preparation; dimensions in m (schematic)
Figure 4.6: Test setup

Figure 4.7: Test preparation at the Blast Research Laboratory of the University of Ottawa

The test specimen was placed in front of the shock tube mouth, fastened with straps to prevent any movement during the blast test. The first camera was facing the side of the box, where the plexiglass was located, to capture sand particle movement. The second camera was facing the back of the specimen.

4.3.3.4 Shock tube

The shock tube consists of four main sections (Figure 4.8). The driver and the spool are the first and second sections, respectively. These are the sections in which the shock energy is built-up and the firing action occurs. The length of the driver section ranges between 305 mm and 5185 mm in 305 mm increments. Based on the required peak reflected pressure and total impulse, a driver length is selected. The driver length has a minor influence on the reflected pressure but has an effect on the impulse (Lloyd, 2010). Since the impulse should be given equal consideration as the reflected pressure (Mays and Smith, 1995), in this experiment, the length of the driver section was kept at 2743 mm. The blast wave formed in the driver section propagates and expands through the expansion section, which starts from 597 mm in diameter and ends with the square test area of 2033 mm by 2033 mm. The test specimen was attached to the opening of the steel plate located at the front of the shock tube. The length of the expansion section is 7 m. The shock tube is operated manually by incrementally increasing the driver pressure and the spool pressure to the required level and then trigger firing by draining pressure from the spool section to cause the aluminum foil diaphragms to rupture.

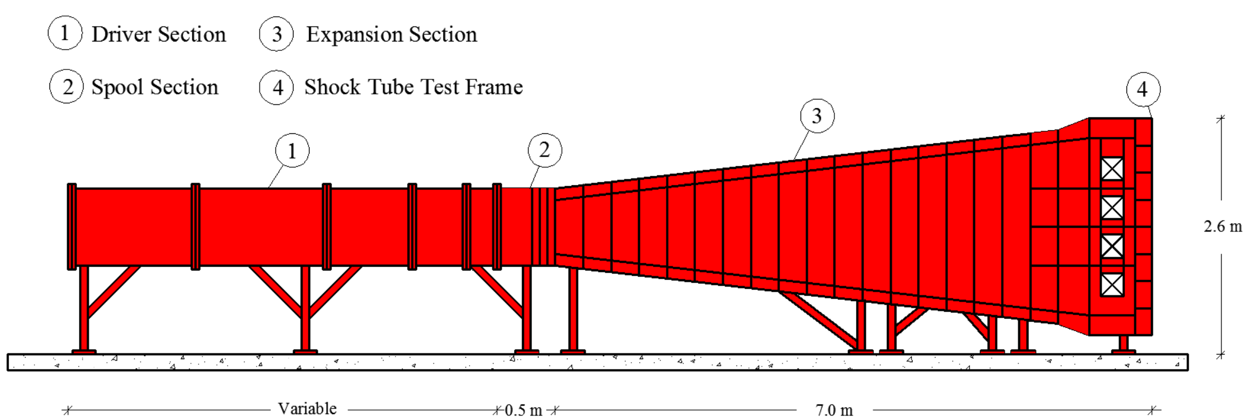

Figure 4.8: Shock tube sections; schematic (Kadhom, 2016)

4.4. Results and Discussion

4.4.1 Modes of Wall Movement

The magnitude and distribution of lateral earth pressures on RW are based on the nature of yielding of the wall. There are three possible modes of wall yielding (soil-structure interaction) for the development of an active state (Das, 2011). These modes are the rotation about the bottom, rotation about the top, and translation. In this paper, the lateral displacement of the RW due to blast loading was investigated.

4.4.1.1 Effect of backfill relative density

Lateral displacement time histories for the wall and backfill in loose, medium, and dense conditions are represented in Figure 4.9. The figure presents the horizontal displacements for the top of the RW, mid-height of the RW, and three layers of the backfill. The specimen was subjected to a maximum reflected pressure of 47 kPa and a reflected impulse over the positive phase of 509 kPa.ms.

For loose backfill, maximum and residual (permanent) horizontal displacements at the top of the RW was -31 mm and -18.6 mm, respectively, and the maximum response occurred at a time greater than the positive phase duration (Figure 4.9a). Displacements of backfill behind the wall had the same trends. The largest maximum and residual displacements (-53 mm and -29.6 mm, respectively) were observed at the top layer of the backfill (SFL1: soil first layer and its position 20 mm behind the RW and 40 mm below the backfill surface) as shown in Figure 4.9a. The soil in this location (SFL1) was fully disturbed, and the particles were rearranged (Figure 4.10). Lateral compressive force induced by blast loading led to the formation of passive pressure in the backfill and resulted in permanent soil displacement. A translation response mode was evident in this test. The wall slid about 25 mm toward the backfill. As mentioned earlier in section 4.2, the passive state is reached when the relative movement (Δ/H) for loose sand is equal to 0.04 (Table 4.1). Though Shamsabadi et al., (2007) recommended that a relative movement of 0.05 is required in order to reach passive earth pressure when sand backfill is used. Thus, the passive state was reached in this test since the relative movement reported was equal to 0.048. Therefore, after this test, the RCRW was removed, and portions of the box were disassembled to limit the effect of stress history (refer to section 4.3.3.1 for the details).

Figure 4.9b depicts the maximum and residual displacements for the RW and backfill in the medium condition. The maximum and residual displacement values for medium dense backfill were lower than equivalent values from loose backfill but possessed the same trends as the loose backfill. Maximum and residual horizontal displacements at the top of the RW were -29 mm and -2.3 mm, respectively. Maximum and residual displacements at the top layer of the backfill (SFL1) were -20.5 mm and 2.2 mm, respectively. The lateral displacement for the mid-height of the wall was also determined from this test. Maximum and residual displacements at the mid-height of the wall were -17.5 mm and 0.7 mm, respectively. The difference between residual displacements at the top and the mid-height of the wall was -3 mm. The results showed that the wall tilted toward the backfill by 3 mm. This relatively small rotation about the bottom was the mode of failure of the wall in this test. However, this permanent displacement is very small and can be ignored. The relative movement of the wall for this test was equal to 0.044, and thus, a passive state was reached.

Figure 4.9c presented the RW movement when dense backfill was used. Maximum and residual lateral displacements at the top of the RW were -9 mm and -1 mm, respectively. Maximum and residual displacements at the top layer of backfill (SFL1) were -12.6 mm and 1.5 mm, respectively. Maximum and residual displacements at the mid-height of the wall were -11.4 mm and 0.1 mm, respectively. These values were lower than the equivalent values obtained from loose and medium conditions (Figure 4.9). The relative movement of the wall was equal to 0.014, which is less than 0.02 (Table 4.1) and therefore, the passive state was not reached. It can be concluded that when dense sand was used, no permanent deformation was noticed.

Based on the abovementioned results, it was noticed that the RW with loose sand backfill condition had the largest deformations in comparison with medium and dense conditions. Soils have the tendency to decrease in volume when subjected to shearing stress. Loose sand contains higher void ratio than medium and dense conditions. Therefore, applying compressive load to the loose soil leads to rearrangement in the soil particles and to reduced space in the voids. As a result, soils with higher void ratio are susceptible to larger deformations.

4.4.1.2 Blast loads intensity effect

In this part of the study, the specimen was subjected to various blast load intensities (26 kPa, 47 kPa, and 71 kPa). Horizontal displacements time histories for the wall and backfill with different blast load intensities are shown in Figure 4.11.

Figure 4.11a shows the maximum and residual displacements for dense backfill when subjected to a reflected pressure of 26 kPa. It was noticed that maximum, and residual displacements at the top of the RW was -7 mm and -1.5 mm, respectively. Maximum and residual displacements at the top layer of backfill (SFL1) were -5.3 mm and 3.6 mm (Figure 4.11a). The relative movement of the wall was equal to 0.01.

Figure 4.9c depicts the maximum and residual displacements for dense backfill when subjected to a reflected pressure of 47 kPa (refer to the section above, 4.4.1.1, for the details).

When the specimen was subjected to a reflected pressure of 71 kPa, maximum and residual displacements at the top of the RW was -11.3 mm and 0.5 mm, respectively. The maximum and residual displacements at the top layer of backfill (SFL1) were -9 mm and 3 mm (Figure 4.11b). The relative movement of the wall was equal to 0.017.

It can be seen that the passive state was not reached in RW with dense backfill, regardless of the blast load intensities that were used in this study.

It was observed that under the same relative density of the backfill, increasing the blast load intensity resulted in greater deformations at the wall and the backfill. This can be explained by the fact that increasing the intensity of blast load led to the generation of higher compressive wave velocity and thus higher shear stress in the sand (Shim, 1995; Smith and Hetherington, 1994).

4.4.1.3 Degree of saturation effect

The lateral displacements time histories for saturated and partially saturated backfills under a reflected pressure of 47 kPa are depicted in Figure 4.12.

Figure 4.12a displays maximum and residual displacements for saturated backfill. The maximum and residual lateral displacements at the top of the RW were -6.6 mm and -0.1 mm, respectively. The maximum and residual displacements at the top layer of the backfill (SFL1) were -5.4 mm and -0.3 mm. The relative movement of the wall was equal to 0.01. The reduction in permanent deformations of saturated backfill was due to the fact that pore water pressure was exerted on the wall and provided extra support to the wall against the passive pressure.

Figure 4.12b exhibits maximum and residual displacements for partially saturated backfill. The maximum and residual lateral displacements at the top of the RW were -8.7 mm and -0.71 mm, respectively. The maximum lateral displacements behind the RW for SFL1, SSL2, and STL1 were -7.9 mm, -5.4 mm, and -5.3 mm. The relative movement of the wall was equal to 0.013.

The passive state was not reached for the RW with saturated and partially saturated backfills.

4.4.1.4 Live load surcharge effect

Figure 4.13 shows the wall movement under the application of a live load surcharge when subjected to a reflected pressure of 47 kPa. The maximum and residual lateral displacements at the top of the RW was -5.2 mm and -0.15 mm, respectively. Maximum and residual displacements at the top layer of backfill (SFL2) were -3.6 mm and -1 mm. Maximum and residual displacements at the mid-height of the wall were -3 mm and -1.5 mm, respectively. The relative movement of the wall was equal to 0.008. The lateral displacements had lower values compared with corresponding values where no live load surcharge was applied (Figure 4.9c). The live load surcharge provided extra support to the wall and prevented the movement of the wall. Once the blast load decayed, the RW returned to its original position, which can be confirmed by the residual displacements of the wall (Figure 4.13). Based on the definition of the Equation of Motion of an undamped system ($m\ddot{u} + ku = F$), if the external force is constant, an increase in the mass of the backfill leads to a reduction in the displacements.

Figure 4.14 displays the lateral movements at the top of the RW for all test conditions. It can be seen that the maximum displacements were experienced when loose and medium backfill were used. When the other varying factors remain unchanged, the lateral displacements for loose and medium backfill conditions were three times greater than the lateral displacement for dense backfill. Loose sand exhibits higher porosity in comparison to dense sand. When blast pressure was applied on the RW with low relative density backfill, the soil particles behind the wall were compacted and this resulted in higher horizontal deformations. On the other hand, when a live load surcharge was applied, a reduction in wall movement was observed, and lower displacement was noticed.

In general, the results showed that relative density, blast load intensity, degree of saturation, and live load surcharge had an impact on the modes of wall rotation. An increase in backfill density led to a reduction in wall movement while increasing the blast load resulted in an increase in wall movement. Furthermore, yielding of the wall was reduced when fully saturated backfill and live load surcharge conditions were applied. Under the same load conditions, dense backfill provided more support to the wall and thus, reduced the wall movement. Distinct failure mechanisms were observed for loose backfill conditions that led to large uniform deformations.

It can be seen that there were no “rigid block” responses in the loose backfill mass (Figure 4.9); however, the results indicated that a uniform acceleration distribution existed within the backfill (Figure 4.18a), which corresponds to a uniform stress field, as assumed in the pseudo-static analyses.

As mentioned earlier, the magnitude and distribution of lateral earth pressures on the RW are affected by wall’s movement. In this study, the relationship between wall relative movements and mobilized earth pressure coefficients was found (Figure 4.15). The dynamic earth pressure coefficient (ΔK_d) was calculated using the dynamic thrust:

$$\Delta K_d = 2P_d/\gamma H^2 \tag{4.1}$$

In this figure, the dynamic earth pressure coefficient is represented as a function of the wall relative movement. The best-fitting equation for the data was the Logarithmic model:

$$K_d = 0.543 ln\left(\frac{\Delta}{H}\right) + 3.9199 \tag{4.2}$$

An increase in the dynamic earth pressure coefficient was observed with an increase of the wall relative movement (Figure 4.15). As the relationship between the ΔK_d and the density is inversely proportional (Equation 4.1), an increase in the density led to a decrease in the ΔK_d and thus, a reduction in wall movement.

The above-obtained model had the similar trends as the LSH model (mobilized logarithmic spiral, LS, failure coupled with modified hyperbolic, H, abutment-backfill stress-strain behavior) that was predicted by Shamsabadi et al., 2007.

The prediction of the residual displacements and failure modes of a RW under dynamic loads is considered a challenge in analytical and design methods. If the residual displacements and failure mechanism of a RW are known, using performance-based design concepts, engineers would be able to base their analysis and design on performance level and desirable failure patterns (Deyanova et al., 2016).

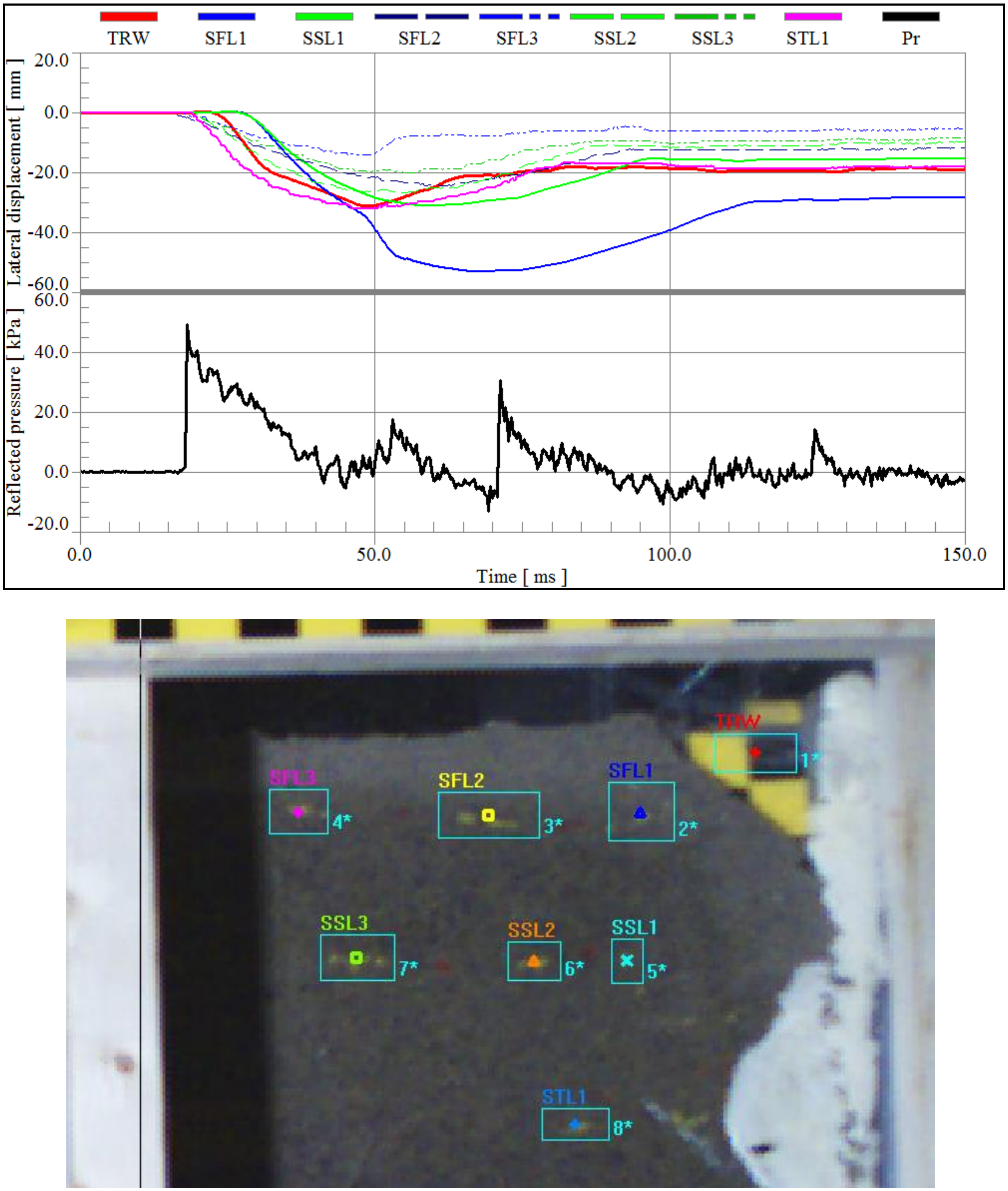
TRW
SFL1
SSL1
SFL2
SFL3
SSL2
SSL3
STL1
Pr
Lateral displacement [mm]
Reflected pressure [kPa]
Time [ms]
20.0
0.0
-20.0
-40.0
-60.0
60.0
40.0
20.0
0.0
-20.0
0.0
50.0
100.0
150.0
TRW
SFL3
SFL2
SFL1
SSL3
SSL2
SSL1
STL1
1*
2*
3*
4*
5*
6*
7*
8*

(a)

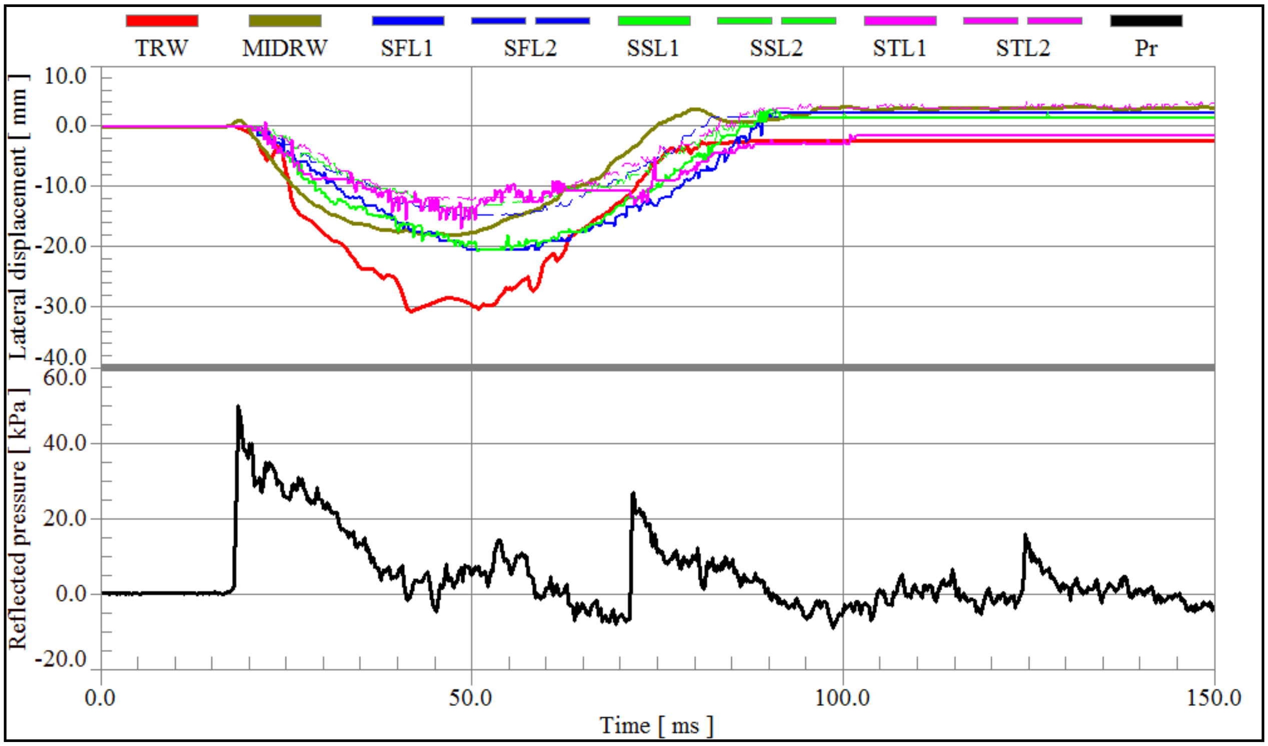

TRW
MIDRW
SFL1
SFL2
SSL1
SSL2
STL1
STL2
Pr
Lateral displacement [mm]
10.0
0.0
-10.0
-20.0
-30.0
-40.0
Reflected pressure [kPa]
60.0
40.0
20.0
0.0
-20.0
0.0
50.0
100.0
150.0
Time [ms]

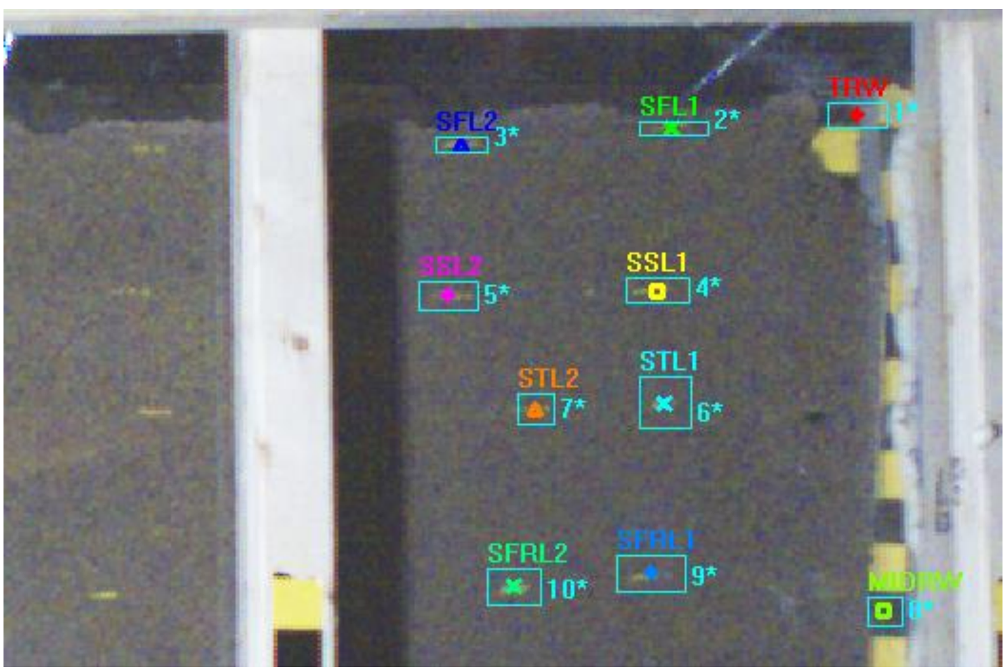

SFL2
3*
SFL1
2*
TRW
SSL2
5*
SSL1
4*
STL2
7*
STL1
6*
SFRL2
10*
SFRL1
9*
MIDRW

(b)

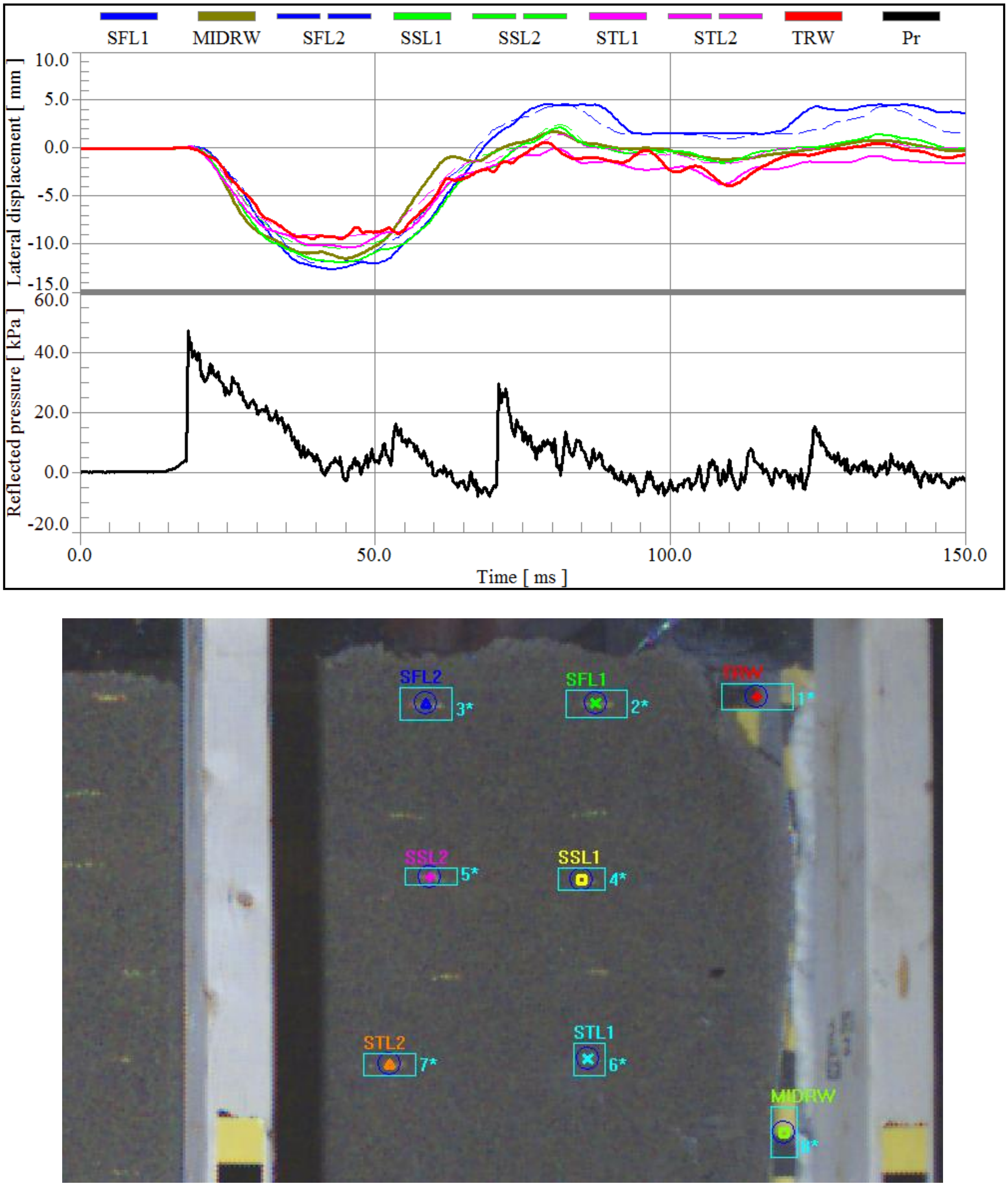

(c)

Figure 4.9: Lateral wall and backfill displacements time histories for; (a) loose, (b) medium, and (c) dense conditions

TRW: top of retaining wall; SFL: soil first layer; SSL: soil second layer; STL: soil third layer; SFRL: soil fourth layer; MIDRW: mid height of retaining wall; Pr: reflected pressure.

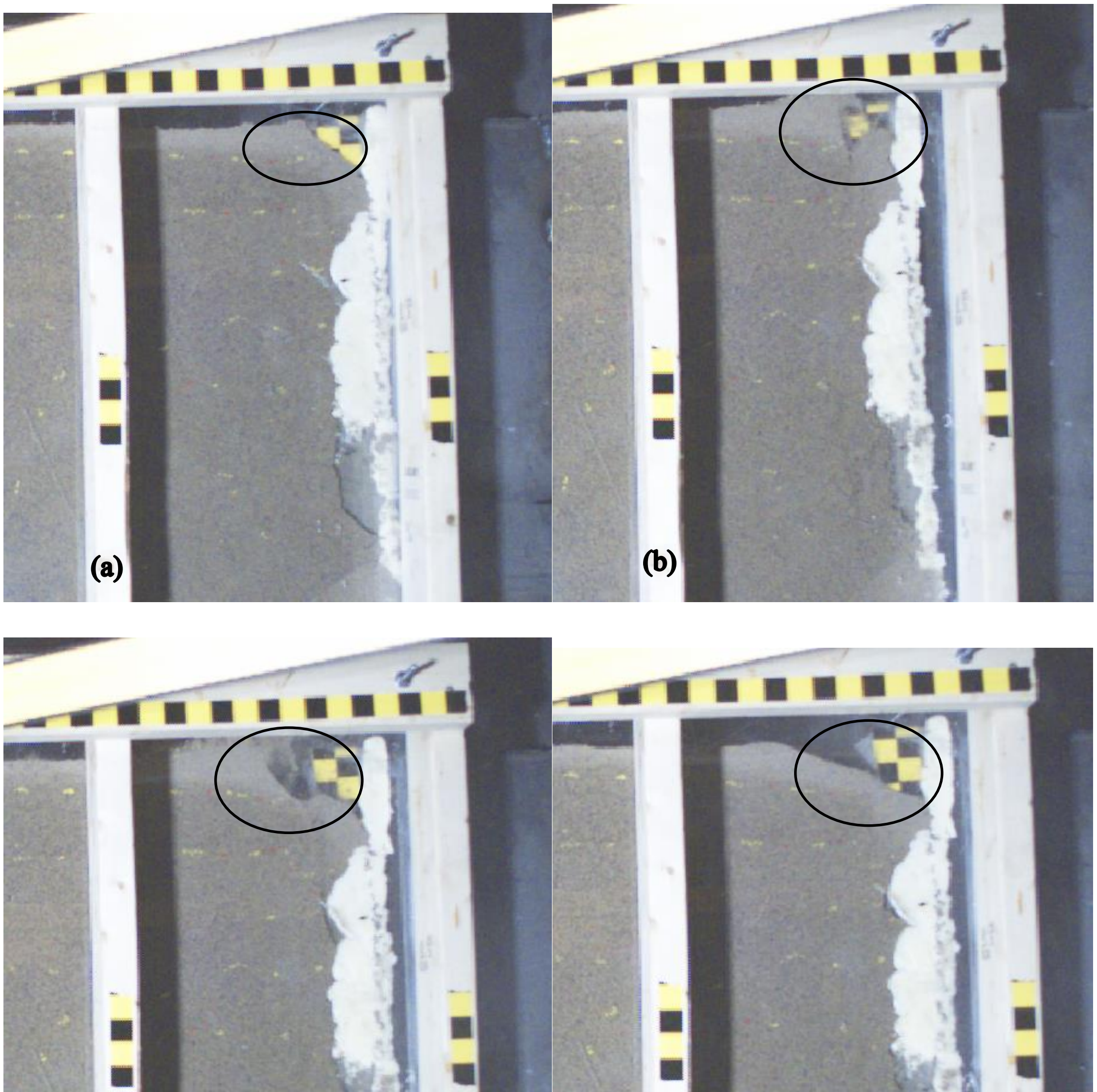

Figure 4.10: Disturbance of soil behind the RW (SFL1) for loose backfill condition; (a) prior to the application of blast load testing, (b) during the test, (c) during the test, (d) at the end of the test. The circle shows the location where the disturbance occurs

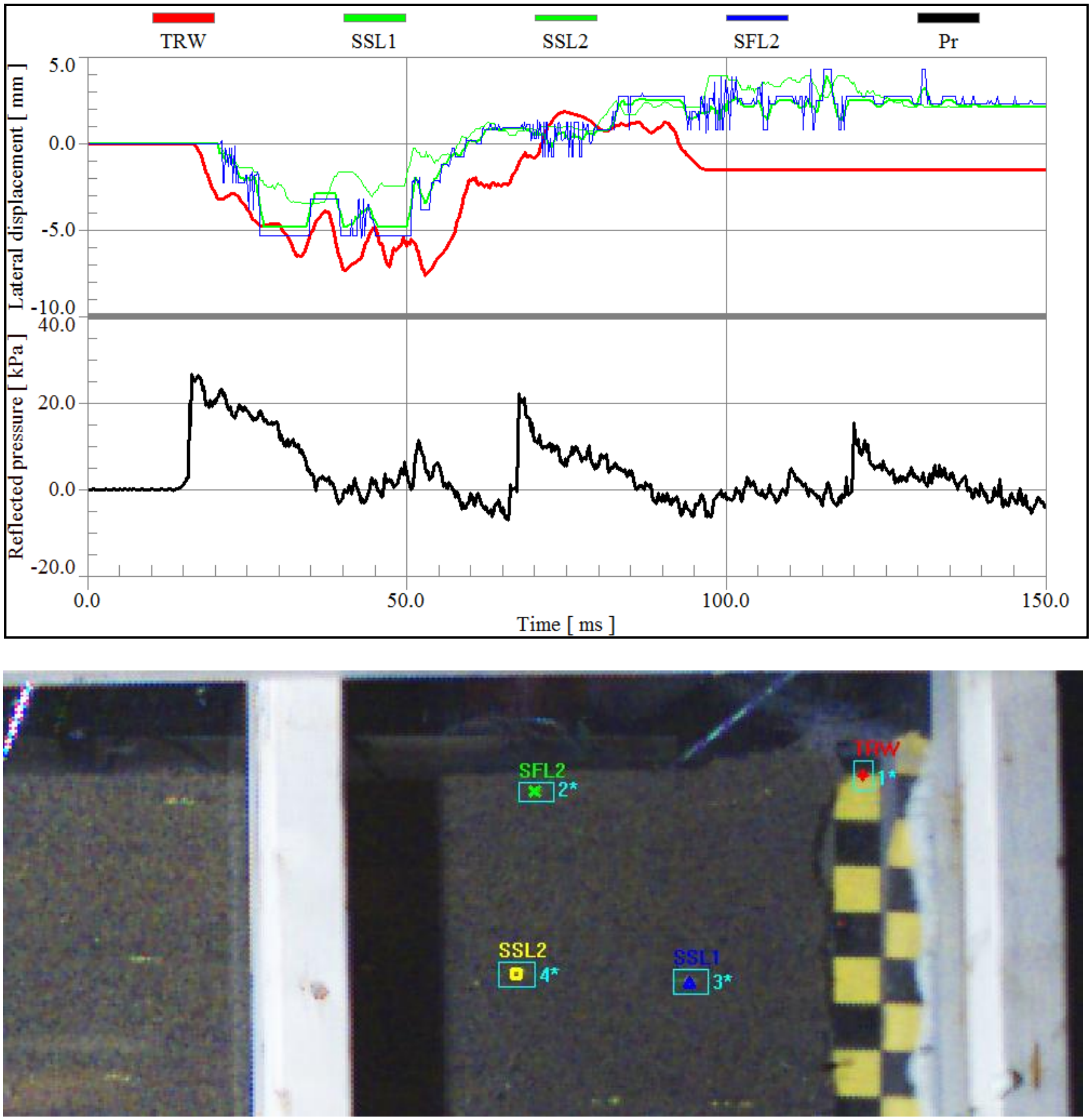

TRW
SSL1
SSL2
SFL2
Pr
5.0
0.0
-5.0
-10.0
Lateral displacement [mm]
40.0
20.0
0.0
-20.0
Reflected pressure [kPa]
0.0
50.0
100.0
150.0
Time [ms]
TRW
1*
SFL2
2*
SSL2
4*
SSL1
3*

(a)

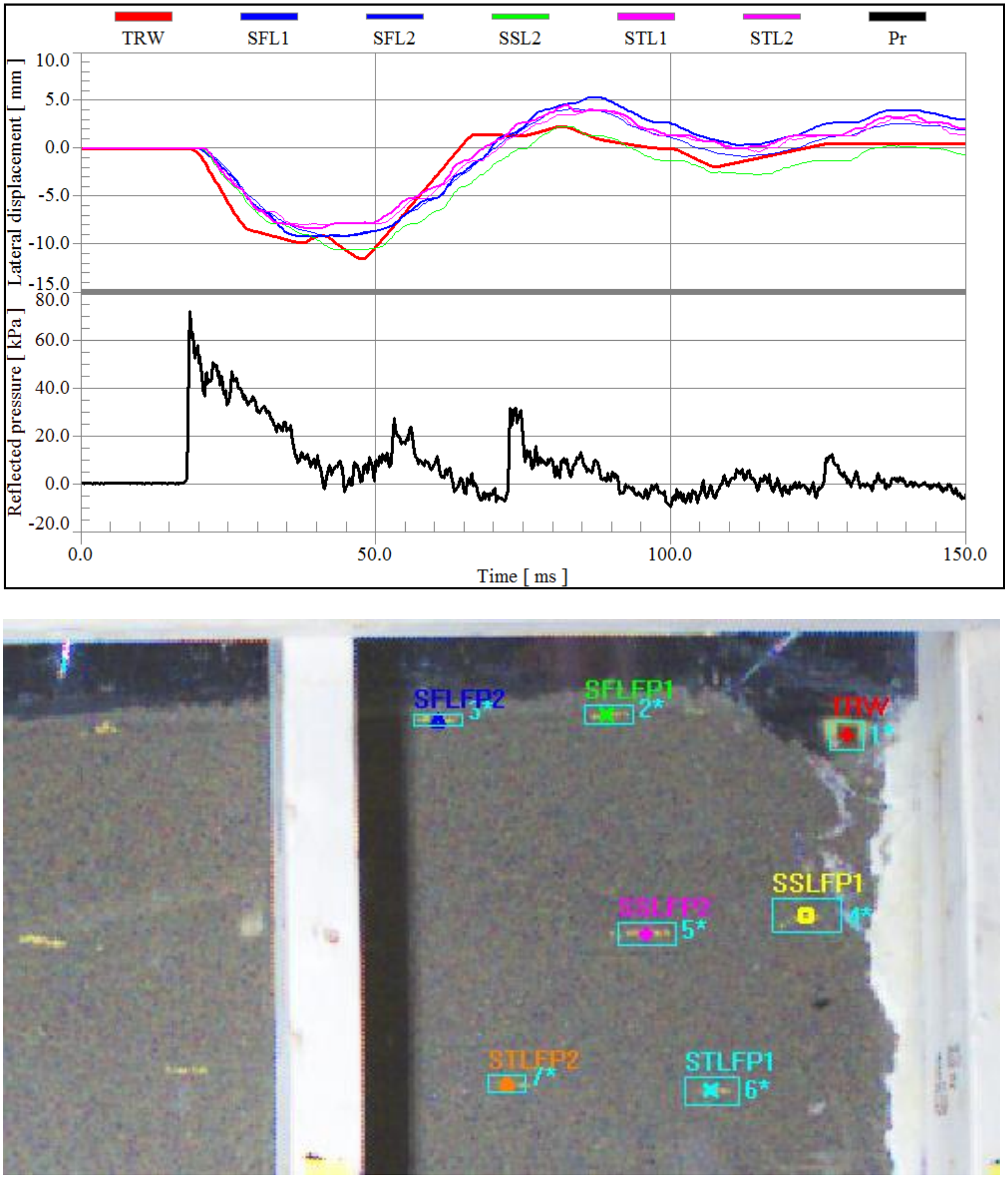

(b)

Figure 4.11: Lateral wall and backfill displacements time histories for; (a) reflected pressure of 26 kPa, (b) reflected pressure of 71 kPa

TRW: top of retaining wall; SFL/SFLFP: soil first layer; SSL/SSLFP: soil second layer; STL/STLFP: soil third layer; Pr: reflected pressure.

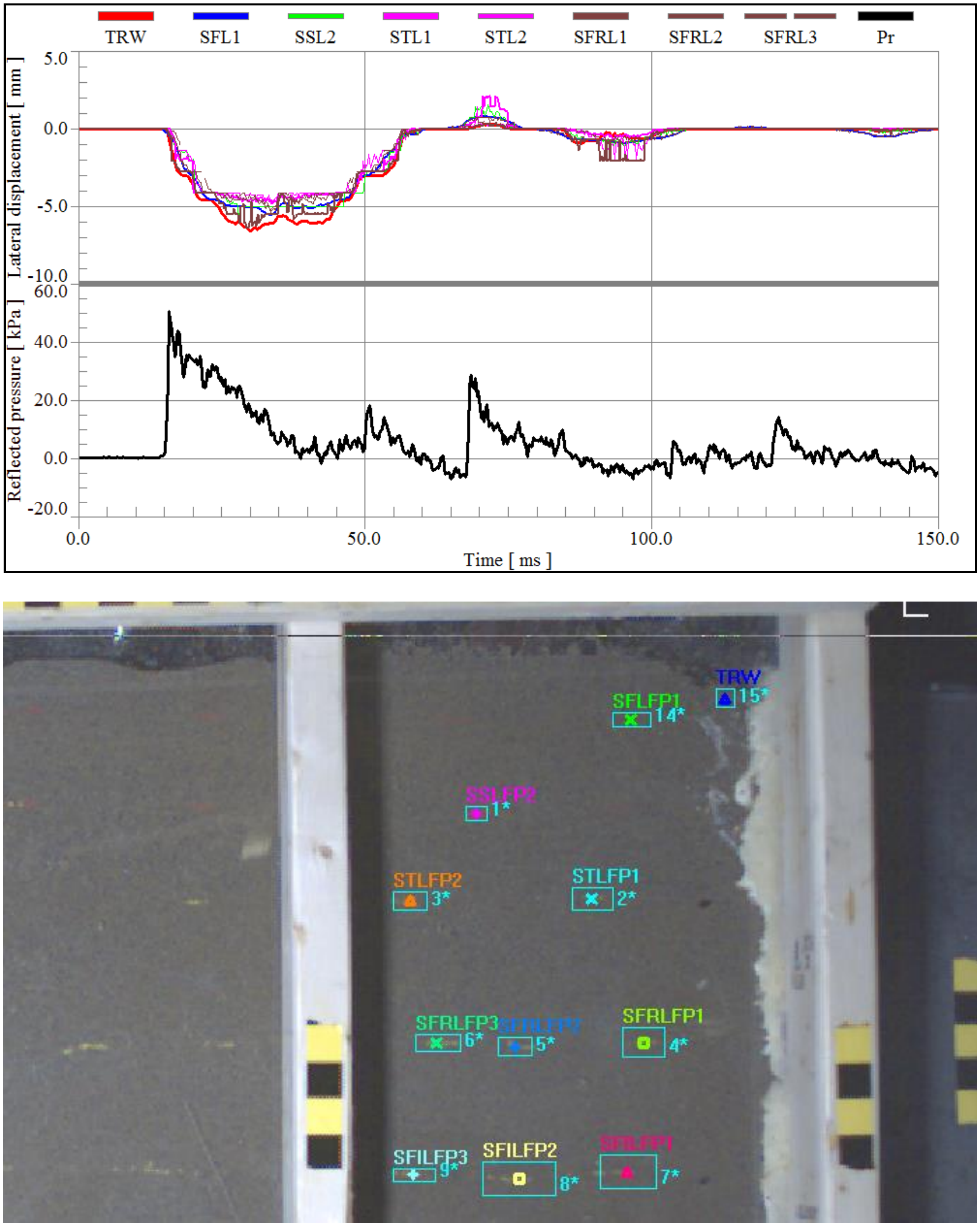
TRW
SFL1
SSL2
STL1
STL2
SFRL1
SFRL2
SFRL3
Pr
Lateral displacement [mm]
5.0
0.0
-5.0
-10.0
Reflected pressure [kPa]
60.0
40.0
20.0
0.0
-20.0
0.0
50.0
100.0
150.0
Time [ms]
TRW
15*
SFLFP1
14*
SSLFP2
1*
STLFP2
3*
STLFP1
2*
SFRLFP3
6*
SFRLFP2
5*
SFRLFP1
4*
SFILFP3
9*
SFILFP2
8*
SFILFP1
7*

(a)

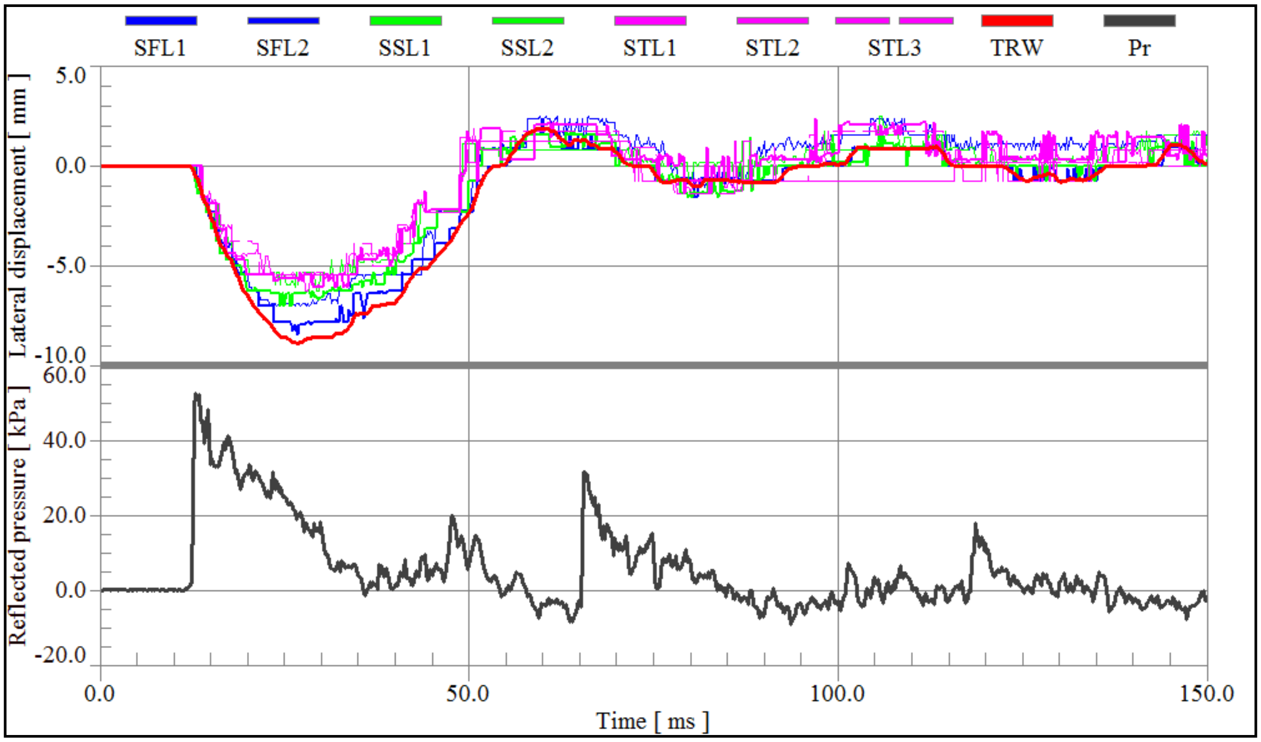

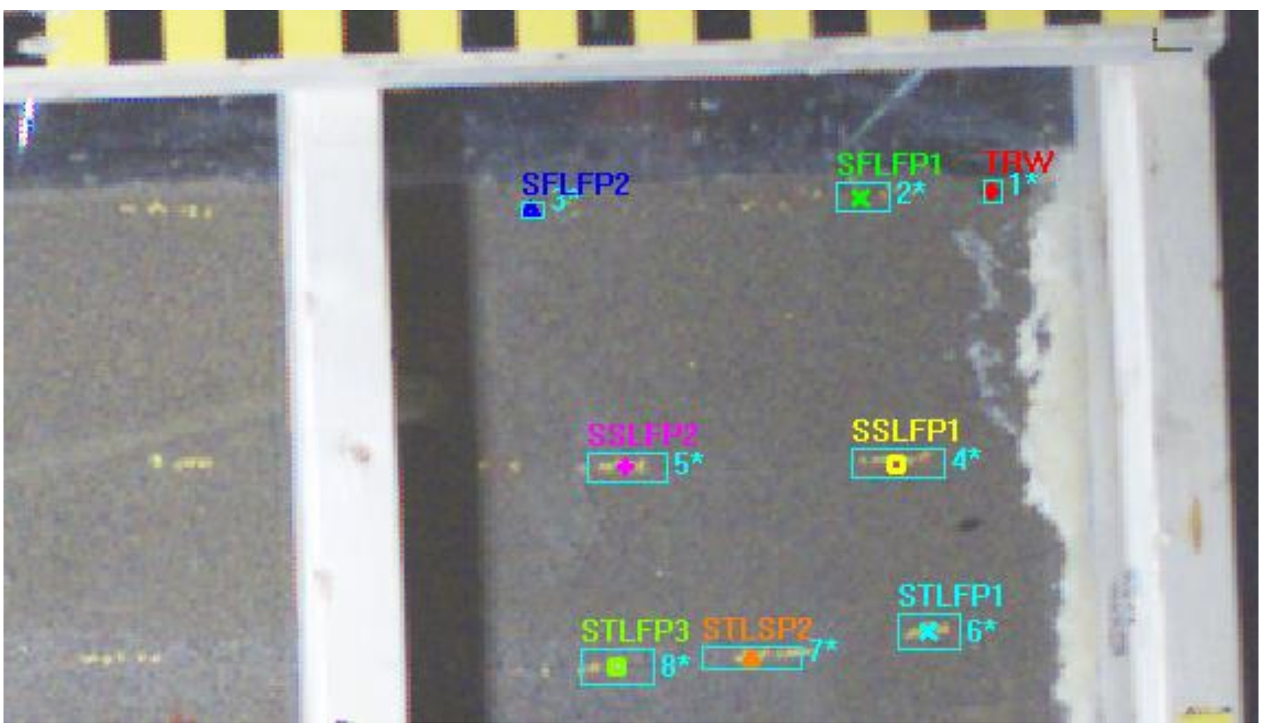

(b)

Figure 4.12: Lateral wall and backfill displacements time histories for; (a) saturated backfill, (b) partially saturated backfill

TRW: top of retaining wall; SFL/SFLFP: soil first layer; SSL/SSLFP: soil second layer; STL/STLFP: soil third layer; SFRLFP: soil fourth layer; SFILFP: soil fifth layer; Pr: reflected pressure.

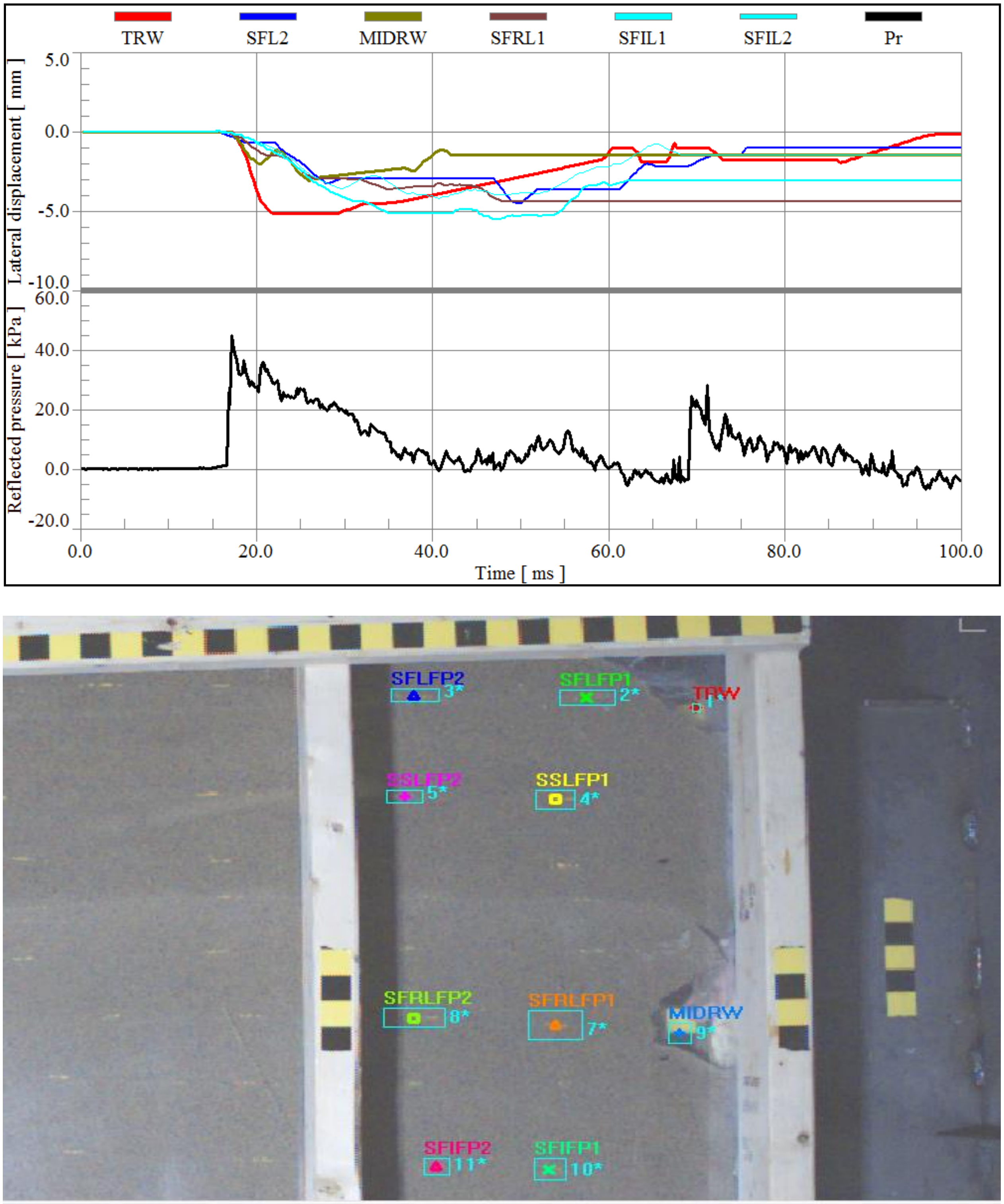

Figure 4.13: Lateral wall and backfill displacements time histories for live load surcharge TRW: top of retaining wall; SFL/SFLFP: soil first layer; SSL/SSLFP: soil second layer; STL/STLFP: soil third layer; SFRLFP: soil fourth layer; SFILFP: soil fifth layer; Pr: reflected pressure.

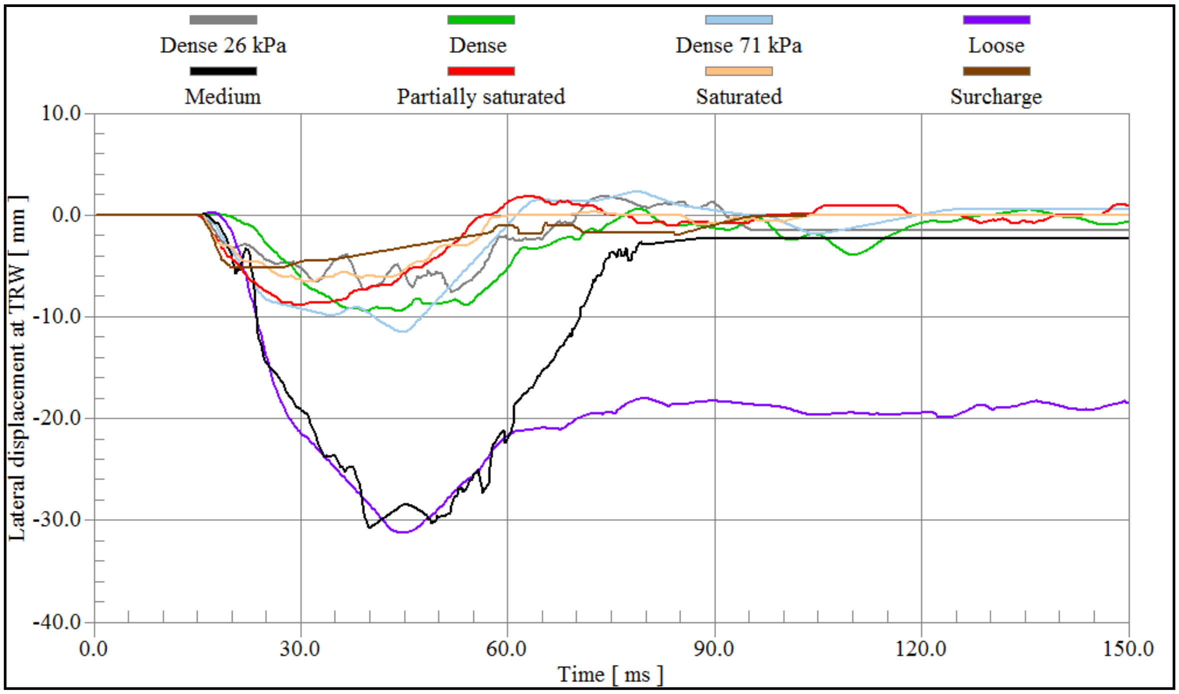

Figure 4.14: Lateral displacement time histories at the top of the RW for all test conditions

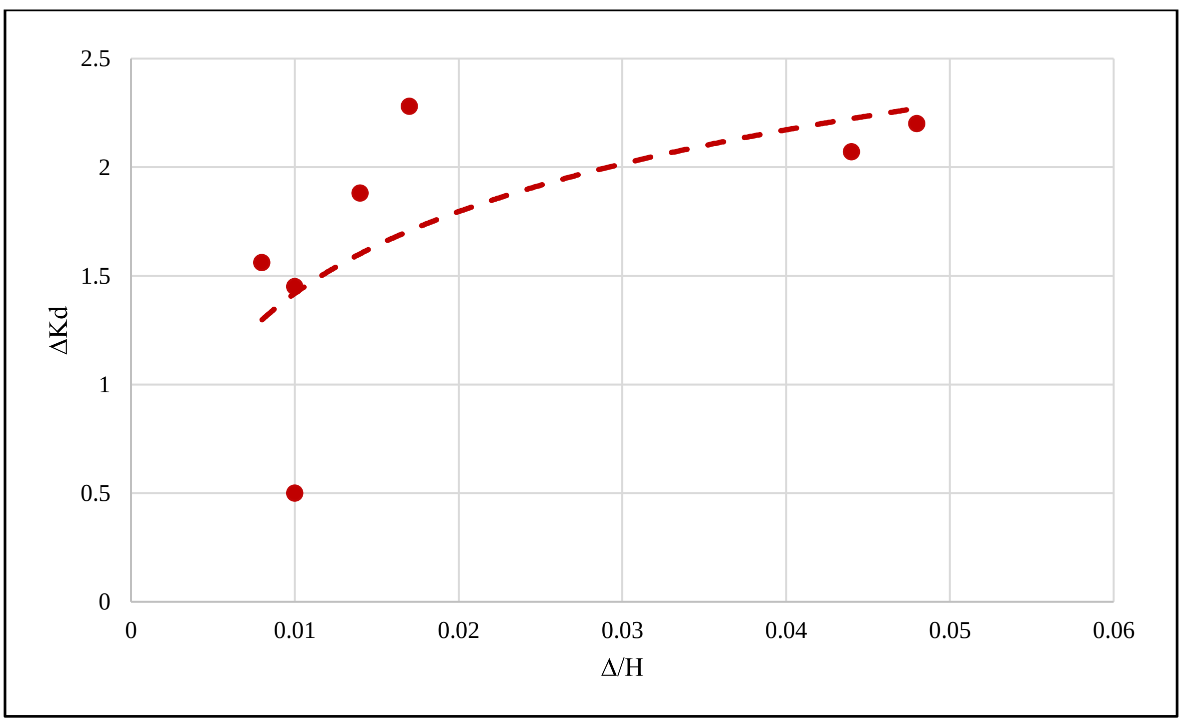

Figure 4.15: Dynamic earth pressure coefficient (ΔKd) as a function of wall's relative movement (Δ/H) for sand backfill

4.4.2 Calculation of the Displacements for RW-Soil System Using an Analytical Method

The step-by-step linear change of acceleration method is used in this section to compute the RW-soil model response. In this method, it is assumed that the acceleration changes linearly during each time step. The relationship between the change in acceleration ($\Delta\ddot{u}$), velocity ($\Delta\dot{u}$), and displacement (Δu) was used to solve the incremental equation of motion (Equation 4.3) (Buchholdt and Nejad, 2012; UFC, 2008; Mays and Smith, 1995).

$$m\Delta\ddot{u}_i + c(t)\Delta\dot{u}_i + k(t)\Delta u_i = \Delta F_i \tag{4.3}$$

$$u_{i+1} = u_i + \Delta u_i \tag{4.4}$$

$$\dot{u}_{i+1} = \dot{u}_i + \Delta\dot{u}_i \tag{4.5}$$

$$\Delta\ddot{u}_{i+1} = \ddot{u}_i + \Delta\ddot{u}_i \tag{4.6}$$

$$\Delta\ddot{u}_i = \frac{6}{\Delta t^2}\Delta u_i - \frac{6}{\Delta t}\dot{u}_i - 3\ddot{u}_i \tag{4.7}$$

$$\Delta\dot{u}_i = 3\frac{\Delta u_i}{\Delta t} - 3\dot{u}_i - \frac{1}{2}\Delta t\ddot{u}_i \tag{4.8}$$

$$\Delta u_i = \frac{\Delta\bar{F}_i}{\bar{k}_i} \tag{4.9}$$

$$\bar{F}_i = \Delta F_i + m\left\{\frac{6}{\Delta t}\dot{u}_i - 3\ddot{u}_i\right\} + c_i\{3\dot{u}_i - \frac{1}{2}\Delta t\ddot{u}_i\} \tag{4.10}$$

$$\bar{k}_i = k_i + \frac{6m}{\Delta t^2} + \frac{3c_i}{\Delta t} \tag{4.11}$$

$$k_i = \frac{8EI_e}{L^3} \tag{4.12}$$

$$I_e = fbd^3 \tag{4.13}$$

where,

u: displacement; $\dot{u}$: velocity; $\ddot{u}$: acceleration; m: equivalent mass; k: stiffness; c: damping; E: modulus of elasticity of concrete; I_e: moment of inertia of cracked section; f: coefficient for moment of inertia of cracked section; L: height of RW; b: width of RW; d: thickness of RW.

The equivalent mass (consisting of the mass of the stem and the mass of the backfill resulted from the static active earth pressure) was multiplied by the load-mass transformation factor (K_{LM}). The

K_{LM} for the cantilever varied between 0.78 for elastic range and 0.66 for plastic range (UFC, 2008). The applied blast force was determined by multiplying the peak reflected pressure by the area of the stem facing the shock tube. This area was obtained by multiplying 0.5 m (width) by 0.59 m (height). The coefficient for the moment of inertia of the cracked section with tension reinforcement only (Mays and smith, 1995) was taken to be 0.049. The maximum response to an impulsive load is reached in a very short time, before the damping forces can absorb considerable energy from the structure and therefore, the damping force was assumed to be zero.

Figure 4.16 represents the theoretical and experimental displacement time histories for the RW-soil model under various conditions. A good agreement was noticed between the experimental and analytical results for dense backfill when subjected to a reflected pressure of 26 kPa, live load surcharge application, and saturated and partially saturated backfills. It can be seen that the maximum theoretical displacements were close to the experimental values. On the other hand, a discrepancy between the experimental and the analytical displacement time histories was noted in loose and medium backfills. It can be seen that the linear acceleration method did not provide sufficient accuracy when applied to predict the response of RW with loose and medium backfills. Furthermore, increasing the blast load intensities led to a time-lag between the theoretical and experimental values (Figure 4.16a).

It seems that the step-by-step linear change of acceleration method was more representative of the dynamic response of the RW model when the “rigid block” response was evident in the retained backfill mass.

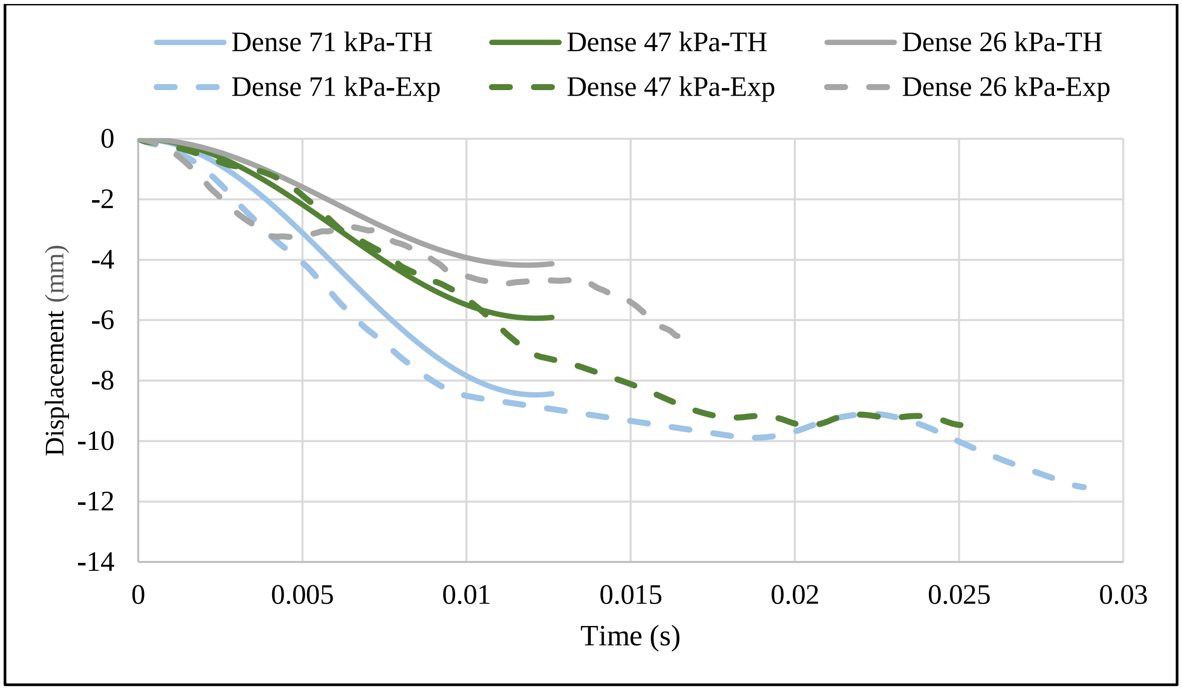

Dense 71 kPa-TH
Dense 47 kPa-TH
Dense 26 kPa-TH
Dense 71 kPa-Exp
Dense 47 kPa-Exp
Dense 26 kPa-Exp
0
-2
-4
-6
-8
-10
-12
-14
Displacement (mm)
0
0.005
0.01
0.015
0.02
0.025
0.03
Time (s)

(a)

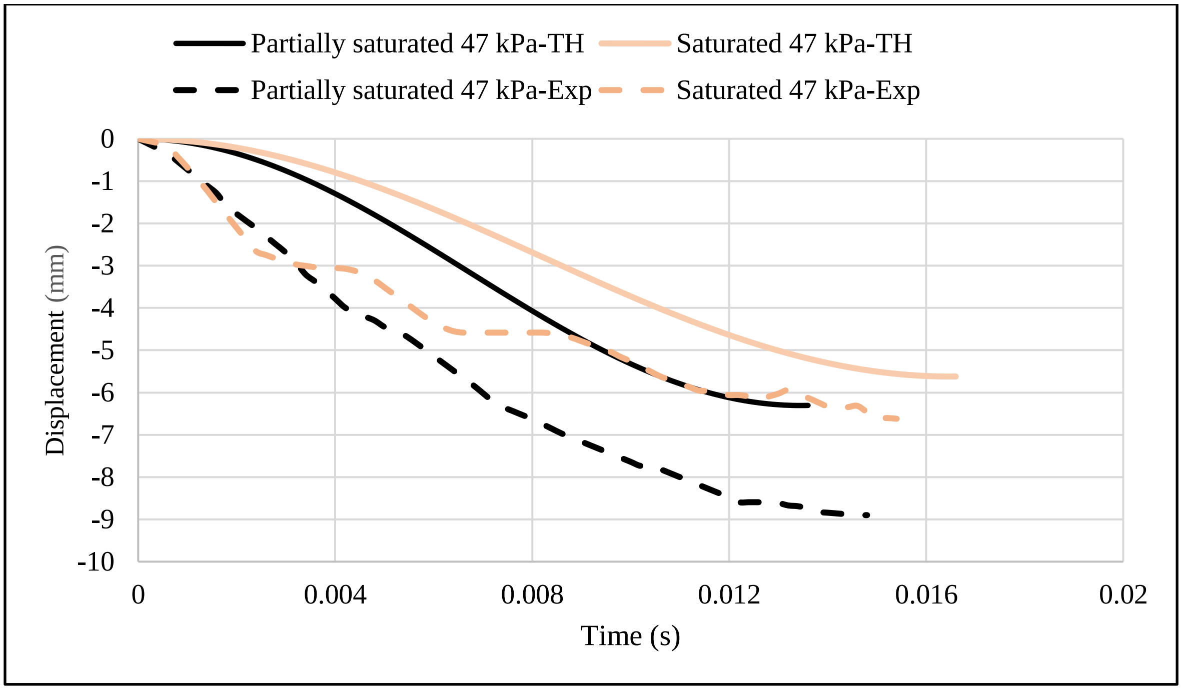

Partially saturated 47 kPa-TH
Saturated 47 kPa-TH
Partially saturated 47 kPa-Exp
Saturated 47 kPa-Exp
0
-1
-2
-3
-4
-5
-6
-7
-8
-9
-10
Displacement (mm)
0
0.004
0.008
0.012
0.016
0.02
Time (s)

(b)

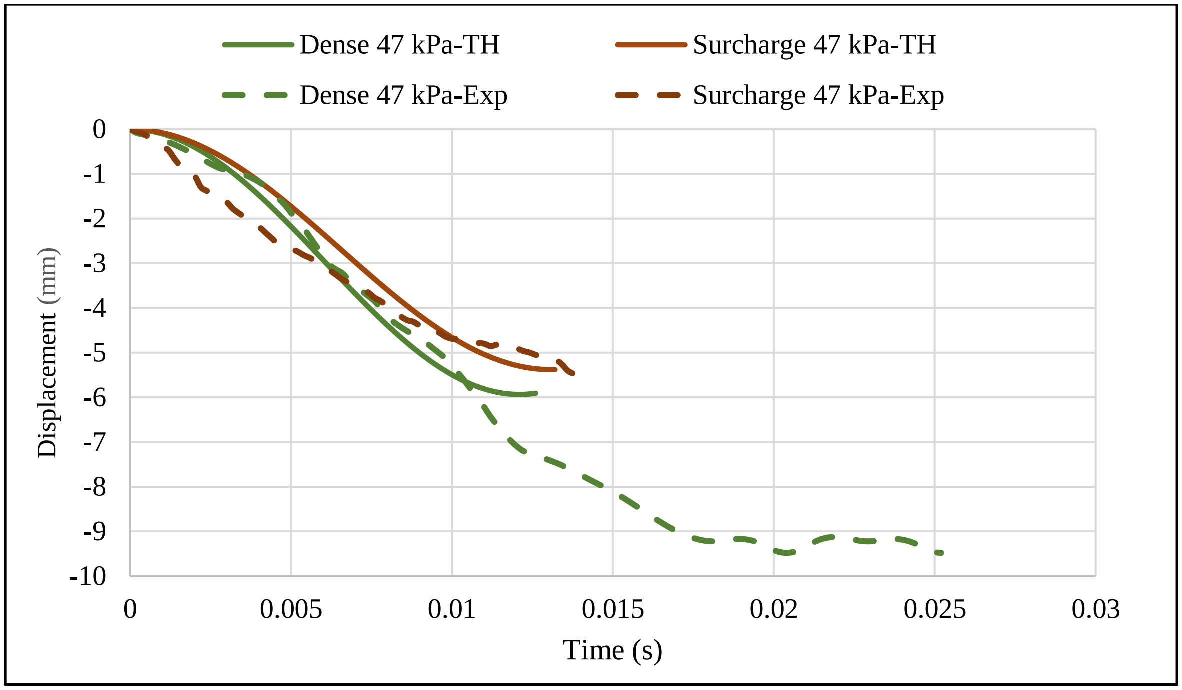

(c)

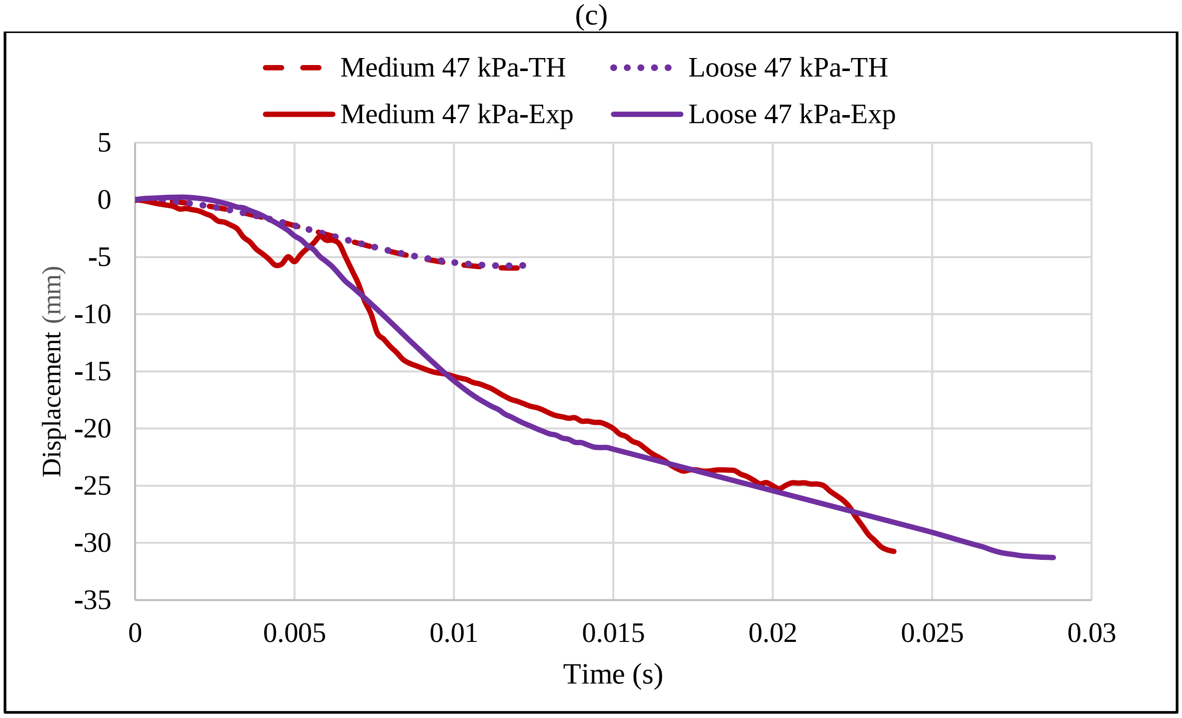

(d)

Figure 4.16: Theoretical and experimental displacement time histories for the RW-soil model Presented are the different soil conditions (dense, medium and loose). A reflected pressure of 47 kPa was used for the medium and loose backfill while pressures of 26 kPa, 47 kPa and 71kPa were used for dense backfill with a degree of saturation of 13 % for all conditions. A reflected pressure of 47 kPa was used for partially saturated backfill, saturated backfill and live load surcharge conditions. Theoretical (TH) and experimental (Exp) displacements were determined for all the above mentioned conditions.

4.4.3 Retaining Wall Passive Resistance

When bridges are subjected to a low-intensity dynamic load (such as small earthquakes) that induces lateral pressure, the response of the bridges remains in the elastic range. However, when a high-intensity dynamic load is applied, a nonlinear dynamic response occurs, and this response is dependent on the nonlinear soil-structure interaction effects between the abutments and the backfill soils (Shamsabadi et al., 2007). James and Bransby (1971) conducted an experimental study which indicated that wall movement is a function of backfill shear strain and mobilized shear strength. Therefore, when a retaining structure is subjected to a horizontal dynamic load, the wall is resisted by a mobilized passive resistance of the backfill as a function of relative displacement (Shamsabadi et al., 2007). The mobilized passive pressure behind the abutment back-wall is used to develop the nonlinear force-displacement capacity of the bridge abutment in a seismic event (Geotechnical Design Manual, 2010, and Shamsabadi et al., 2007, Shamsabadi and Kapuskar, 2006).

In this study, the mobilized passive resistance of the RW backfill that was caused by blast loading was used to determine the force-displacement relationship (Figure 4.17). Three curves that represent the RW with loose, medium, and dense backfill were subjected to a blast force of 13.75 kN, one curve representing the RW with dense backfill was subjected to a blast force of 19.2 kN, and one curve representing the RW with densely saturated backfill was subjected to a blast force of 13.75 kN. These curves were determined from the measured displacement and the passive force-time histories. Displacements at the top of the wall were measured using a high definition camera. The displacement time history of the wall was obtained using ProAnalyst software. The passive forces time history was computed by multiplying the dynamic earth pressures induced by blast load by the area of the RW's stem (Geotechnical Design Manual, 2010). The dynamic earth pressures were measured using soil pressure gauges (refer to technical paper I section 3.4.2 for the details). The area was obtained by multiplying 0.5 m by 0.65 m.

$$p_{wall} = 0.5P_d \tag{4.14}$$

$$F = (p_{wall})(H_{wall})(b_{wall}) \tag{4.15}$$

p_{wall}: Wall pressure distribution along the height of the wall in kPa

P_d: Measured pressure induced by blast load in kPa

F : Maximum passive force applied on RW in kN

H_{wall}: Height of the wall in m

b_{wall}: Width of the wall in m

It can be seen from Figure 4.17 that in dense backfill condition (under reflected pressures of 47 kPa and 71 kPa), the displacements were lower than the ultimate displacements and, therefore, the shear strength of the backfill was not fully mobilized. As a result, the passive wedge failure was not formed behind the RW. It is important to mention that at each level of displacement, there was a formation of a mobilized passive wedge and, consequently, a development of a passive resistance force. However, for medium and loose conditions, the shear strength might have been fully mobilized as wall deformations were close to the ultimate displacements. Thus, the backfill passive capacities were reached. The lowest passive resistance force was shown in saturated soil. This is due to the fact that the presence of water in the soil led to a reduction in its shear resistance (Das, 2016). As a result, the force-displacement capacity of the RW was affected.

The average soil stiffness can be determined from the force-displacement relationship for all above mentioned conditions (Geotechnical Design Manual, 2010).

Force-displacement relationship, which is referred to as a backbone curve, provides crucial information with regards to abutment/RW soil capacity when a bridge is designed for dynamic loads (Shamsabadi et al., 2007). The geotechnical engineer should provide the structural engineer with a soil stiffness (K) and the maximum displacement that occurred when the ultimate force was applied on the RW (Geotechnical Design Manual, 2010).

The prediction of nonlinear abutment backfill stiffness can have a strong impact on the dynamic response characteristics of bridges. Proper evaluation and design of bridge's abutment-backfill leads to the development of infrastructure systems that are sustainable and resilient.

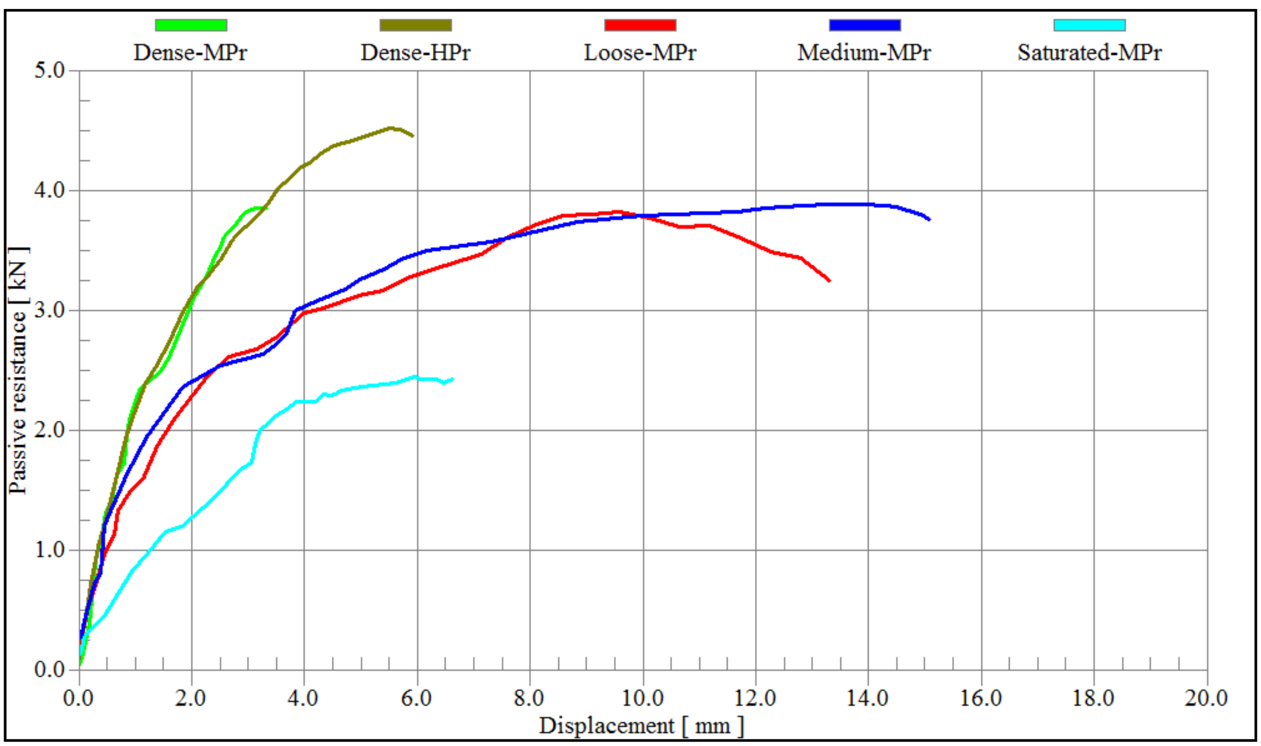

Figure 4.17: Force-displacement relationship

Dense-MPr: dense backfill-medium intensity reflected pressure (47 kPa); Dense-HPr: dense backfill-high intensity reflected pressure (71 kPa); Loose-MPr: loose backfill-medium intensity reflected pressure (47 kPa); Medium-MPr: medium dense backfill-medium intensity reflected pressure (47 kPa); Saturated-MPr: saturated backfill-medium intensity reflected pressure (50 kPa). Displacements were measured at the top of the wall. Degree of saturation was 13 % for all conditions except saturated backfill.

4.4.4 Acceleration Response of the Retaining Wall-Backfill Model

Acceleration design response curves for RW/backfill are another set of crucial information that should be provided by geotechnical engineers in order to design bridges for dynamic loads (Geotechnical Design Manual, 2010). Acceleration time histories for RW/backfill were plotted for all conditions (Figure 4.18). The acceleration response of the RW/backfill system was determined at the same locations where lateral displacements were tracked.

It was observed that the acceleration responses for loose backfill were lagging behind the acceleration response for the top of the RW. Furthermore, the acceleration response for the top of the wall was higher for loose backfill in comparison with medium and dense backfill under the same load intensity conditions. Blast loads generated high accelerations on the wall with loose backfill. This is because of the limited lateral support that loose backfill provided to the RW. As a result, large lateral displacements and sliding failure were noticed in this condition (Figure 4.14).

On the other hand, the acceleration responses for the wall were higher than the acceleration response of the backfill for all conditions. This is due to the mass of the wall being smaller than the mass of the backfill. Therefore, the result seen is substantiated when considering that the relationship between acceleration and mass is inversely proportional (Equation 4.3). The highest acceleration responses for the wall and backfill were produced when dense backfill was subjected to a reflected pressure of 71 kPa as the relationship between the force and the acceleration is proportional (Equation 4.3).

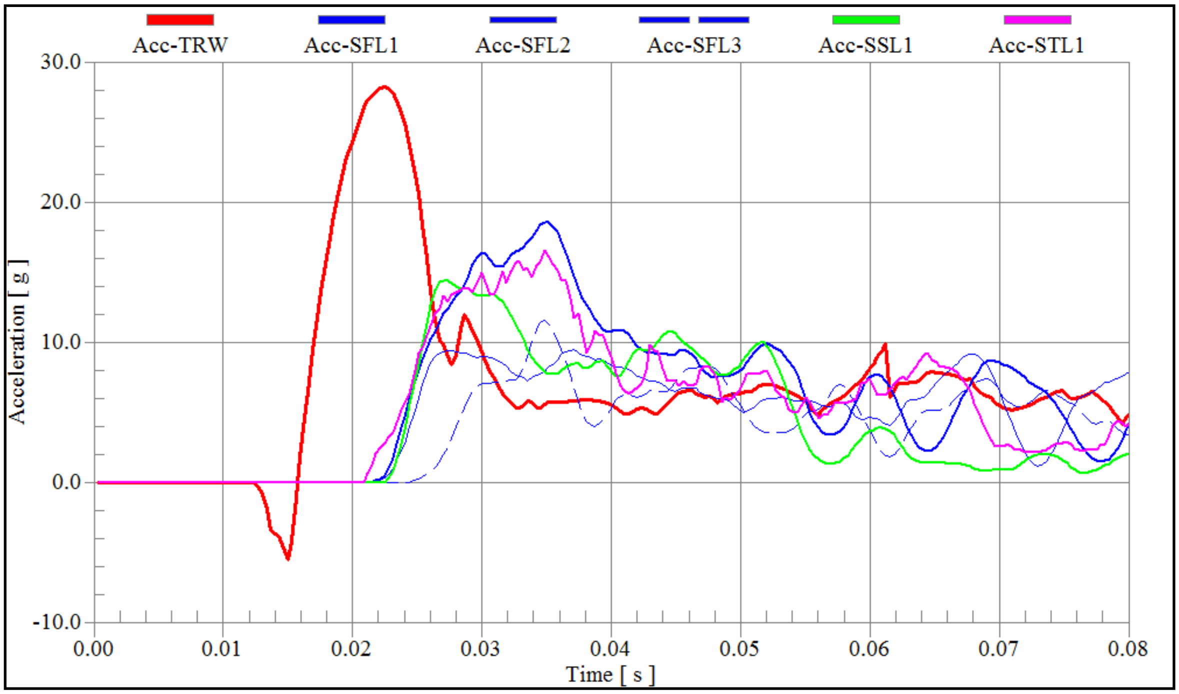
Acc-TRW
Acc-SFL1
Acc-SFL2
Acc-SFL3
Acc-SSL1
Acc-STL1
30.0
20.0
10.0
0.0
-10.0
Acceleration [g]
0.00
0.01
0.02
0.03
0.04
0.05
0.06
0.07
0.08
Time [s]

(a)

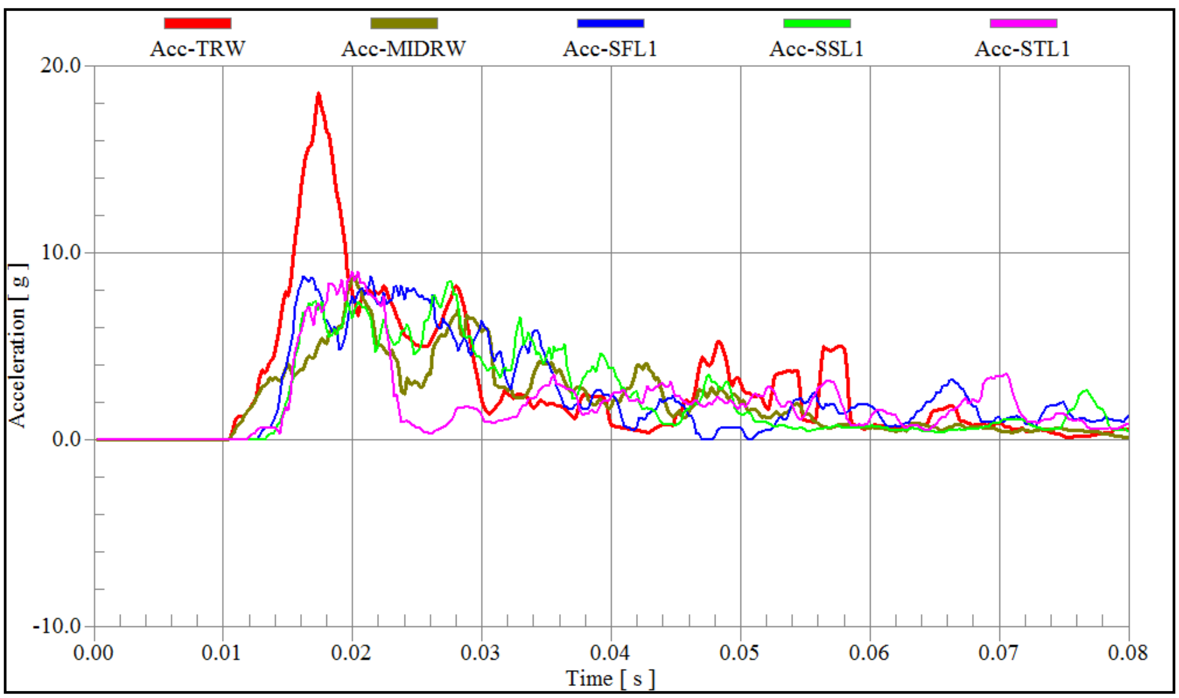
Acc-TRW
Acc-MIDRW
Acc-SFL1
Acc-SSL1
Acc-STL1
20.0
10.0
0.0
-10.0
Acceleration [g]
0.00
0.01
0.02
0.03
0.04
0.05
0.06
0.07
0.08
Time [s]

(b)

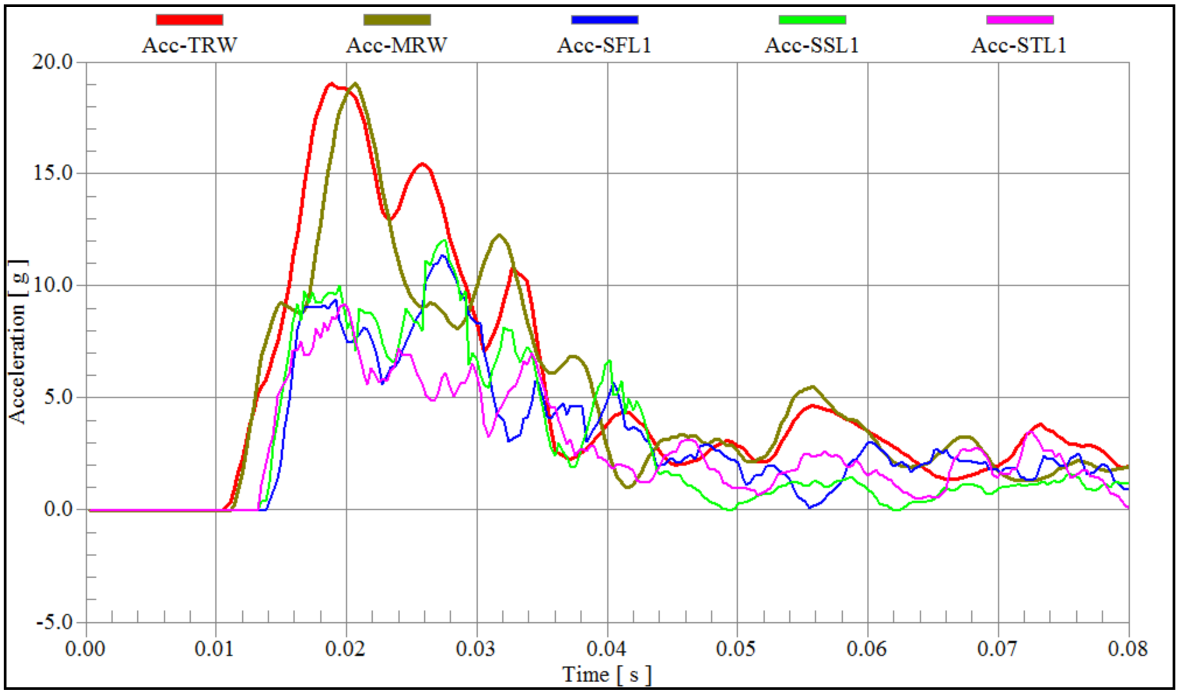
Acc-TRW
Acc-MRW
Acc-SFL1
Acc-SSL1
Acc-STL1
20.0
15.0
10.0
5.0
0.0
-5.0
Acceleration [g]
0.00
0.01
0.02
0.03
0.04
0.05
0.06
0.07
0.08
Time [s]

(c)

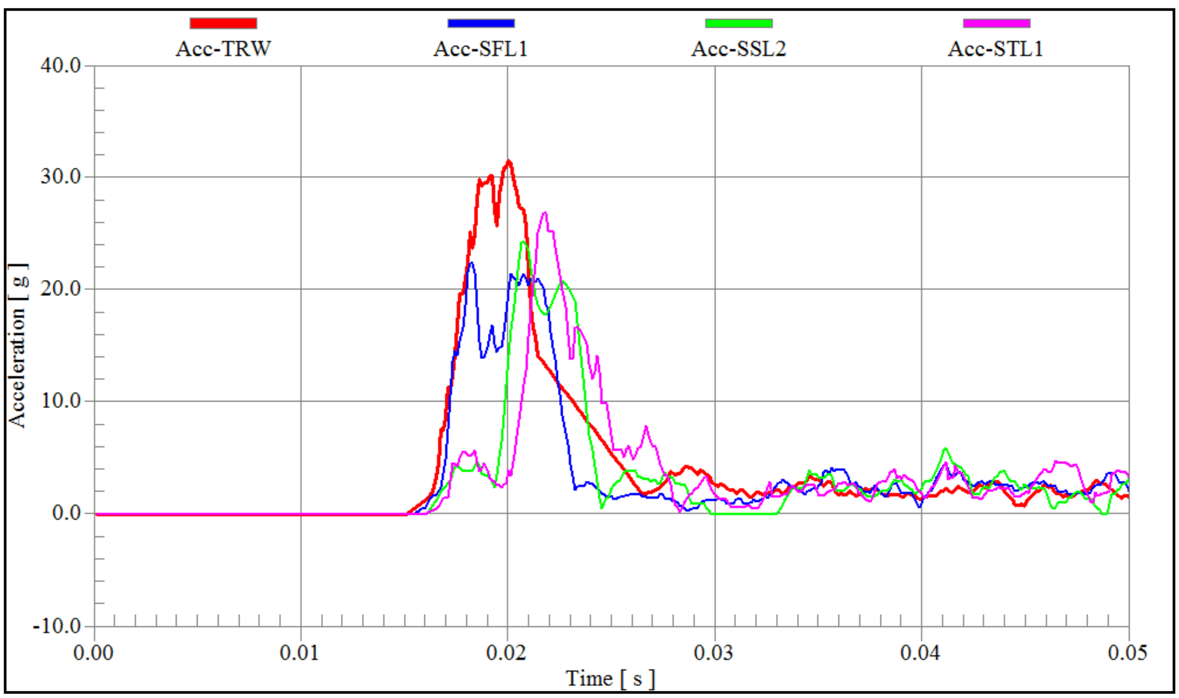
Acc-TRW
Acc-SFL1
Acc-SSL2
Acc-STL1
40.0
30.0
20.0
10.0
0.0
-10.0
Acceleration [g]
0.00
0.01
0.02
0.03
0.04
0.05
Time [s]

(d)

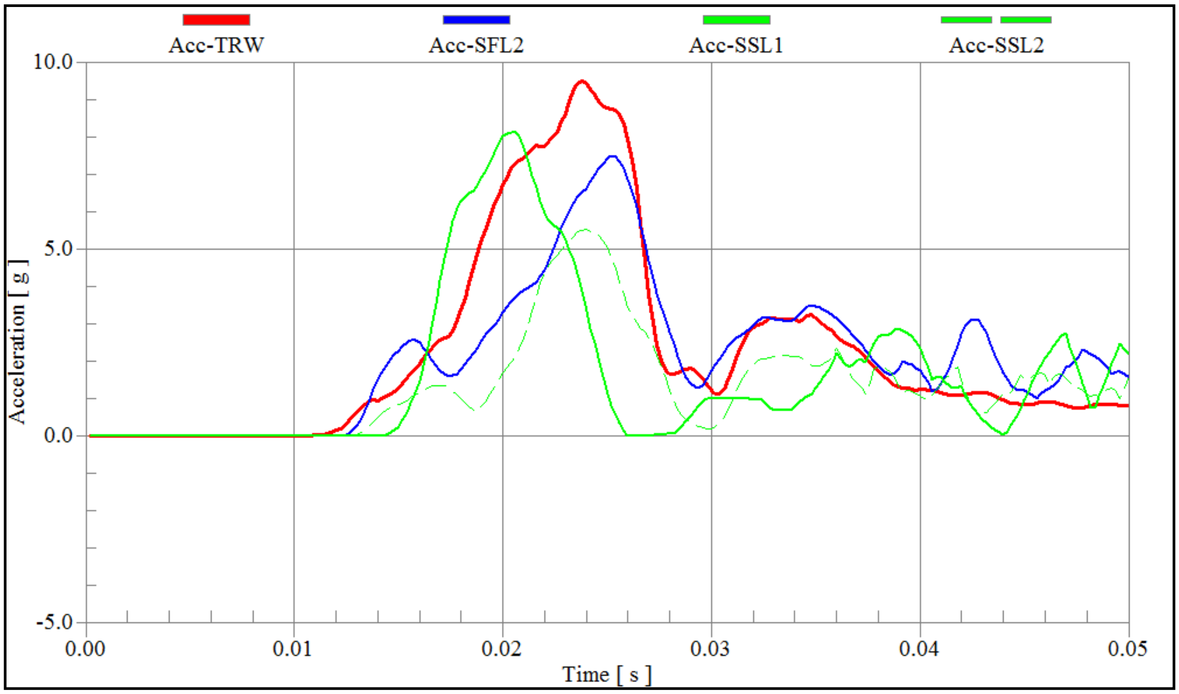
Acc-TRW
Acc-SFL2
Acc-SSL1
Acc-SSL2
10.0
5.0
0.0
-5.0
Acceleration [g]
0.00
0.01
0.02
0.03
0.04
0.05
Time [s]

(e)

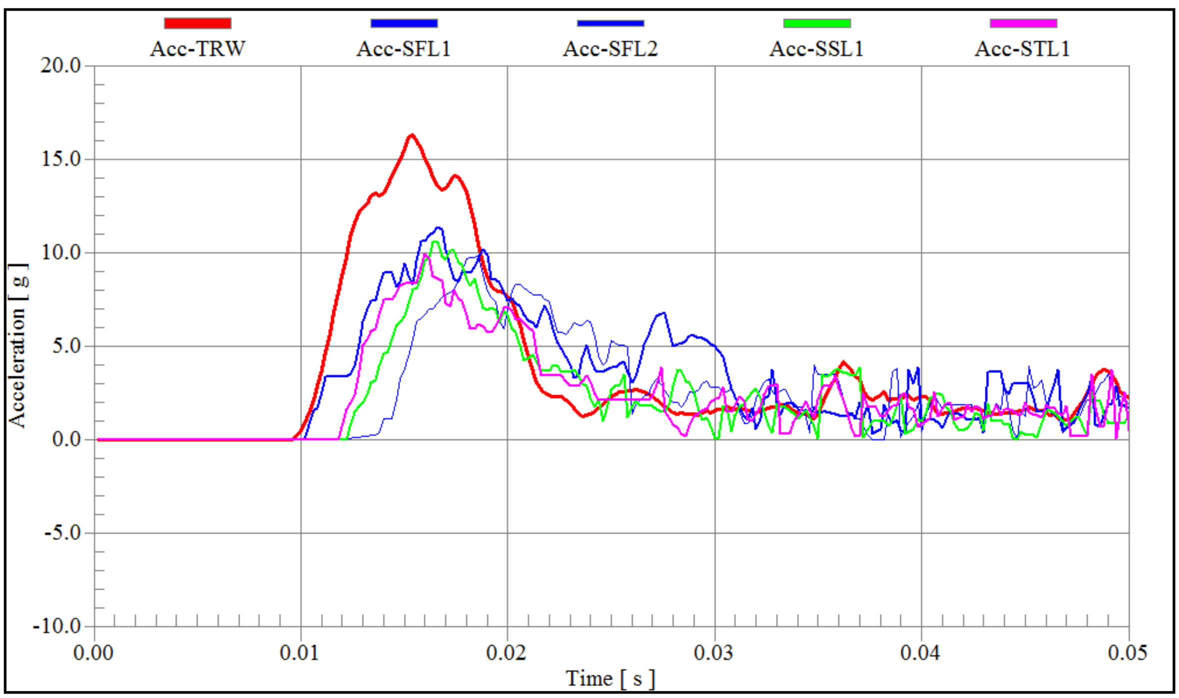
Acc-TRW
Acc-SFL1
Acc-SFL2
Acc-SSL1
Acc-STL1
20.0
15.0
10.0
5.0
0.0
-5.0
-10.0
Acceleration [g]
0.00
0.01
0.02
0.03
0.04
0.05
Time [s]

(f)

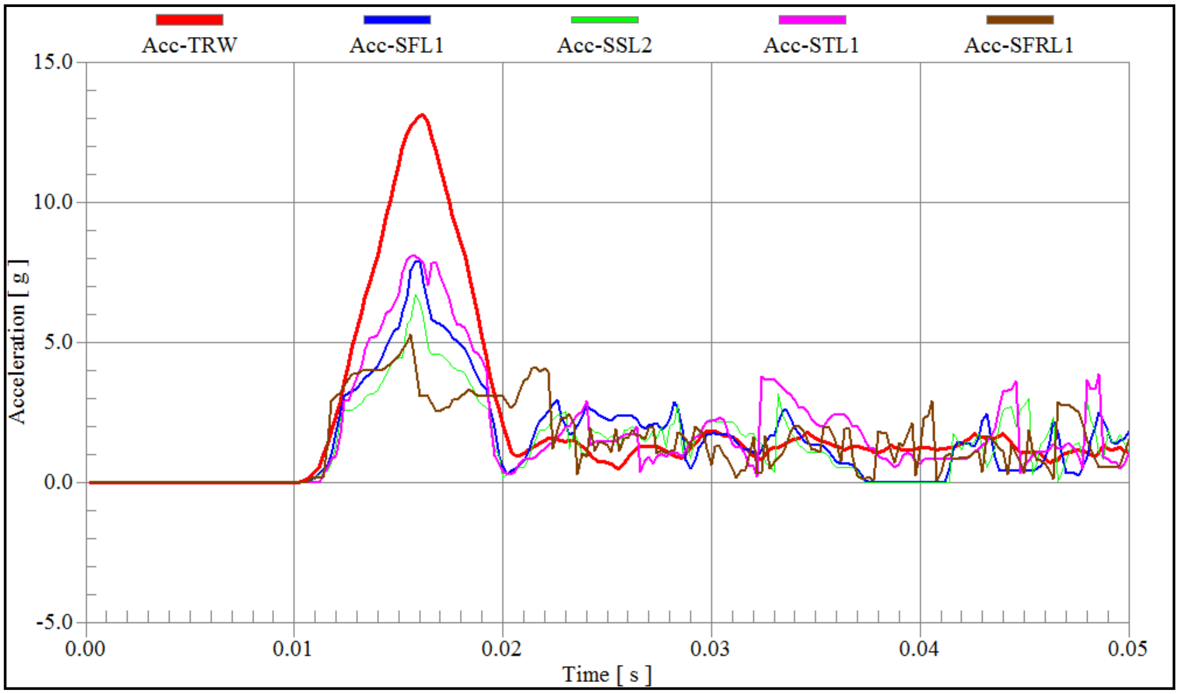

(g)

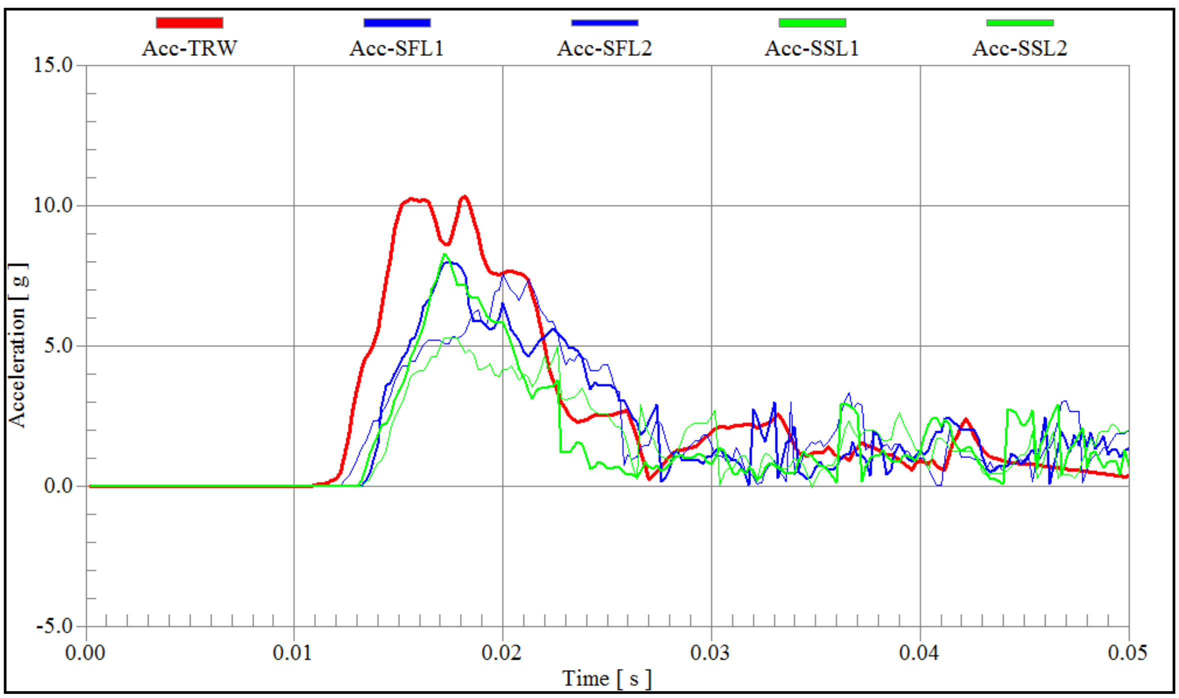

(h)

Figure 4.18: Acceleration time histories for RW/backfill; (a) loose, (b) medium, and (c) dense conditions, (d) reflected pressure 71 kPa, (e) reflected pressure 26 kPa, (f) partially saturated backfill, (g) saturated backfill, (h) live load surcharge

TRW: top of retaining wall; SFL: soil first layer; SSL: soil second layer; STL: soil third layer; MIDRW: mid height of retaining wall; SFRL: soil forth layer (same locations where lateral displacements were tracked as shown in Figures 4.9, 4.11, 4.12, and 4.13)

4.5. Summary and Conclusion

A soil-RW model was built at the structural laboratory of the University of Ottawa and was subjected to simulated blast loads using a shock tube. The ProAnalyst software was used to capture the soil particles' movement and to track the transient and permanent displacements of the wall.

Backfill materials with various relative densities and degrees of saturation were subjected to different blast shot intensities to assess the modes of RW movement. Moreover, the force-displacement relationship was determined from the mobilized passive resistance of the RW backfill that was induced by blast loading.

The results showed that the modes of wall rotation were affected by the backfill relative density, blast load intensities, and degree of saturation. Reduction in the wall movement was noticed in a dense condition of backfill while increasing the blast load led to an increase in the wall movement. Furthermore, wall yielding was reduced when fully saturated backfill and live load surcharge conditions were applied.

The nonlinear force-displacement capacity of the bridge abutment was developed from the mobilized passive pressure of the RW backfill. A possible formation of passive wedge failure was noticed in medium and loose conditions. The backfill passive capacities were not reached in dense backfill, regardless of the blast load intensities that were used in this study.

Acceleration time histories for RW/backfill showed that there was a time-lag between the acceleration responses of the wall and the loose backfill. The RW with loose backfill exhibited higher acceleration than the RW with medium and dense backfill under the same load intensity.

Furthermore, the highest acceleration responses for the wall and backfill were developed when the RW with dense backfill was subjected to a reflected pressure of 71 kPa.

The findings of this research will provide tools that help in the design of bridge abutments and the development of resilient infrastructure systems.

4.6 References

Al Atik, L. F. (2008). Experimental and Analytical Evaluation of Seismic Earth Pressures on Cantilever Retaining Structures. Doctoral thesis, University of California, Berkeley.

Agrawal, K. A., Yi, Z. (2009). Blast Load Effects on Highway Bridges. University Transportation Research Center.

American Society of Civil Engineers (ASCE). (2010). Design of Blast-Resistant Buildings in Petrochemical Facilities, Second Edition.

American Society of Civil Engineers (ASCE). (1985). Design of Structures to Resist Nuclear Weapons Effects. Manual 42. Washington, D.C.

American Society of Civil Engineers (ASCE). (1999). Structural Design for Physical Security: State of the Practice. The Structural Engineering Institute Task Committee.

American Society of Civil Engineers (ASCE). (2005). Minimum Design Loads for Buildings and Other Structures. ASCE/SEI 7-05, Reston, Virginia.

ASTM (American Society for Testing and Materials) C136/C136M−14 Standard for Sieve Analysis of Fine and Coarse Aggregates.

ASTM D854-14 Standard for Specific Gravity of Soil Solids by Water Pycnometer.

ASTM D4254-16 Standard for Minimum Index Density and Unit Weight of Soils and Calculation of Relative Density.

ASTM D4253-16 Standard for Maximum Index Density and Unit Weight of Soils Using a Vibratory Table.

ASTM, D3080-11 Standard for Direct Shear Test of Soils under Consolidated Drained Conditions.

ASTM C31/C31M-19 Standard for Making and Curing Concrete Test Specimens in the field.

ASTM C39/C39M-18 Standard for Compressive Strength of Cylindrical Concrete Specimens.

Bakr, J. A. (2018). Displacement-Based Approach for Seismic Stability of Retaining Structures. Doctoral thesis, School of Mechanical, Aerospace and Civil Engineering. University of Manchester.

Bang, S. (1985).Active Earth Pressure behind Retaining Walls. Journal of Geotechnical Engineering, 111, 407-41.

Biggs, J. M. (1964). Introduction to Structural Dynamic, McGraw-Hill, Inc. U.S.

Buchholdt, H.A. and Nejad, S.E. M. (2012). Structural Dynamics for Engineers. Second Edition.

Crawford, E. R., Higgins, C. J., and Bultmann, E. H. (1974). The Air Force Manual for Design and Analysis of Hardened Structures. AFWL-TR-74-102, Air Force Weapons Laboratory, Kirtland Air Force Base, New Mexico.

Das, B. M. (2016). Principles of Foundation Engineering, Eighth Edition, Boston, MA, U.S.

Das, B. M. (1999). Principles of Foundation Engineering, Fourth Edition, Pacific Grove, CA, U.S.

Das, B. M. (1993). Principles of Soil Dynamics, Second Edition, Stamford, CT, U.S.

Deyanova, M., Lai, G. C., and Martinelli, M. (2016). Displacement–Based Parametric Study on the Seismic Response of Gravity Earth-Retaining Walls. Soil Dynamics and Earthquake Engineering, 80, 210-224.

DOD. (2003) Uniform Facilities Criteria: Department of Defense Minimum Antiterrorism Standard for Buildings. UFC 4-010-01, Department of Denfence.

Federal Highway Administration, United States Department of Transportation. (2008). Standard Specifications for Construction of Roads and Bridges on Federal Highway Projects FP-14.

Fujikura, S., Bruneau, M., Lopez-Garcia, D. (2008). Experimental Investigation of Multihazard Resistant Bridge Piers Having Concrete-Filled Steel Tube under Blast Loading. Journal of Bridge Engineering, ASCE, 13 (6), 586-594.

Geotechnical Design Procedure (GDP-9). (2015). Liquefaction Potential of Cohesionless Soils. State of New York department of transportation, geotechnical engineering bureau.

GSA. (2003). ISC Security Design Criteria for New Federal Office Buildings and Major Modernization Projects, U.S. General Services Administration.

Hao, H., Wu, C. (2005). Numerical Study of Characteristic of Underground Blast Induced Surface Ground Motion and Their Effect on Above-Ground Structures Part II. Effects on Structural Responses. Soil Dynamics and Earthquake Engineering, 25, 39-53.

ISC. (2001). ISC Security Design Criteria for New Federal Office Buildings and Major Modernization Projects, Washington, D.C., General Services Administration, Interagency Security Committee.

James, R. G., and Bransby, P. L. (1971). Experimental and theoretical investigations of a passive earth pressure problem. Geotechnique, 20(1), 17–36.

Jo, S-B, Ha, J-G, Lee, J-S, Kim, D-S. (2017). Evaluation of the Seismic Earth Pressure for Inverted T-Shape Stiff Retaining Wall in Cohesionless Soils via Dynamic Centrifuge. Soil Dynamics and Earthquake Engineering 92, 345–357.

Kadhom, B. (2015). Blast Performance of Reinforced Concrete Columns Protected by FRP Laminates. Doctoral thesis, University of Ottawa, Ontario, Canada.

Kloukinas, P., Scotto di S., Anna, P., Augusto, D., Matthew, E., Aldo, L. Simonelli, A., Taylor, C., Mylonakis, G. (2015). Investigation of Seismic Response of Cantilever Retaining Walls: Limit Analysis vs Shaking Table Testing. Soil Dynamics and Earthquake Engineering, 77, 432–445.

Liu, F. (2014). Lateral Earth Pressures Acting on Circular Retaining Walls. International Journal of Geomechanics, 14 (3), 04014002.

Mays, G.C. and Smith, P.D. (1995). Blast Effects on Buildings. First edition.

Mikola, R. G. (2012). Seismic Earth Pressures on Retaining Structures and Basement Walls in Cohesionless Soils. Thesis, University of California, Berkeley.

Mikola, R. G. and Sitar, N. (2013). Seismic Earth Pressures on Retaining Structures in Cohesionless Soils. Department of Civil and Environmental Engineering University of California, Berkeley.

Mittal, R. K., Gupta, M.K. and Singh, S. (2004). Liquefaction Behaviour of Sand during Vibrations. 13th World Conference on Earthquake Engineering, Vancouver, B.C., Canada, 1-6.

Mononobe, N. & Matsuo, M. (1929). On the determination of earth pressures during earthquakes. Proceedings, World Engineering Congress 179-187.

Morris, D. V., and Delphia, J. G. (1999). Specifications for Backfill of Reinforced-Earth Retaining Walls. Texas Department of Transportation in Cooperation with the U.S. Department of Transportation Federal Highway Administration.

MULTIQUIP INC. (2011). Soil Compaction Handbook.

National Research Council. (1985). Liquefaction of Soils during Earthquakes, Washington DC.

Newmark, N. M., and Haltiwanger, J. D. (1962). Air force Design Manual. AFSWC-TDR-62-138, Air Force Special Weapons Center, Kirland Air force Base, New Mexico.

Nishimura, T., Hirabayashi, Y., Fredlund, D. G., and Gan, J. K.-M. (1999). Influence of Stress History on the Strength Parameters of an Unsaturated Statically Compacted Soil. Canadian Geotechnical Journal, 36, 251–261.

Ngo, T., Mendis, P., Gupta, A. & Ramsay, J. (2007). Blast Loading and Blast Effects on Structures – An Overview. EJSE Special Issue: Loading on Structures.

Okabe, S. (1926). General theory of earth pressure. Journal of the Japanese Society of Civil Engineers, 12, 311.

Peng, S.-Q., Li, X.-B., Fan, L. & Liu, A.-H. (2012). A General Method to Calculate Passive Earth Pressure on Rigid Retaining Wall for all Displacement Modes. Transactions of Nonferrous Metals Society of China, 22, 1526-1532.

Potts, D. & Fourie, A. (1986). A numerical Study of the Effects of Wall Deformation on Earth Pressures. International journal for numerical and analytical methods in geomechanics, 10, 383-405.

Psarropoulos, P. N., Tsompanakis Y., Papazafeiropoulos, G. (2009). Effects of soil non-linearity on the seismic response of restrained retaining walls. Structure and Infrastructure Engineering, 1–12.

Richards, R. & Elms, D. G. (1979). Seismic behavior of gravity retaining walls. Journal of Geotechnical and Geoenvironmental Engineering, 105, 249-264.

SCDOT. (2010). Geotechnical Design Manual, Chapter 14 Geotechnical Seismic Design.

Shamsabadi, A., Rollins, M. K., and Kapuskar, M. (2007). Nonlinear Soil–Abutment–Bridge Structure Interaction for Seismic Performance-Based Design. Geotechnical and Geoenvironmental Engineering, 133, 6.

Shamsabadi, A., and Kapuskar, M. (2006). Nonlinear Seismic Soil-Abutment-Structure Interaction Analysis of Skewed Bridges. In: 5th National Seismic Conference on Bridges and Highways, San Francisco, B18.

Shamsabadi, A., Ashour, M. & Norris, G. (2005). Bridge Abutment Nonlinear Force Displacement-Capacity Prediction for Seismic Design. Journal of Geotechnical and Geoenvironmental Engineering, 131, 151-161.

Sladen, J. A., D'Hollande, R. D., &Krahn, J. (1985). The Liquefaction of Sands, a Collapse Surface Approach. Canadian Geotechnical Journal, 22.

Soil Compaction Handbook (MULTIQUIP INC.), 2011.

Steedman, R. S. & Zeng, X. (1991). Centrifuge modeling of the effects of earthquakes on free cantilever walls. Centrifuge′91, Ko (ed.), Balkema, Rotterdam.

TM 5-1300. (1990). Structures to Resist the Effects of Accidental Explosions. Departments of the Army, the Navy, and the Air Force.

Tsuchida, H. (1970). Prediction and Countermeasure against the Liquefaction in Sand Deposits, pp. 3.1-3.33 in Abstract of the Seminar in the Port and Harbor Research Institute in Japanese.

Unified Facilities Criteria (UFC). (2008). Structures to Resist the Effects of Accidental Explosions. Departments of the Defense.

USDOA. (1969). Structures to Resist the Effects of Accidental Explosions. Air Force Manual 88-22, Army Technical Manual 5-1300, and Navy Publication NAVFAC P-397, Departments of the Air Force, Army, and Navy, Washington, DC.

USDOA. (1990). Structures to Resist the Effects of Accidental Explosions. Army Technical Manual 5-1300/Navy Publication NAVFAC P-397/Air Force Manual (AFM) 88-22 (TM 5-1300), U.S. Department of Army, Washington, D.C.

USDOA. (1992). A Manual for the Prediction of Blast and Fragment Loading on Structures. DOE/TIC-11268, U.S. Department of the Army, U.S. Department of Energy., Washington, D.C.

USDOA. (1998). Design and analysis of hardened structures to conventional weapons effects. TM 5-855-1, Headquarters, U.S. Department of the Army, Washington, DC.

Whitman R & S, L. (1984). Seismic Design of Gravity Retaining Walls. Proceedings of 8th world conference on earthquake engineering, San Francisco, 3, 533-540.

Wilson, P. & Elgamal, A. (2010). Large-Scale Passive Earth Pressure Load-Displacement Tests and Numerical Simulation. Journal of geotechnical and geoenvironmental engineering, 136, 1634-1643.

Xu, T. (2015). Numerical simulation of embankment dams subjected to blast loadings, PhD Thesis. The Hong Kong University of Science and Technology, Hong Kong.

Chapter 5 Technical Paper III: Blast Impact on Cantilever Retaining Wall: Response of the Sand Backfill

Najlaa Abdul-Hussain, Mamadou Fall, Murat Saatcioglu

5.1 Abstract

The development of excess pore pressure in the sand backfill behind the retaining wall (RW) induced by blast loading can lead to loss of strength or stiffness of the backfill. The loss of strength or stiffness of the ground can result in settlement of structures, failure of earth dams and retaining structures, and landslides. Since the retaining walls are an important portion of many infrastructures, studying their dynamic behaviour is considered crucial to ensure structural integrity, especially in the context of explosive loading. Yet, there have not been any studies addressing the dynamic response of retaining walls when subjected to blast loading. Thus, an experimental study was conducted to examine the influence of blast loads on the dynamic behaviour of reinforced concrete retaining wall (RCRW) with sand as a backfill material. A shock tube was utilized to produce blast loads on the soil-RW model. The influence of the relative density, backfill saturation, blast load intensity, and live load surcharge on the blast behaviour of RCRW with sand backfill was studied. The results showed that the maximum pore pressure responses for saturated backfill were at a time greater than the positive phase duration, while the maximum pore pressure response for the foundation was at the end of the positive phase duration. The susceptibility of the RW with saturated dense sand to liquefaction was examined, and it was ascertained that liquefaction was not triggered. Settlement, lateral displacement and peak particle velocity time histories were determined for the sand behind the RW. The findings of this research will provide performance-based recommendations for more effective blast design of retaining structures.

Keywords: Shock tube, Retaining wall, Pore pressure, Peak particle velocity; Blast

5.2 Introduction

Infrastructures might be exposed to two types of dynamic events induced hazards during their lifetime. There are man-made hazards in the form of blasts as well as natural hazards, such as earthquakes and wind. Highway bridges are considered to be vital infrastructures due to their use in transportation and the movement of goods. Therefore, the serviceability of bridges has a huge economic impact and garners high public interest. In order to maintain the bridge's functionality, bridges and their components should be designed to resist the impacts of dynamic loads. The abutment/retaining structure is a component of a bridge that provides vertical support to the bridge superstructure at bridge ends and withstands lateral earth pressure.

Retaining wall failures during dynamic events (Kobe, Japan 1995 and Lefkada, Greece 2003) can have a great effect on the economy of the regions (Psarropoulos et al., 2009). In the early versions of AASHTO design manuals, the seismic effects on the retaining walls were not considered. However, currently, seismic forces are taken into consideration in the design of retaining walls (RWs), especially in areas that are prone to earthquakes (Chen and Duan, 2014). On the other hand, to the best of the authors' knowledge, the blast effects on RWs have not been taken into account yet in the design of abutments/retaining structures.

In order to minimize the possible buildup of the hydrostatic pressure behind the wall, each RW should be provided with a drainage system embedded in the RW backfill. If for any reason the drainage system is clogged, the backfill and the foundation soil would become saturated. The reduction in shear strength of saturated cohesionless soils in the backfill and the foundation is often the cause of the dynamic vulnerability of RWs. The process that leads to the loss of shear strength is called soil liquefaction.

Some effects of liquefaction can be catastrophic (such as flow failures of slopes or earth dams, settling and tipping of building and piers of bridges, and total or partial collapse of retaining walls) while other effects (such as large deformation and settlement) can be less harsh, yet can also cause severe damages to highways, railroads, etc. (NRC, 1985). The concept of liquefaction is used for any excessive deformations or movements as a result of dynamic loads on saturated cohesionless soils. Therefore, flow failures and deformation failures are both considered liquefaction failures. Liquefaction behaviour of saturated cohesionless soils during earthquake events has been investigated extensively in the literature (Pan and Yang, 2017, Mittal et al., 2004, Wu, 2004, Rauch, 1997, Sladen et al., 1985). Gazetas et al. (2004) stated that retaining walls' performance during seismic loading is based on the presence of liquefaction-prone loose sand backfills. Cases result from major earthquakes show that retaining walls supporting loose saturated backfills are susceptible to strong seismic loading (Al Atik, 2008).

It was however noticed that none of the available literature investigated the geotechnical response (such as pore pressures, settlements, lateral displacements, and liquefaction) of the backfill of the RW when subjected to blast loading.

Thus, in this paper, backfills with various relative densities and degrees of saturation were subjected to different blast shot intensities to address the effects of pore pressure in the backfill and the foundation of the RW as well as to evaluate the potential for soil liquefaction. Furthermore, settlements and lateral deformations of the retained backfill were assessed.

5.3. Experimental Program

5.3.1 Description of Test Specimens and Material Properties

5.3.1.1 Backfill soil

Sand is commonly used as a backfill material for retaining wall systems. The high permeability of sand helps in releasing the hydrostatic pressure behind the wall stem. Sand has been used extensively in experimental research (e.g. Jo et al., 2017, Kloukinas et al., 2015, and Mikola and Sitar, 2013) to address the dynamic response of soil retaining walls due to seismic loads.

In this study, both the backfill and foundation soil layers consisted of sand. The grain size distribution and sand properties were determined, according to the ASTM (American Society for Testing and Materials) C136/C136M−14 at the Geotechnical Laboratory of the University of Ottawa. The sand had a mean grain size (D50) of 0.54 mm, an effective size (D_{10}) of 0.21 mm, a uniformity coefficient (C_u) of 3.05 and a coefficient of gradation (C_z) of 0.9. Figure 5.1 depicts the grain size distribution of the sand.

The specific gravity of the sand was 2.64, and it was determined according to the ASTM D854-14. Minimum and maximum dry densities of 13.0 kN/m^3 and 18.8 kN/m^3 were found following the procedure described by the ASTM D4254-16 and D4253-16, respectively. The friction angle of the sand was 34° and it was determined using the direct shear test described in the ASTM, D3080-11. Table 5.1 summarizes the soil properties of this research.

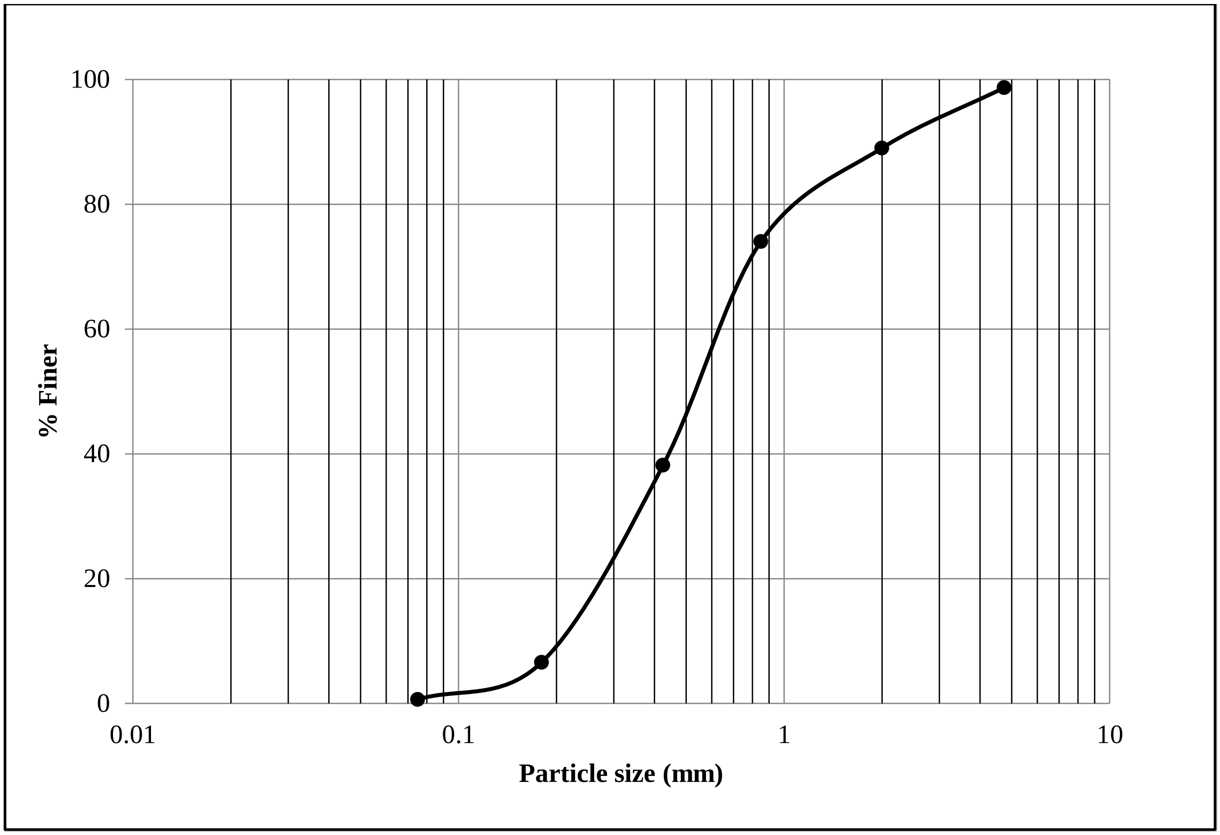

Figure 5.1: Grain size distribution of sand

Table 5.1: Soil properties

Descriptions	Values
Grain size distribution effective size (D_{10})	0.67 mm
Uniformity coefficient (C_u)	3.05
Coefficient of gradation (C_z)	0.9
Specific gravity (Gs)	2.64
Maximum unit weight	18.8 kN/m^3
Minimum void ratio	0.38
Minimum unit weight	13.0 kN/m^3
Maximum void ratio	0.99
Friction angle	34°

5.3.1.2 Wall

The reinforced concrete retaining wall model with an L shape, depicted in Figure 5.3, was designed, built and used in this study. The RW was designed using the Rankine earth pressure theory for stability. The RW was checked for overturning, sliding along the base and bearing capacity failure. The RW investigated was modelled at the $1/10^{th}$ scale. As shown in Figures 5.2 and 5.3, the dimensions of the stem and the heel of the retaining wall in this study were 650 mm (height) x 500 mm (width) x 60 mm (thickness) and 400 mm (width) x 500 mm (length) x 60 mm (thickness), respectively. Scaling relations of the physical modeling are shown in Table 5.2 (Altaee and Fellenius, 1994).

Two RWs were constructed at the Structural Laboratory of the University of Ottawa. The second wall was built as a replacement in case of failure of the first wall. Both concrete RWs were reinforced longitudinally and laterally with 6.3 mm rebars spaced at 50 mm c/c. The details of retaining wall reinforcement are presented in Figure 5.4. A concrete mixer and an electric concrete vibrator were used to mix and consolidate the fresh concrete, respectively. The heel of the retaining wall was first cast, and 14 days later, the stem was cast (Figure 5.2). At the end of each casting process, the specimens were covered with two layers of wet burlap and a plastic sheet in order to allow for curing for 30 days. Seven concrete cylinders (100 mm diameter x 200 mm height) were prepared for standard cylinder tests. The cylinders were prepared and cured according to the ASTM C31/C31M-19. The cylinders were also cured for 30 days following the same curing approach adopted for the RC wall. The compressive strength of the concrete was 38 MPa after 120 days. Concrete cylinders were tested according to the ASTM C39/C39M-18.

Table 5.2: Scaling relations of the physical modeling approach (Altaee and Fellenius, 1994)

Parameters	**Full scale (real structure)**	**Model**
Linear dimension	1	n
Area	1	n^2
Volume	1	n^3
Acceleration	1	1
Stress	1	N
Strain	1	1
Displacement	1	n
Force	1	Nn^2

Note: Geometric scale: $n = L_m/L_p$: is the relationship between the dimension of model and the real structure. Stress scale: $N = \sigma_m/\sigma_p$ stress scale ratio is the relationship between the stress of model and the real structure.

5.3.1.3 Model geometry and instrumentation

As mentioned earlier, in this study, sand was used as the: (1) backfill material behind the retaining wall, and (2) foundation soil under the heel of the retaining wall (Figures 5.4 and 5.5). The sand was placed in a box (1300 mm in length, 500 mm in width, and 1565 mm in height) that was made of wood. The soil below the foundation/heel was a dense layer with a relative density of 80 %. The height of the foundation layer was 915 mm, while the height of the backfill behind the stem was 650 mm. The sand backfill extended behind the wall for 1300 mm, which was double the RW height. The backside of the box was made of a flexible material (reinforced rubber sheet) in order to prevent soil confinement. One side of the box's wall was made of plexiglass in order to capture the movement of the soil-RW model by a high definition camera during the testing event. Furthermore, the sand in the box was surrounded by an impermeable membrane to avoid water leakage. The restricted testing area was considered during the selection of the model geometry.

Various instruments were placed in the soil-RW model to capture the dynamic response of the model during the blast event. Four pore water pressure sensors (PWP-1, PWP-2, PWP-3, and PWP-4) were used to measure the hydrostatic pressure in the sand. The sensors were connected to a high-speed data acquisition system that was employed for the collection of test data. Four dielectric water potential sensors (MPS-1, MPS-2, MPS-3, and MPS-4) were used to monitor the suction of the backfill and the foundation. Figure 5.4 shows the locations of the sensors. The ProAnalyst software (software guide) was used to capture the soil particles' movement and track the wall's transient and permanent displacements. Two high definition cameras were used in this experimental program. These cameras, equipped with a digital high-speed imaging system, were capable of recording thousands of high-resolution frames per second. Yellow beads were added to the sand particles facing the plexiglass to track the movement of these particles during the test. Soil model preparation was conducted at the Blast Research Laboratory of the University of Ottawa.

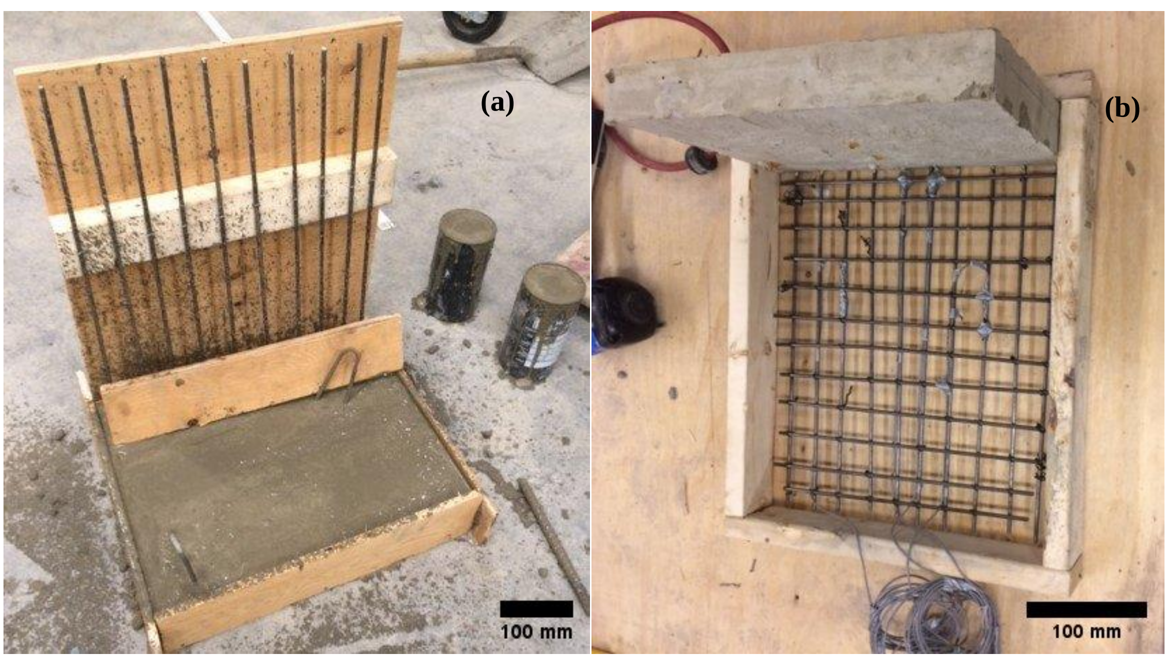

Figure 5.2: Reinforced concrete retaining wall
(a) the picture shows the heel was already cast. The reinforcement of the stem was not yet completed.
(b) the picture shows the heel was cured, and the stem was ready to be cast.

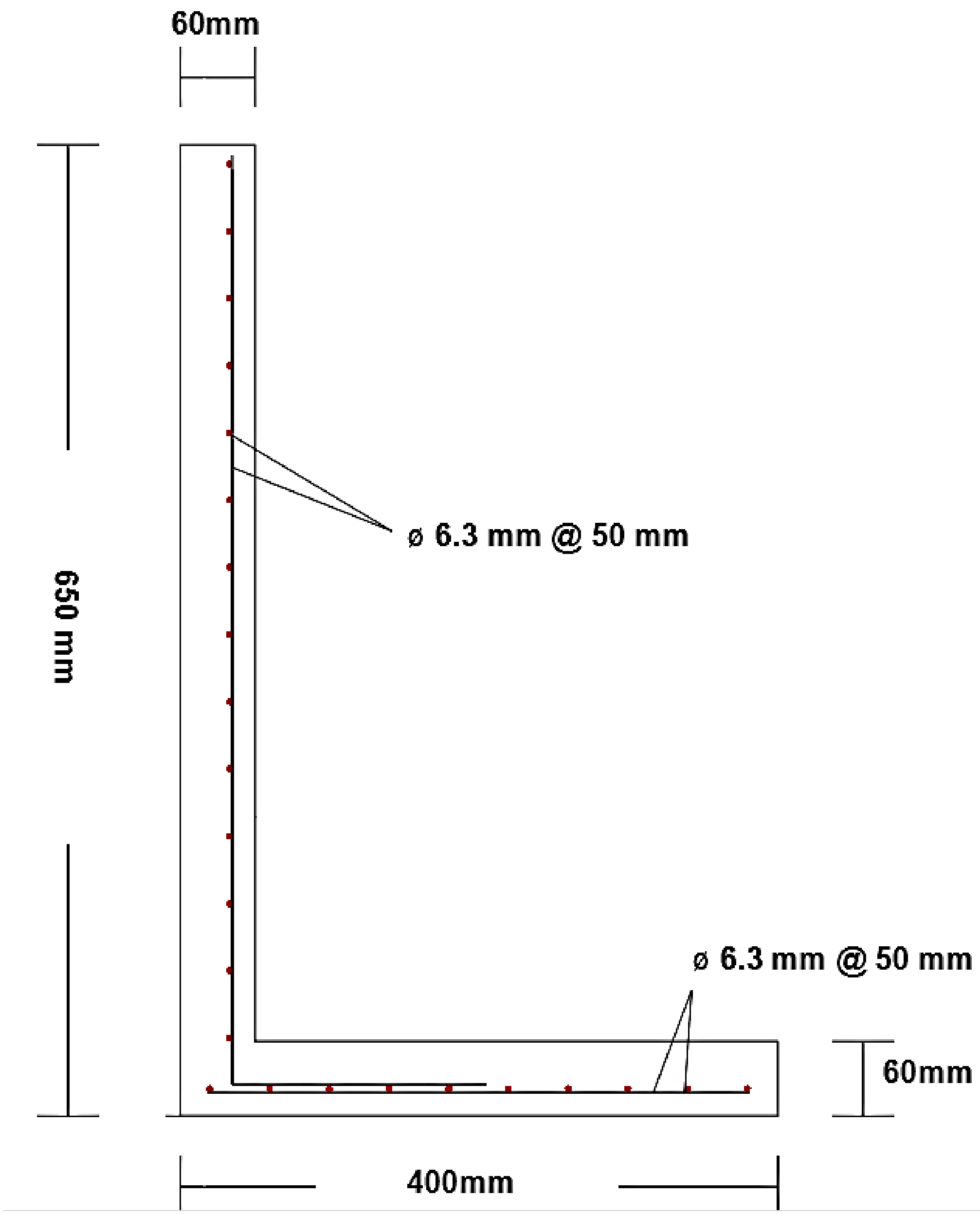

Figure 5.3: Details of retaining wall reinforcement

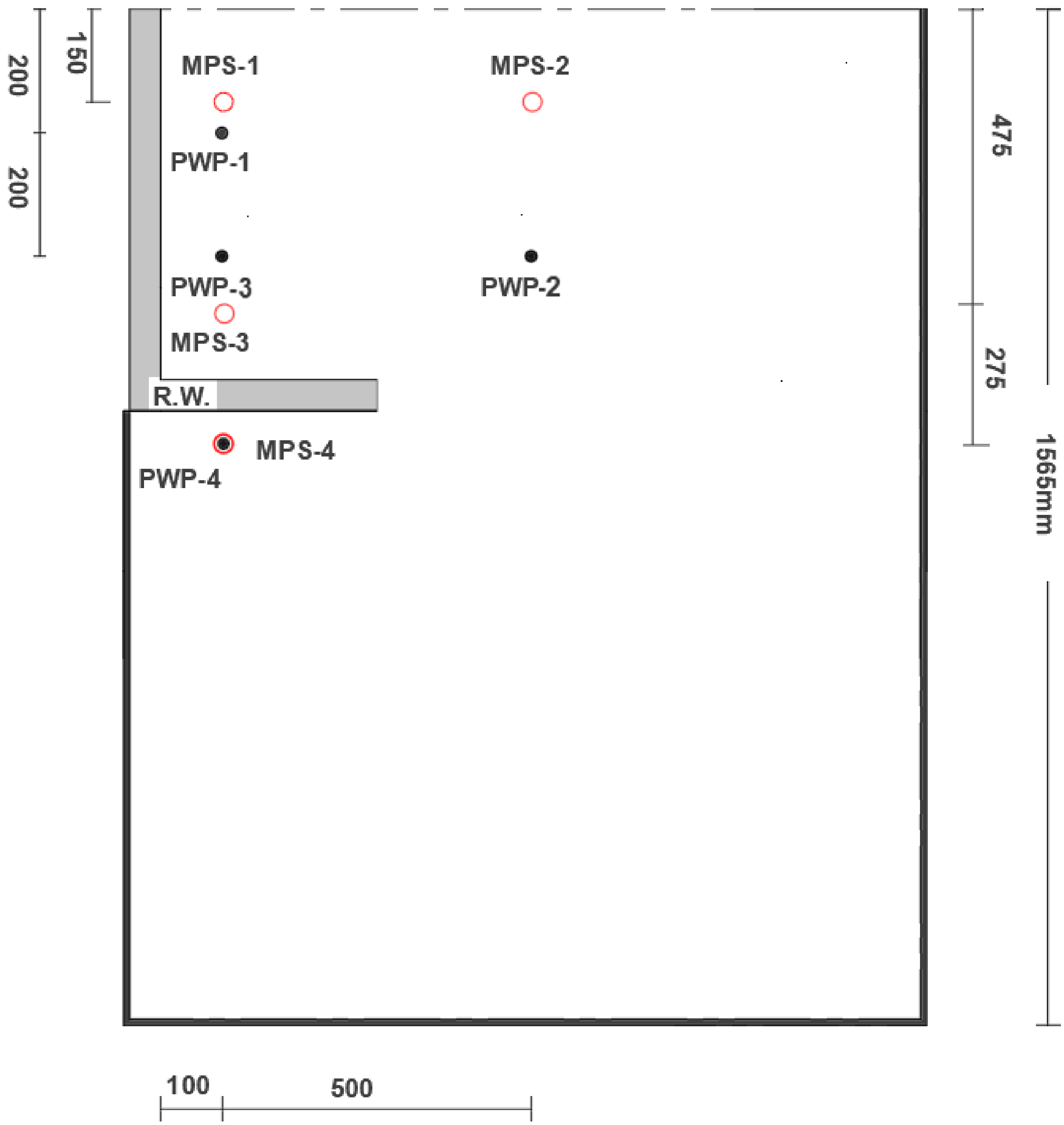

Figure 5.4: Locations of pore water pressure sensors and water potential sensors (dimensions in mm)
PWP: pore water pressure sensor; MPS: water potential sensor

5.3.2 Test Procedure

The test was devoted to studying the influence of various relative densities, degrees of saturation of backfill and live load surcharge on the dynamic response of soil-RW model when subjected to different blast load intensities. For every test conducted in this study, the system (RW and soil) was subjected to a single blast shot.

5.3.2.1 Relative density of the sand backfill and foundation

Three sand samples with various relative densities (loose, medium, and dense) were prepared and then subjected to pressure simulating a blast-induced shock wave. Relative densities of 30 %, 45 %, and 65 % were used for loose soil, medium soil, and dense soil, respectively (Das, 2016). Table 5.3 shows the state of granular soils at different ranges of relative density.

The space between the bottom of the wooden box and the bottom of the RW footing was filled with 200 mm thick successive layers of sand. Each sand layer was densified using a mechanical vibration technique (modified electrical drill) to reach a relative density of 80 %. The backfill was also formed by pouring sand in equal successive 200 mm thick layers. Each sand layer was manually compacted to the desired relative density. Figure 5.6 shows the steps for the box preparation and soil compaction.

Once the compaction of each layer was completed, three samples were taken and tested to ensure that the required relative density was reached.

A vibrating table compaction test was conducted to determine the optimum moisture content and maximum dry density. The test was run in accordance with the ASTM D4253-16. A water content of 2 – 3 % was chosen to reach the required relative densities in the foundation and the backfills (loose, medium, and dense).

Table 5.3: General correlation between relative density and denseness of a cohesionless soil (Das, 2016)

Relative density, Dr (%)	**Description**
0-15	Very loose
15-35	Loose
35-65	Medium
65-85	Dense
85-100	Very dense

5.3.2.2 Degree of saturation

Three sand backfill samples with different saturation degrees (100 %, 85 %, and 13 %) were tested. To achieve the fully saturated condition, the groundwater table was maintained at the surface level. The soil is considered partially saturated when the degree of saturation is around 85 %. To satisfy this condition, the groundwater table was kept at 250 mm below the top surface of the backfill. This means, the layer below the water table was saturated and the layer above the water table was partially saturated. When the degree of saturation is 0 %, the soil reaches dry condition. However, dry backfill is not applicable or common in the field. Therefore, in this study, moist backfill with a degree of saturation of 13 % was used instead of the dry condition. The degree of saturation of moist soil was calculated by dividing the volume of water by the volume of the void. The volume of the void can be determined by knowing the moist and dry densities of the sand, while the volume of water can be calculated from the water content and specific gravity of the sand.

The backfill was compacted to meet in-situ dry density (Federal Highway Administration, FHWA, specifications, 2008 and Morris and Delphia, 1999). The dry density of the backfill was 16 kN/m^3, which was within the acceptable range recommended by the above-mentioned specifications.

The degree of saturation of the foundation was 100 % when the degree of saturation of the backfill was 100 % and 85 %. On the other hand, the degree of saturation of the foundation was 13 % when the degree of saturation of the backfill was 13 %.

5.3.2.3 Blast loads intensity

Three driver pressures were adopted in this study. A driver pressure of 137 kPa resulted in a maximum reflected pressure (Pr) of 26 kPa. The second driver pressure was equal to 241 kPa, which resulted in a maximum Pr of 47 kPa. Lastly, a driver pressure of 379 kPa was used to generate a maximum Pr of 71 kPa. The reflected pressures were selected to cause a different level of damage on the RW-soil system, ranging from elastic to full plastic failure. Furthermore, a scaling chart (Cormie, Mays, and Smith, 2009) was utilized to match the reflected pressures used in this paper to a specific field blast parameter. For example, detonation of a 227 kg TNT hemispherical charge at a distance of 36 m produced a reflected pressure of 71 kPa.

5.3.2.4 Live load surcharge

Lateral earth pressure, lateral hydrostatic pressure, and vertical traffic loads that generate supplemental lateral load on the RW are the three major loads acting on a RW. Highway traffic load equivalent surcharge can be neglected if the traffic load location is far enough from the wall (Chen and Duan, 2014). As per AASHTO design codes (AASHTO 2002, and 2012), live load surcharge can be equivalent to a soil height of 600 mm placed on the top level of the wall.

To address the influence of the live load surcharge on the behaviour of RW backfill in this study, 60 mm (the wall is modeled at the 1/10th scale, Table 5.2) of soil was added to the top level of the backfill. This added layer was compacted to achieve the in-situ required density.

Figure 5.5: Steps of box preparation and soil compaction

The box was built in stages, **step 1** represents the first stage of the box. The height of this portion of the box was 400 mm. The sand for the foundation layer has been compacted using mechanical vibration technique (modified electrical drill). **Step 2** presents the front view of the specimen where the wall is located. In this step the compaction of the foundation is completed and the wall is placed in the box. **Step 3** shows the side view of the box where the plexiglass is located. The box was moved in front of the shock tube and the backfilling process then performed.

5.3.3 Test Setup

5.3.3.1 Soil-retaining wall model

All tests in this study were conducted using the shock tube at the Blast Research Laboratory of the University of Ottawa. The test specimen (soil-RW model) was placed at the centre of the shock tube's mouth. The rest of the shock tube's mouth was covered with a very stiff steel plate. The test specimen consisted of a reinforced concrete retaining wall and a box filled with sand. The top of the box was left open to allow soil filling and compaction. The RCRW was placed on the side of the box that faced the shock tube, as shown in Figure 5.5. The test specimen was attached to the shock tube by straps to prevent the specimen from moving away from the shock tube during the blast test. The blast pressure formed by the shock tube was transferred directly to the test specimen, and it was uniformly distributed over the area of the RCRW. The shock tube was controlled by a firing system to start the test. Figures 5.6 and 5.7 show the test setup adopted in this study.

In-situ, soils usually experience a stress history that can change the soil structure. Many factors, such as climatic environment changes or man-made construction, can lead to a changing stress state or stress history in soils. A total stress ratio (TSR) is used as a measure of the stress history of compacted soil (Nishimura et al., 1999). TSR is the ratio of the compaction pressure to the current confining pressure.

In order to limit the effect of stress history, backfill material was removed from the box after each test. The sand was then mixed and used to refill the box. The backfill material was compacted to meet the required compaction level for each test.

The soil under the wall's footing level (heel) was not disturbed by the blast shocks applied; thus, with the exception of the loose backfill condition test, the soil was not compacted after each test. Once the loose backfill condition test was carried out, the RC wall was removed, and portions of the box were disassembled. The soil below the heel was dug out, mixed on a tarp, then put back and compacted again to reach the required relative density. Prior to the excavation of the foundation layers, the sand was tested to determine if there was any change in the soil's relative density below the RW. The results showed that the TSR was 1.02, which was within the acceptable range, indicating that the changes were insignificant.

5.3.3.2 Blast loading protocol

Prior to testing, the specimen was attached firmly to the shock tube, using three straps (Figure 5.7). The two high-speed video cameras were set up and connected to the data acquisition system, and a laptop was used for video monitoring. A trigger signal was induced to confirm that the data acquisition device and cameras were recording at the same time. The driver and spool sections of the shock tube were then filled up to the required level of pressurized air. The test started by draining pressure from the spool section, which led to an imbalance in pressures on both sides of the aluminum diaphragm. As a result, the aluminum diaphragm was ruptured, and the pressurized air was passed at a very high speed towards the expansion shock tube nozzle.

5.3.3.3 Data acquisition

The data acquisition system used in this research was two digital oscilloscopes readings at 100,000 Hz (samples per second). Four channels recorded pore water pressure readings and two channels were used to record reflected pressure. Pressure sensors were adopted to measure the reflected pressure located at the side and bottom of the shock tube’s mouth.

5.3.3.4 Shock tube

The shock tube consists of four main sections (Figure 5.8). The driver and the spool are the first and second sections, respectively. These are the sections in which the shock energy is built-up, and the firing action occurs. The length of the driver section ranges between 305 mm and 5185 mm in 305 mm increments. Based on the required peak reflected pressure and total impulse, a driver length is selected. The driver length has a minor influence on the reflected pressure but has an effect on the impulse (Lloyd, 2010). Since the impulse should be given equal consideration as the reflected pressure (Mays and Smith, 1995), in this experiment, the length of the driver section was kept at 2743 mm. The blast wave formed in the driver section propagates and expands through the expansion section, which starts from 597 mm in diameter and ends with the square test area of 2033 mm by 2033 mm. The test specimen was attached to the opening of the steel plate located at the front of the shock tube. The length of the expansion section is 7 m. The shock tube is operated manually by incrementally increasing the driver pressure and the spool pressure to the required level and then trigger firing by draining pressure from the spool section to cause the aluminum foil diaphragms to rupture.

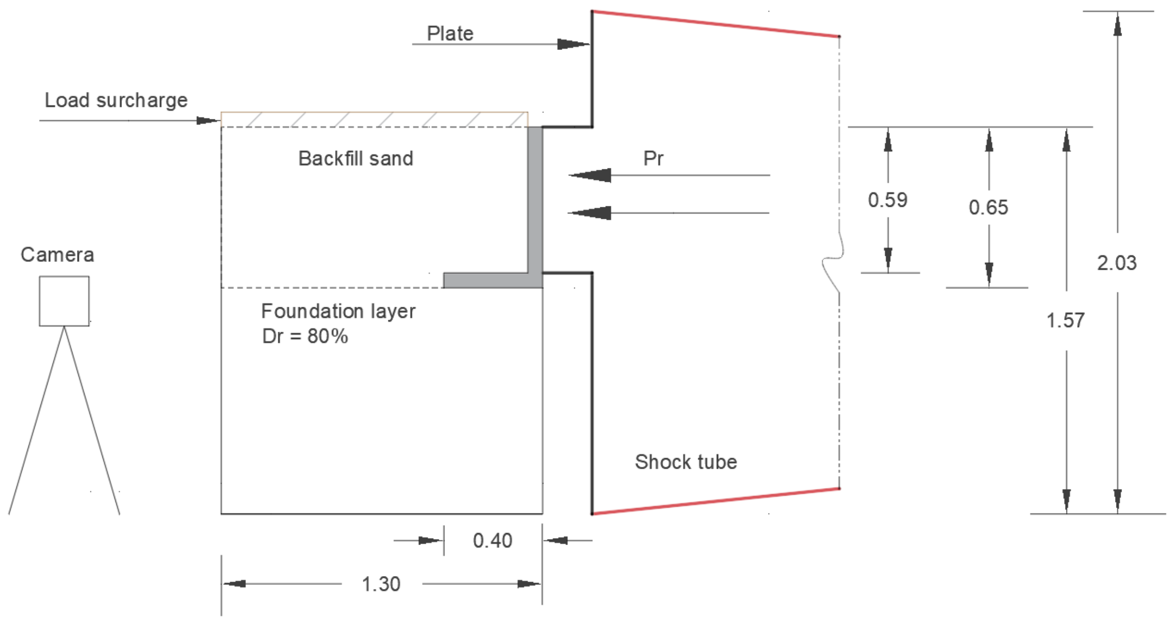

Figure 5.6: Test setup and preparation; dimensions in m (schematic)

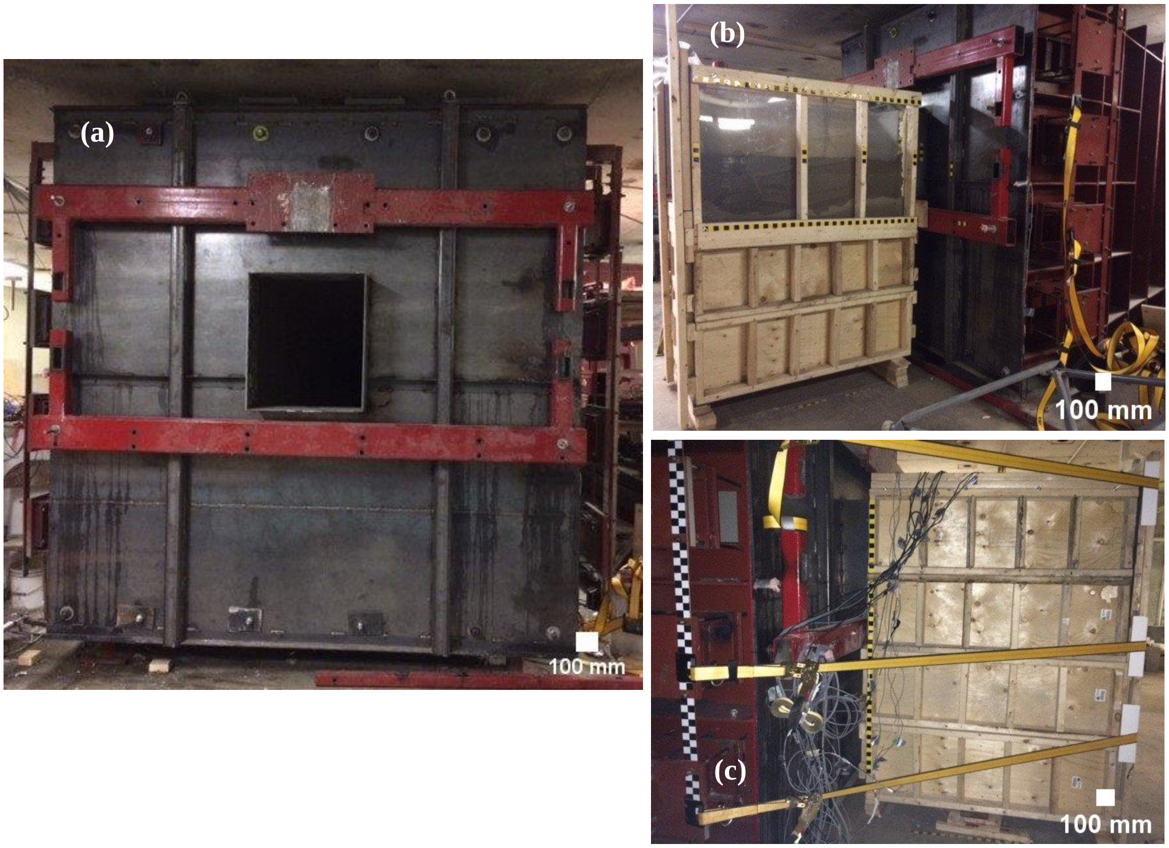

Figure 5.7: Test setup (a) covering the shock tube's mouth with a stiff plate; (b) placing the test specimen at the centre of the shock tube; (c) fastening the test specimen to the shock tube using straps

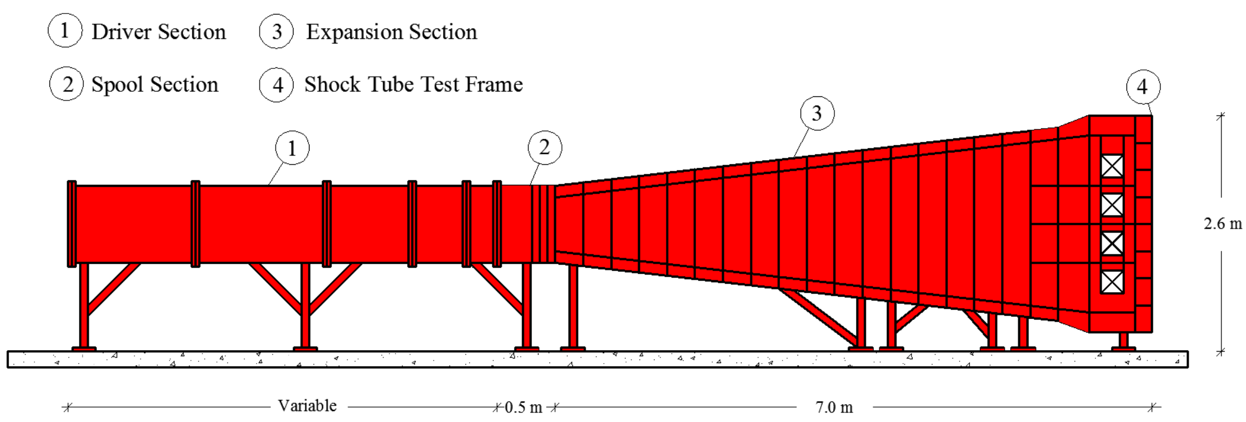

Figure 5.8: Shock tube sections; schematic (Kadhom, 2016)

5.4. Results and Discussion

5.4.1 Pore Water Pressure Changes

Table 5.4 and Figure 5.5 give the locations of the pore water pressure sensors used to measure the pore water pressures (PWPs) in the backfill and the foundation. It was noticed during the tests that PWP-2 was defective; therefore, no results were obtained from this sensor. Initial and excess pore water pressure-time histories are represented in Figure 5.9. The figure shows pore water pressure fluctuation for the backfill and the foundation with different relative densities, degrees of saturation, live load surcharge, and various blast load intensities.

Table 5.4: Locations of pore water pressure sensors

Pore water pressure sensor	Depth from the top of the wall	Horizontal distance behind the wall
PWP-1	200 mm	100 mm
PWP-2	400 mm	600 mm
PWP-3	400 mm	100 mm
PWP-4	750 mm	200 mm

5.4.1.1 Relative density

The increase in the pore water pressures (Δu) for loose backfill is presented in Figure 5.9a. There was no result obtained from PWP-1 for this test since the sensor did not provide any useful data. Regarding PWP-3, it can be seen that the maximum response was within the positive phase duration. A small increase occurred in the pore pressure above the initial value and then dropped below the initial value at the end of the positive phase duration. Loose soil tends to decrease in volume when subjected to loading (Rauch, 1997). Applying blast load on the RW caused the sand grains behind the RW to compact and rearrange, which reduced the space in the voids. Since the voids contained some water, a reduction in the pore size forced the water out. As a result, a small increase in pore water pressure was developed. After the blast pressure decayed, the sand backfill reached the unloading condition, where no more shear stress was applied. This might have released the pore pressure which explains the reduction in pore pressure observed. As mentioned earlier, the degree of saturation for the backfill of this test was 13%. As the sand was in the unsaturated condition, it was unexpected to have a sharp change in the pore pressure or generation of excess pore pressures.

A slight increase in the pore pressure was noticed in PWP-4 as well, and it was within the positive phase duration. On the other hand, a reduction in the pore pressure below the initial value was shown in PWP-4 at a time greater than the positive phase duration. It seems that the impact of the blast loading generated a fluctuation in the pore pressure below the foundation (PWP-4). First, the blast pressure might have resulted in compacting the dense foundation layer, which resulted in increasing the pore pressure (Das, 2011). However, after a certain period, dilation in the sand of the foundation layer could occur, which caused a slight drop in the pore pressure. As mentioned in section 5.3.3.1, the foundation layer was readjusted after this test due to the translation movement in the wall. Table 5.5 displays the values for the maximum Δu.

Figure 5.9b depicts the pore pressure-time history for medium dense backfill. A drop in the pore pressure below the initial value in PWP-3 for medium backfill was observed. A slight increase in the pore pressure in PWP-1 was noticed at a time greater than the positive phase duration. There was no development in the excess pore pressure in PWP-3. The maximum response for PWP-4 was within the positive phase duration (Table 5.5). It can be seen from the results of all PWP sensors that pore water pressure kept fluctuating and then dissipated at a time close to 100 ms. When the blast load hit the RW, the sand particles behind the RW had a tendency to move and rearrange to absorb a portion of the blast energy, which could be the reason for the fluctuation. During this process, the sand backfill deformed vertically and laterally, as shown in Figures 5.11 and 5.12, respectively. These deformations led to a change in the space in the voids, and thus, based on the size of the pores, the pore pressure conditions changed.

Figure 5.9c presents the maximum responses for dense backfill. The excess pore water pressure for PWP-1 and PWP-3 was noticed at a time greater than the positive phase duration. A drop in pore water pressure was observed during the positive phase duration for PWP-1 and PWP-3. From the settlement results for dense backfill (Figure 5.11c), it was noticed that the sand grains moved up (increase in volume) during the positive phase duration and then settled back to below or at the original locations. This can be the reason for the decrease in the pore pressures during the positive phase duration and then the increase in the pore pressure at time greater than the positive phase duration. For PWP-4, the maximum response occurred at the end of the positive phase duration. The fluctuation in pore pressure at PWP-4 showed a similar trend to the PWP-4 for medium backfill. This could be explained by the fact that the foundation layer for both conditions had the same relative density. Furthermore, almost equal blast load intensities were applied on them. The relative density of the backfills was the only variable.

It was noticed that the increases in pore water pressures were dissipated after 100 ms and returned to the initial stage (Figures 5.9a, 5.9b, and 5.9c). This can be explained by the fact that when the blast load effects diminished, the pore pressure returned to its unloading stage. This means that the blast load had a temporary influence on the development of excess pore water pressure for this test and the backfill response remained in the elastic range.

5.4.1.2 Blast loads intensity

In this part of the study, the specimen was subjected to various blast load intensities (26 kPa, 47 kPa, and 71 kPa). There were no results obtained from the sensors when dense backfill was subjected to a reflected pressure of 26 kPa. The maximum excess pore water pressure for dense backfill when subjected to a reflected pressure of 47 kPa is addressed in section 5.4.1.1.

The influence of a reflected pressure of 71 kPa on the pore water pressure in dense backfill is shown in Figure 5.9d. The maximum responses in all sensors were at a time greater than the positive phase duration (Table 5.5). A drop in pore water pressure was noticed in PWP-3 within the positive phase duration and then raised above the initial values at a time greater than the positive phase duration. The reason for the decrease in pore pressure is explained earlier in section 5.4.1.1, when analysing dense backfill under a reflected pressure of 47 kPa. There was a marginal increase in the pore pressure below the heel (PWP-4). It can be seen from Figures 5.9c and 5.9d that the fluctuation in the PWP-4 had a similar trend for dense backfill under reflected pressures of 47 kPa and 71 kPa.

5.4.1.3 Degree of saturation

Figure 5.9e represents the pore pressure time histories for partially saturated backfill. The water level in the specimen was at 250 mm below the backfill surface. The maximum Δu for PWP-1 and PWP- 3 were reached at a time greater than the positive phase duration. A drop in the pore pressure in PWP-3 was observed during the positive phase duration. There was no excess pore pressure in PWP-4. A slight drop in the pore pressure at PWP-4 was noticed beyond the positive phase duration. It is important to mention that both PWP-3 and PWP-4 were located below the groundwater level, and thus, the sand at these locations was considered saturated.

For saturated backfill, the maximum responses for PWP-1 and PWP-3 were at a time greater than the positive phase duration. The pore pressures at PWP-1 and PWP-3 showed fluctuation with time. On the other hand, a small drop in the pore pressure was noticed at PWP-4 during the positive phase duration and then increased to reach the maximum Δu at the end of the period (Figure 5.9f). When dense saturated sand is subjected to a dynamic load, the tendency of dilation results in a decrease of pore pressure to the point that it can become negative (Rauch, 1997). This can explain the drop in pore water pressure immediately after the application of blast loading (Figures 5.9e and 5.9f).

It can be seen that for all tests, the excess pore water pressures below the foundation were very low. This means that the effect of blast loads was very limited on the dense backfill below the heel, and the stress state of the foundation layer was not altered.

Table 5.5: The maximum excess pore water pressure

Condition of backfill	Pore water pressure sensor	Δu (kPa)	Time (ms)
Loose backfill, max Pr = 49 kPa at 18.2 ms	PWP-1	-	-
	PWP-3	0.9	29.4
	PWP-4	0.9	30.6
Medium backfill, max Pr = 50 kPa at 18.6 ms	PWP-1	0.6	104
	PWP-3	-	-
	PWP-4	1.0	35
Dense backfill, max Pr = 47 kPa at 18.6 ms	PWP-1	0.9	104.2
	PWP-3	0.7	107
	PWP-4	1.0	39.2
Dense backfill, max Pr = 71.7 kPa at 18.6 ms	PWP-1	0.7	110.6
	PWP-3	0.8	110.6
	PWP-4	0.9	43.2
Partially saturated backfill, max Pr = 52.65 kPa at 18 ms	PWP-1	1.4	106.8
	PWP-3	1.4	106.2
	PWP-4	-	-
Saturated backfill, max Pr = 50.47 kPa at 18.6 ms	PWP-1	0.8	105.8
	PWP-3	1.1	108.6
	PWP-4	1.0	43

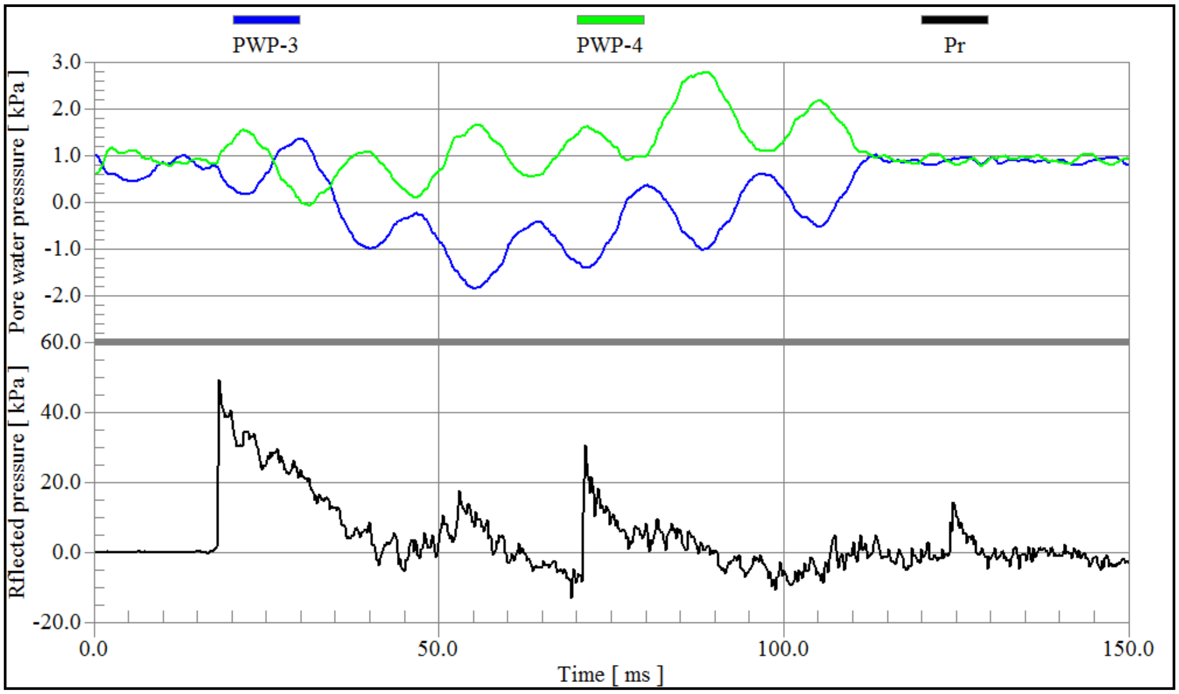

PWP-3
PWP-4
Pr
Pore water presssure [kPa]
Rflected pressure [kPa]
Time [ms]

(a)

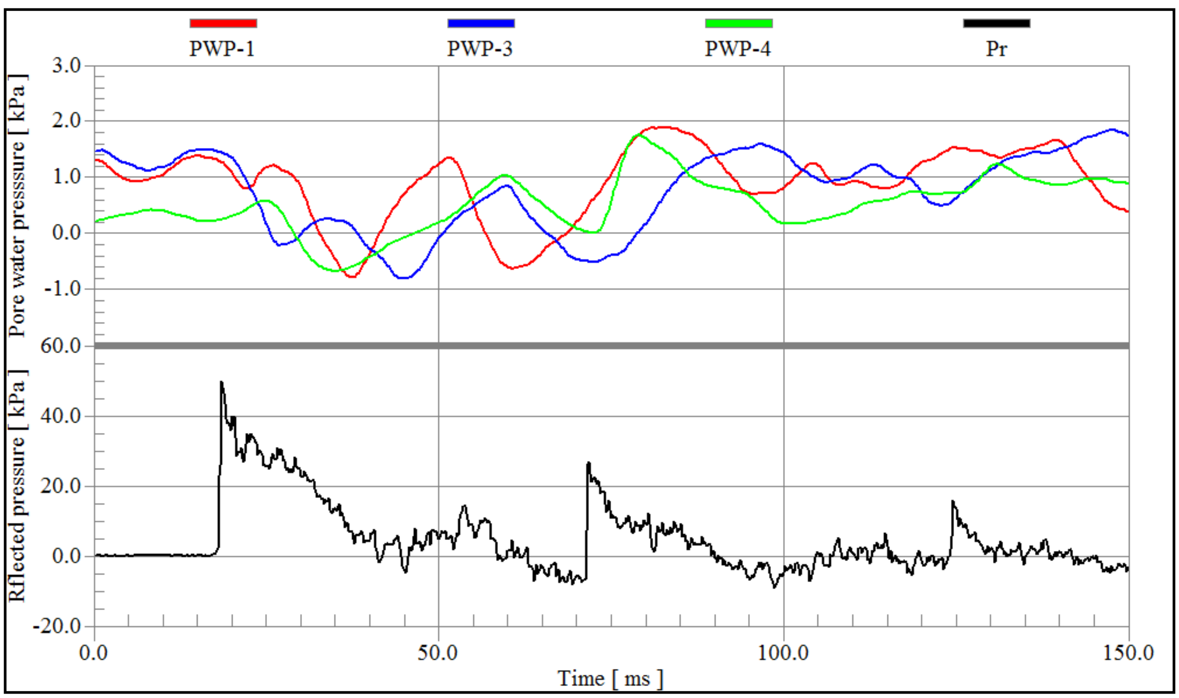

PWP-1
PWP-3
PWP-4
Pr
Pore water presssure [kPa]
Rflected pressure [kPa]
Time [ms]

(b)

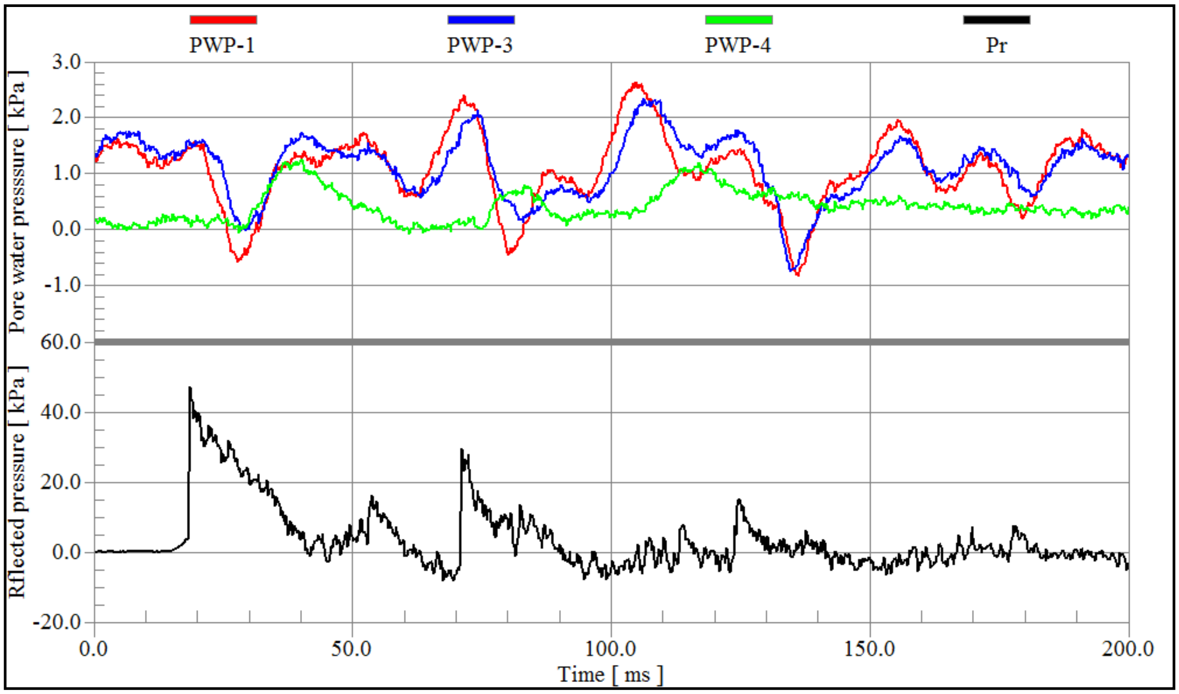
PWP-1
PWP-3
PWP-4
Pr
Pore water presssure [kPa]
Rflected pressure [kPa]
3.0
2.0
1.0
0.0
-1.0
60.0
40.0
20.0
0.0
-20.0
0.0
50.0
100.0
150.0
200.0
Time [ms]

(c)

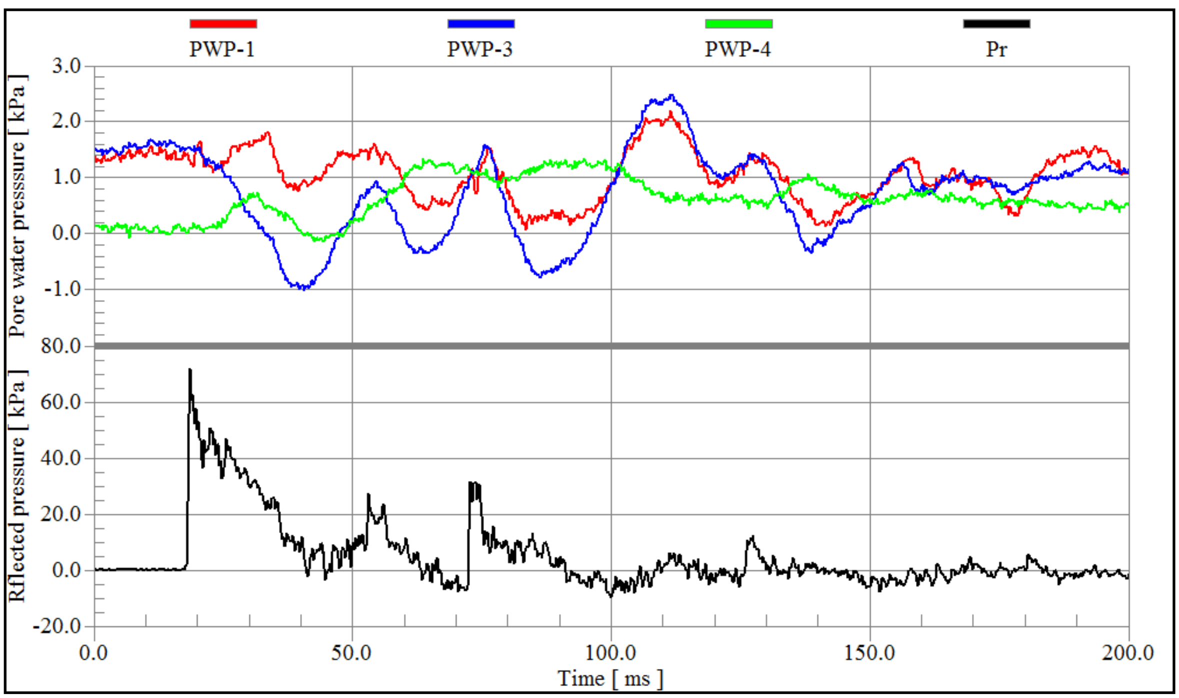
PWP-1
PWP-3
PWP-4
Pr
Pore water presssure [kPa]
Rflected pressure [kPa]
3.0
2.0
1.0
0.0
-1.0
80.0
60.0
40.0
20.0
0.0
-20.0
0.0
50.0
100.0
150.0
200.0
Time [ms]

(d)

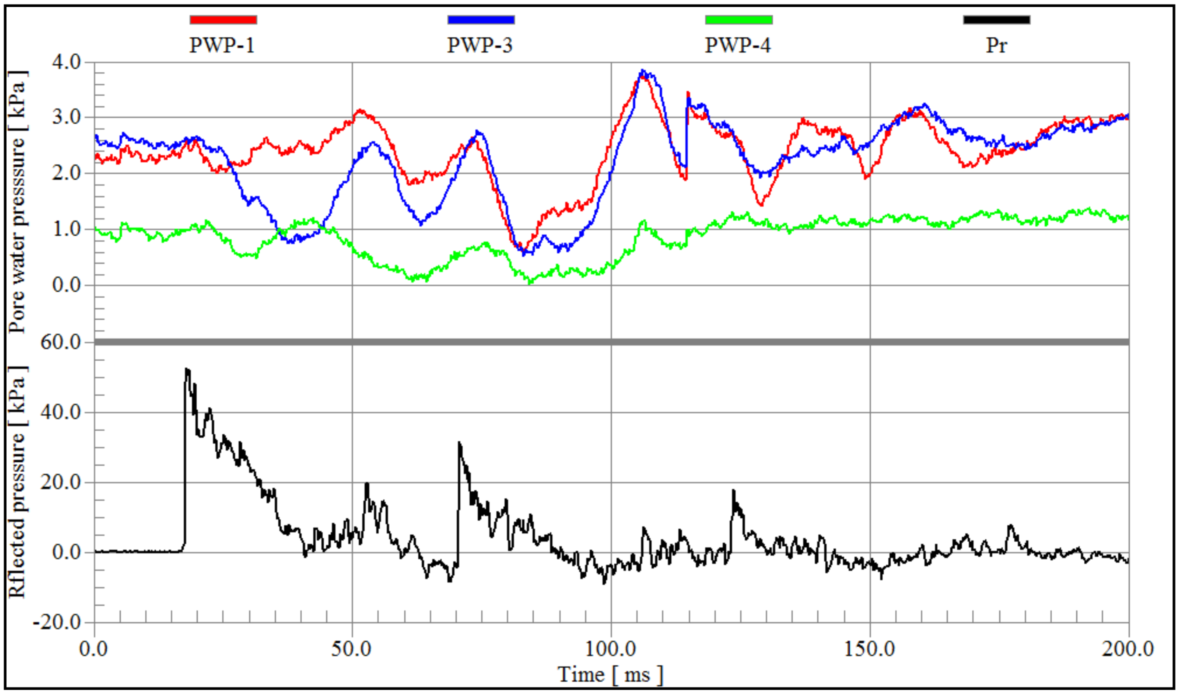

(e)

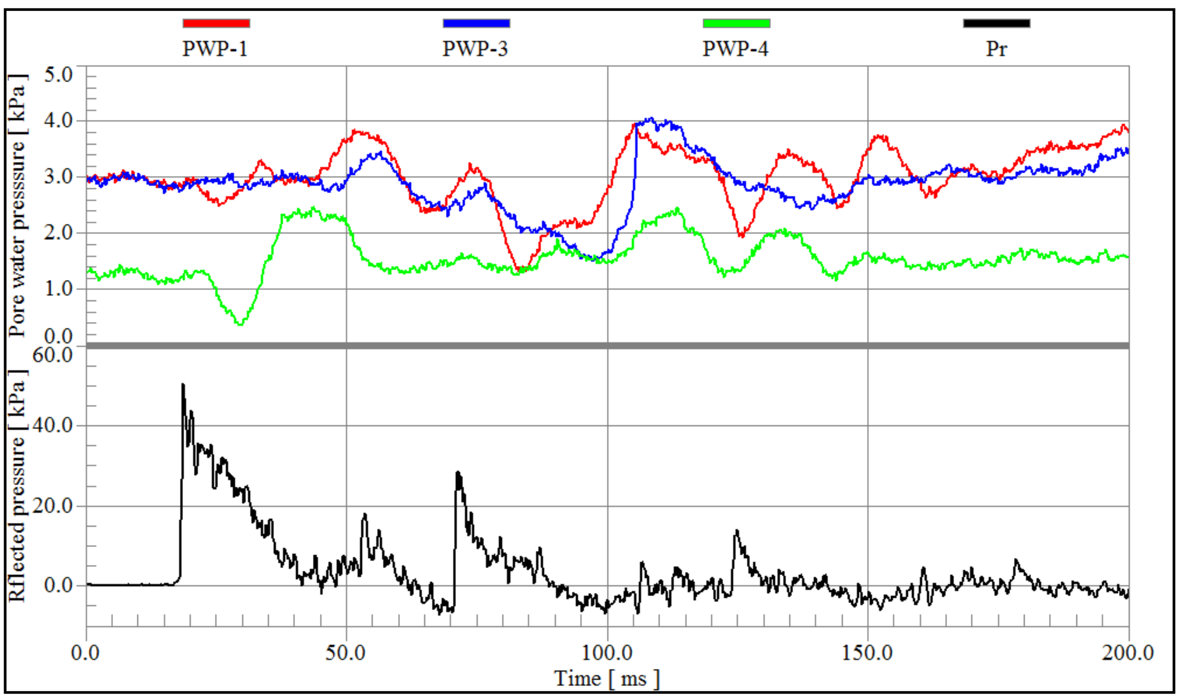

(f)

Figure 5.9: Initial and excess pore water pressure time histories for; (a) loose, (b) medium, and (c) dense backfill, (d) reflected pressure of 71 kPa, (e) partially saturated backfill, (f) saturated backfill

PWP: pore water pressure, Pr: reflected pressure

5.4.2 Suction Variations

Table 5.6 and Figure 5.5 give the locations of the sensors used to monitor the suction. The sensors recorded one reading every minute. Since the blast responses were in milliseconds, the data from these sensors were used for qualitative evaluation. The sensors started recording 30 minutes prior to testing and continued to record around 10 minutes after testing.

Figure 5.10 presents the suction time histories of backfill and foundation. The figure shows the changes in suction due to different relative densities and degrees of saturation when subjected to various blast load intensities. It was noticed that no readings were recorded at MPS-1 and MPS-3 during the blast tests. The suction for the sensor close to the surface (MPS-2) ranged between -10 kPa and -12 kPa for all conditions (Figure 5.10a). On the other hand, the suction for the sensor below the foundation (MPS-4) ranged between -11 kPa and -18 kPa (Figure 5.10b).

The results showed that there was no noticeable development in suction during the application of blast loads. The reason might be that the data logger was not designed to capture the data from impulsive loads, or that the intensities of blast load were not strong enough to affect the soil's suction. More tests will be needed in this area.

Table 5.6: Locations of water potential sensors

Water potential sensor	Depth from the top of the wall	Horizontal distance behind the wall
MPS-1	150 mm	100 mm
MPS-2	150 mm	600 mm
MPS-3	440 mm	100 mm
MPS-4	750 mm	200 mm

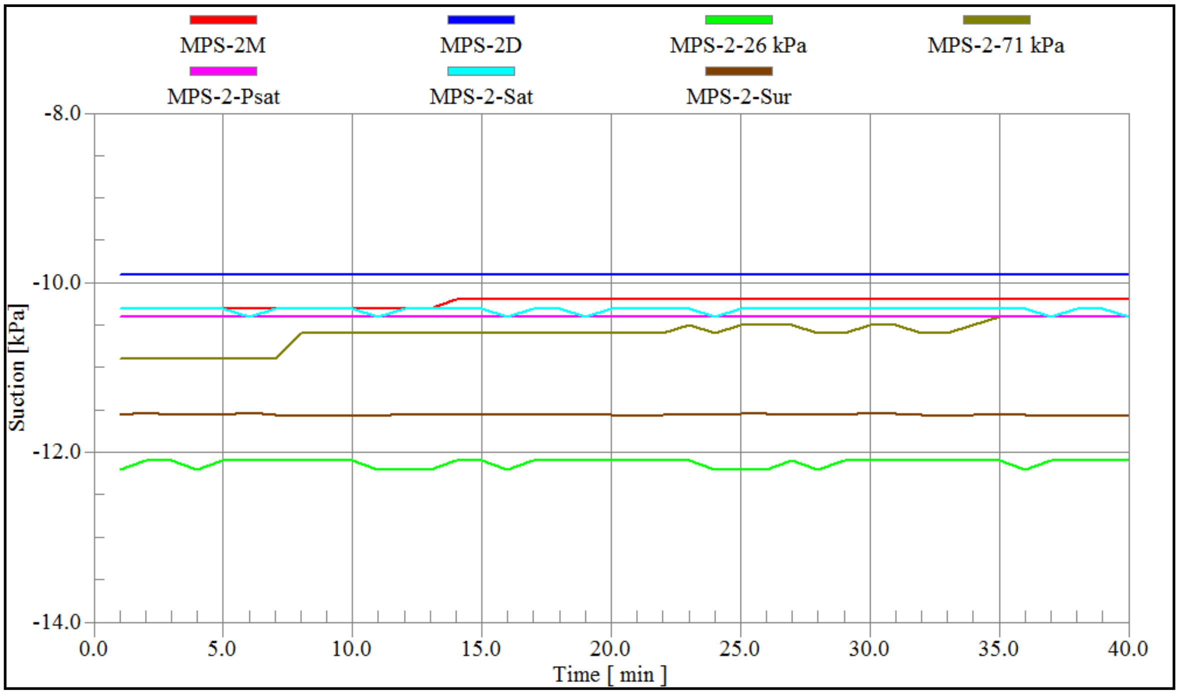

(a)

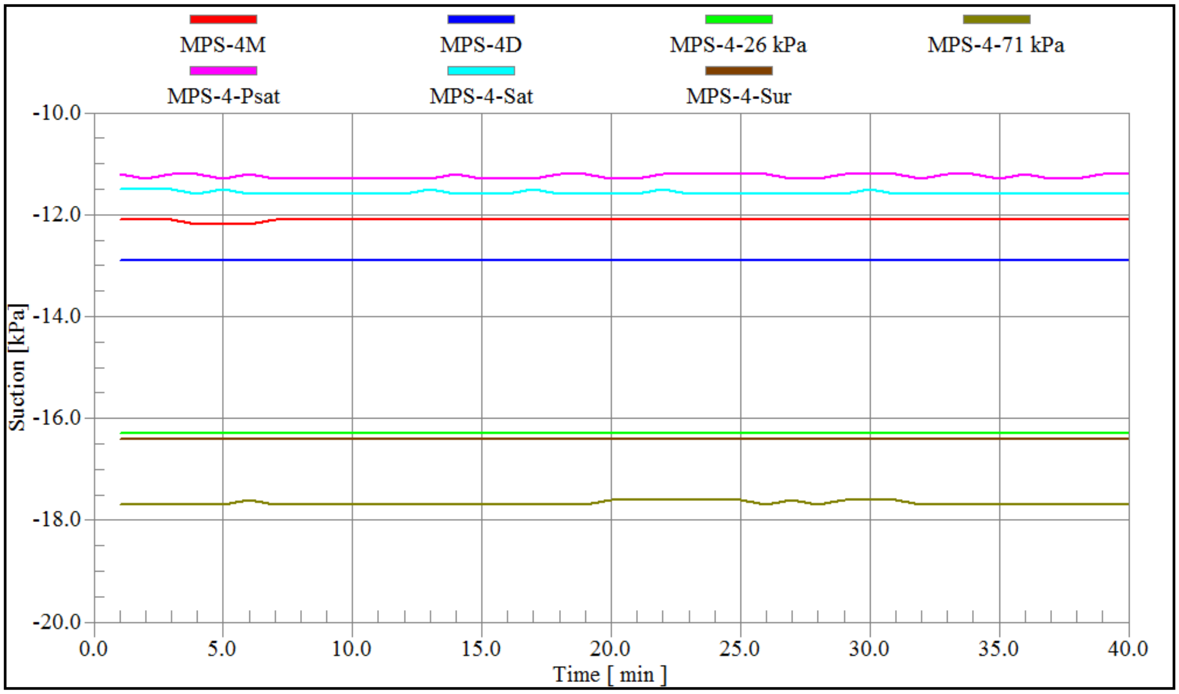

(b)

Figure 5.10: Suction time histories for backfill and foundation; (a) data from MPS-1 and MPS-2, (b) data from MPS-3 and MPS-4.
M: medium, **D**: dense, **26 kPa**; a reflected pressure of 26 kPa, **71 kPa**: a reflected pressure of 71 kPa, **Psat**: partially saturated backfill, **Sat**: saturated backfill, **Sur**: live load surcharge

5.4.3 Settlements

Vertical displacement time histories for backfill sands are presented in Figure 5.11. The vertical displacements were measured along the height of the backfill. Randomly selected points were chosen at each layer to measure the backfill settlements. The thickness of each layer was around 200 mm.

It can be seen that the largest settlements occurred in loose and medium backfill sands (Figures 5.11a and 5.11b). Since loose and medium backfills had more space between the particles than dense sand, applying the blast pressure led to compacting the sand grains and reducing the sand's volume. On the other hand, for all tests, the vertical displacements in the backfill (in this paper, backfill represents the sand above the heel) were larger than the vertical displacements in the sand behind the footing. As the blast waves propagated through the sand, they generated shear stress and strains/deformations. However, wave energy and amplitude decreased with distance as the energy dissipated in the sand (Smith and Hetherington, 2011). Consequently, the vertical displacements decreased with distances further from the RW.

In all conditions, there were no settlements in the RW. The figures showed that the RW jumped up a few millimetres and then returned to its initial position. This is because the foundation layer was very dense, and the impact from the blast loads had no effect on it.

It was noticed that immediately after the blast, the retained soil dilated along the positive phase duration and then, beyond the positive phase duration, different levels of settlements happened for each condition. The soil dilation was very limited in loose sand. It is well documented that all soils, except the loose ones, tend to dilate when substantial shear strains/deformations begin to develop (Das, 2011, WU et al., 2004, Rauch, 1997).

In general, very limited settlements were noticed in dense sand with different blast load intensities and various degrees of saturation.

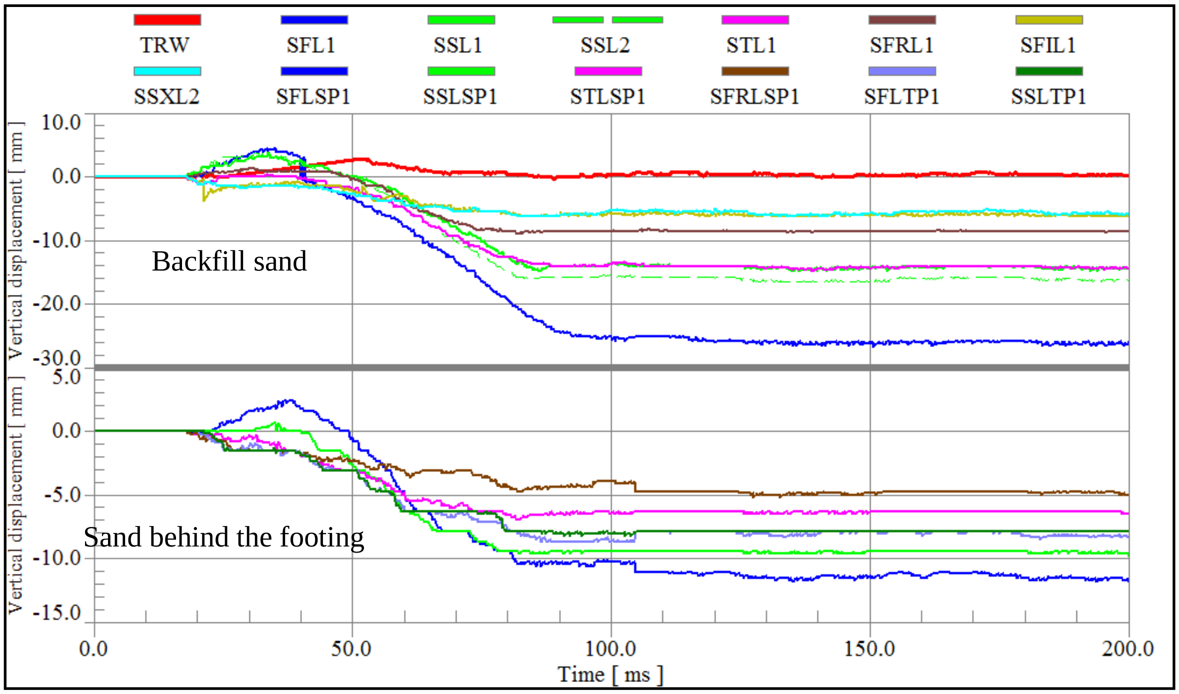

(a)

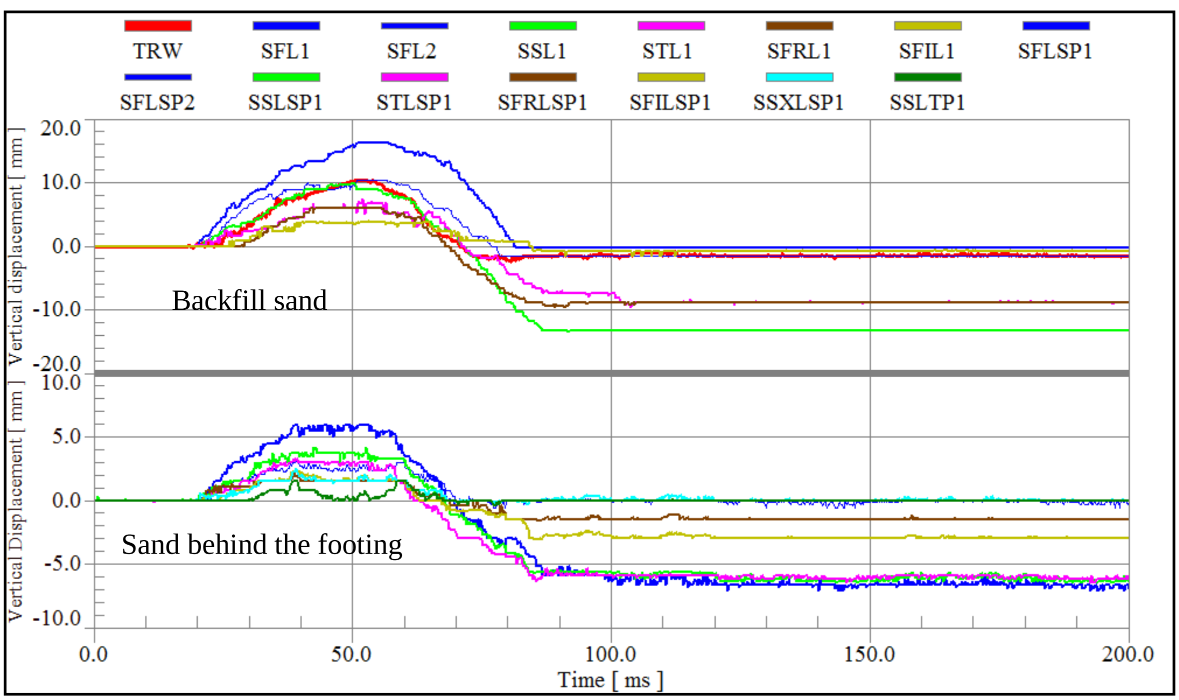

(b)

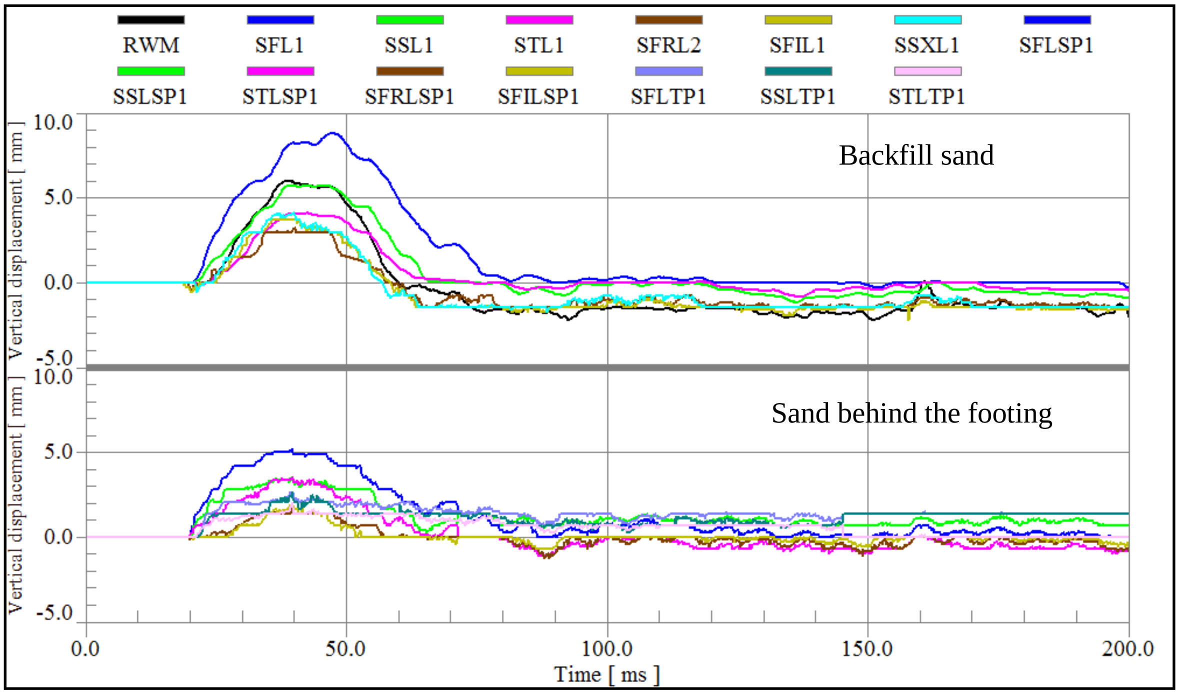
RWM
SFL1
SSL1
STL1
SFRL2
SFIL1
SSXL1
SFLSP1
SSLSP1
STLSP1
SFRLSP1
SFILSP1
SFLTP1
SSLTP1
STLTP1
Backfill sand
Sand behind the footing
Vertical displacement [mm]
Vertical displacement [mm]
10.0
5.0
0.0
-5.0
10.0
5.0
0.0
-5.0
0.0
50.0
100.0
150.0
200.0
Time [ms]

(c)

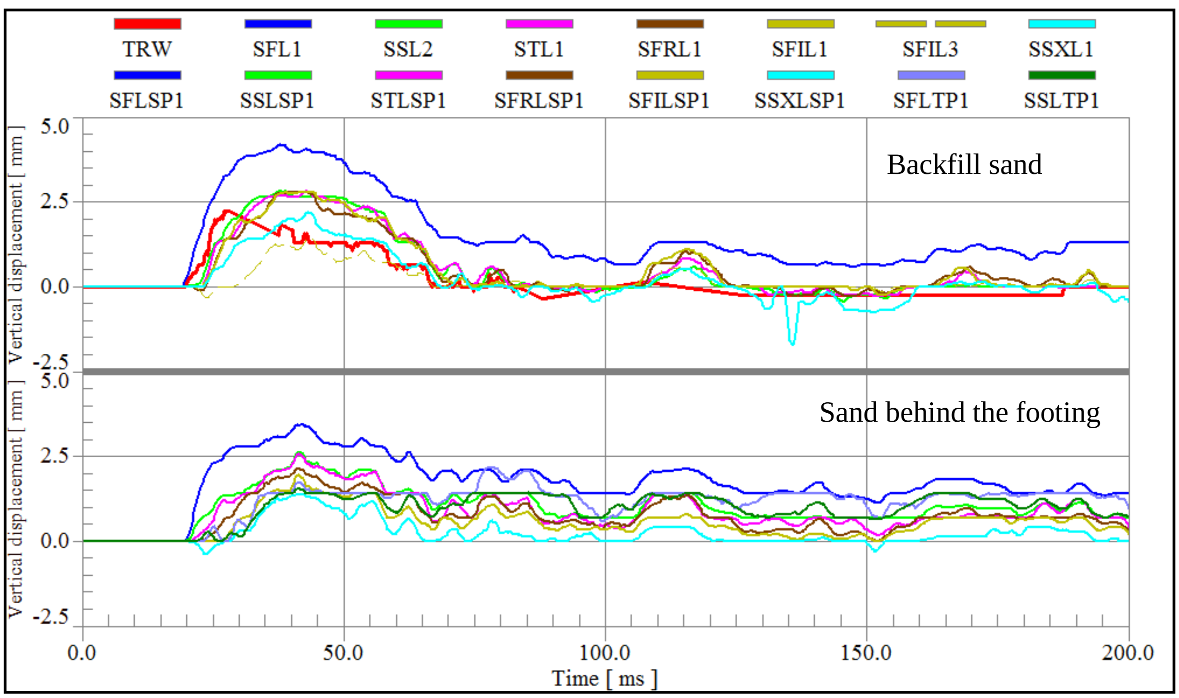
TRW
SFL1
SSL2
STL1
SFRL1
SFIL1
SFIL3
SSXL1
SFLSP1
SSLSP1
STLSP1
SFRLSP1
SFILSP1
SSXLSP1
SFLTP1
SSLTP1
Backfill sand
Sand behind the footing
Vertical displacement [mm]
Vertical displacement [mm]
5.0
2.5
0.0
-2.5
5.0
2.5
0.0
-2.5
0.0
50.0
100.0
150.0
200.0
Time [ms]

(d)

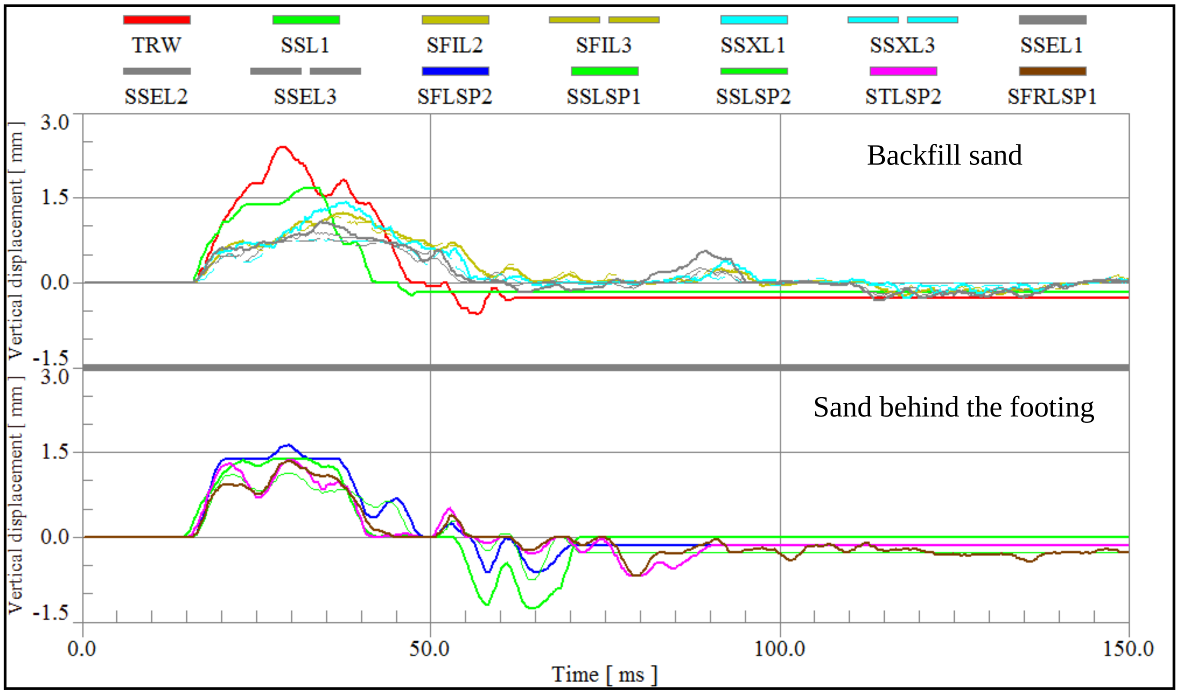
TRW
SSL1
SFIL2
SFIL3
SSXL1
SSXL3
SSEL1
SSEL2
SSEL3
SFLSP2
SSLSP1
SSLSP2
STLSP2
SFRLSP1
Backfill sand
Sand behind the footing
Vertical displacement [mm]
Time [ms]

(e)

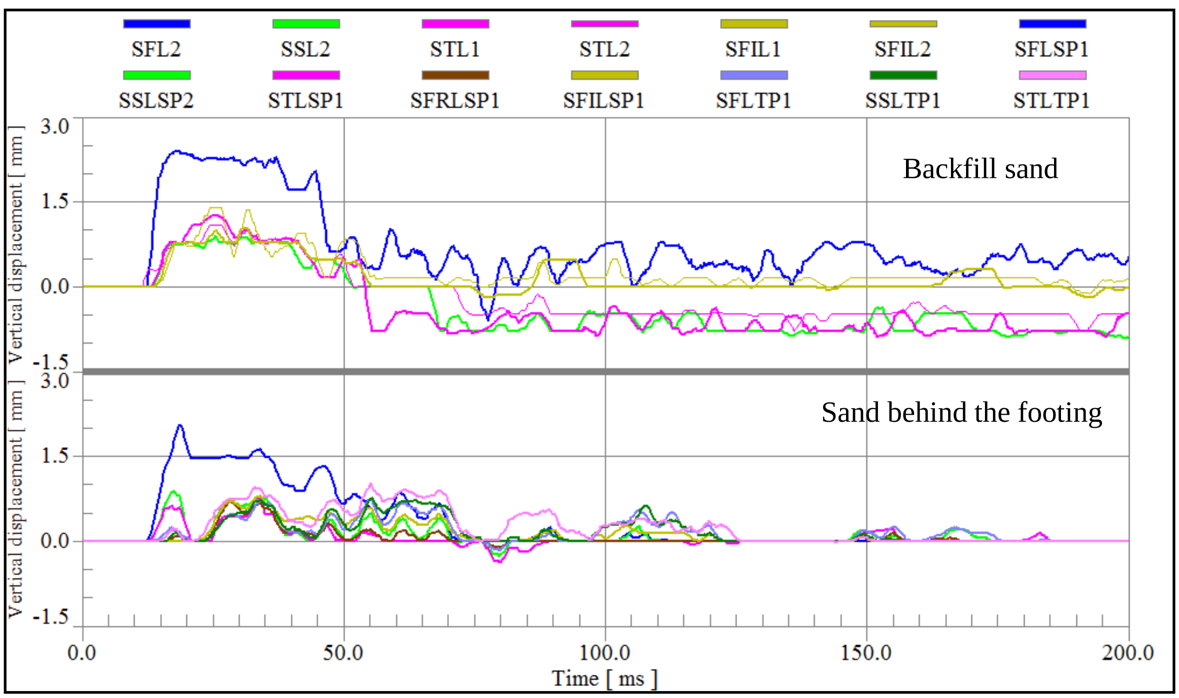
SFL2
SSL2
STL1
STL2
SFIL1
SFIL2
SFLSP1
SSLSP2
STLSP1
SFRLSP1
SFILSP1
SFLTP1
SSLTP1
STLTP1
Backfill sand
Sand behind the footing
Vertical displacement [mm]
Time [ms]

(f)

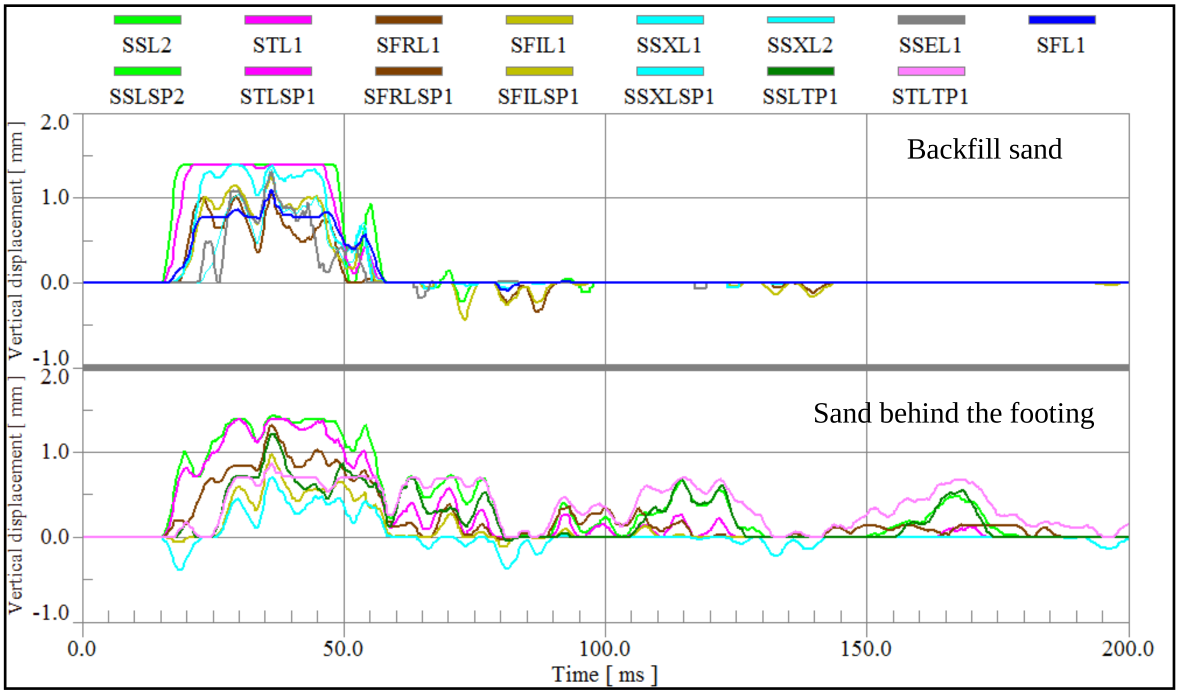

(g)

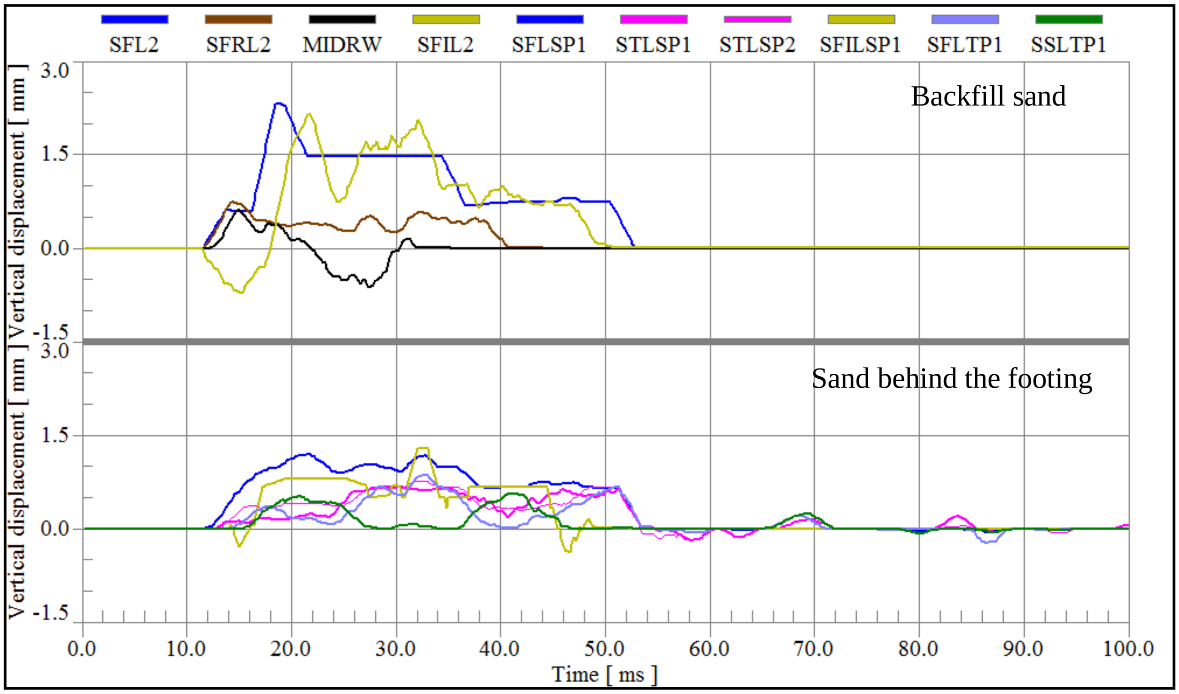

(h)

Figure 5.11: Vertical displacement time histories for the backfill sand; (a) loose, (b) medium, (c) dense, (d) reflected pressure 71 kPa, (e) reflected pressure 26 kPa, (f) partially saturated backfill, (g) saturated backfill, (h) live load surcharge

Table 5.7: Locations and symbol definitions of tracked soil particles

Symbol	Depth from the top of the wall	Horizontal distance behind the wall
TRW: top of retaining wall	0 mm	0 mm
SFL1: soil first layer 1	40 mm	70 mm
SFL2: soil first layer 2	40 mm	170 mm
SSL1: soil second layer 1	100 mm	70 mm
SSL2: soil second layer 2	100 mm	170 mm
STL1: soil third layer 1	150 mm	70 mm
SFRL1: soil fourth layer 1	200 mm	70 mm
SFIL1: soil fifth layer 1	300 mm	70 mm
SSXL1: soil sixth layer 1	400 mm	70 mm
SSXL2: soil sixth layer 2	400 mm	170 mm
SFLSP1: soil first layer 1	40 mm	370 mm
SSLSP1: soil second layer 1	100 mm	370 mm
STLSP1: soil third layer 1	150 mm	370 mm
SFRLSP1: soil fourth layer 1	200 mm	370 mm
SFLTP1: soil first layer 1	40 mm	775 mm
SSLTP1: soil second layer 1	100 mm	775 mm
STLTP1: soil third layer 1	150 mm	775 mm

5.4.4 Lateral Displacement of Retained Soil

Figure 5.12 depicts lateral displacement time histories for the backfill sand for various relative densities, degree of saturation and different load intensities. Randomly selected points were chosen from each layer of the retained soil in order to compare the lateral displacements between the backfill and the sand behind the footing.

It can be seen that loose and medium sand yielded the highest lateral displacements. On the other hand, the backfill sand exhibited slightly higher deformations than the sand behind the footing for all conditions. Furthermore, it was noticed that the displacements for the retained sand decreased with depth. As explained earlier in the settlement section (5.4.3), blast load intensity decreases with the distance, which led to the small reduction in soil particle deformation in the sand behind the footing compared to the backfill. However, blast-induced dynamic lateral earth pressure can generate deformations in both the backfill and sand behind the footing, resulting in relatively similar effects on both regions. On the other hand, the increase in the overburden pressure with depth can contribute to the slight reduction in displacements with depth.

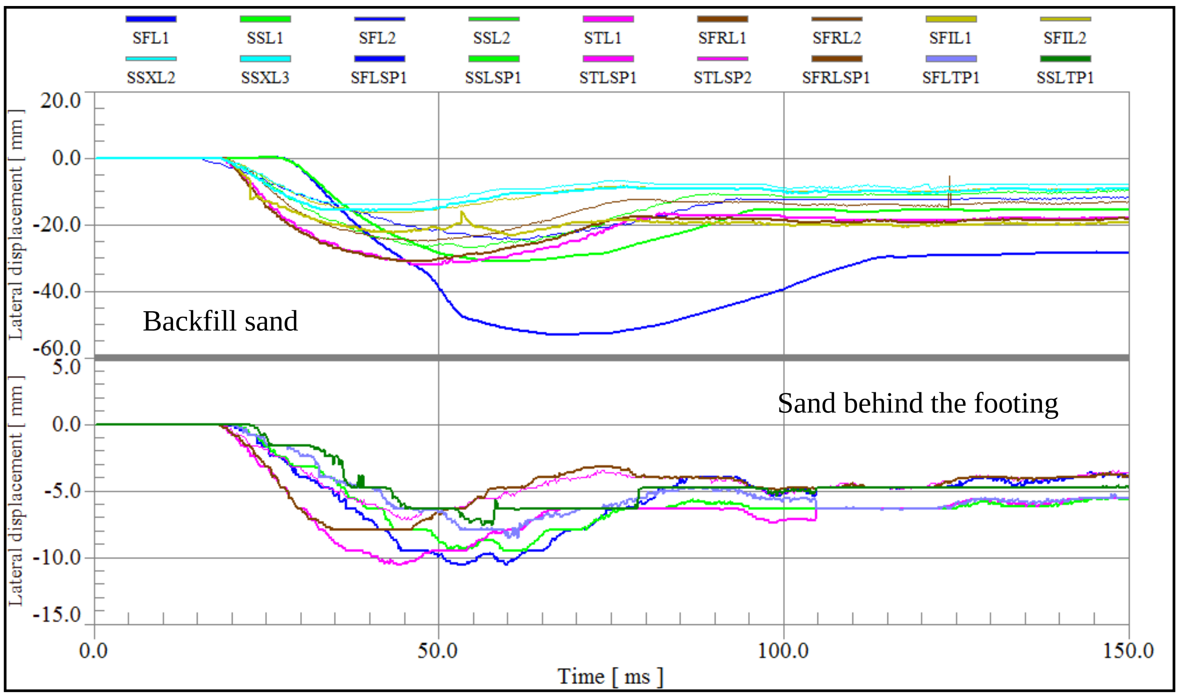

(a)

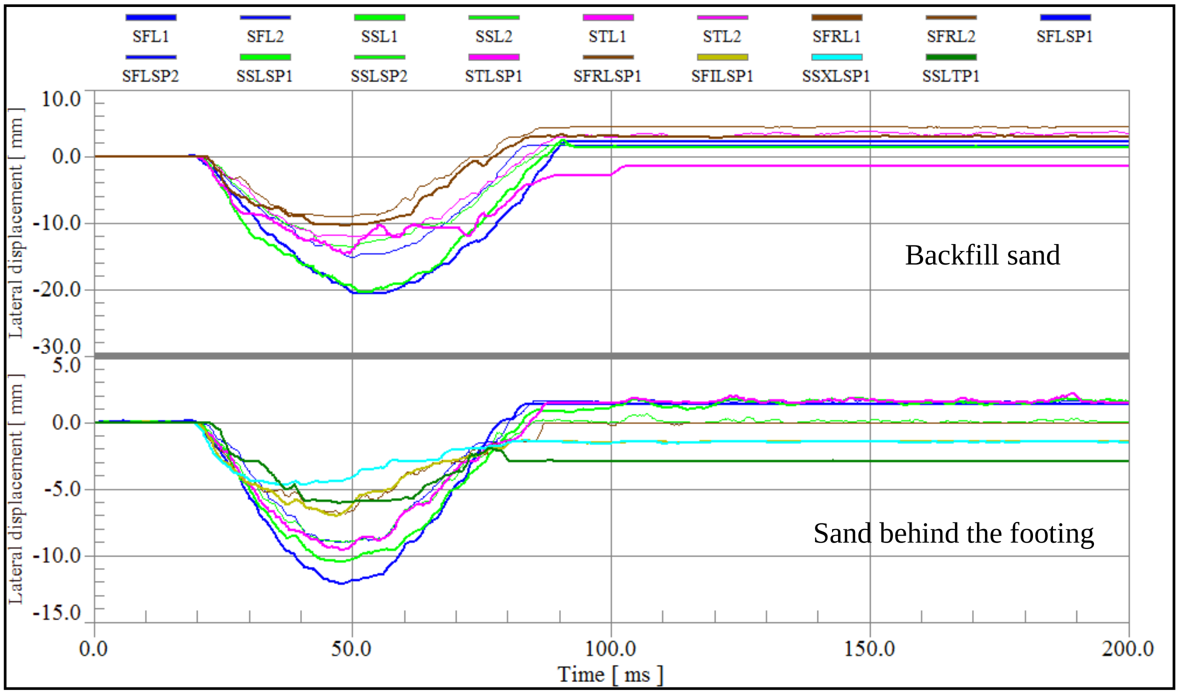

SFL1
SFL2
SSL1
SSL2
STL1
STL2
SFRL1
SFRL2
SFLSP1
SFLSP2
SSLSP1
SSLSP2
STLSP1
SFRLSP1
SFILSP1
SSXLSP1
SSLTP1
Lateral displacement [mm]
Backfill sand
Sand behind the footing
Time [ms]

(b)

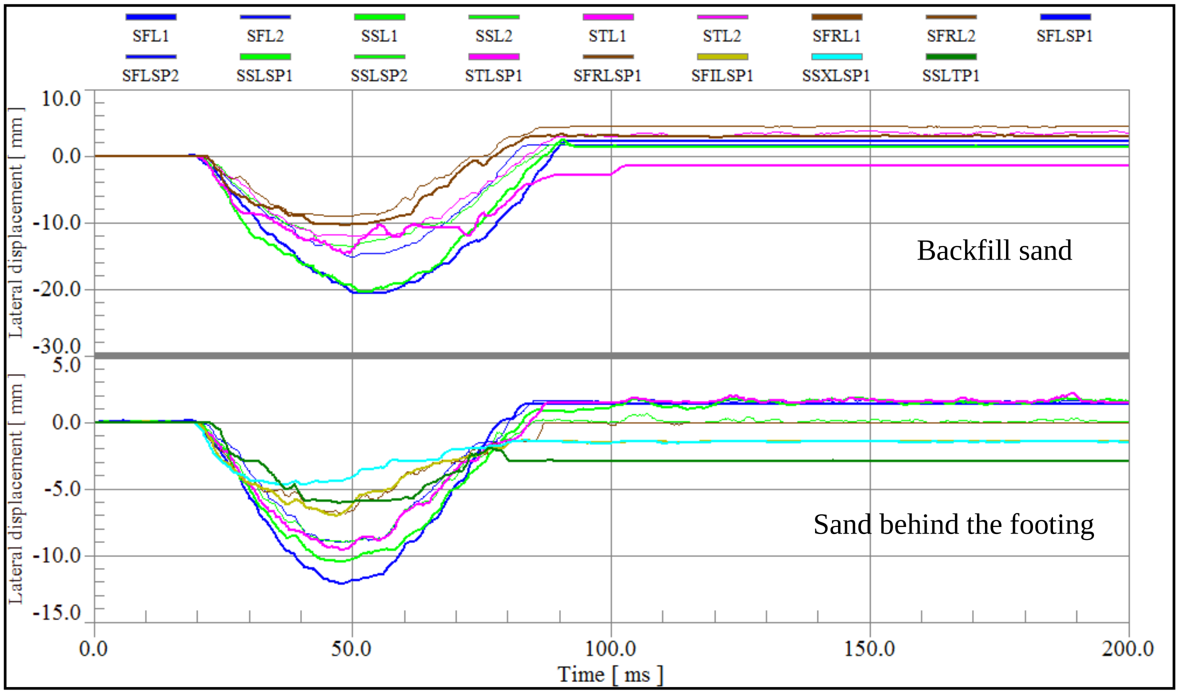

SFL1
SFL2
SSL1
SSL2
STL1
STL2
SFRL1
SFRL2
SFLSP1
SFLSP2
SSLSP1
SSLSP2
STLSP1
SFRLSP1
SFILSP1
SSXLSP1
SSLTP1
Lateral displacement [mm]
Backfill sand
Sand behind the footing
Time [ms]

(c)

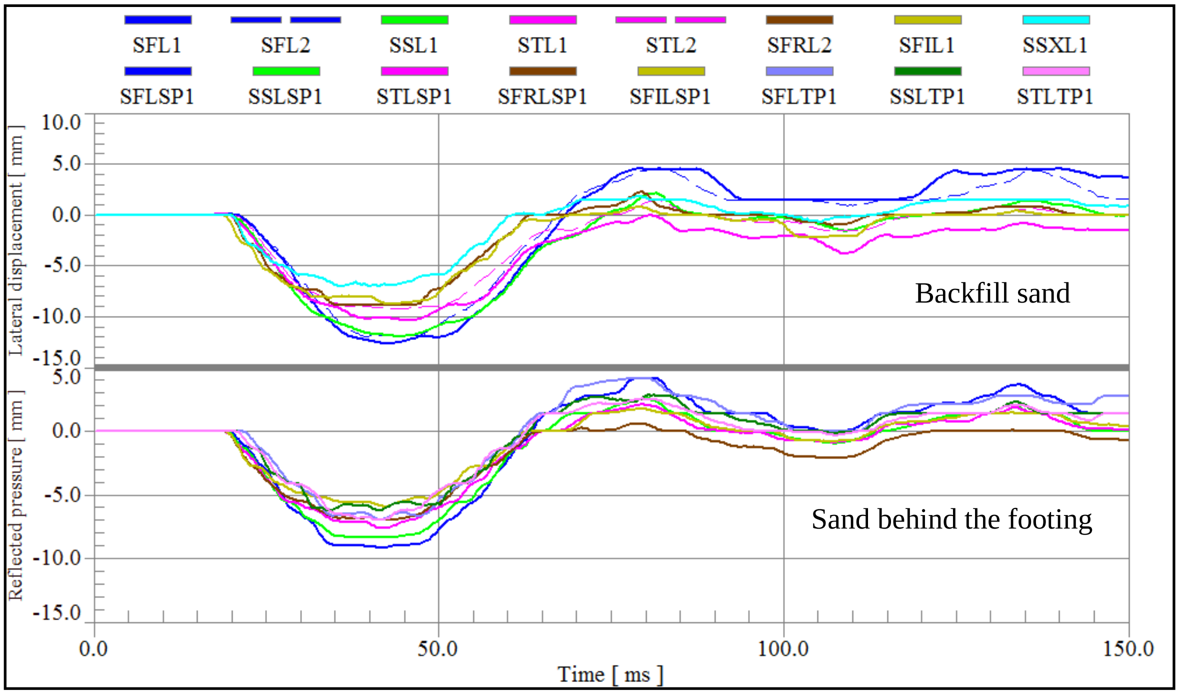
SFL1
SFL2
SSL1
STL1
STL2
SFRL2
SFIL1
SSXL1
SFLSP1
SSLSP1
STLSP1
SFRLSP1
SFILSP1
SFLTP1
SSLTP1
STLTP1
Lateral displacement [mm]
Backfill sand
Reflected pressure [mm]
Sand behind the footing
Time [ms]

(d)

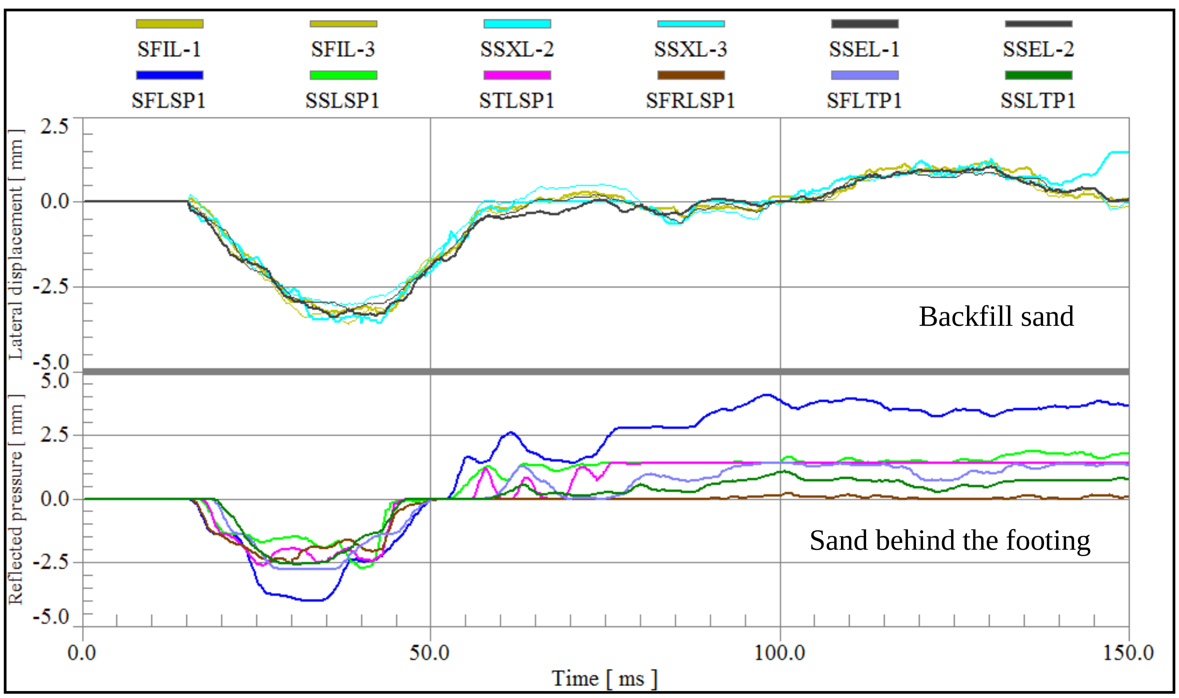
SFIL-1
SFIL-3
SSXL-2
SSXL-3
SSEL-1
SSEL-2
SFLSP1
SSLSP1
STLSP1
SFRLSP1
SFLTP1
SSLTP1
Lateral displacement [mm]
Backfill sand
Reflected pressure [mm]
Sand behind the footing
Time [ms]

(e)

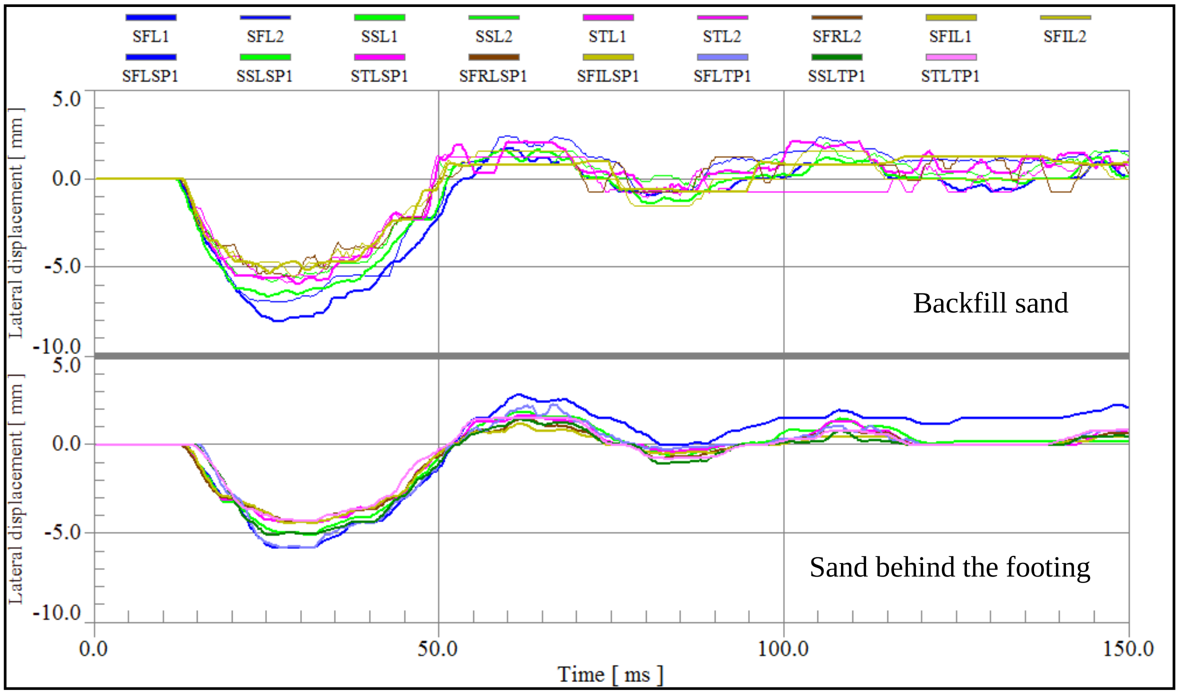
SFL1
SFL2
SSL1
SSL2
STL1
STL2
SFRL2
SFIL1
SFIL2
SFLSP1
SSLSP1
STLSP1
SFRLSP1
SFILSP1
SFLTP1
SSLTP1
STLTP1
Lateral displacement [mm]
Backfill sand
Sand behind the footing
Time [ms]

(f)

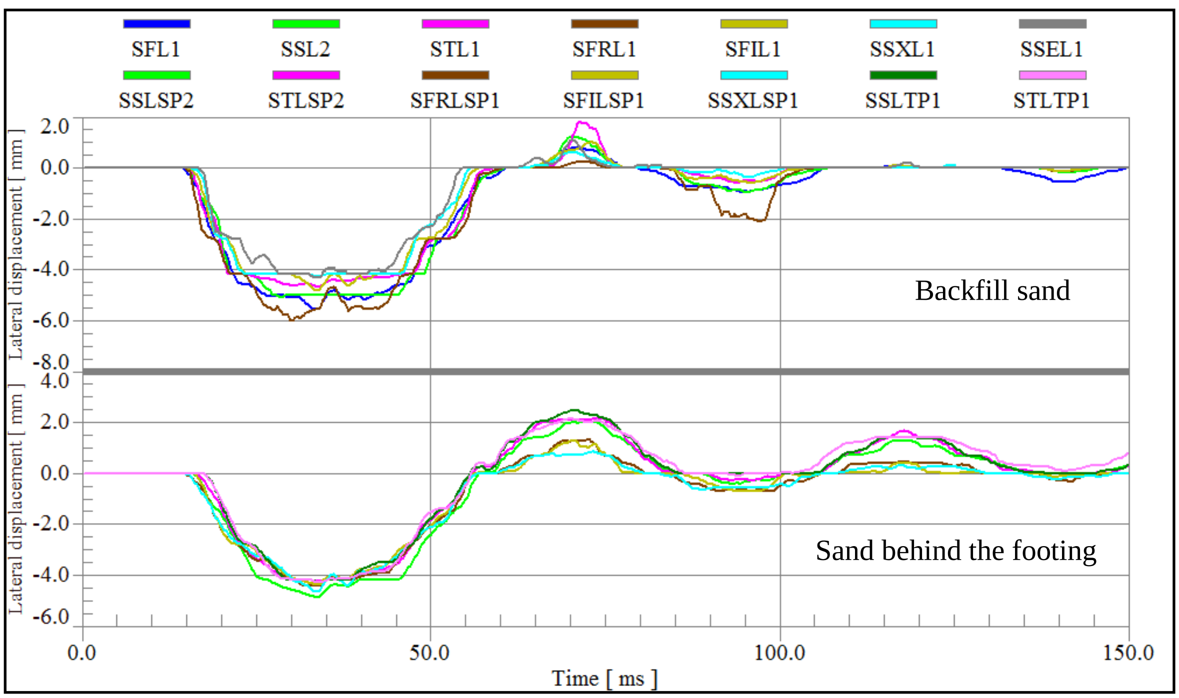
SFL1
SSL2
STL1
SFRL1
SFIL1
SSXL1
SSEL1
SSLSP2
STLSP2
SFRLSP1
SFILSP1
SSXLSP1
SSLTP1
STLTP1
Lateral displacement [mm]
Backfill sand
Sand behind the footing
Time [ms]

(g)

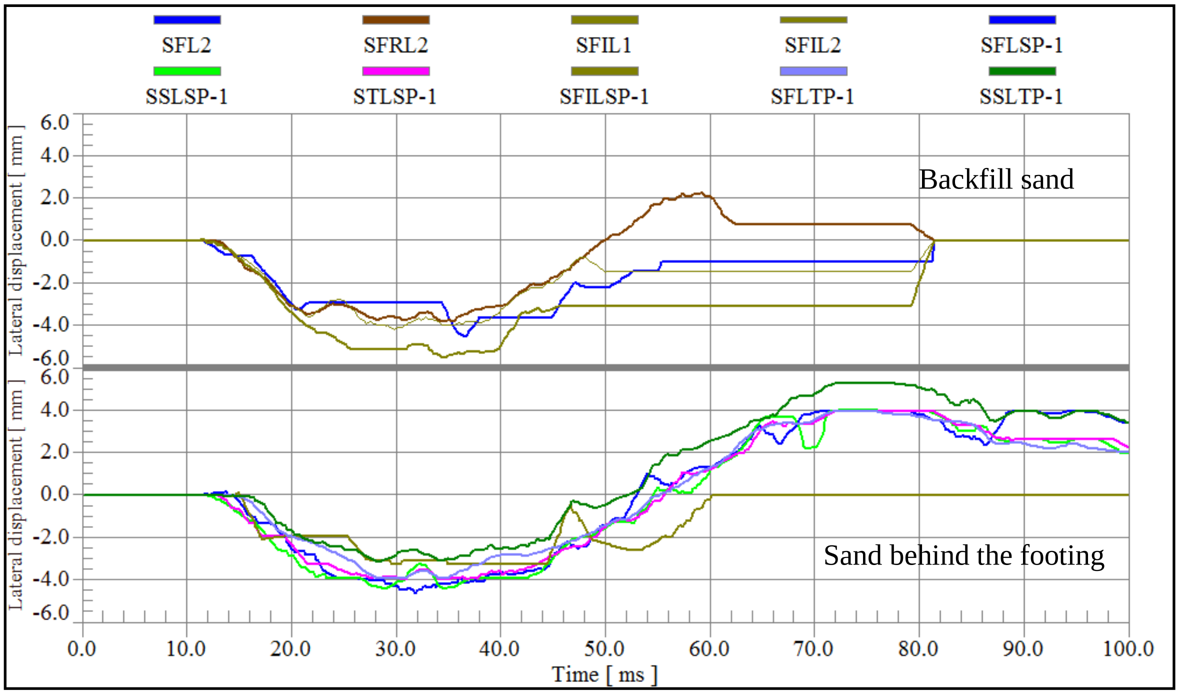

(h)

Figure 5.12: Lateral displacement time histories for the backfill sand; (a) loose, (b) medium, (c) dense, (d) reflected pressure 71 kPa, (e) reflected pressure 26 kPa, (f) partially saturated backfill, (g) saturated backfill, (h) live load surcharge; same symbol definitions as in Table 5.7.

5.4.5 Susceptibility of Saturated Sand to Liquefaction

A continuing debate in the geotechnical field has been about the accurate and concise definition for soil liquefaction. Liquefaction is defined by Sladen (1985) as "a phenomenon wherein a mass of soil loses a large percentage of its shear resistance, when subjected to monotonic, cyclic, or shock loading, and flows in a manner resembling a liquid until the shear stresses acting on the mass are as low as the reduced shear resistance". It is well-known that the phenomenon of soil liquefaction depends on three main factors. These factors are excess pore pressure, shear strength, and shear strain/deformation of the soil (Wu et al., 2004 and Rauch, 1997). There are many definitions for soil liquefaction in the literature. However, some of these definitions focus only on one factor instead of all three (Wu et al., 2004).

For pore water pressure-based criteria, soil liquefaction occurs when the excess pore water pressure ratio (r_u) reaches 1.0. The ratio approaches 1.0 when the increase in the pore water pressure (Δu) becomes equal to the vertical effective stress (σ_v). For strength-based criteria, soil liquefies when the effective confining stress becomes zero. This means the soil loses its shear strength and behaves like a viscous fluid. This approach is equivalent to pore pressure-based criteria. Strain/deformation-based criterion is the third approach to define soil liquefaction. The potential for triggering liquefaction is assessed using the threshold strain. Wu (2014) concluded that the initialization of the flow shear strain occurred when the maximum single amplitude shear strain reached about 3%. Shear strain/deformation is a good approach to be used for seismic performance assessment as it provides important information about soils performance level during liquefaction (Wu et al., 2004). Studies have confirmed that these three approaches are closely interrelated (Rauch, 1997, and Dobry et al., 1982). The last method to identify liquefaction is energy-based criteria. This approach was first introduced by Nemat-Nasser and Shakooh (1979). They stated that the occurrence of shear displacement during cyclic shearing could affect the rearrangement of sand particles and consequently influence the shear energy to trigger liquefaction. Shear energy is referred to as the dissipation of energy into the soil of unit volume (Sassa et al., 2005) and is denoted in Equation 5.1.

$$W = \sum_{i=1}^{n-1} \frac{1}{2} (\tau_i + \tau_{i+1})(l_{i+1} - l_i) \tag{5.1}$$

W is the shear energy in J/m^2; τ is the shear resistance in kPa; l is the shear displacement in m; n is the number of points recorded.

Researchers suggested that the difference between liquefaction and cyclic mobility should be addressed (Rauch, 1997 and Castro and Poulos, 1977). The failure mechanisms of saturated soil that result from the build-up of pore pressure during undrained dynamic loads are usually called liquefaction. The term cyclic mobility, which can also be called limited liquefaction, is used to describe shear resistance development after initial liquefaction that prevents large deformations in densely saturated sands (Seed, 1979).

Loose sands, which are also called contractive soils, tend to compact under loading, and when there is no drainage, an increase in pore water pressure can be developed. When the loose cohesionless soils are subjected to dynamic loads, excess pore pressures are generated. Without drainage, the pore pressures accumulate, and the effective stress reduces and moves towards zero. For dense sands (dilative soils), an excess pore pressure may be developed at a small strain. However, at a larger strain, the soil particles start to rearrange and increase soil volume, which leads to a decrease in the pore pressures, and the pressures might reach negative values (Rauch, 1997).

In this paper, the RW with saturated dense sand was examined to determine if liquefaction was triggered by a reflected pressure of 50 kPa.

The excess pore water pressure ratio (r_u) was calculated for partially saturated and saturated backfill to determine if the build-up in the pore water pressure during blast loading triggered liquefaction. The r_u was computed by dividing the excess pore pressure by the effective stress (σ_v). The effective stress was calculated by multiplying the dry density of the sand by the height where the pore pressure was measured. For partially saturated and saturated sand, the excess pore water pressure ratios were below one. Since the excess pore water pressure ratios were less than one, it is assumed that liquefaction was not triggered based on pore water pressure-based criterion. However, pore water pressure-based criterion has a main drawback: it cannot assess or reflect the dynamic behaviour of liquefiable dense sand (Wu et al., 2004). Dense sand does not usually exhibit pore pressure build-up (Rauch, 1997).

Figure 5.13 shows the response of the dilative soil (dense sand) to blast loading. A slight accumulation of excess pore pressure was first noticed due to the pore pressure generation during the application of blast loading. Though the sand grains started to dilate after a certain point, the pore pressures fell below the initial values. Dilation of the sand reduced the pore pressure and might have helped in increasing the strength of the soil. This is referred to as cyclic mobility, as mentioned above.

Figure 5.14 depicts the shear strain time history for saturated sand. The shear strain was calculated from the lateral deformation of the saturated backfill (Figure 5.12g) and is shown in Equation 5.2 (Das, 2011).

$$\gamma = \frac{\Delta}{2h} \tag{5.2}$$

γ is the shear strain (%).

Δ is the lateral deformation (mm).

h is the height of the backfill.

The maximum shear strain for the saturated backfill was below 0.6%. Thus, flow shear strain was not initialized, and consequently, soil liquefaction was not triggered in this test based on the strain/deformation approach.

For the strength-based criteria, in order for liquefaction to occur, the shear stress at any depth of the backfill sand induced by dynamic loads should be equal or greater than the shear strength. The shear strength of the sand can be determined using the dynamic triaxial test or the cyclic shear test. The shear stress can be calculated using Equation 5.3 (Seed and Idriss, 1971). Since the shear strength tests were beyond the scope of this study, the strength-based approach was not implemented to identify liquefaction.

Figure 5.15 shows the shear stress induced by blast loads in the saturated backfill sand with depth.

$$\tau_{max} = (\frac{\gamma h}{g}) a_{max} \tag{5.3}$$

τ_{max} is the shear stress in kPa.

γ is the unit weight of the sand.

h is the height of the backfill.

a_m is the peak acceleration due to blast loading.

g is the acceleration due to gravity.

It can be concluded that based on the obtained results shown above, liquefaction was not triggered when the RW with saturated backfill was subjected to a blast load of 50 kPa. It seems that when a RW with dense backfill is subjected to blast loading, it can keep its structural integrity even if the backfill becomes saturated. However, more tests, using higher blast pressures, need to be conducted to confirm this statement.

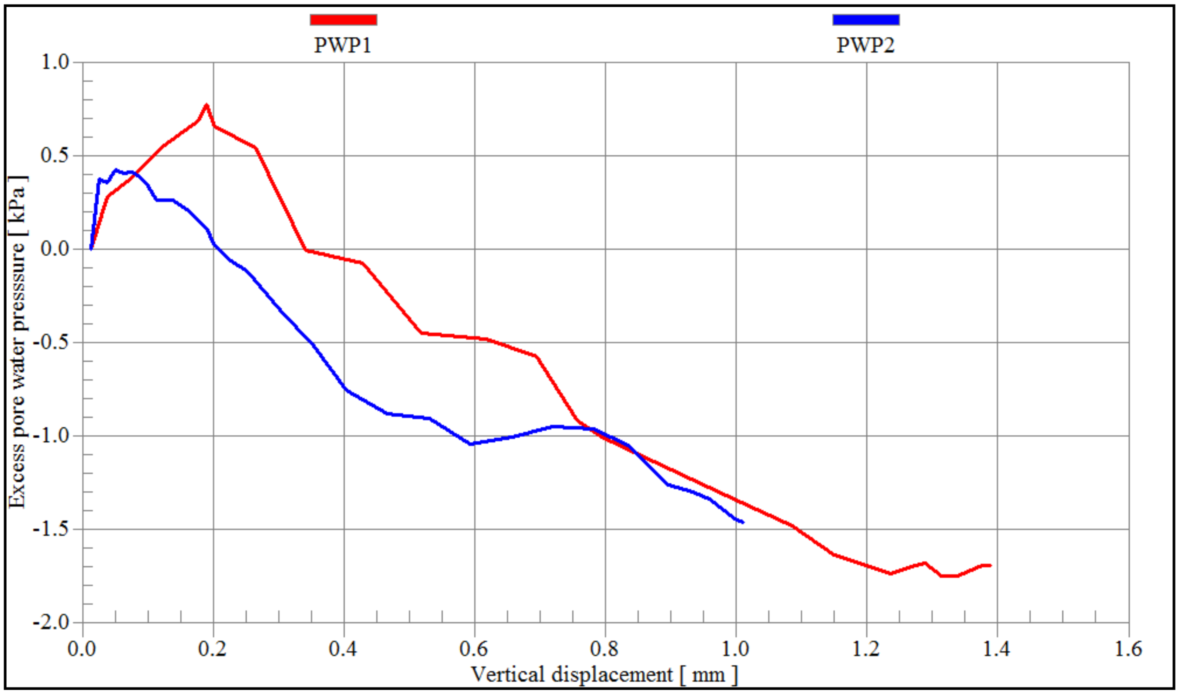

Figure 5.13: The response of saturated dense sand to blast loading

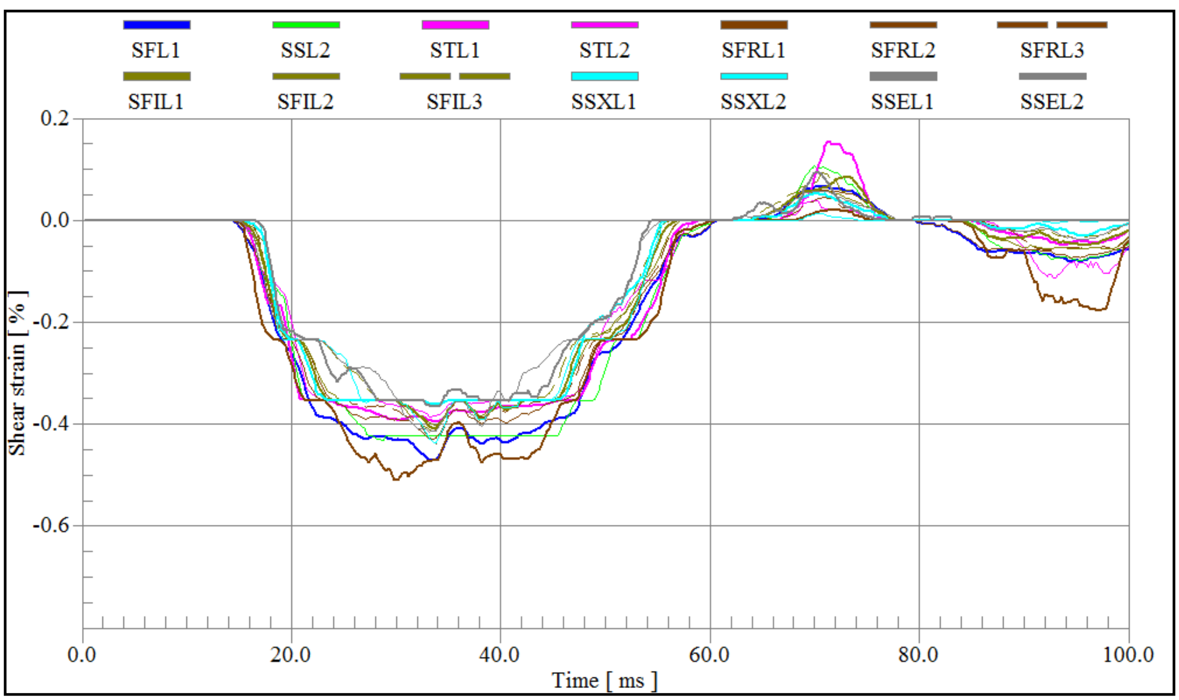

Figure 5.14: Shear strain time history for saturated sand; same symbol definitions as in Table 5.7

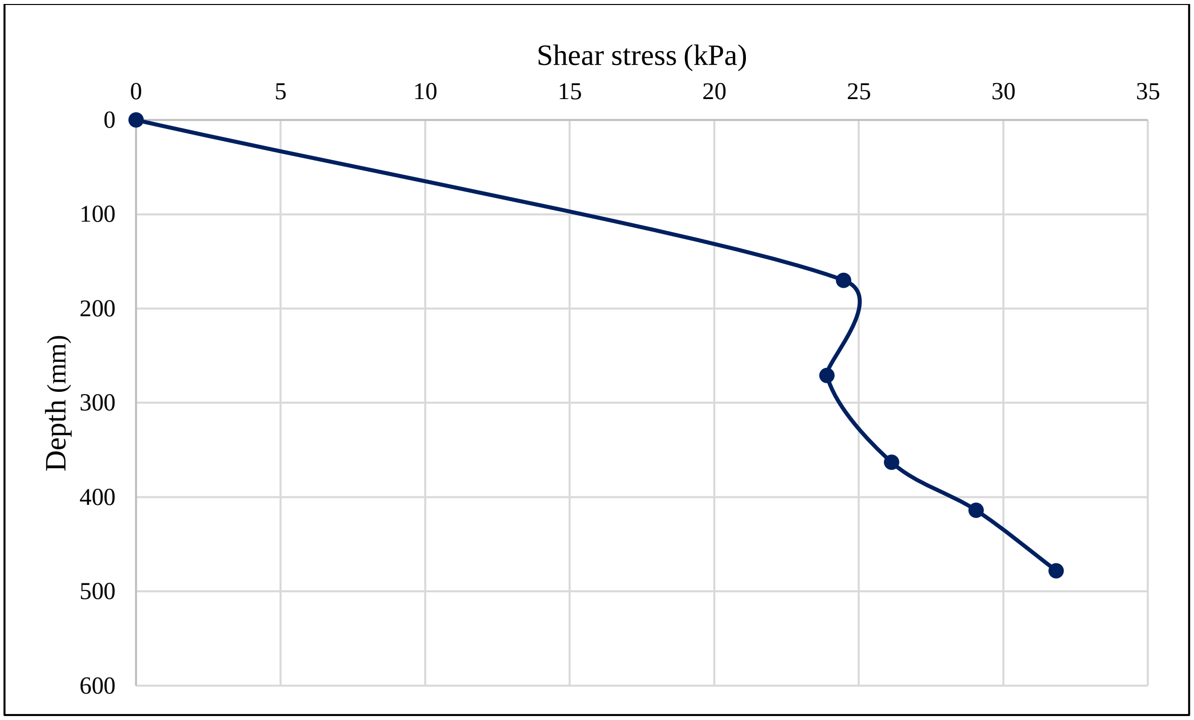

Figure 5.15: Shear stress with depth for saturated sand

5.4.6 Peak Particle Velocity

The reading of the peak particle velocity (PPV) is used as the standard for measuring the ground vibration intensity (Nicholson, 2005). Figure 5.16 presents the peak particle velocity time histories of sand backfill for various relative densities, degrees of saturation and different load intensities. The PPVs were determined using the ProAnalyst software. The measured velocities were taken at depths of 200 mm below the ground surface (BGS) and 400 mm BGS, assuming that the top of the wall represents the ground surface.

It can be seen that for the same relative density, a higher amplitude of blast load intensity led to higher PPV. Furthermore, the variations in sand backfill parameters had a limited impact on the PPV. This is because the PPV is a function of the intensity of the stress, as shown in Equations 5.4 and 5.5 (Das, 2011 and An, 2010).

$$u = (\frac{\sigma_x}{E})(v_c t) \tag{5.4}$$

$$PPV = \frac{u}{t} = \frac{\sigma_x v_c}{E} \tag{5.5}$$

$$v_c = \sqrt{\frac{E}{\rho}} \tag{6.6}$$

u is the displacement in m.

σ_x is the compressive stress pulse in kPa.

PPV is the peak particle velocity in m/s.

t is the duration in s.

ρ is the density of the soil in kg/m^3.

v_c is the seismic/longitudinal wave velocity in m/s.

E is the modulus of elasticity of the soil in kPa.

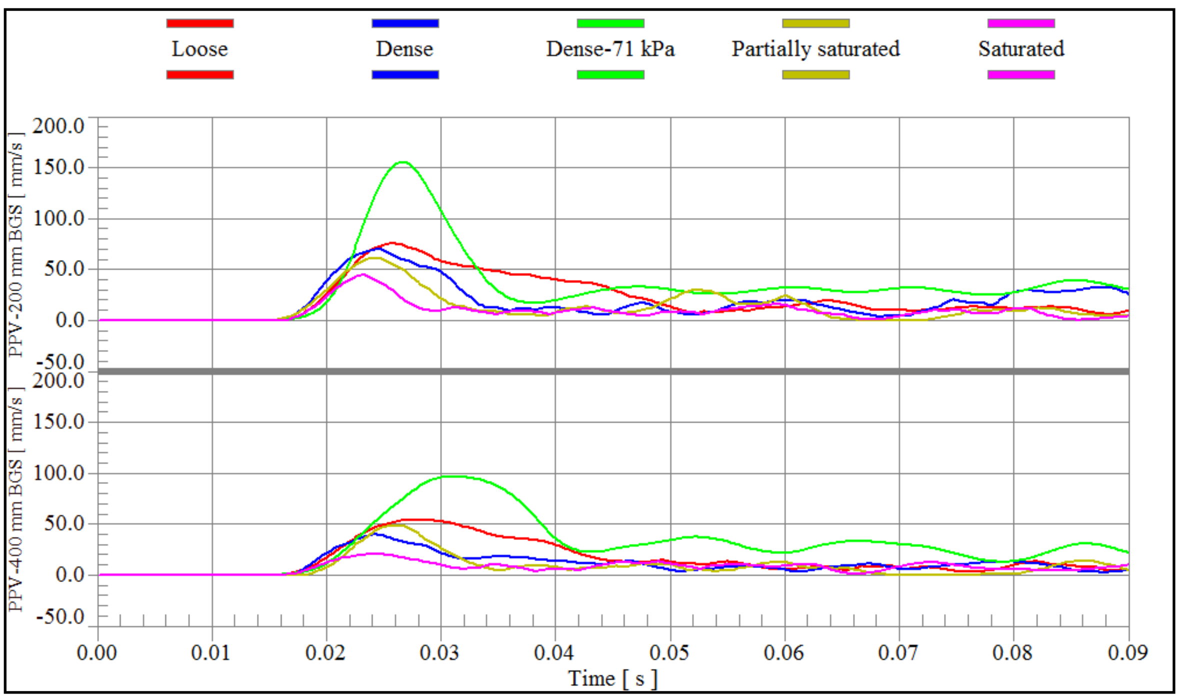

Figure 5.16: Peak particle velocity time histories of sand backfill

5.5 Summary and Conclusion

The reinforced concrete retaining wall with sand backfill was subjected to blast loading. The blast load was generated by the shock tube at the Blast Research Laboratory of the University of Ottawa. Various instruments were placed in the soil-RW model to evaluate the dynamic response of the model during the blast event. The ProAnalyst software was used to capture the soil particles' movement and to track the transient and permanent displacements of the wall.

Backfill materials with various relative densities and degrees of saturation were subjected to different blast shot intensities (26 kPa, 47 kPa, and 71 kPa) to evaluate the pore pressure development in the retained sand. The susceptibility of saturated sand to liquefaction was also addressed. Furthermore, settlements, lateral displacements and PPV of the retained soil were determined.

The results showed that the maximum pore pressure responses for saturated backfill were at a time greater than the positive phase duration, while the maximum pore pressure response for the foundation was at the end of the positive phase duration. The excess pore water pressure ratios for saturated backfill were determined, and it was noticed that the ratios were less than 1. The susceptibility of the RW with saturated dense sand to liquefaction was examined. It was ascertained that liquefaction was not triggered based on pore water pressure-based criteria and shear strain-based criteria.

Settlement time histories for RW/backfill showed that there were large deformations in loose and medium backfill. On the other hand, for all the tests, a reduction was observed in the vertical displacements with distances further from the RW. Very limited settlements were noticed in dense sand with different blast load intensities and various degrees of saturation. Additionally, there were no settlements in the RW for all conditions.

The lateral displacements between the backfill and the sand behind the footing were compared by choosing random points. It was observed that loose and medium sand yielded the highest lateral displacements. For all conditions, the backfill sand exhibited slightly lower deformations with distances further from the RW. Furthermore, it was noticed that the displacements for the retained sand decreased with depth.

The PPVs were determined using the ProAnalyst software. The measured velocities were taken at depths of 200 mm and 400 mm. The sand backfill peak particle velocity time histories showed that an increase in the blast load intensity caused higher PPV.

The findings of this research will provide beneficial insight into the improvement of blast design of retaining structures.

5.6 References

Al Atik, L. F. (2008). Experimental and Analytical Evaluation of Seismic Earth Pressures on Cantilever Retaining Structures. Doctoral thesis, University of California, Berkeley.

Altaee, A. and Fellenius, B. H. (1994). Physical Modeling in Sand. Canadian Geotechnical Journal 31, 420-43 1.

Agrawal, K. A., Yi, Z., (2009). Blast Load Effects on Highway Bridges. University Transportation Research Center.

American Society of Civil Engineers (ASCE). (2010). Design of Blast-Resistant Buildings in Petrochemical Facilities, Second Edition.

American Society of Civil Engineers (ASCE). (1985). Design of Structures to Resist Nuclear Weapons Effects. Manual 42. Washington, D.C.

American Society of Civil Engineers (ASCE). (1999). Structural Design for Physical Security: State of the Practice. The Structural Engineering Institute Task Committee.

American Society of Civil Engineers (ASCE). (2005). Minimum design loads for buildings and other structures. ASCE/SEI 7-05, Reston, Virginia.

Anderson, D. G., Martin, G. R., Lam, I. P. and Wang, J. N. (2008). Seismic Analysis and Design of Retaining Walls, Buried Structures, Slopes, and Embankments. NCHRP (National Cooperative Highway Research Program). Rep. 611, eds., National Academies, Washington, DC.

ASTM (American Society for Testing and Materials) C136/C136M−14 Standard for Sieve Analysis of Fine and Coarse Aggregates.

ASTM D854-14 Standard for Specific Gravity of Soil Solids by Water Pycnometer.

ASTM D4254-16 Standard for Minimum Index Density and Unit Weight of Soils and Calculation of Relative Density.

ASTM D4253-16 Standard for Maximum Index Density and Unit Weight of Soils Using a Vibratory Table.

ASTM, D3080-11 Standard for Direct Shear Test of Soils under Consolidated Drained Conditions.

ASTM C31/C31M-19 Standard for Making and Curing Concrete Test Specimens in the field.

ASTM C39/C39M-18 Standard for Compressive Strength of Cylindrical Concrete Specimens.

An, J. (2010). Soil Behavior under Blast Loading. University of Nebraska-Lincoln.

Bakr, J. A. (2018). Displacement-Based Approach for Seismic Stability of Retaining Structures. Doctoral thesis, School of Mechanical, Aerospace and Civil Engineering. University of Manchester.

Bang, S. (1985). Active earth pressure behind retaining walls. Journal of Geotechnical Engineering, 111, 407-412.

Biggs, J. M. (1964). Introduction to Structural Dynamic, McGraw-Hill, Inc. U.S.

Castro, G., and Poulos, S. J. (1977). Factors Affecting Liquefaction and Cyclic Mobility. Journal Geotechnical Engineering Div., ASCE, 103, GT6, 501-516.

Chen, W-F, Duan, L. (2014). Substructure Design. Bridge Engineering Handbook, Second Edition.

Cormie, David, Mays, G.C. and Smith, P.D. (2009). Blast Effects on Buildings. Second edition.

Crawford, E. R., Higgins, C. J., and Bultmann, E. H. (1974). The Air Force Manual for Design and Analysis of Hardened Structures. AFWL-TR-74-102, Air Force Weapons Laboratory, Kirtland Air Force Base, New Mexico.

Das, B. M. (2016). Principles of Foundation Engineering, Eighth Edition, Boston, MA, U.S.

Das, B. M. (1999). Principles of Foundation Engineering, Fourth Edition, Pacific Grove, CA, U.S.

Das, B. M. (1993). Principles of Soil Dynamics, Second Edition, Stamford, CT, U.S.

Dobry, R., Ladd, R. S., Yokel, F. Y., Chung, R. M., and Powell, D. (1982). Prediction of Pore Water Pressure Buildup and Liquefaction of Sands during Earthquakes by the Cyclic Strain Method. National Bureau of Standards Building Science Series, Report No. 138.

Federal Highway Administration, United States Department of Transportation. (2008). Standard Specifications for Construction of Roads and Bridges on Federal Highway Projects FP-14.

Finn, W. D. L. (1990). Analysis of post-liquefaction deformation in soil structures. Proc., H. Bolton Seed Memorial Symposium, BiTech Pub., Richmond, British Columbia, 2, 291-311.

Fujikura, S., Bruneau, M., Lopez-Garcia, D. (2008). Experimental Investigation of Multihazard Resistant Bridge Piers Having Concrete-Filled Steel Tube under Blast Loading. Journal of Bridge Engineering, ASCE, 13 (6), 586-594.

Gazetas, G., Psarropoulos, P.N., Anastasopoulos, I., and Gerolymos, N. (2004). Seismic Behaviour of Flexible Retaining Systems Subjected to Short-Duration Moderately Strong Excitation, Soil Dynamics and Earthquake Engineering, 24, 537-550.

Geotechnical Design Procedure (GDP-9). (2015). Liquefaction Potential of Cohesionless Soils. State of New York Department of Transportation, Geotechnical Engineering Bureau.

Hao, H., Wu, C. (2005). Numerical Study of Characteristic of Underground Blast Induced Surface Ground Motion and Their Effect on Above-Ground Structures Part II. Effects on Structural Responses. Soil Dynamics and Earthquake Engineering, 25, 39-53.

Ishihara, K. (1993). Liquefaction and flow failure during earthquakes. Thirty-third Rankine Lecture, Geotechnique, 43, (3), 351-415.

Ishihara, K. (1994). Evaluation of residual strength of sandy soils. Proceeding 13th International Conference Soil Mechanics Foundation Engineering. New Delhi, India, 5, 175-181.

Jayasinghe, L. B. (2014). Blast Response and Vulnerability Assessment of Piled Foundations. Queensland University of Technology. Brisbane, Australia.

Jo, S-B, Ha, J-G, Lee, J-S, Kim, D-S. (2017). Evaluation of the Seismic Earth Pressure for Inverted T-Shape Stiff Retaining Wall in Cohesionless Soils via Dynamic Centrifuge. Soil Dynamics and Earthquake Engineering, 92, 345–357.

Kadhom, B. (2015). Blast Performance of Reinforced Concrete Columns Protected by FRP Laminates. Doctoral thesis, University of Ottawa, Ontario, Canada.

Kloukinas, P., Scotto di S., Anna, P., Augusto, D., Matthew, E., Aldo, L. Simonelli, A., Taylor, C., Mylonakis, G. (2015). Investigation of Seismic Response of Cantilever Retaining Walls: Limit Analysis vs Shaking Table Testing. Soil Dynamics and Earthquake Engineering, 77, 432–445.

Lloyd, A. (2015). Blast Retrofit of Reinforced Concrete Columns. Doctoral thesis, University of Ottawa, Ontario, Canada.

Lloyd, A. (2010). Performance of Reinforced Concrete Columns under Shock Tube Induced Shock Wave Loading. Master thesis, University of Ottawa, Ontario, Canada.

Mays, G.C. and Smith, P.D. (1995). Blast Effects on Buildings. First edition.

Mikola, R. G. and Sitar, N. (2013). Seismic Earth Pressures on Retaining Structures in Cohesionless Soils. Department of Civil and Environmental Engineering University of California, Berkeley.

Mittal, R. K., Gupta, M.K. and Singh, S. (2004). Liquefaction Behaviour of Sand during Vibrations. 13th World Conference on Earthquake Engineering, Vancouver, B.C., Canada, 1-6.

National Research Council. (1995). Liquefaction of Soils during Earthquakes, Washington DC.

Nemat-Nasser, S. and Shakooh, A. (1979). A Unified Approach to Densification and Liquefaction of Cohesionless Sand in Cyclic Shearing. Canadian Geotechnical journal, 16(4), 659-678.

Ngo, T., Mendis, P., Gupta, A. and Ramsay, J. (2007). Blast Loading and Blast Effects on Structures-An Overview. EJSE Special Issue: Loading on Structures.

Nicholson, R. F. (2005). Determination of Blast Vibrations Using Peak Particle Velocity at Bengal Quarry, in St Ann, Jamaica. Thesis, Lulea University of Technology.

Nishimura, T., Hirabayashi, Y., Fredlund, D. G., and Gan, J. K.-M. (1999). Influence of Stress History on the Strength Parameters of an Unsaturated Statically Compacted Soil. Canadian Geotechnical Journal, 36, 251–261.

Okabe, S. (1926). General theory of earth pressure. Journal of the Japanese Society of Civil Engineers, 12, 311.

Psarropoulos, P. N., Tsompanakis Y., Papazafeiropoulos, G. (2009). Effects of soil non-linearity on the seismic response of restrained retaining walls. Structure and Infrastructure Engineering, 1–12.

Rauch, Alan F. (1997). An Empirical Method for Predicting Surface Displacements due to Liquefaction-Induced Lateral Spreading in Earthquakes. Thesis, Virginia Polytechnic Institute and State University.

Robertson, P. K. (1994). Design considerations for liquefaction. Proceeding 13th International Conference Soil Mechanics Foundation Engineering. New Delhi, India, 5, 385-188.

Sassa K., Wang G., Fukuoka H., Vankov DA. (2005). Shear-Displacement-Amplitude Dependent Pore-Pressure Generation in Undrained Cyclic Loading Ring Shear Tests: An Energy Approach. Journal of Geotechnical and Geoenvironmental Engineering ASCE, 131(6):750–761.

Seed, H. B. (1979). Soil Liquefaction and Cyclic Mobility Evaluation for Level Ground during Earthquakes. Journal Geotechnical Engineering Div., ASCE, 105, GT2, 201-255.

Seed, H. B., and Idriss, I. M. (1971). Simplified Procedure for Evaluating Soil Liquefaction Potential. Journal Soil Mechanics Foundation Div., ASCE, 97, SM9, 1249-1273.

Sladen, J. A., D'Hollande, R. D., and Krahn, J. (1985).The Liquefaction of Sands, a Collapse Surface Approach. Canadian Geotechnical Journal, 22.

Smith, P. D. and Hetherington, J. G. (2011). Blast and ballistic loading of structures.

Soil Compaction Handbook (MULTIQUIP INC.), 2011.

Pan, K. and Yang, Z. X. (2018). Effects of Initial Static Shear on Cyclic Resistance and Pore Pressure Generation of Saturated Sand. Acta Geotechnica 13, 473–487.

TM 5-1300. (1990). Structures to Resist the Effects of Accidental Explosions. Departments of the Army, the Navy, and the Air Force.

Tsuchida, H. (1970). Prediction and Countermeasure against the Liquefaction in Sand Deposits, pp. 3.1-3.33 in Abstract of the Seminar in the Port and Harbor Research Institute in Japanese.

Wu, J., Kammerer, A.M., Riemer, M.F., Seed, R.B., and Pestana, J.M. (2004). Laboratory Study of Liquefaction Triggering Criteria. 13th World Conference on Earthquake Engineering. Vancouver, B.C., Canada. August 1-6, Paper No. 2580.

Xu, T. (2005). Numerical simulation of embankment dams subjected to blast loadings, PhD Thesis. The Hong Kong University of Science and Technology, Hong Kong.

Chapter 6 Synthesis and Integration of the Results

6.1 Introduction

The blast response of the retaining wall with sand backfill is strongly influenced by the variations in the applied blast load intensities, relative densities and degrees of saturation of the backfill.

The probability of RW failures rises with an increase of the lateral earth pressure and/or excessive displacement of the RW. Therefore, the dynamic lateral earth pressure behind the RW was evaluated in Chapter 3, and the modes of RW movement were addressed in Chapter 4.

When saturated soil is subjected to rapid dynamic loads that prevent outflow of water, undrained conditions occur. As a result, a buildup of excess pore water pressure may happen, which might trigger liquefaction. Thus, the effect of pore pressure in the backfill and the foundation of the RW was discussed in Chapter 5.

Ten tests were conducted on the soil-RW model using the shock tube at the Blast Research Laboratory of the University of Ottawa. An L shape reinforced concrete retaining wall model with sand backfill material was placed inside a box. The overall height of the box was 1565 mm. The retained backfill extended behind the wall for 1300 mm, which was double the stem's height. The dimensions of the stem and heel of the retaining wall were 650 mm (height) x 500 mm (width) x 60 mm (thickness) and 400 mm (width) x 500 mm (length) x 60 mm (thickness), respectively. The influence of various relative densities, blast load intensities, degrees of saturation of the backfill, and live load surcharge on soil-RW's dynamic response was addressed. The soil-RW model was placed at the centre of the shock tube's mouth. The rest of the shock tube mouth was covered with a very stiff steel plate. The test specimen was attached to the shock tube by straps to prevent the specimen from moving away from the shock tube during the blast test. The backfill material was removed from the box after each test. Then the sand was mixed and reused to refill the box. The backfill material was compacted to meet the required compaction level for each test.

6.2 Blast Induced Lateral Earth Pressures

In chapter 3, the dynamic earth pressure was determined for sand backfill with various relative densities, degrees of saturation, and live load surcharge when subjected to different blast load intensities. Soil pressure gauges were used to measure the dynamic earth pressures. The readings from these gauges represent the total lateral earth pressure (static and dynamic) induced by blast loading.

It was noticed that the lateral earth pressures for dense backfill were slightly below the lateral earth pressures for loose and medium backfill. Furthermore, the lateral earth pressures increased with the increase in blast load intensities. This can be explained by the proportional relationship between the blast pressure wave and the acoustic impedance (Equation 3.2). Increasing the blast load intensity led to the generation of higher compressive wave velocity and consequently higher pressure in the backfill. However, increasing the backfill density caused a reduction of compressive wave velocity and thus dropped the pressure in the backfill.

It was observed that the dynamic earth pressure increased with depth, and it formed a triangular like shape. Similar results were obtained by some researchers (Kloukinas et al., 2015, Mikola et al. 2013 and Al-Atik, 2008) when centrifuge and shaking table tests were carried out. They concluded that the dynamic earth pressure has a triangular shape and that the point of the dynamic thrust is 0.33 H above the wall base.

The development of internal resistance for the retaining wall to resist blast loads was investigated using experimentally obtained force-deformation relationships in the form of resistance functions.

It was observed from the results that the maximum resistance of the section was below the ultimate resistance of the wall. The moment capacity of the RW was determined in section 3.4.4.

6.3 Effect of Blast Loads on the Modes of Wall Movement

Chapter 4 addressed the lateral displacement time histories of the wall and the sand backfill with various relative densities, degrees of saturation, and live load surcharge when subjected to different blast load intensities. The ProAnalyst software was used to capture the soil particles' movement and track the transient and permanent displacements of the wall.

The results showed that failure mode was evident in the retaining wall with loose sand backfill. This can be explained by the fact that under the same load condition, loose sand exhibited the largest lateral deformations in the wall and the backfill in comparison with medium and dense states. The RW with loose sand backfill slid about 25 mm toward the backfill, and a translation response mode was obvious in this condition. The support provided by loose sand backfill is limited as loose sand contains higher void ratio than medium and dense conditions. When compressive load is applied on the loose sand, it tended to decrease in volume and rearrange the soil particles. As a result, soils with higher void ratio are more susceptible to larger deformations. On the other hand, it was observed that under the same relative density of the backfill, increasing the blast load intensity resulted in more significant deformations at the wall and the backfill. Applying high intensity blast load led to the generation of higher compressive wave velocity and thus higher shear stress in the sand.

Based on the finding of this chapter, it was concluded that violation of the equilibrium of the RW could occur in two situations: (i) when the backfill in loose or medium condition, with relative density less than 50%, was used; and (ii) when blast load with high intensity was applied.

In addition, the nonlinear force-displacement capacity of the bridge abutment was developed from the mobilized passive pressure of the RW backfill. The results showed a possible formation of passive wedge failure in loose and medium backfill conditions, which explains the large deformations in these conditions. The passive capacities of the backfill were not reached in dense backfill, regardless of the blast load intensities that were used in this study.

It is important to mention that when the permanent displacements and failure modes of a RW under dynamic loads are identified, using performance-based design concepts, engineers would be able to analyze and design retaining walls based on performance level and desirable failure patterns.

Furthermore, soil stiffness and maximum displacement that occurred when the ultimate force was applied on the RW was provided by the force-displacement relationship. This relationship provides key information with regards to abutment/RW soil capacity when a bridge is designed for dynamic loads.

6.4 Effect of Blast Loads on Pore Pressures Development

In chapter 5, the development of excess pore pressure in the sand backfill behind the retaining wall induced by blast loading was investigated. Pore water pressure sensors were used to measure the pore water pressures in the backfill and the foundation.

The pore pressures were determined for all conditions, and the RW with the saturated dense sand condition was examined to determine if liquefaction was triggered by blast loading. The definition of liquefaction can be related to the following factors: (i) excess pore pressure, (ii) shear strength of the soil, (iii) shear strain/deformation of the soil.

The excess pore pressure ratio was calculated for saturated sand to investigate whether there was a pore pressure build-up. The results showed that the ratio was less than 1, and therefore, liquefaction was not triggered based on pore water pressure-based criteria.

The shear strain was calculated from the lateral deformation of the saturated backfill and the maximum shear strain was below 0.6%. The flow shear strain's initialization occurred when the maximum single amplitude shear strain reached about 3% (Wu et al., 2004). Therefore, flow shear strain was not initialized, and consequently, soil liquefaction was not triggered based on the shear strain or deformation-based criteria.

For strength-based criteria, in order for liquefaction to occur, the shear stress at any depth of the backfill sand induced by dynamic loads should be equal or greater than the shear strength. The shear strength of the sand can be determined using the dynamic triaxial test or cyclic shear test. The shear stress was calculated in chapter 5, while the shear strength tests were beyond the scope of this study. Thus, the strength-based criteria were not used to define liquefaction.

Based on the findings of this chapter, it can be concluded that liquefaction was not triggered when the RW with saturated backfill was subjected to a blast load of 50 kPa. It seems that when a RW with dense backfill is subjected to blast loading, it can keep its structural integrity even if the backfill becomes saturated. Liquefaction or cyclic mobility is unlikely to happen in dense saturated sand. However, more tests using higher blast pressures need to be done to confirm this statement.

6.5 Stability and Design of RW Resistant to Blast Loads

The results and observations from the simulated blast load experiments using a shock tube can be used to provide design recommendations for blast resistant cantilever retaining walls with sand backfill. The effects of static lateral earth pressures, dynamic earth pressure increments and inertial forces of the wall should be considered to effectively design RWs. On the other hand, the magnitude and distribution of lateral earth pressures on the RW are affected by the wall’s movement. The results showed that applying blast load on the RW with loose sand backfill led to an increase in the earth pressures and wall movements in comparison with other backfill conditions.

When abutments/retaining walls are subjected to a blast load that induces lateral pressure, a nonlinear dynamic response occurs. The response is dependent on the nonlinear soil-structure interaction effects between the abutments and the backfill soils (Shamsabadi et al., 2007). As mentioned in section 4.4.3, wall movement is a function of backfill shear strain and mobilized shear strength. Therefore, the relative displacement was used to determine if the active state or the passive state was developed. In this study, force-displacement relationships were determined for different relative densities and various blast load intensities (Figure 4-17) using the mobilized passive resistance of the RW backfill. This relationship provides crucial information concerning abutment/RW soil capacity when a bridge is designed for dynamic loads. These data can be used in the computation of the resistance function of the retaining structure.

The resistance function is a relationship between force and deflection that defines strength and stiffness of a structure. This relation is important to determine the dynamic response of a structure or of a member. The resistance function is one of three sets of data that are required for SDOF dynamic analysis. The other two sets of data are impulsive forcing function and RW mass. The latter sets of data are available for any structural element. The calculation procedure for these three parameters was addressed in chapter 3 section 3.4.5.

6.6 References

Alainachi, I. H. (2020). Shaking Table Testing of Cyclic Behaviour of Fine-Grained Soils Undergoing Cementation: Cemented Paste Backfill. Doctoral thesis, University of Ottawa, Ontario, Canada.

Al Atik, L. F. (2008). Experimental and Analytical Evaluation of Seismic Earth Pressures on Cantilever Retaining Structures. Doctoral thesis, University of California, Berkeley.

Altaee, A. and Fellenius, B. H. (1994). Physical Modeling in Sand. Canadian Geotechnical Journal 31, 420-431.

Kloukinas, P., Scotto di S., Anna, P., Augusto, D., Matthew, E., Aldo, L. Simonelli, A., Taylor, C., Mylonakis, G. (2015). Investigation of Seismic Response of Cantilever Retaining Walls: Limit Analysis vs Shaking Table Testing. Soil Dynamics and Earthquake Engineering, 77, 432–445.

Mikola, R. G. and Sitar, N. (2013). Seismic Earth Pressures on Retaining Structures in Cohesionless Soils. Department of Civil and Environmental Engineering University of California, Berkeley.

SCDOT (2010). Geotechnical Design Manual, Chapter 14 Geotechnical Seismic Design.

Shamsabadi, A., Rollins, M. K., and Kapuskar, M. (2007). Nonlinear Soil–Abutment–Bridge Structure Interaction for Seismic Performance-Based Design. Geotechnical and Geoenvironmental Engineering, 133, 6.

Wu, J., Kammerer, A.M., Riemer, M.F., Seed, R.B., and Pestana, J.M. (2004). Laboratory Study of Liquefaction Triggering Criteria. 13th World Conference on Earthquake Engineering. Vancouver, B.C., Canada. August 1-6, Paper No. 2580.

Chapter 7 Summary, Conclusions and Recommendations

7.1 Summary and Conclusions

The following conclusions can be drawn from the present study:

1. The dynamic earth pressures were measured at selected locations in the backfill and foundation layer using soil pressure gauges. The maximum dynamic earth pressure responses were at time greater than the positive phase duration regardless of the backfill condition. From total earth pressure distribution along the height of the wall, it was noticed that the magnitude of total earth pressure for loose and medium backfill at the mid-height of the wall slightly exceeded the dense backfill. In addition, an increase in blast load intensities led to an increase in the lateral earth pressures.
2. Relationships between the dynamic earth pressure coefficient (ΔK_{bd}) and accelerations of the wall and backfill were developed. The dynamic earth pressure coefficient was calculated from the dynamic thrust.
3. Theoretical values for the moment capacity of the retaining wall and the ultimate resistance were calculated. The blast resistance of RCRW under different conditions was studied using experimentally obtained force-deformation relationships in the form of resistance functions. The blast resistance of the RW reached its maximum value when a high-intensity pressure was applied, but it was still below the design capacity of the section.
4. The modes of RW movement was assessed by measuring the lateral displacement of the stem and the backfill. A translation response mode was evident when loose backfill was used. Reduction in the lateral displacement of the soil-RW was observed in the dense backfill condition however, increasing the blast load intensity led to an increase in the

lateral displacement. Moreover, under fully saturated backfill and live load surcharge conditions, the wall movement was reduced.

5. The nonlinear force-displacement capacity of the RW was developed from the mobilized passive pressure of the RW backfill. A possible formation of passive wedge failure was noticed in medium and loose conditions. The passive capacities of backfill were not reached in dense backfill, regardless of the blast load intensities that were used in this study.
6. Settlement time histories for RW/backfill showed that there were large deformations in loose and medium backfill. On the other hand, for all the tests, a reduction was observed in the vertical displacements with distances further from the RW. Minimal settlements were noticed in dense sand with different blast load intensities and various degrees of saturation. Additionally, there were no settlements in the RW for all conditions.
7. The PPVs were determined using ProAnalyst software. The measured velocities were taken at depths of 200 mm and 400 mm. The sand backfill peak particle velocity time histories showed that an increase in the blast load intensity caused higher PPV.
8. Acceleration time histories for RW/backfill showed that there was a time-lag between the acceleration responses of the wall and the loose backfill. The RW with loose backfill exhibited higher acceleration than the RW with medium and dense backfill under the same load intensity. Furthermore, the highest acceleration responses for the wall and backfill were developed when the RW with dense backfill was subjected to a reflected pressure of 71 kPa.
9. The development of excess pore pressure in the sand backfill behind the retaining wall induced by blast loading was investigated. Pressure sensors were used to measure the pore water pressures in the backfill and the foundation. The results showed that the maximum

pore pressure responses for saturated backfill were at a time greater than the positive phase duration, while the maximum pore pressure response for the foundation was at the end of the positive phase duration. The excess pore water pressure ratios for saturated backfill were determined, and it was noticed that the ratios were less than 1. The susceptibility of the RW with saturated dense sand to liquefaction was examined. It was ascertained that liquefaction was not triggered based on pore water pressure-based criteria and shear strain-based criteria.

7.2 Recommendations for Future Work

The following recommendations are suggested for future research projects:

1. Taking into consideration the restricted testing area, the RW was modelled at the 1/10th scale. Therefore, using a larger scale of 1/2 for example, can provide better representation of the in situ condition. The model can be subjected to similar boundary conditions of real retaining structures.
2. Conduct a numerical simulation study using a finite-element method. Full scale retaining wall can be modelled and subjected to the same environment and boundary conditions of real abutment/retaining walls. The current experimental model can be used to validate the numerical model. Then, the numerical model can be used to simulate various conditions and scenarios until failure occurs. Below are some situations that can be simulated in order to provide a greater understanding of RW behaviour:
    a. Increasing the blast load intensity, as the blast pressure in the shock tube is limited to 100 kPa;
    b. Using loose saturated sand backfill;
    c. Using different materials, such as silty sand for the foundation layer;

    d. Using various geometries and shapes of cantilever RW;
    e. Applying axial load on the top of the RW.

3. The soil/RW model in this study was subjected to blast pressures of 26 kPa, 47 kPa, and 71 kPa. It was noticed that the intensities of the shots were below the design capacity of the model. Thus, increasing the blast load intensity can provide further understanding of the geotechnical response of the RW.

Appendix

1- Design of the retaining wall:

Assumption of the wall cross section:

The height of the wall (H) = 6 m; the width of the base = 4 m; the thickness of the wall and the base = 0.6 m.

Soil parameters determined in the laboratory:

Friction angle (ϕ) = 34°

Dry unit weight of sand (γ_d) = 15 kN/m^3

Calculation of active earth pressure:

$$P_a = \frac{1}{2}\gamma H'^2 K_a$$

$$K_a = tan^2(45 - \frac{\emptyset}{2})$$

$$H' = H_1 + H_2$$

$$H' = 5.9 + 0.6 = 6.5\, m$$

$$P_a = 88.72\,\frac{kN}{m}$$

$$K_a = 0.28$$

a- Check for overturning:

Section	Area (m^2)	Weight (kN/m)	Arm (m)	Moment (kN.m)
1	0.6 x 5.9 = 3.54	3.54 x 23.58 = 83.47	0.3	83.47 x 0.3 = 25.04
2	0.6 x 4 = 2.4	2.4 x 23.58 =56.59	2	56.59 x 2 = 113.18
3	3.4 x 5.9 = 20.06	20.06 x 15 = 300.09	2.3	300.09 x 2.3 = 690.2
Sum		**440.15**		**828.42**

Overturning moment (M_o)

$$M_\circ = Ph\left(\frac{H'}{3}\right) = 88.72\left(\frac{6.5}{3}\right) = 192.23\; kN.m$$

$$FS = \frac{\sum MR}{M_\circ} = \frac{828.42}{192.23} = 4.31 > 2 \quad OK$$

b- Factor of safety against sliding:

$$FS_{sliding} = \frac{\sum V tan(k_1\varphi_2) + Bk_2c_2 + Pp}{Ph}$$

$$k_1 = k_2 = \frac{2}{3}$$

Pp = 0

$c_2 = 0$

$$FS_{sliding} = \frac{440.15 \tan\left(\frac{2}{3} * 34\right)}{88.72} = 2.07 \; > 1.5 \; OK$$

c- Factor of safety against bearing capacity:

$$e = \frac{B}{2} - \frac{\sum MR - \sum M_\circ}{\sum V}$$

$$e = \frac{4}{2} - \frac{828.42 - 180.66}{440.15} = 0.528 \; < \; \frac{B}{6} = \frac{4}{6} = 0.666$$

$$q_{\max toe} = \frac{\sum V}{B}\left(1 + \frac{6e}{B}\right) = \frac{440.15}{4}\left(1 + \frac{0.528*6}{4}\right) = 197.19 \; kN/m^2$$

$$q_{\min heel} = \frac{\sum V}{B}\left(1 - \frac{6e}{B}\right) = \frac{440.15}{4}\left(1 - \frac{0.528 * 6}{4}\right) = 22.89 \; kN/m^2$$

$$qu = CN_cF_{cd}F_{ci} + qN_qF_{qd}F_{qi} + \frac{1}{2}\gamma B' N_\gamma F_{\gamma d}F_{\gamma i}$$

c = 0

q = 0

$$B' = B - 2e = 4 - 2(0.528) = 2.944 \; m$$

$$F_{\gamma d} = 1$$

$$F_{\gamma i} = (1 - \frac{\vartheta}{\varphi})^2$$

$$\vartheta = \tan^{-1}(\frac{Ph}{\sum V}) = \tan^{-1}(\frac{88.72}{440.15}) = 11.4^{\circ}$$

$$F_{\gamma i} = (1 - \frac{11.4}{34})^2 = 0.44$$

$$qu = \frac{1}{2}(15)(2.944)(66.19)(1)(0.44) = 643.05\,\frac{kN}{m^2}$$

$$FS = \frac{qu}{q_{max}} = \frac{643.05}{197.19} = 3.26\ > 3\ \ OK$$

2- Scale relation of the physical modeling

In order to extrapolate the results obtained from small-scale experiments to real structure behaviour, scaling relations should be developed. For instance, this relationship can be established considering the lateral earth pressure induced by blast loading on a model RW of 0.65 m height in relationship to a real RW of 6.5 m height. This relation combines the effects of geometric and stress scales. The geometric scale ratio (n) between the model and the prototype (or real structure) is expressed in Equation 1, while the stress scale ratio (N) between the model and the prototype is defined in Equation 2. Using these ratios can lead to extrapolation of all parameters (Table 1).

$$n = \frac{L_m}{L_p}$$

$$N = \frac{\sigma_m}{\sigma_p}$$

L_m is the length dimension in the model.

L_p is the length dimension in the prototype.

σ_m is the stress in the model.

σ_p is the stress in the prototype.

Below is an example that shows the calculation of the lateral earth pressure scale ratio:

$$\frac{P_m}{P_p} = \frac{0.5\gamma_m H_m'^2 K_{am}}{0.5\gamma_p H_p'^2 K_{ap}} = \frac{n^2}{1} = n^2$$

As: $\gamma_m = \gamma_p;\ K_{am} = K_{ap}$

P_m is the lateral earth pressure in the model.

P_p is the lateral earth pressure in the prototype.

γ_m is the soil density in the model.

γ_p is the soil density in the prototype.

K_{am} is the earth pressure coefficient in the model.

K_{ap} is the earth pressure coefficient in the prototype.

H_m is the height of the RW in the model.

H_p is the height of the RW in the prototype.

Scaling relations of the physical modeling approach (Altaee and Fellenius, 1994)

Parameters	**Full scale (real structure)**	**Model**
Linear dimension	1	n
Area	1	n^2
Volume	1	n^3
Acceleration	1	1
Stress	1	N
Strain	1	1
Displacement	1	n
Force	1	Nn^2